Bioresponsive
Molecular Imaging Probes

Sander van Duijnhoven

Bioresponsive Molecular Imaging Probes

PROEFSCHRIFT

ter verkrijging van de graad van doctor aan de
Technische Universiteit Eindhoven, op gezag van de
rector magnificus, prof.dr.ir. C.J. van Duijn, voor een
commissie aangewezen door het College voor
Promoties in het openbaar te verdedigen
op dinsdag 11 september 2012 om 16.00 uur

door

Sander Martinus Johannes van Duijnhoven

Geboren te Boekel

Dit proefschrift is goedgekeurd door de promotor:

prof. dr. H. Grüll

Copromotoren:
prof. dr. K. Nicolay
en
dr. M.S. Robillard

Committee:

prof. dr. H. Grüll
prof. dr. K. Nicolay
dr. M.S. Robillard
prof. dr. ir. L. Brunsveld
prof. dr. T.M. Hackeng
prof. dr. M. Schäfers
prof. dr. O.C. Boerman
prof. dr. P.A.J. Hilbers (chairman)

Contents

Chapter 1

Introduction:

Bioresponsive molecular imaging probes

1.1 Molecular Imaging

Molecular imaging involves the non-invasive visualization and quantitative detection of biomolecules *in vivo* by means of target-specific probes (1-5). Valuable applications of molecular imaging are accurate disease detection, phenotyping, and staging by gathering information on molecular pathways underlying biological and cellular processes in the diseased tissue (1-6). Hence, molecular imaging is likely to play a pivotal role in the stratification of patients for personalized treatment. Furthermore, molecular imaging is clinical relevant in the discovery and development of drugs and for the real-time assessment of the efficiency and efficacy of drug therapy (7,8). Next, it can contribute to improved interventions by image-guided drug delivery and image-guided surgery (9-12). Finally, molecular imaging has impact in the development of regenerative medicine and stem cell therapies (6). In most molecular imaging approaches, target-specific molecular probes are engineered to enhance image contrast at the target site. These conventional targeting molecular imaging probes consist of a ligand that binds to an endogenous molecular target and an imaging label for readout. Typically, the molecular imaging probes are designed to be injected intravenously for targeting biomolecules accessible via the blood circulation. For example, the active site of enzymes has been targeted with conventional probes, providing a read-out for enzyme abundance (13). However, these probes lack the possibility to detect the *in vivo* enzymatic activity as they are typically limited to a 1:1 probe-target binding fashion. In that respect, a new subset of molecular imaging probes, known as bioresponsive molecular probes, has generated a lot of attention. These activatable probes exploit full advantage of the nature of the target. For example, protease bioresponsive probes have been directed to the active site of the enzymes resulting in the cleavage and activation of the imaging probe (14). Importantly, this will lead to signal amplification since the molecular target can continuously activate the imaging probe and, moreover, it offers a read-out of enzyme activity instead of enzyme abundance. Although bioresponsive probes have been mainly restricted to fluorescence and bioluminescence optical imaging, recent progress has led to the development of bioresponsive probes for multispectral optoacoustic tomography (MSOT), magnetic resonance imaging (MRI), and the nuclear imaging modalities single photon emission computed tomography (SPECT) and positron emission tomography (PET) (14-18). For optical imaging and MRI, bioresponsive probes have been reported that show signal amplification by direct activation of the imaging label (*i.e.* probes that go from an "off" to an "on" state) or by specific retention of the imaging probe at the site of interaction through a specific biological or chemical mechanism. Bioresponsive radiolabeled probes for SPECT/PET have been designed to show local retention and accumulation at the site of interaction (Table 1.1). In this Chapter, the rationale behind the design of bioresponsive molecular imaging probes will be discussed and their potential *in vivo* application will be highlighted for the detection of endogenous molecular targets.

Table 1.1: *Overview of the two major types of bioresponsive molecular imaging probes and their application in several imaging modalities.*

Bioresponsive Probes	Activation of Imaging Label	Local Retention
Optical Imaging	X	X
Magnetic Resonance Imaging	X	X
Nuclear Imaging		X

1.2 Bioresponsive optical probes: Activation of the optical imaging label

1.2.1 Protease sensitive bioresponsive optical probes

Proteases play crucial roles in physiology and pathology and have been identified as attractive targets for molecular imaging of a variety of diseases, including cancer, atherosclerosis, myocardial infarction, and neurological diseases (14-19). Multiple types of protease bioresponsive optical probes have been developed in the last decades that are specifically directed at the activity of the enzyme instead of enzyme abundance. These probes include fluorescent auto-quenched probes, self-quenched or homo-fluorescence resonance energy transfer (homo-FRET) probes, dual-labeled FRET probes, and luminescent probes (14-19).

Fluorescent auto-quenched probes
Auto-quenched probes consist of peptide substrates typically linked via an amide to fluorescein/rhodamin spirolactam or spirolacton derivatives, which are essentially optically silent (20). The probe regains its fluorescence upon hydrolysis of the amide bond into an amine and subsequent ring-opening of the corresponding spirolactam/lacton (11,21-24) (Fig. 1.1). For example, a caspase-3 and -7 auto-quenched probe was designed by conjugating the peptide substrate DEVD to a rhodamine sphirolacton derivative. Release of DEVD peptide by intracellular caspase-3 or -7 resulted in ring-opening of the sphirolacton, followed by a strong enhancement of fluorescence (25) (Scheme 1.1).

So far, these probes use fluorophores that emit light in the visible region. Compared to visible light, near-infrared radiation penetrates tissues more efficiently, up to several centimeters, and show decreased absorption by natural proteins like hemoglobin (15,26,27). Therefore, the development of auto-quenched probes based on near-infrared fluorophores is the most promising route towards *in vivo* applications to visualize specific proteases.
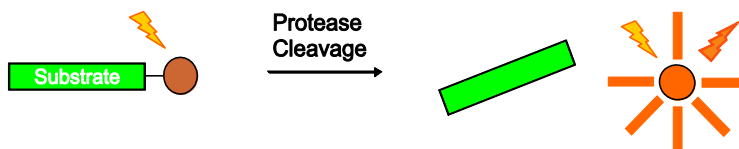
Figure 1.1: *Auto-quenched probe. Attachment of a protease substrate to a fluorophore is designed to result in a non-fluorescent structure. Proteolytic removal of the substrate results in the restoration of fluorescence.*
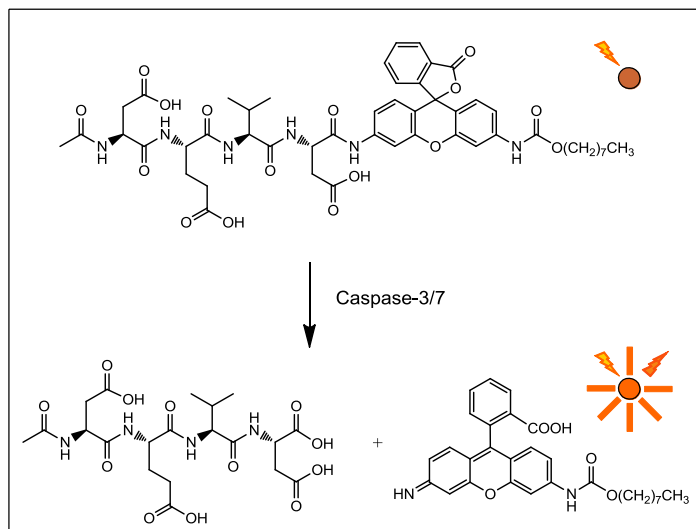
Scheme 1.1: *A caspase-3/7 sensitive auto-quenched probe. The rhodamine fluorophore is activated upon release of the DEVD peptide substrate by caspase-3/7 (25).*

Fluorescent self-quenched probes

Self-quenched probes or homo-FRET probes are typically large molecular imaging probes that make use of multiple near-infrared fluorophores that are in close proximity to each other. When excited, the fluorophores absorb energy from each other resulting in self-quenching. The efficiency of energy transfer between the fluorophores is given by:

$$E = \frac{R_0^{\,6}}{R_0^{\,6} + r^6} \qquad [1.1]$$

where r is the distance between the fluorophores (Å) and R_0 is the Förster distance (Å) (28). The Förster distance R_0 is the distance at which the energy transfer efficiency is 50% and is typically in the range of 20-60 Å. Proteolytic activation of these probes liberates the fluorophores, resulting in the loss of homo-FRET, activating fluorescence.

Weissleder and coworkers functionalized a poly-*L*-lysine backbone with methoxy-terminated poly(ethylene glycol) and multiple self-quenched near-infrared Cy5.5 fluorophores. Degradation of the poly-*L*-lysine backbone by lysosomal cysteine/serine proteases resulted in liberation and activation of the fluorophores (29-33). The range of applications of these macromolecular probes (molecular weight of 450-500 kDa), was extended by inclusion of various peptide substrates between the fluorophores and the backbone (Fig. 1.2). Following this approach, activatable probes were developed for a variety of enzyme targets like caspase-1, cathepsins D, E and K, HIV-1 protease, urokinase, and matrix metalloproteinase-2 and -9 (34-45). For example, matrix metalloproteinase-2 (MMP-2) selectivity was achieved by inserting the peptide GPLG-VRGK, an MMP-2 sensitive peptide sequence,

between the backbone and the fluorophore (42). This probe showed a 3-fold enhancement in fluorescence signal in tumor xenografts overexpressing MMP-2, compared to tumor xenografts that were treated with an MMP inhibitor (Fig. 1.2). These self-quenched imaging probes have been applied for *in vivo* protease detection in cancer, atherosclerosis, arthritis, and heart failure in rodent models (29-46).

Protease	Substrate	Ref
Caspase-1	GWEHD-GK	34
Cathepsin D	GPIC$_{Et}$F-FRLGK	35
Cathepsin E	AGFSL-PAGC	36
Cathepsin K	GHPG-GPQK	37
HIV-1 protease	GVSQNY-PIVGK	38
Urokinase	GGSGR-SANAK	39
MMP-2	GPLG-VRGK	40-43
MMP-2 / MMP-9	GGPRQ-ITAG	44,45
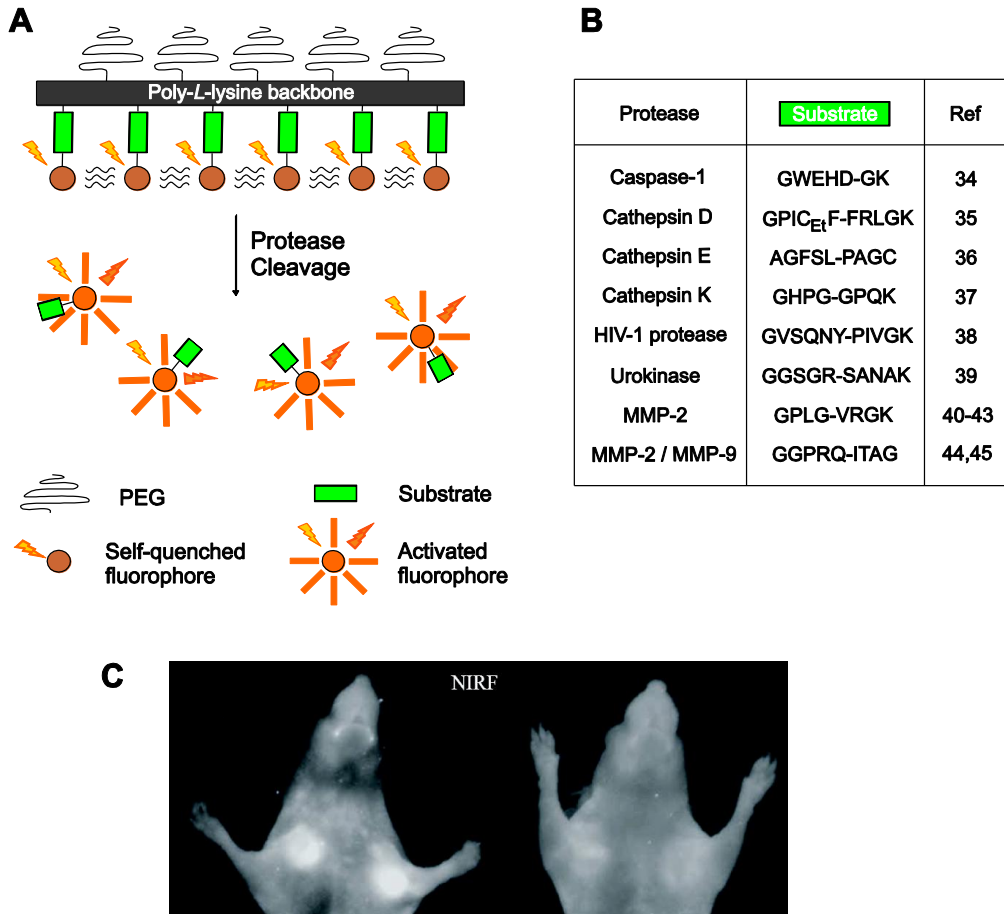
Figure 1.2: *(A) Schematic representation of a self-quenched polymer-based probe. Multiple fluorophores coupled to a backbone lead to self-quenching of the fluorophores. Upon proteolytic degradation of the probe, the fluorescence is restored. (B) The table shows applied peptide substrates resulting in the development of a variety of enzyme-specific self-quenched probes (34-45). (C) In vivo near-infrared fluorescence (NIRF) image of MMP-2 positive HT-1080 tumor-bearing animals using an MMP-2 sensitive self-quenched probe. A 3-fold higher fluorescent signal was observed in tumors of untreated tumor-bearing mice (left) compared to tumor-bearing mice that were treated with the MMP inhibitor prinomastat (right). Figure C is reprinted with permission from (42).*

In recent years, several other activatable self-quenched fluorescent imaging probes have been developed for protease sensing. An MMP-9 sensitive liposomal nanoparticle was developed that showed protease triggered release and activation of encapsulated fluorophores in the presence of MMP-9 (47,48). Here, MMP-9 cleavable lipopeptides were incorporated into the liposome bilayer. Degradation of the lipopeptide resulted in destabilization of the bilayer and subsequent leakage and activation of the fluorescent dyes that were present in the lumen of liposomes (Fig. 1.3).
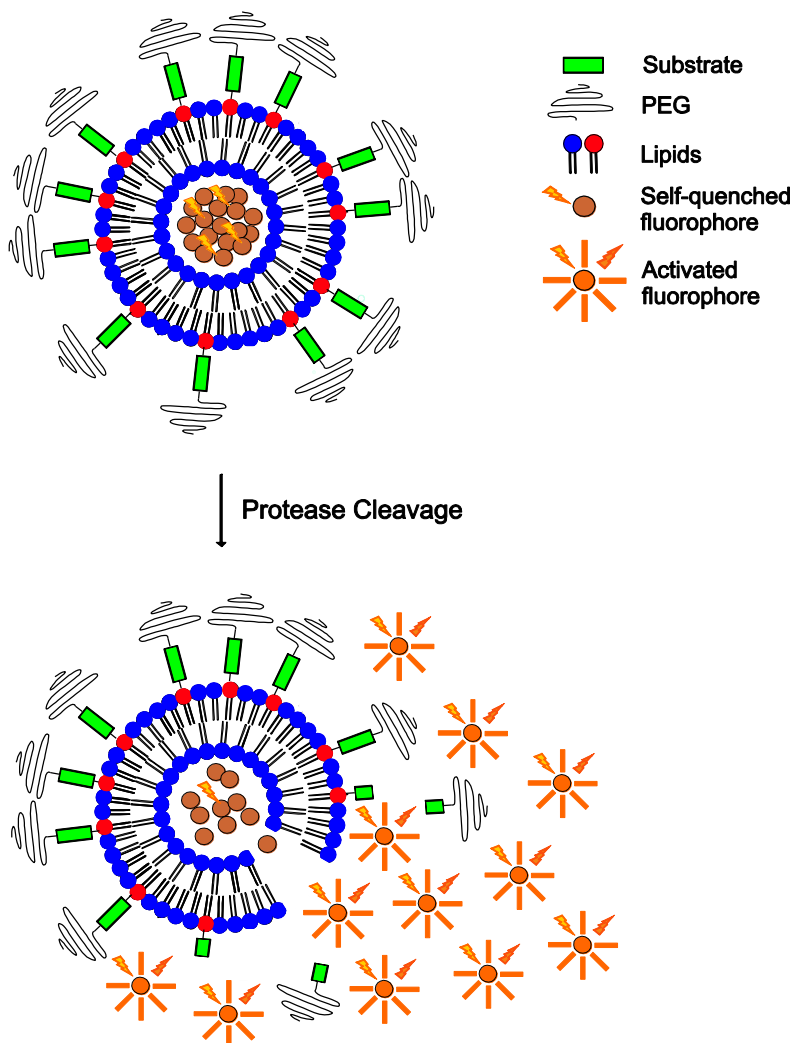
Figure 1.3: *Depiction of a self-quenched probe based on protease-degradable liposomes. Multiple fluorophores encapsulated in the aqueous lumen of a liposome lead to self-quenching of the fluorophores. Upon proteolytic degradation, the liposomes fall apart and the fluorophore is released resulting in restoration of fluorescence.*

Another activatable self-quenched approach focused on the protease triggered release and activation of fluorophores from a nanofiber precursor for the detection of urokinase activity (49). The probe was composed of a self-assembling peptide sequence to which a fluorophore was coupled via a urokinase sensitive peptide moiety. Spontaneous self-assembly of the peptide probe resulted in an optically quenched nanofiber, in which the fluorophore was released and activated upon urokinase digestion *in vitro*. In a similar approach, a near-infrared triple helical peptide-based optical probe was developed. Each peptide strand was flanked by two NIR fluorescent dyes. In the triple-helical structure, the fluorescence was reduced due to quenching. *In vivo* studies in tumor-bearing mice showed MMP-mediated degradation of the triple-helical peptide in tumors, resulting in the local release of fluorophore labeled peptides and amplification of the fluorescent signal (50).

Fluorescent dual-labeled FRET-probes
The common feature of protease sensitive dual-labeled FRET-based molecular imaging probes is the loss of FRET between a donor fluorophore and a distinct acceptor fluorophore or non-fluorescent quencher upon enzymatic degradation of a substrate initially holding the fluorophores together. For the first class, the distance between the two distinct fluorophores, typically smaller than Förster radius (Equation 1.1), results in efficient FRET from the donor fluorophore to an acceptor fluorophore yielding predominantly light emission of the acceptor fluorophore. Proteolysis of the peptide substrate results in separation of the fluorophores and loss of energy transfer (Fig. 1.4A). For the second class, efficient energy transfer will take place between the donor fluorophore and a non-fluorescent quencher, resulting in a low fluorescent signal from the donor fluorophore. Degradation of the substrate results in the dissociation of the fluorophore-quencher pair and leads to a significant enhancement in fluorescence (Fig. 1.4B). A wide variety of FRET-probes, also classified as peptide-based molecular beacons, has been described in the literature (51-71).
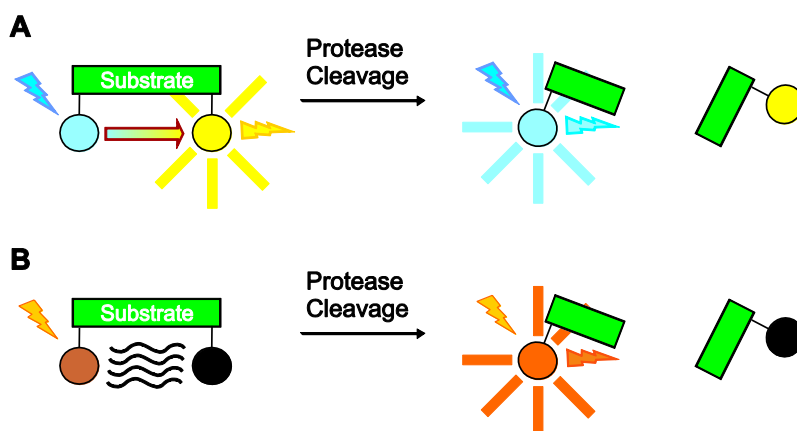
Figure 1.4: *Dual-labeled FRET-based probes, based on protease substrates labeled with (A) two distinct fluorophores or (B) a fluorophore-quencher pair.*

Genetically encoded fluorescent sensors consisting of two distinct fluorescent proteins are generally aimed for the colorimetric detection of intracellular proteases such as caspases or kinases (51,52). These probes typically consist of a protease cleavable substrate (51) or a conformationally responsive domain (52) sandwiched between two mutants of the green fluorescent protein (GFP) capable of FRET. Degradation of the cleavable substrate or a protease-induced conformational change of the linker domain is associated with a change in distance between the two fluorescent proteins and thus a change in FRET. For example, the genetically encoded caspase-sensitive FRET probe consisted of a cyan fluorescent protein (CFP) and a yellow fluorescent protein (YFP) joined by a peptide domain sensitive for caspase-1 or caspase-3 (51). Proteolysis of the peptide domains significantly enhanced the distance between CFP and YFP, and resulted in a decrease in FRET. Recently, novel genetically encoded biosensors have been reported that visualize MMPs at the extracellular surface of the cell membrane (53-55). However, a specific limitation of these genetically encoded probes for *in vivo* molecular imaging is the need for gene transfection of the corresponding gene, which makes this approach a research instrument rather than a tool for clinical translation.

In other strategies, organic near-infrared fluorophores have been successfully employed in low molecular weight activatable FRET-based probes. For example, an MMP-7 substrate was flanked with the organic Cy5.5 fluorophore and the organic near-infrared quencher NIRQ820 (56). A seven-fold increase in fluorescence was observed upon MMP-7 incubation. Recent research has resulted in the development of activatable organic FRET-probes specifically targeting extracellular proteases (57-65). One of these probes, a membrane-type matrix metalloproteinase sensitive probe, consisting of the MMP-14 peptide substrate GRIGF-LRTAKGG and a Cy5.5/BHQ-3 near-infrared (NIR) dye-quencher pair, was successfully used to detect MMP-14 activity in tumor-bearing mice (Fig. 1.5) (65). Moreover, intracellular enzymes have been effectively targeted with organic activatable FRET imaging probes. For example, cell-permeable caspase activatable probes were developed for the noninvasive detection of apoptosis *in vivo* (66-68). These probes consisted of a Tat-peptide-based permeation sequence and a caspase recognition sequence (DEVD) flanked by a near-infrared (NIR) dye-quencher pair.

Apart from organic fluorophores, inorganic particles like quantum dots and gold nanoparticles have recently been exploited as donor and acceptor pairs for energy-transfer based imaging probes (69,70). Gold nanoparticles demonstrated a 71% reduction of quantum dot photoluminescence as was shown for a matrix metalloproteinase-activatable quantum dot based luminescent probe (71). Quantum dots have advantages over organic fluorophores, such as strong fluorescence, higher photostability against bleaching and changes in physical environment, such as temperature and pH, and a narrow emission bandwidth. Nevertheless quantum dots have limitations for *in vivo* use due to potential cellular toxicity associated with Cd^{2+} or Se^{2-} ion release from the quantum dot core (72).
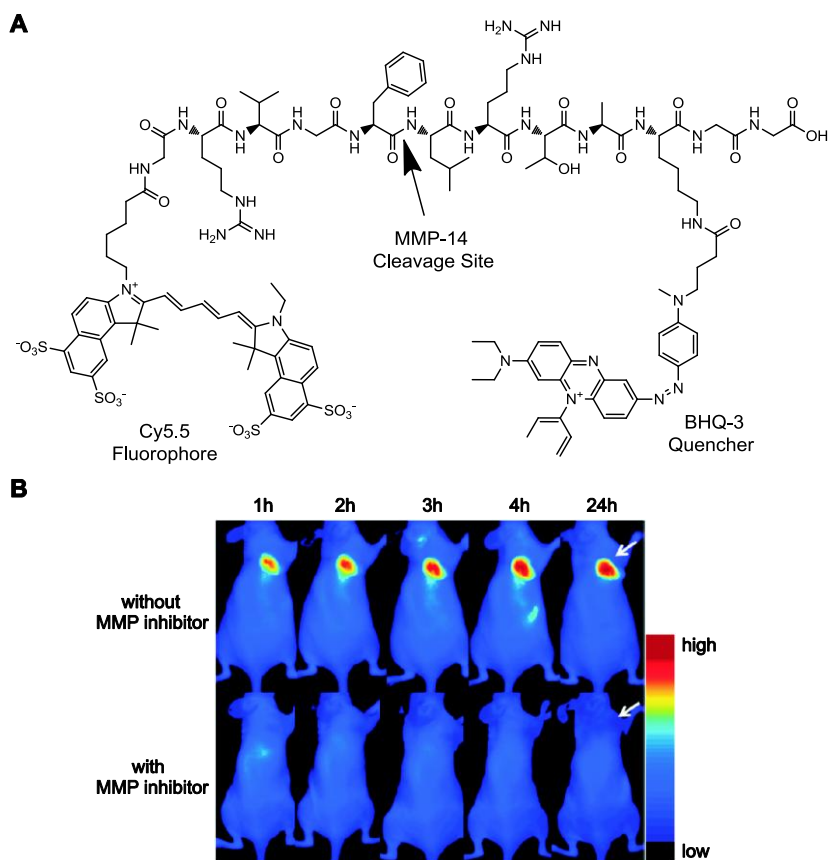
Figure 1.5: *(A) Molecular structure of the MMP-14 substrate GRIGF-LRTAKGG flanked by the NIR dye Cy5.5 and the NIR quencher BHQ-3. (B) In vivo NIRF image of MMP-14 positive MDA-MB-435 tumor-bearing animals using the MMP-14 FRET probe. A 3-to-4-fold higher fluorescent signal was observed in tumors of untreated mice (top row) compared to mice that were treated with the MMP inhibitor prinomastat (bottom row). Figure B is reprinted with permission from (65).*

Recently, the principles of FRET imaging and photodynamic therapy (PDT) have been combined into the development of enzyme activatable photodynamic molecular beacons (73-76). In photodynamic therapy (PDT), the cytotoxic agent $^1O_2$ is generated by light activation of a photosensitizer in the presence of oxygen (77). Furthermore, near-infrared light emission from the photosensitizer is typically observed. Activatable photodynamic molecular beacons have been developed for matrix metalloproteinase-7, caspase 3, and fibroblast activation protein, by flanking enzyme-specific substrates with a photosensitizer and a fluorescence/$^1O_2$ quencher (74-76). Near-infrared fluorescence imaging of a matrix metalloproteinase-7 sensitive photodynamic molecular beacon showed tumor-specific activation *in vivo*, suggesting tumor-specific delivery of the photosensitizer, which potentially will contribute to improved tumor-specific photodynamic therapy (74).

Bioresponsive luminescent probes

Bioluminescence is typically observed upon enzymatic oxidation of specific substrates by luciferases (78). In bioluminescence imaging, the light production does not rely on external excitation, and therefore background signals due to tissue autofluorescence are not present. Luminescent activatable probes, also known as caged luciferase substrates, combine the production of bioluminescence by luciferases with the enzymatic activity of other proteases. In these probes, *D*-luciferin, the substrate for luciferase, is typically protected by a specific enzymatic trigger (Scheme 1.2). The presence of the enzymatic trigger prevents the enzymatic oxidation of the probe by luciferase. However, upon enzymatic digestion of the trigger, *D*-luciferin is released and will produce a bioluminescent signal once consumed by luciferase. This strategy has been employed to visualize a variety of enzymes *in vivo* in disease, including β-galactosidase, β-lactamase, caspase, and furin (79-82). Similarly to fluorescent genetically encoded FRET probes, activatable luminescent probes are valuable for pre-clinical studies, but clinical translation is restricted due to need for gene transfection of the luciferase gene.
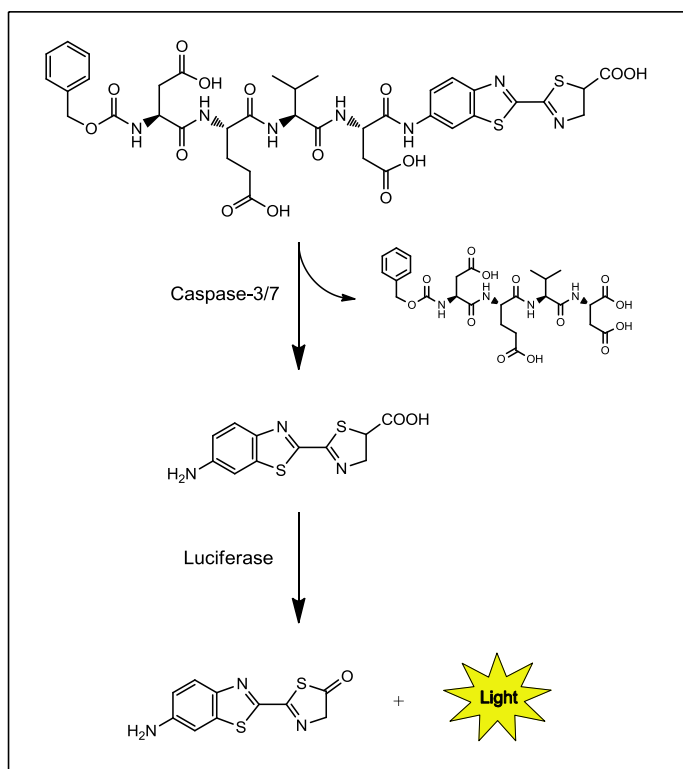
Scheme 1.2: *A caspase-3/7 sensitive activatable bioluminescent probe. D-luciferin is released upon cleavage of the DEVD peptide substrate by caspase-3/7 and is subsequently consumed by luciferase resulting in a bioluminescent signal (81).*

1.2.2 pH-sensitive optical probes.

The important role of intracellular pH in cell, enzyme, and tissue activity as well as the recognition that the tumor's extracellular microenvironment is relatively acidic compared to normal tissue has stimulated the development of pH-sensitive fluorescent imaging probes (83-93). In the early days, pH-dependent probes were aimed at the enhancement of fluorescence of the green fluorescent protein upon a decrease in pH (83). Other strategies focussing on pH-dependent activation of the fluorescent imaging label used pH-sensitive nanoparticles, *e.g.* liposomes or polypeptides that showed release and activation of fluorescence of self-quenched fluorophores at low pH (87-89). More recently, a variety of low molecular weight pH-sensitive auto-quenched fluorescent probes have been developed (Fig. 1.6). Most of these probes are specifically targeted to tumors and become fluorescent once accumulated in acidic lysosomes (90-92). For example, a near-infrared pH-activatable fluorophore conjugated to a RGD-peptide was successfully used for the targeting of $\alpha_v\beta_3$ integrin expressing tumors (92). Subsequent $\alpha_v\beta_3$ integrin-mediated internalization of the probe into acidic lysosomes resulted in an enhancement of fluorescence.
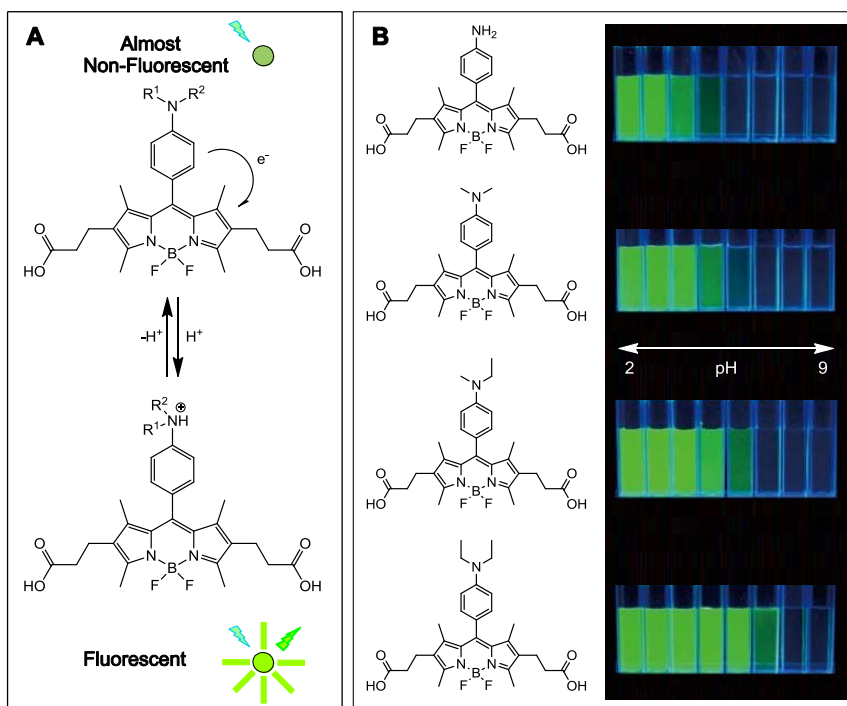
Figure 1.6: *(A) Reaction mechanism showing the reversible pH-dependent fluorescence activation of a pH-sensitive optical probe. In the native state, the probe is essentially non-fluorescent due to intramolecular photon-induced electron transfer from the aniline moiety to the fluorophore. Once protonated, the probe becomes highly fluorescent. (B) pH profiles of fluorescence for various pH-sensitive fluorescence probes. The pH ranges from pH 2 (left) to pH 9 (right) in single pH unit increments. Figure B is adapted with permission from (90).*

1.2.3 Optical probes activated by reactive oxygen/nitrogen species

Reactive oxygen species (ROS) and reactive nitrogen species (RNS) play a crucial role in maintaining normal physiology. However, excessive production of ROS/RNS has been associated to a variety of pathological diseases, such as cancer and cardiovascular disease (94,95). Activatable fluorescent imaging probes for ROS/RNS detection are mainly based on auto-quenched probes in which a fluorophore is coupled to a ROS/RNS trigger, resulting in a non-fluorescent molecule (20,96). Reaction of these probes with ROS/RNS results in the activation of the fluorescent moiety (Scheme 1.3). This approach has been extensively exploited resulting in activatable fluorescent probes for a variety of ROS/RNS, including hydrogen peroxide (H_2O_2) (97-104), peroxynitrite ($ONOO^-$) (105-109), superoxide (O_2^-) (110-112), nitric oxide (NO) (113-115), hypochlorous acid (HOCl) (105-107,116-118), and hydroxyl radical ($\cdot OH$) (107,119). Other imaging approaches have focused on the colorimetric detection of ROS/RNS (120-123) or used genetically encoded biosensors (124-126).

ROS/RNS imaging methods have been applied in *in vitro* cell culture experiments, but strategies to visualize ROS/RNS *in vivo* have been limited (105,127,128). The first *in vivo* study employed nanoparticles formulated from peroxalate esters and fluorescent dyes (127). Reaction of the peroxalate esters with hydrogen peroxide resulted in high-energy dioxetanedione intermediates that subsequently facilitated excitation of the encapsulated dye. This probe was used to detect hydrogen peroxide in the peritoneal cavity of mice during a lipopolysaccharide-induced inflammatory response. Hydrogen peroxide production was also visualized in tumor-bearing mice using a peroxy-caged luciferin-1 bioluminescent probe (128). Selective reaction of this probe with hydrogen peroxide released firely luciferin that subsequently was converted to a bioluminescent active moiety by firefly luciferase. This probe was studied in firefly luciferase tumor-bearing mice and showed tumor-specific activation. Panizzi *et al.* developed a ROS/RNS nanoparticle to which quenched oxazine reporters were conjugated (105). Release of the oxazine reporters by ROS/RNS interaction, in particular peroxynitrite and hypochlorous acid, resulted in restoration of its fluorescence. This nanoparticle was studied in a mouse model of myocardial infarction and showed enhancement of oxazine fluorescence in the infarcted areas of the heart.

1.2.4 Optical probes activated upon target binding

The final class of bioresponsive fluorescent imaging probes take advantage of a change in conformation upon binding to its target facilitating a change in FRET between a donor fluorophore and acceptor fluorophore or quencher. For instance, genetically encoded FRET sensors based on GFP-mutants allow the intracellular colorimetric detection of *e.g.* ATP, glucose, and metal ions like calcium, zinc, and cadmium (129-133). Shi and colleagues developed a FRET oligonucleic acid-based aptamer probe in which a fluorescent label was efficiently activated upon a conformational change of the probe induced by binding to a tumor-specific receptor *in vivo* (134) (Fig. 1.7). In another strategy, a FRET-quenched fluorophore of an oligonucleotide-based aptamer probe was activated upon binding to viral RNA in virus-infected cells (135).
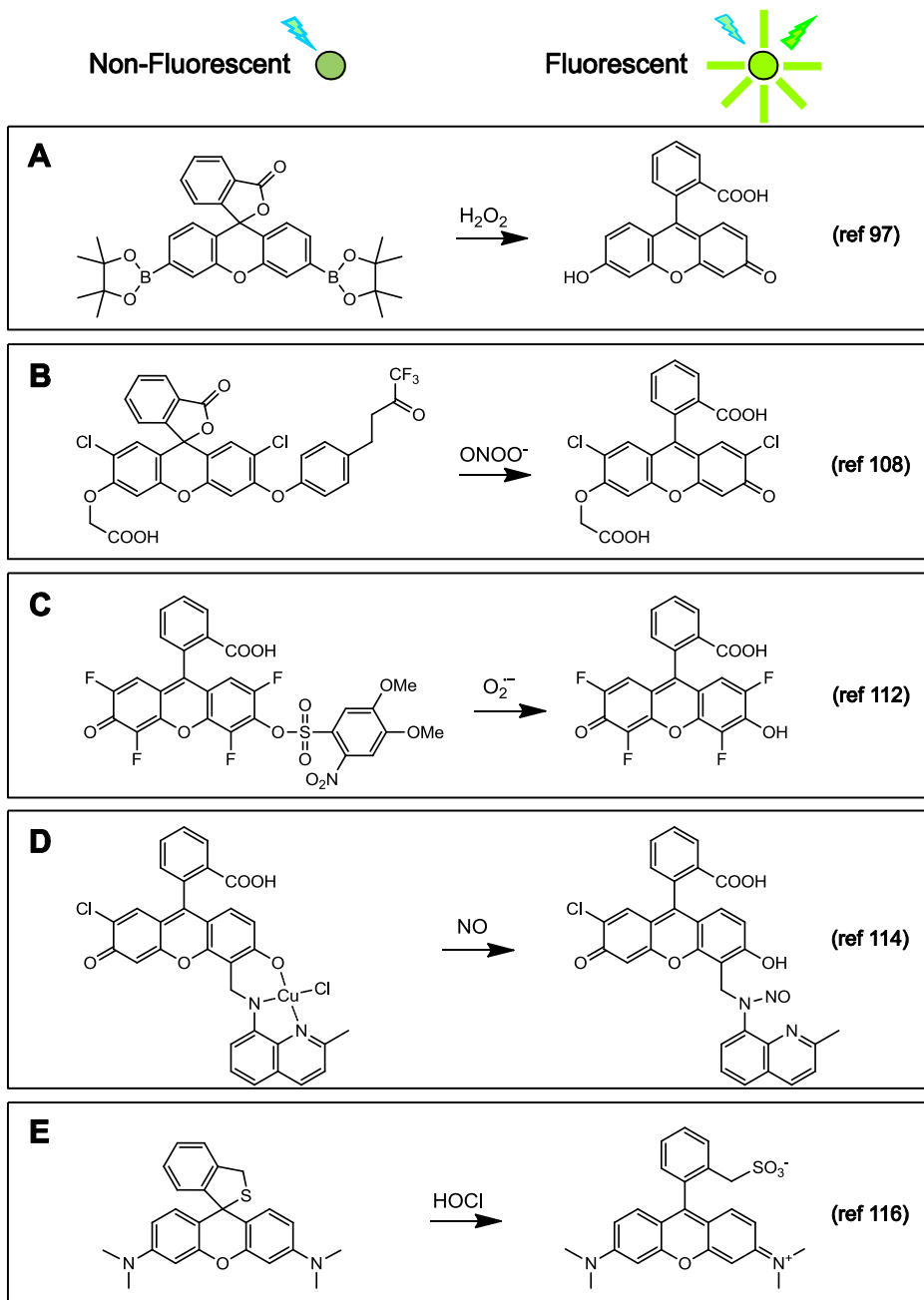
Scheme 1.3: *Reaction mechanism of various ROS/RNS activatable fluorophores. Shown are turn-on fluorescein derivatives for (A) hydrogen peroxide, (B) peroxynitrite, (C) superoxide, (D) nitric oxide, and (E) hypochlorous acid.*
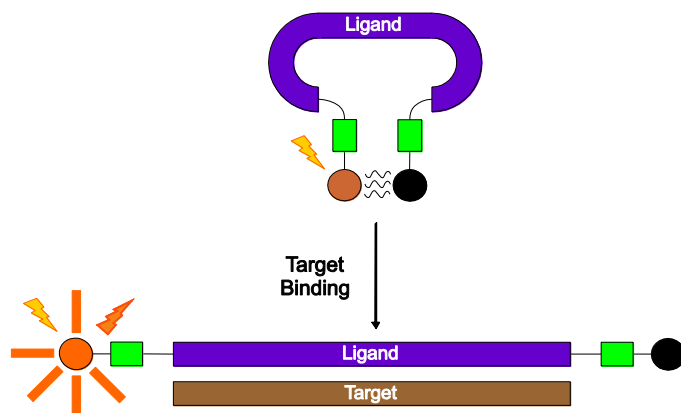
Figure 1.7: *Schematic representation of an activatable aptamer probe. In the absence of a target, the probe is typically in a hairpin conformation, resulting in quenched fluorescence. Upon target binding, its conformation is altered, resulting in activation of the fluorophore.*

1.2.5 Fluorescence life-time imaging

For most fluorescence techniques, the increased fluorescence intensity upon activation of the optical imaging probe is used as a measure of activation. Next to fluorescence intensity, the fluorescence lifetime (FLT) properties of the fluorophores change after the activation of the probe (136). The fluorescence lifetime describes the length of time between the excitation of a fluorophore and subsequent fluorescent emission and can be influenced by changes in the environment. For example, energy transfer between the donor and acceptor fluorophore in FRET-based imaging probes results in a lower quantum yield as well as decrease of the fluorescence lifetime of the donor fluorophore (137). Upon probe activation, the quantum yield and lifetime are restored, resulting in an increase in fluorescence intensity and lifetime of the donor fluorophore. Consequently, monitoring the fluorescence lifetime can be utilized to assess whether *in vivo* probe activation has occurred.

1.2.6 Multispectral optoacoustic tomography

Recently, it has been shown that near-infrared fluorophores can be used for multispectral optoacoustic tomography (MSOT) (138). This technique is based on the monitoring of ultrasonic signals generated in response to light absorption of fluorescent imaging probes and enables a reduction in scattering compared to traditional fluorescence imaging (15). Typically, near-infrared dyes are characterized by a relatively low quantum yield. Therefore, a major part of the extinction energy, more than 80%, is transferred to optoacoustic signals, which can be detected up to several centimeters in large animals and humans (15). A self-quenched MMP-2/9 probe (Fig. 1.2) as well as an MMP-2/9 sensitive FRET-probe has been successfully applied as optoacoustic imaging probes (15,139). Proteolytic degradation of these probes led to activation of fluorescence and a change in the spectral extinction characteristics of the donor fluorophores (Fig. 1.8), allowing high accurate 3-dimensional MSOT imaging of probe distribution in human carotid plaques (15).

14
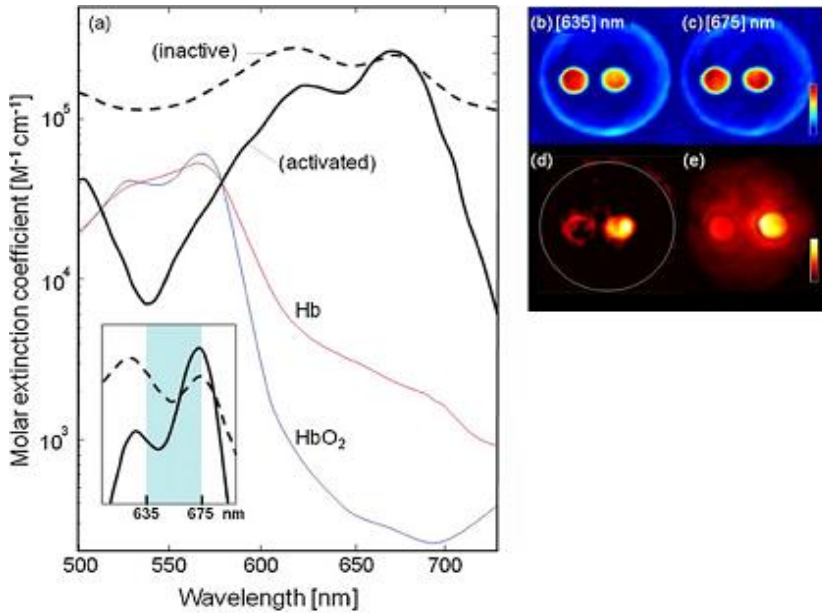
Figure 1.8: *(A) Extinction spectra of a non-activated (dotted line) versus activated (solid line) MMP-2/9 sensitive self-quenched probe. Extinction spectra of oxy- and deoxyhemoglobin (solid red and blue line, respectively) are shown for reference. The inset shows the wavelength range that was used for MSOT imaging. (B,C) Optoacoustic image of phantoms, containing the non-activated probe in the left insertion and the activated probe in right insertion, at 635 nm and 675 nm excitation, respectively. (D) Multispectrally resolved (MSOT) image showing the different state of the non-activated and activated probe. (E) Planar fluorescence image (top view) for the non-activated and activated probe showing the appearance of background due to light diffusion. Figure adapted with permission from (15).*

In summary, a unique feature of optical imaging is that the imaging probes can be turned on upon activation by a specific endogenous molecular target, allowing high target-to-background ratios compared to conventional targeting probes. However, the limited depth of light penetration through human tissue hampers the application of both optical and optoacoustic imaging probes for image-based whole-body *in vivo* diagnostics. Nevertheless, these probes have a high potential to find applications in imaging of surface-located tissues such as those encountered during endoscopic or optically guided surgical interventions (6,10-12,140-142).

1.3 Bioresponsive MRI probes: Activation of the MRI contrast agent

In contrast to optical imaging, magnetic resonance imaging (MRI) can be employed for whole-body diagnostic imaging. MRI presents an attractive platform for molecular imaging due to the conjunction of high resolution anatomical imaging and mapping of the activity of specific biomarkers by MRI contrast agents. Unlike optical or radiolabeled molecular imaging probes, MRI contrast agents, such as gadolinium chelates, do not directly generate a signal but are detected through their ability to shorten the water proton relaxation times, *i.e.* the longitudinal (spin-lattice) and transverse (spin-spin) relaxation times (T_1 and T_2, respectively) (143). In a T_1-weighted MRI image, T_1-shortening results in positive contrast (bright spots), whereas in a T_2-weighted image, T_2-shortening generates negative contrast (dark areas). The longitudinal relaxivity (r_1) of a contrast agent is modulated by several parameters (144,145), including the number of inner sphere water molecules directly coordinated to paramagnetic complex (q), τ_m the exchange rate of the metal-coordinated water molecule with the bulk water, and τ_R the rotational correlation time of the contrast agent (Fig. 1.9). Smart MRI contrast agents have been developed that show a change in one of these parameters upon interaction with a biochemical stimulus. Typically, these MRI contrast agents go from an "off" state, with minimal effect on T_1/T_2, to an "on" state, with large effect on T_1/T_2 shortening (17,145,146). In the next paragraphs MRI imaging probes will be discussed that generate a change in contrast as a result of activation of the MRI contrast agent.
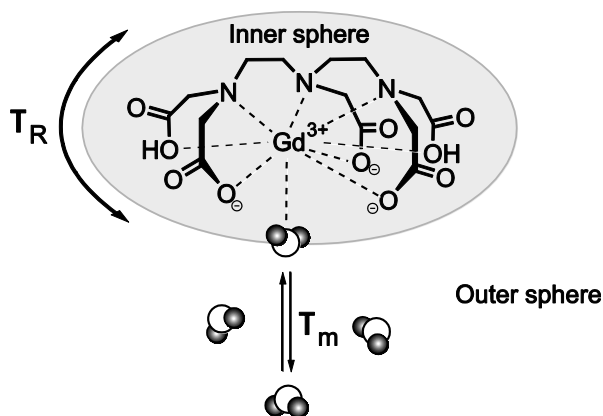
Figure 1.9: *Schematic representation of the most relevant parameters that influence the relaxation of a gadolinium-DTPA-based MRI contrast agent: the rotational correlation time (τ_R), and the mean residence time of the water molecules at the inner sphere (τ_m).*

1.3.1 Bioresponsive T_1–weighted MRI contrast agents

<u>Longitudinal relaxivity enhancement via modulation of water coordination sites</u>
Several strategies have been explored to enhance the longitudinal relaxivity of paramagnetic gadolinium complexes after its activation due to an increase in the number of water molecules directly coordinated to the metal centre (Scheme 1.4). The first enzymatic activatable agent has been reported by Meade and coworkers (147,148), in which the water coordination site of gadolinium complex was blocked with a galactopyranosyl ring. Its enzymatic cleavage by β-galactosidase resulted in opening of the water coordination site and efficient T_1-shortening. Another class of gadolinium based agents can interact with endogenous metal ions, such as Ca^{2+} and Zn^{2+}, resulting in an increase in water coordination sites and thus improved longitudinal relaxivity (149,150). A third class of activatable MRI contrast agents uses pH-responsive gadolinium chelates that display relaxation enhancement at acidic conditions (151-153).
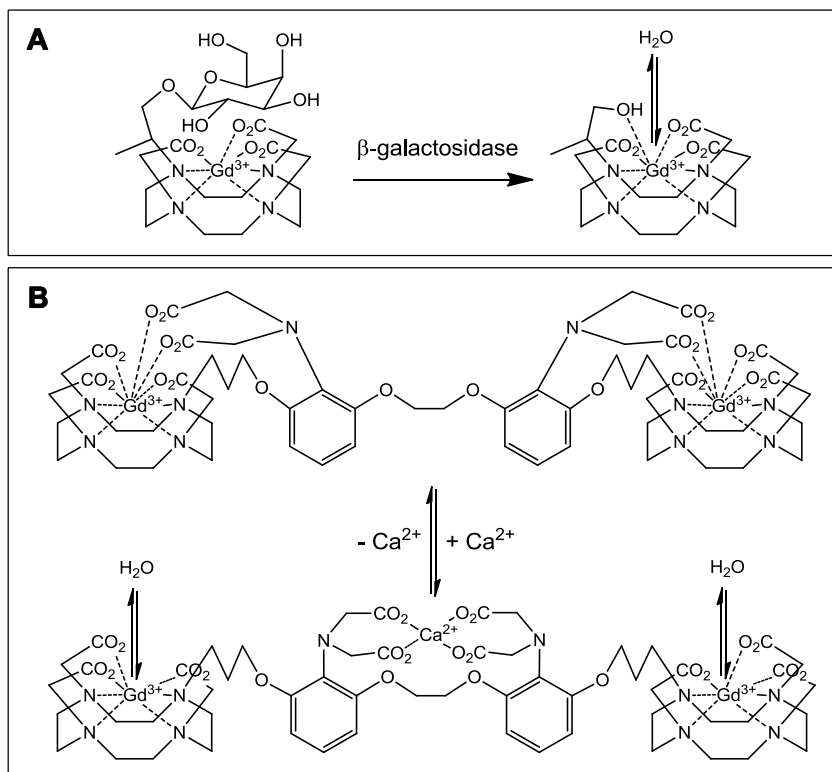
Scheme 1.4: Gd^{3+}-based MRI contrast agents displaying an increase in water coordination sites upon activation, and thus enhanced longitudinal relaxivity. (A) Enzymatic activation of a galactopyranosyl-masked Gd^{3+}-DOTA by β-galactosidase (148). (B) Activation of an MRI contrast agent by a conformational change upon Ca^{2+} target binding (149).

Changes in the longitudinal relaxivity of the protons of water molecules can also be modulated by reducing the water mobility as has been reported for pH sensitive liposomes containing gadolinium based complexes in its lumen (154,155). The liposomes are characterized by a limited transmembrane water exchange rate. Therefore, the gadolinium chelates encapsulated in the aqueous lumen of the liposomes have a low effect on the longitudinal relaxivity of the protons of the bulk water molecules. At low pH, the contrast agents are released and a strong increase in the longitudinal relaxivity is observed.

Relaxativity enhancement via modulation of rotational correlation time

T_1-shortening of the protons of water molecules can be achieved by slowing down the molecular tumbling rate of the paramagnetic complex ($1/\tau_R$) (156). Nivorozhkin and coworkers have developed a carboxypeptidase B activatable MRI contrast agent that gained affinity for the high molecular weight protein albumin upon activation resulting in a reduced tumbling rate and therefore higher relaxivity (157). In similar approaches, activatable albumin/protein binding Gd-based MRI contrast agents have been developed for the *in vitro* detection of β-galactosidase and carbonic anhydrase (158-160). In another approach, Gd-based MRI contrast agents showed polymerization upon specific activation by myeloperoxidase (MPO), resulting in a slower tumbling rate and therefore in an enhancement of the longitudinal relaxivity (161-165) (Fig. 1.10). In this approach, Gd-labeled phenol derivatives are oxidized by myeloperoxidase resulting in tyrosyl radicals, which will form dityrosine cross-links. Using this approach, MPO activity was visualized *in vivo* in a mouse model of myocardial infarction (162).
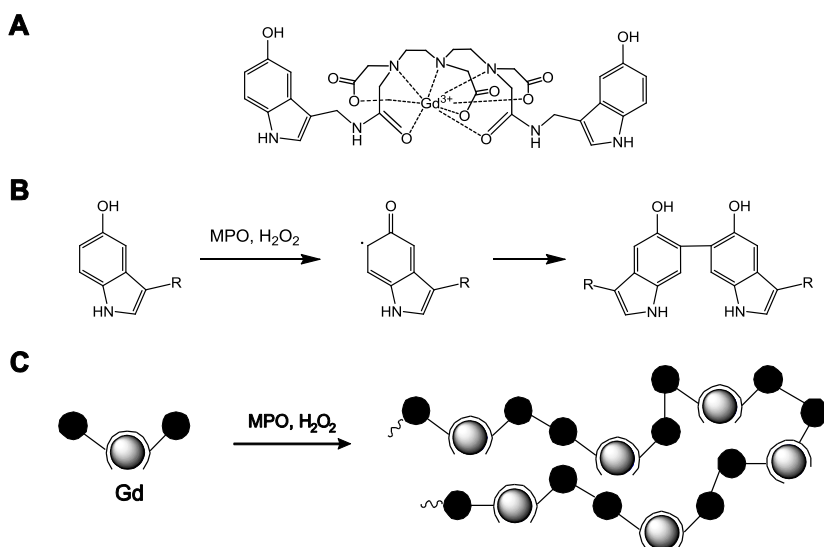
Figure 1.10: *(A) Chemical structure of a myeloperoxidase (MPO) polymerizable Gd^{3+}-DTPA based MRI contrast agent (161). (B,C) Mechanism of MPO catalyzed polymerization resulting in an increased local concentration of the MRI contrast agent Gd^{3+} and enhanced T_1-relaxivity.*

1.3.2 Bioresponisve T_2–weighted MRI contrast agents

Superparamagnetic iron oxide (SPIO) nanoparticles are widely used as T_2-weighted MRI contrast agents. Recently, it has been shown that clusters of SPIOs display faster T_2 relaxation properties of the individual iron oxide cores compared to the non-clustered iron oxide cores. Furthermore, clustering results in an increased concentration of the MRI contrast agent and, therefore, both processes contribute to an enhanced transverse relaxivity (166). Activatable SPIOs have been developed that cluster upon activation by myeloperoxidase. In this approach, dopamine was attached to the surface of the SPIOs. In the presence of myeloperoxidase and hydrogen peroxide, this phenol derivative is transformed into a tyrosyl radical that causes dityrosine cross-links between the nanoparticles (167). In another strategy, biotin and neutravidin coated SPIOs were shielded with polyethylene glycol (PEG) that could be proteolytically removed by matrix metalloproteinase-2 to initiate self-assembly (168,169) (Fig. 1.11).
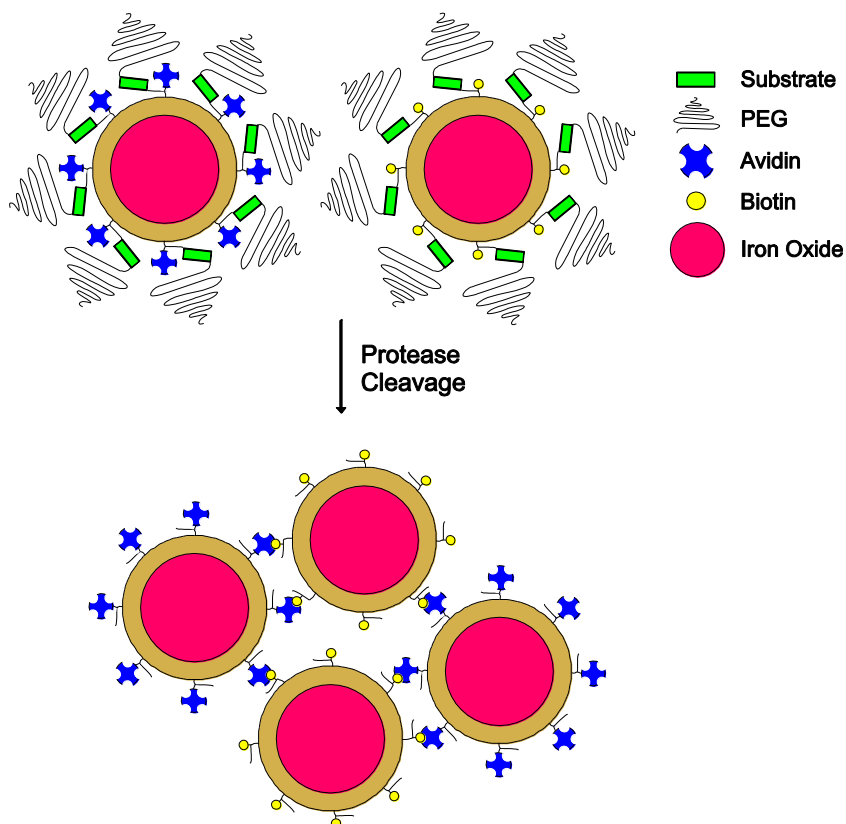
Figure 1.11: *Mechanism of proteolytic actuation of iron oxide self-assembly. Avidin- and biotin functionalized iron oxide nanoparticles are shielded by PEG chains. Upon proteolytic removal of PEG, biotin and neutravidin particles self-assemble into clusters resulting in an enhanced transverse relaxivity.*

In a similar approach, Schellenberger *et al.* designed iron oxide particles sterically stabilized by PEG that showed significant aggregation by inter-particle electrostatic and magnetic attraction upon matrix metalloproteinase-9 induced dePEGylation (170). Finally, Atanasijevic *et al.* reported on SPIOs that were functionalized with the Ca^{2+} sensing protein calmodulin and showed Ca^{2+} dependent protein-protein interaction driving particle clustering (171).

In contrast to the clustering of SPIOs, several iron oxide based imaging probes have been developed that show disassembly upon probe activation resulting in a loss of relaxivity enhancement. In these disassembly approaches, the individual iron oxide particles are connected to each other by cleavable linkers. Following this strategy, probes has been developed for the sensing of caspase-3, MMP-2, and endonucleases in *in vitro* experimental settings (172-174). The fact that enzyme activation results in loss of relaxivity enhancement challenges applications of this approach for *in vivo* imaging.

1.3.3 Bioresponsive paramagnetic CEST MRI agents

The last class of activatable paramagnetic MRI contrast agents induces MR contrast enhancement utilizing chemical exchange saturation transfer (CEST) (17,175). Typically, these CEST MRI contrast agents consist of metal-complexes containing exchangeable water protons with a large chemical shift compared to the bulk water protons. Upon irradiation of these exchangeable water protons using a selective radiofrequency pulse, the intensity of the bulk water signal is reduced via chemical exchange saturation transfer. Bioresponsive paramagnetic CEST agents have been designed that display a change in the CEST effect upon interaction with a biochemical stimulus (17,175). For instance, Tóth and coworkers reported on a self-immolative paramagnetic CEST agent that showed enzyme-specific degradation, whereby a carbamate was cleaved and transformed into an amine (176). Due to the fact that the carbamate and amine differ in both the exchange rate and chemical shift, a different CEST effect was observed upon activation (Fig. 1.12). Furthermore, other enzymatic activatable and pH-responsive CEST agents have been developed by several groups (177-182).
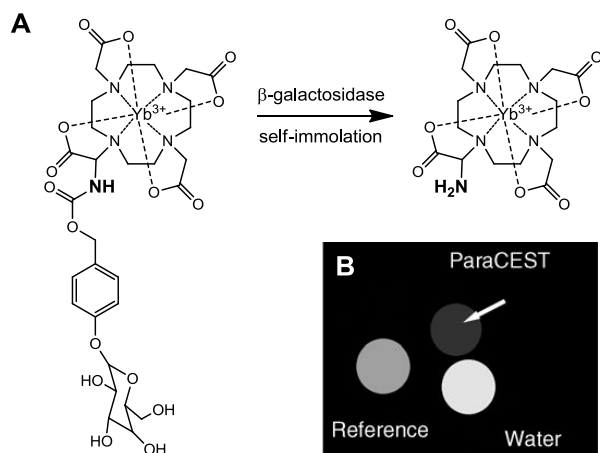
Figure 1.12: *(A) β-galactosidase specific cleavage and subsequent self-decomposition results in the transformation of a carbamate into an amine. (B) MR image of a phantom containing three tubes filled with water, a solution of the non-activated (reference) and cleaved paramagnetic CEST agent. The arrow shows the paraCEST effect. Figure B is reprinted with permission from (176).*

1.4 Bioresponsive Probes Facilitating Site-Specific Retention of the Imaging Label

Activation of autoquenched, self-quenched, and FRET optical probes results in the transition of a fluorophore from an "off" state to an "on" state. For the imaging probes that are activated by extracellular proteases, *e.g.* matrix metalloproteinases, the fluorophores may diffuse away from the cleavage site, resulting in lower signal-to-background ratios (183). Similarly, activatable MRI contrast agents might also show wash-out after activation, except for the activatable SPIOs. In order to avoid wash-out, a special class of activatable probes have been developed in which not the fluorescent or MRI imaging label is activated, but probe activation leads to retention of the imaging probe at the activation site, thereby accumulating the imaging label in the target tissue and thus increasing signal. Importantly, these types of imaging probes are not limited to one specific imaging modality. Hence, probes were successfully developed for nuclear imaging strategies as well. In the following paragraphs the different approaches to get specific retention of the imaging label will be addressed. First, probes will be discussed that require the presence of a specific target for activation and are not amendable to the detection of other targets. Thereafter, activatable molecular imaging probes will be discussed of which its retention can be modulated for a wider variety of targets by including different substrates/triggers.

1.4.1 Bioresponsive probes showing retention, but lacking tuning possibilities for novel targets

An example of an activatable imaging probe that has a narrow target-application range has been developed by the group of Ruoslahti (184,185). In their work, fluorescent probes have been developed that specifically penetrate integrin and neuropilin overexpressing cells upon proteolytic activation. These probes were successfully targeted to tumors through a three-step process: first an RGD-peptide motif mediated binding to integrins on tumor endothelium. Subsequent proteolytic degradation of the probe exposed a C-terminal R/KXXR/K motif, which mediated neuropilin-1-dependent cellular penetration (185).

In another approach, fluorescent, MRI, and radiolabeled probe analogs have been developed displaying specific cross-linking to thrombi by the activity of the transglutaminase FXIIIa (186-190). Transglutaminase FXIIIa activity in a mouse model of myocardial infarction was successfully detected using a radiolabeled analog (Fig. 1.13) (189,190). Re-design of this probe aiming for cross-linking upon interaction with other enzymatic targets not showing transglutaminase activity, such as matrix metalloproteinases, is not possible and therefore this type of imaging probe can not be adapted to detect a wide range of other targets.
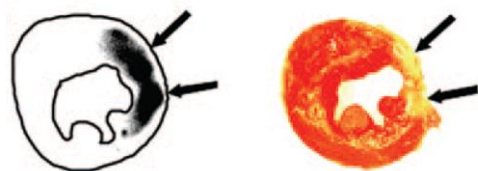
Figure 1.13: *Autoradiography of a FXIIIa-targeted radiolabeled probe (left) and a histological viability stain (right) of a myocardial transversal slice. Pale areas in the viability stain reflect regions of infarct. Figure is reprinted with permission from (189).*

Differences in pH between diseased and healthy tissue has been used to mediate the retention of imaging probes in acidic diseased tissues. For example, an electro statically quenched cell penetrating micelle was selectively activated at the lower extracellular pH of the tumor microenvironment (pH 6.6), resulting in retention and dequenching of the fluorescent dye in cells (Fig. 1.14). An alternative approach aimed for the local release and accumulation of iron-oxide particles from pH-responsive polymeric micelles at acidic conditions (191). This activatable T_2 MRI contrast agent was used for the detection of ischemic areas in the brain of rats. Furthermore, pH-dependent cell membrane insertion peptides containing either a fluorescent or a radioactive imaging label were developed and showed efficient membrane tagging and specific retention in acidic tumor tissues (192,193).
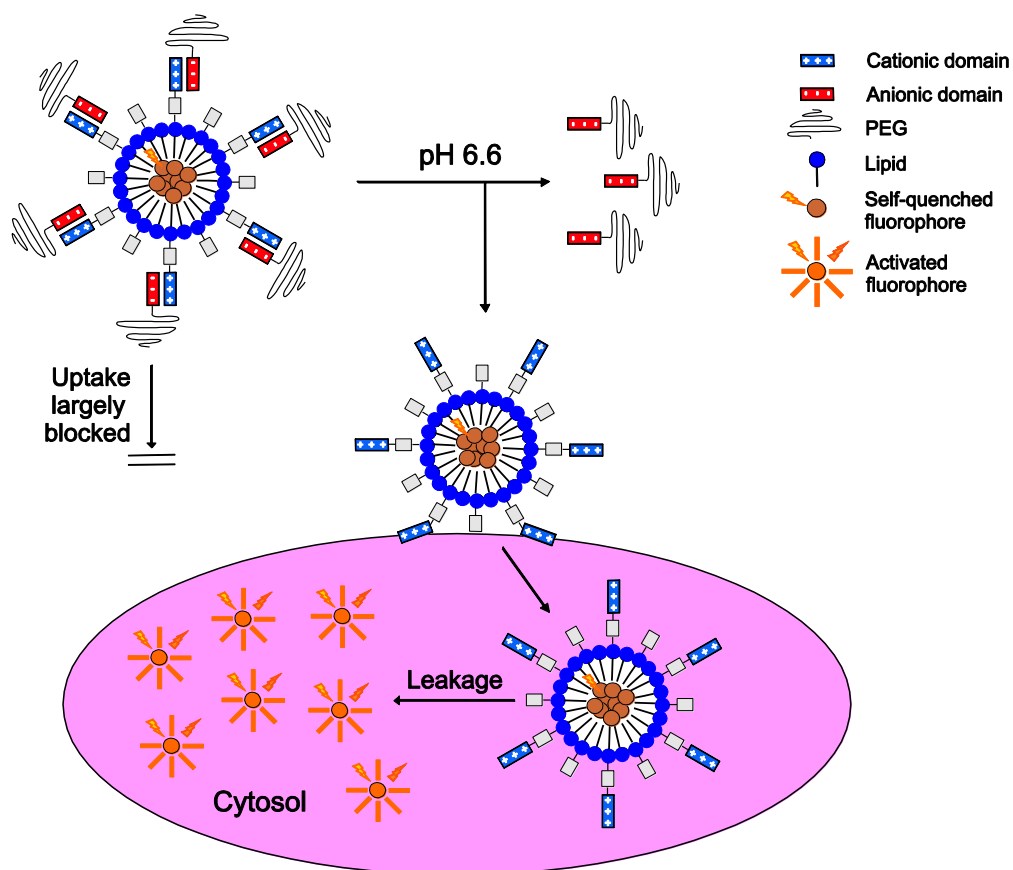
Figure 1.14: *Mechanism of a pH-dependent cell penetrating micelle. The cell penetrating property of polycationic peptide functionalized micelles is masked by polyanionic polymers. At pH 6.6 dissociation will take place, leading to cellular uptake of the micelle. Subsequent leakage of the fluorophores will result in restoration of fluorescence.*

Intracellular enzymatic targets have been successfully targeted with radiolabeled probes showing increased retention upon enzymatic activation. A well-known example is the clinically applied PET imaging probe ^{18}F-fluorodeoxyglucose (FDG) that is used for imaging of glucose metabolism (194). Cancerous tissue typically has a high metabolic activity characterized by an increased uptake of glucose/FDG. Subsequently, the elevated intracellular activity of the enzyme hexokinase enables efficient phosphorylation of FDG resulting in cellular entrapment and subsequent accumulation of the radiolabeled probe (Scheme 1.5). Another intracellular target that can phosphorylate radiolabeled probes, leading to cellular probe accumulation, is herpes simplex virus-1 thymidine kinase. This enzyme is extensively used in reporter gene imaging approaches using PET or SPECT (195,196). Furthermore, radiolabeled cell-penetrating caspase substrates were developed for SPECT imaging and showed enhanced retention in apoptotic cells (197).
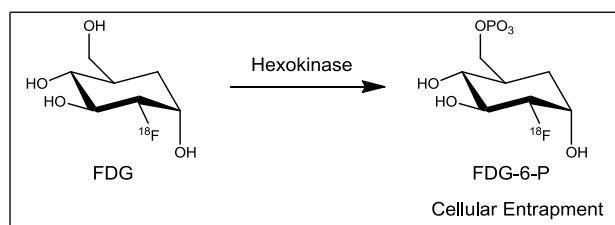
Scheme 1.5:

Phosphorylation of FDG.

In this section, a wide variety of activatable imaging probes has been discussed that show retention and accumulation of the imaging label upon activation. All of these probes are designed to be specifically activated by a unique target (*e.g.* one specific enzyme, pH) and lack the possibility to be adapted to a wide variety of targets. In other approaches, the probes were developed enabling targeting to a wide variety of enzymes, but retention at the site or activation requires the presence of a specific target. For example, protease-induced probe activation was designed to result in specific internalisation of a fluorescently labelled probe by active macrophages (198). Furthermore, a fluorescent probe showed enhanced binding to collagen fibers upon proteolytic activation (199). In the next section, bioresponsive molecular imaging probes will be discussed that need no special requirements, such as a receptor protein, for site-specific retention after its activation. Additionally, these probes can be applied for the detection of a wide variety of targets.

1.4.2 Bioresponsive imaging probes showing retention and enabling tuning for target specificity

A first class of probes shows hydrophobic clustering upon proteolytic removal of a hydrophilic counterpart thereby decreasing the *in vivo* clearance rate from the target tissue (200-202) (Fig. 1.15). These probes showed good promise *in vivo* for the detection of matrix metalloproteinase-2 and -7 employing MRI T_1-contrast agents as imaging labels (200-202). Recently, this concept was further developed for PET purposes. Hereto, an ^{18}F-labeled hydrophobic tetramethylrhodamine moiety was conjugated to a hydrophilic PEG linker by an MMP-2 cleavable substrate (203).
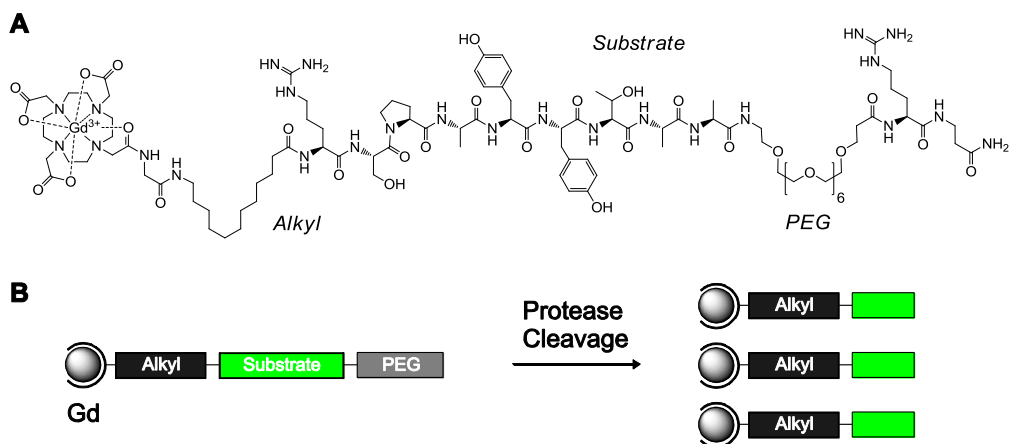
Figure 1.15: *(A) Chemical structure of an MMP-2 activatable solubility switchable MRI T_1-contrast agent (201). A Gd^{3+}-DOTA functionalized hydrophobic alkyl chain is conjugated to a hydrophilic PEG chain via an MMP-2 cleavable peptide substrate (RSPAY-YTAA). (B) Schematic representation; upon proteolytic removal of the hydrophilic PEG chain, the alkyl chain will provide a decrease in solubility resulting in tissue retention of the Gd-labeled domain at the target site and subsequent enhanced T_1-relaxivity.*

A second elegant imaging concept was proposed by Tsien and coworkers. They reported on a fluorescently-labeled activatable cell penetrating peptide (ACPP) imaging probe (204-208) (Fig. 1.16A). This 3-4 kDa construct consisted of an MMP-2/9 substrate inserted in between a polyanionic peptide and a polycationic cell penetrating peptide (CPP) conjugated to a Cy-5 fluorophore. The cell penetrating property of the polycationic peptide was neutralized due to intramolecular electrostatic interactions with the polyanionic domain, preventing cellular uptake of the probe. Cleavage of the substrate by tumoral MMP-2/9 released the polycationic from the polyanionic domain, thereby triggering cellular adhesion and subsequent uptake of the imaging label-functionalized polycationic peptide in tumors (Fig. 1.16B,C). A 3-fold higher tumor uptake was observed for MMP-2/9 ACPP compared to a scrambled negative control (204).

Cell penetrating peptide uptake mechanism
For the ACPP imaging probes, poly-arginine was used as polycationic cell-penetrating peptide (CPP) domain. This peptide domain, once released, shows efficient cellular uptake via macropinocytosis (209,210). The first step of cellular entry is the association of the guanidine residues of the CPP with sulfated glycans present on the cell membrane. Then, macropinocytotic uptake will lead to entrapment of the CPP in intracellular vesicles, typically followed by endosomal escape into the cytoplasm. Though, the precise mechanism of this escape remains unclear (211).
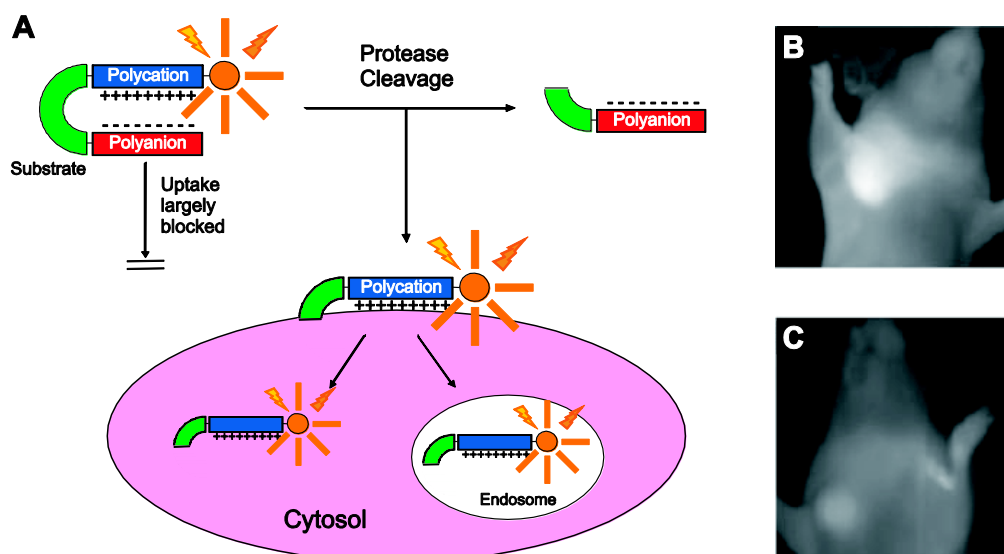
Figure 1.16: *(A) Mechanism of a fluorescently-labeled protease activatable cell penetrating peptide (ACPP). The cell penetrating property of a polycationic peptide is masked by a polyanionic peptide. Proteolytic degradation of the linker releases the polycationic cell penetrating peptide, which will transfer the fluorophore cargo across the cell membrane. (B) In vivo NIRF image of MMP-2 positive HT-1080 tumor-bearing showed a 3-fold higher tumor uptake of a fluorescently labeled MMP-2/9 ACPP compared to (C) a fluorescently labeled scrambled control. HT-1080 tumors were implanted into the mammary fat pad. Figure is adapted with permission from (204).*

The ACPP imaging concept was further developed for the *in vitro* detection of several disease-related enzymes such as urokinase, enterokinase, prostate-specific antigen, and plasmin (204,212,213) as well as acidic conditions by employing a reduction-sensitive disulfide bridge between the polycationic and polyanionic domain (204). A novel tumor-homing ACPP, predominantly sensitive for elastases, was identified by a parallel *in vitro* and an *in vivo* selection with phage display employing a library of ACPPs (214). Introduction of a near-infrared quencher at the polyanionic domain led to development of MMP-2 and MMP-7 FRET-based ACPP imaging probes that showed both activation of fluorescence as well as *in vitro* cellular retention upon cleavage (139,215). Recently, it was shown that *in vitro* cellular uptake of ACPP-functionalized quantum dots could be modulated by MMP-2 (216). MMP-induced *in vitro* cellular uptake of quantum dots was demonstrated by dePEGylation of CPP functionalized quantum dots (217). Furthermore, the concept of activatable cell penetrating peptides (ACPPs) was translated to MRI applications for MMP sensing by either direct labeling of the cell penetrating peptide domain with gadolinium (218) or via functionalization of dendritic nanoparticles with ACPP and Gd^{3+} (207). In the latter approach, the nanoparticles were used for the *in vivo* detection of MMP expression in tumors. Next, radiolabeled proteolytic activatable cell penetrating imaging probes have been designed for MMP-14 and

prostate specific antigen (PSA) for applications in nuclear imaging (219,220). *In vivo* evaluation of these radiolabeled probes, however, has not been reported so far. Finally, the first activatable probe for optoacoustic tomography was developed based on an MMP-2 activatable cell penetrating peptide (139). The ACPP imaging probes that have been applied *in vivo* were solely studied in tumor-bearing mice. Recently, the first progress was made in the application of ACPP imaging probes in cardiovascular disease (221). In this work, a fluorescently-labeled ACPP was developed for detection of thrombin in carotid atherosclerotic plaques (221).

In another approach, cell-internalisation was achieved upon activation of a lipidated probe (222). In the latter research, a lipidated FRET reporter was targeted to the plasma membrane. Activation of the probe by MMP-12 resulted in efficient internalization and retention of the donor fluorophore. Finally, protease-induced probe activation was designed to result in tagging of the probe to the cell membrane (223).

1.5 Clinical translations

In this Chapter, the design and application of bioresponsive imaging probes was reviewed. Optical and MRI imaging probes showed signal amplification by either direct activation of the imaging label or by specific retention of the imaging probe. Because radiolabels are always "on", bioresponsive radiolabeled probes for SPECT/PET relied on local retention upon interaction with a stimulus. Both SPECT and PET provide a very attractive method for molecular imaging. Both nuclear techniques are characterized by a picomolar sensitivity and are highly quantitative (224). Therefore, only a small dose of radiolabeled imaging probes is required compared to MRI contrast agents, for which typically a millimolar range of concentration is needed. Furthermore, SPECT and PET have superb tissue penetration capabilities and therefore offer the possibility to visualize deeply-located tissues, while this is not possible for optical imaging due to the limited penetration depth of light.

An intracellular target such as hexokinase has been efficiently detected with radiolabeled FDG and this probe has found wide application in clinical oncology for diagnostic cancer imaging. On the other hand, the *in vivo* imaging of extracellular biomarkers using radiolabeled bioresponsive probes is limited. So far, extracellular biomarkers are mainly visualized with bioresponsive optical imaging probes. These probes may find application in optical-guided surgery and endoscopy, but are not suited for whole-body diagnostic imaging. For example, activatable cell penetrating peptides (ACPP) have been used in pre-clinical optical guided surgery (208). On the other hand, two radiolabeled ACPP analogs, sensitive for MMP-14 and PSA, have been developed and may find application in diagnostic imaging (219,220). However, *in vivo* application of these probes has not been reported so far.

1.6 Aim and outline of the thesis

The primary aim of the work described in this thesis was to develop radiolabeled activatable cell penetrating imaging probes (ACPPs) for the *in vivo* detection of molecular biomarkers associated with cardiovascular disease and/or cancer, with a predominant future application in whole-body diagnostic imaging (Fig. 1.17). In the first part of this thesis, the development and detailed characterization of MMP-2/9 activatable cell penetrating imaging probes is presented. Chapter 2 describes the synthesis and radiolabeling of these peptide constructs. Subsequently, the enzyme specificity as well as the cellular uptake efficiency before and after activation was addressed. Finally, the biodistribution of the radiolabeled MMP-2/9 activatable probe was assessed in MMP-positive tumor-bearing mice. In Chapter 3, the same probes were explored to detect MMP-2/9 in a mouse model of myocardial infarction (MI). Chapter 4 presents the expansion of the ACPP family towards long-circulating ACPP-probes, which facilitate an increased exposure time to the target proteases. Chapters 5 and 6 deals with the development of radiolabeled ACPPs for the endopeptidase MMP-14 and carboxy exopeptidase angiotensin converting enzyme (ACE), respectively. In Chapter 7, a strategy is proposed towards self-immolative ACPPs for H_2O_2 detection. In Chapter 8, a general discussion is presented.
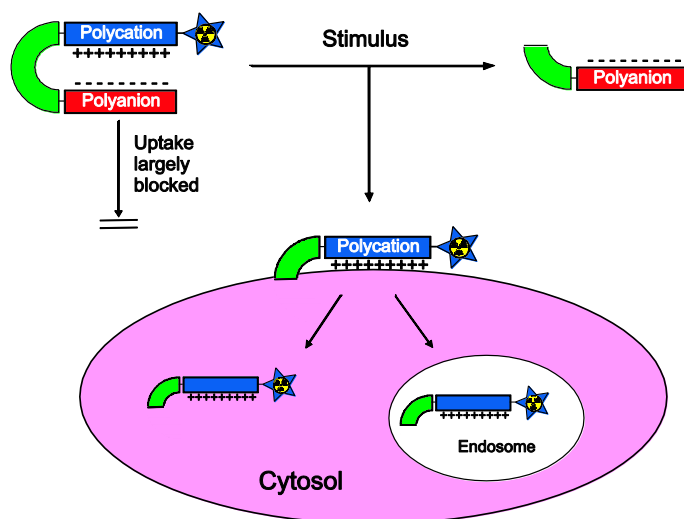
Figure 1.17: *Proposed mechanism of radiolabeled bioresponsive ACPPs. The cell penetrating property of a polycationic peptide will be masked by a polyanionic peptide. Interaction of the ACPP with a chemical or biological stimulus will result in degradation of the linker, followed by the release of the polycationic cell penetrating peptide and subsequent transfer of the radionuclide across the cell membrane. The trapped radioactivity can be visualized by SPECT or PET imaging.*

References

1. Mankoff DA. A Definition of Molecular Imaging. *J Nucl Med.* 2007;48:18N-21N

2. Hoffman JM, and Gambhir SS. Molecular Imaging: The Vision and Opportunity for Radiology in the Future. *Radiology*. 2007;244:39-47

3. Massoud TF, and Gambhir SS. Integrating Noninvasive Molecular Imaging into Molecular Medicine: An Evolving Paradigm. *Trends Mol Med.* 2007;13:183-191

4. Weissleder R, and Pittet MJ. Imaging in the Era of Molecular Oncology. *Nature.* 2008;452:580-589

5. Pysz MA, Gambhir SS, and Willmann JK. Molecular Imaging: Current Status and Emerging Strategies. *Clinical Radiology.* 2010;65:500-516

6. Contag CH. In Vivo Pathology: Seeing with Molecular Specificity and Cellular Resolution in the Living Body. *Annu Rev Pathol.* 2007;2:277-305

7. Willmann JK, Bruggen NV, Dinkelborg LM, et al. Molecular Imaging in Drug Development, *Nat Rev Drug Discov.* 2008;7:591–607

8. Herschman HR. Molecular Imaging: Looking at Problems, Seeing Solutions. *Science.* 2003:302;605–608

9. Lammers T, Kiessling F, Hennink WE, et al. Nanotheranostics and Image-Guided Drug Delivery: Current Concepts and Future Directions. *Mol Pharm.* 2010;7:1899-1912

10. Ntziachristos V, Yoo JS, and van Dam GM. Current Concepts and Future Perspectives on Surgical Optical Imaging in Cancer. *J Biomed Opt.* 2010;15:066024

11. Urano Y, Sakabe M, Kosaka N, et al. Rapid Cancer Detection by Topically Spraying a γ-Glutamyltranspeptidase-Activated Fluorescent Probe. *Sci Transl Med.* 2011;3:110ra119

12. Frangioni JV. New Technologies for Human Cancer Imaging. *J Clin Oncol.* 2008;26:4012–4021

13. Van de Wiele C, and Oltenfreiter R. Imaging Probes Targeting Matrix Metalloproteinases. Cancer Biother Radiopharm. 2006;21:409-417

14. Razgulin A, Ma N, and Rao J. Strategies for In Vivo Imaging of Enzyme Activity: An Overview and Recent Advances. *Chem Soc Rev.* 2011;40:4186-4216

15. Razansky D, Harlaar NJ, Hillebrands JK, et al. Multispectral Optoacoustic Tomography of Matrix Metalloproteinase Activity in Vulnerable Human Carotid Plaques. *Mol Imaging Biol.* 2011, DOI: 10.1007/ s11307-011-0502-6

16. Mahmood U, and Weissleder R. Near-Infrared Optical Imaging of Proteases in Cancer. *Mol Cancer Ther.* 2003;2:489-496

17. Elias DR, Thorek DLJ, Chen AK, et al. In Vivo Imaging of Cancer Biomarkers Using Activatable Molecular Probes. *Cancer Biomarkers.* 2008;4:287-305

18. Law B, and Tung CH. Proteolysis: A Biological Process Adapted in Drug Delivery, Therapy, and Imaging. *Bioconjug Chem.* 2009;20:1683-1695

19. Neefjes J, and Dantuma NP. Fluorescent Probes for Proteolysis: Tools for Drug Discovery. *Nat Rev Drug Dis.* 2004;3:58-69

20. Chen X, Pradhan T, Wang F, et al. Fluorescent Chemosensors Based on Spiroring-Opening of Xanthenes and Related Derivatives. *Chem Rev.* 2012;112:1910–1956

21. McGrath W, Pia Abola A, Toledo D, et al. Characterization of Human Adenovirus Proteinase Activity in Disrupted Virus Particles. *Virology.* 1996;217:131–138

22. Van Noorden CJF, Boonacker E, Bissell E, et al. Ala-Pro-cresyl violet, a synthetic fluorogenic substrate for the analysis of kinetic parameters of dipeptidyl peptidase IV (CD26) in individual living rat hepatocytes. *Anal Biochem.* 1997;252:71–77

23. Ho NH, Weissleder R, and Tung CH. Development of a dual fluorogenic and chromogenic dipeptidyl peptidase IV substrate. *Bioorg Med Chem Lett.* 2006;16:2599–2602

24. Nicholls SB, Chu J, Abbruzzese G, et al. Mechanism of a Genetically-Encoded Dark-to-Bright Reporter for Caspase Activity. *J Biol Chem.* 2011;286:24977-24986

25. Cai S, Zhang H, Guastella J, et al. Design and Synthesis of Rhodamine 110 Derivative and Caspase-3 Substrate for Enzyme- and Cell-based Fluorescent Assay. *Bioorg Med Chem Lett.* 2001;11:39-42

26. Weissleder R, and Ntziachristos V. Shedding Light onto Live Molecular Targets. *Nat Med.* 2003;9:123-128

27. Mahmood U, Tung CH, Bogdanov A, et al. Near Infrared Optical Imaging of Protease Activity for Tumor Detection. *Radiology.* 1999;213:866–870

28. Lakowicz JR. Principles of Fluorescence Spectroscopy, Second Edition" *Kluwer Academic/Plenum Publishers* 1999

29. Weissleder R, Tung CH, Mahmood U, et al. In Vivo Imaging of Tumors with Protease-Activated NIRF Probes. *Nat Biotechnol.* 1999;17:375–378

30. Ntziachristos V, Bremer C, Tung CH, et al. Imaging Cathepsin B Up-Regulation in HT-1080 Tumor Models Using Fluorescence-Mediated Molecular Tomography (FMT). *Acad Radiol.* 2002;9:S323-S325

31. Chen J, Tung CH, Mahmood U, et al. In Vivo Imaging of Proteolytic Activity in Atherosclerosis. *Circulation*. 2002;105:2766–2771

32. Wunder A, Tung CH, Muller-Ladner U, et al. In Vivo Imaging of Protease Activity in Arthritis: A Novel Approach for Monitoring Treatment Response. *Arthritis Rheum.* 2004;50:2459-2465

33. Jaffer FA, Vinegoni C, John MC, et al. Real-Time Catheter Molecular Sensing of Inflammation in Proteolytically Active Atherosclerosis. *Circulation.* 2008;118:1802-1809

34. Messerli SM, Prabhakar S, Tang Y, et al. A Novel Method for Imaging Apoptosis Using a Caspase-1 Near-Infrared Fluorescent Probe. *Neoplasia.* 2004;6:95–105

35. Tung CH, Mahmood U, Bredow S, et al. In Vivo Imaging of Proteolytic Enzyme Activity Using a Novel Molecular Reporter. *Cancer Res.* 2000;60:4953–4958

36. Abd-Elgaliel WR, Cruz-Monserrate Z, Logsdon C, et al. Molecular Imaging of Cathepsin E-Positive Tumors in Mice Using a Novel Protease-Activatable Fluorescent Probe. *Mol Biosystems.* 2011;7:3207-3213

37. Jaffer FA, Kim DE, Quinti L, et al. Optical Visualization of Cathepsin K Activity in Atherosclerosis With a Novel Protease-Activatable Fluorescence Sensor. *Circulation.* 2007;115:2292-2298

38. Shah K, Tung CH, Chang CH, et al. In Vivo Imaging of HIV Protease Activity in Amplicon Vector-Transduced Gliomas. *Cancer Res.* 2004;64:273-278

39. Law B, Curino A, Bugge TH, et al. Design, Synthesis, and Characterization of Urokinase Plasminogen-activator Sensitive Near-Infrared Reporter. *Chem Biol.* 2004;11:99-106

40. Bremer C, Tung CH, Bogdanov A, et al. Imaging of Differential Protease Expression in Breast Cancers for Detection of Aggressive Tumor Phenotypes. *Radiology.* 2002;222:814–818

41. Bremer C, Bredow S, Mahmood U, et al. Optical Imaging of Matrix Metalloproteinase-2 Activity in Tumors: Feasibility Study in a Mouse Model. *Radiology.* 2001;221:523–529

42. Bremer C, Tung CH, and Weissleder R. In Vivo Molecular Target Assessment of Matrix Metalloproteinase Inhibition. *Nat Med.* 2001;7:743-748

43. Bremer C, Tung CH, and Weissleder R. Molecular Imaging of MMP Expression and Therapeutic MMP Inhibition. *Acad Radiol.* 2002;9:S314–315

44. Chen J, Tung CH, Allport JR, et al. Near-Infrared Fluorescent Imaging of Matrix Metalloproteinase Activity after Myocardial Infarction. *Circulation.* 2005;111:1800-1805

45. Deguchi JO, Aikawa M, Tung CH, et al. Inflammation in Atherosclerosis: Visualizing Matrix Metalloproteinase Action in Macrophages In Vivo. *Circulation.* 2006;114:55-62

46. von Burstin J, Eser S, Seidler B, et al. Highly Sensitive Detection of Early-Stage Pancreatic Cancer by Multimodal Near-Infrared Molecular Imaging in Living Mice. *Int J Cancer.* 2008;123:2138-2147

47. Sarkar N, Banerjee J, Hanson AJ, et al. Matrix Metalloproteinase-Assisted Triggered Release of Liposomal Contents. *Bioconjug Chem.* 2008;19:57-64

48. Elegbede AI, Banerjee J, Hanson AJ, et al. Mechanistic Studies on the Triggered Release of Liposomal Contents by Matrix Metalloproteinase-9. *J Am Chem Soc.* 2008;130:10633-10642

49. Malik R, Qian S, and Law B. Design and Synthesis of a Near-Infrared Fluorescent Nanofiber Precursor for Detecting Cell-secreted Urokinase Activity. *Anal Biochem.* 2011;412:26-33

50. Akers WJ, Xu B, Lee H, et al. Detection of MMP-2 and MMP-9 Activity In Vivo with a Triple-Helical Peptide Optical Probe. *Bioconjug Chem.* 2012;23:656-663

51. Mahajan NP, Harrison-Shostak DC, Michaux J, et al. Novel Mutant Green Fluorescent Protein Protease Substrates Reveal the Activation of Specific Caspases During Apoptosis. *Chem Biol.* 1999;6:401-409

52. Zhang J, Ma Y, Taylor SS, et al. Genetically Encoded Reporters of Protein Kinase A Acitivity Reveal Impact of Substrate Tethering. *Proc Nat Acad Sci USA.* 2001;98:14997-15002

53. Yang J, Zhang Z, Lin J, et al. Detection of MMP Activity in Living Cells by a Genetically Encoded Surface-Displayed FRET Sensor. *Biochim Biophys Acta.* 2007;1773:400-407

54. Zhang Z, Yang J, Lu J, et al. Fluorescence Imaging to Assess the Matrix Metalloproteinase Activity and its Inhibitor In Vivo. *J Biomed Opt.* 2008;13:011006

55. Ouyang M, Huang H, Shaner NC, et al. Simultaneous Visualization of Protumorigenic Src and MT1-MMP Activities with Fluorescence Resonance Energy Transfer. *Cancer Res.* 2010;70:2204-2212

56. Pham W, Choi Y, Weissleder R, et al. Developing a peptide-based near-infrared molecular probe for protease sensing. *Bioconjug Chem.* 2004;15;1403–1407

57. McIntyre JO, Fingleton B, Wells FS. Development of a Novel Fluorogenic Proteolytic Beacon for In Vivo Detection and Imaging of Tumour-Associated Matrix Metalloproteinase-7 Activity. *Biochem J.* 2004;377:617-628

58. Lee S, Park K, Lee SY, et al. Dark Quenched Matrix Metalloproteinase Fluorogenic Probe for Imaging Osteoarthritis Development In Vivo. *Bioconjug Chem.* 2008;19:1743-1747

59. Yoon SM, Myung SJ, Kim IW, et al. Application of Near-Infrared Fluorescence Imaging Using a Polymeric Nanoparticle-Based Probe for the Diagnosis and Therapeutic Monitoring of Colon Cancer. *Dig Dis Sci.* 2011;56:3005-3013

60. Lin X, Xie J, Zhu L, et al. Hybrid Ferritin Nanoparticles as Activatable Probes for Tumor Targeting. *Angew Chem Int Ed.* 2011;50:1569-1572

61. Liu TW, Akens MK, Chen J, et al. Imaging of Specific Activation of Photodynamic Molecular Beacons in Breast Cancer Vertebral Metastases. *Bioconjug Chem.* 2011;22:1021-1030

62. Moss ML, and Rasmussen FH. Fluorescent Substrates for the Proteinases ADAM17, ADAM10, ADAM8, and ADAM12 Useful for High-Throughput Inhibitor Screening. *Anal Biochem.* 2007;366:144-148

63. Zhu L, Xie J, Swierczewska M, et al. Dual-Functional, Receptor-Targeted Fluorogenic Probe for In Vivo Imaging of Extracellular Protease Expressions. *Bioconjug Chem.* 2011;22:1001-1005

64. Zhu L, Xie J, Swierczewska M, et al. Real-Time Video Imaging of Protease Expression In Vivo. *Theranostics.* 2011;1:18-27

65. Zhu L, Zhang F, Ma Y, et al. In Vivo Optical Imaging of Membrane-Type Matrix Metalloproteinase (MT-MMP) Activity. *Mol Pharm.* 2011;8:2331-2338

66. Bullok K, and Piwnica-Worms D. Synthesis and Characterization of a Small, Membrane-Permeant, Caspase-Activatable Far-Red Fluorescent Peptide for Imaging Apoptosis. *J Med Chem.* 2005;48:5404-5407

67. Bullok KE, Maxwell D, Kesarwala AH, et al. Biochemical and In Vivo Characterization of a Small, Membrane-Permeant, Caspase-Activatable Far-Red Fluorescent Peptide for Imaging Apoptosis. *Biochemistry.* 2007;46:4055-4065

68. Maxwell D, Chang Q, Zhang X, et al. An Improved Cell-Penetrating, Caspase-Activatable, Near-Infrared Fluorescent Peptide for Apoptosis Imaging. *Bioconjug Chem.* 2009;20:702-709

69. Lee S, Cha EJ, Park K, et al. A Near-Infrared-Fluorescence-Quenched Gold-Nanoparticle Imaging Probe for In Vivo Drug Screening and Protease Activity Determination. *Angew Chem Int Ed.* 2008;120:2846-2849

70. Kim YP, Oh YH, Oh E, et al. Energy Transfer-Based Multiplexed Assay of Proteases by Using Gold Nanoparticle and Quantum Dot Conjugates on a Surface. *Anal Chem.* 2008;80:4634-4641

71. Chang E, Miller JS, Sun J, et al. Protease-Activated Quantum Dot Probes. *Biochem Biophys Res Comm.* 2005;334:1317-1321

72. Kersemans V, and Cornelissen B. Targeting the Tumour: Cell Penetrating Peptides for Molecular Imaging and Radiotherapy. *Pharmaceuticals.* 2010;3:600-620

73. Lovell JF, Liu TWB, Chen J, et al. Activatable Photosensitizers for Imaging and Therapy. *Chem Rev.* 2010;110:2839-2857

74. Zheng G, Chen J, Stefflova K, et al. Photodynamic Molecular Beacon as an Activatable Photosensitizer Based on Protease-Controlled Singlet Oxygen Quenching and Activation. *Proc Nat Acad Sci USA.* 2007;104:8989-8994

75. Chen J, Stefflova K, Niedre MJ, et al. Protease-Triggered Photosensitizing Beacon Based on Singlet Oxygen Quenching and Activation. *J Am Chem Soc.* 2004;126:11450-11451

76. Lo P, Chen J, Stefflova K, et al. Photodynamic Molecular Beacon Triggered by Fibroblast Activation Protein on Cancer-Associated Fibroblasts for Diagnosis and Treatment of Epithelial Cancers. *J Med Chem.* 2009;52:358-368

77. Agostinis P, Berg K, Cengel KA, et al. Photodynamic Therapy of Cancer: An Update. *CA Cancer J Clin.* 2011;61:250-281

78. Marques SM, and Esteves da Silva JC. Firefly Bioluminescence: A Mechanistic Approach of Luciferase Catalyzed Reactions. *IUBMB Life.* 2009;61:6-17

79. Wehrman TS, von Degenfeld G, Krutzik PO, et al. Luminescent Imaging of Beta-Galactosidase Activity in Living Subjects Using Sequential Reporter-Enzyme Luminescence. *Nat Methods.* 2006;3:295-301

80. Yao H, So MK, Rao J. A Bioluminogenic Substrate for In Vivo Imaging of ß-Lactamase Activity. *Angew Chem Int Ed.* 2007;46:7031-7034

81. Shah K, Tung CH, Breakefield XO, et al. In Vivo Imaging of S-TRAIL-Mediated Tumor Regression and Apoptosis. Mol Ther. 2005;11:926-931

82. Dragulescu-Andrasi A, Liang G, and Rao J. In Vivo Bioluminescence Imaging of Furin Activity in Breast Cancer Cells Using Bioluminogenic Substrates. *Bioconjug Chem*. 2009;20:1660-1666

83. Kneen M, Farinas J, Li Y, et al. Green Fluorescent Protein as a Noninvasive Intracellular pH Indicator. *Biophys J.* 1998;74:1591-1599

84. Han J, and Burgess K. Fluorescent Indicators for Intracellular pH. *Chem Rev.* 2010; 110:2709-2728

85. Hilderbrand SA, Kelly KA, Niedre M, et al. Near Infrared Fluorescence-Based Bacteriophage Particles for Ratiometric pH Imaging. *Bioconjug Chem.* 2008;19:1635–1639

86. Hilderbrand SA, and Weissleder R. Optimized pH Responsive Cyanine Fluorochromes for Detection of Acidic Environments. *Chem Comm (Camb.)* 2007:2747–2749

87. Kirpotin D, Hong K, Mullah N, et al. Liposomes with Detachable Polymer Coating: Destabilization and Fusion of Dioleoylphosphatidelyethanolamine Vesicles Triggered by Cleavage of Surface-Grafted Poly(Ethylene Glycol). *FEBS Lett.* 1996;388:115-118

88. Bellomo EG, Wyrsta MD, Pakstis L, et al. Stimuli-Responsive Polypeptide Vesicles by Conformation-Specific Assembly. *Nature Mat.* 2004;3:244-248

89. Park HS, Lee JE, Cho MY, et al. pH-Stimuli-Responsive Near-Infrared Optical Imaging Nanoprobe Based on Poly(y-Glutamic Acid)/Poly(b-Amino Ester) Nanoparticles. *Nanotechnology*. 2011;22: 465603

90. Urano Y, Asanuma D, Hama Y, et al. Selective Molecular Imaging of Viable Cancer Cells with pH-Activatable Fluorescence Probes. *Nat Med.* 2009;15:104–109

91. Ogawa M, Kosaka N, Regino CA, et al. High Sensitivity Detection of Cancer In Vivo Using a Dual-controlled Activation Fluorescent Imaging Probe Based on H-Dimer Formation and pH Activation. *Mol Biosyst.* 2010;6:888-893

92. Lee H, Akers W, Bhushan K, et al. Near-Infrared pH-Activatable Fluorescent Probes for Imaging Primary and Metastatic Breast Tumors. *Bioconjug Chem.* 2011;22:777-784

93. Sethuraman VA, and Han Bae Y. TAT Peptide-Based Micelle System for Potential Active Targeting of Anti-Cancer Agents to Acidic Solid Tumors. *J Cont Release.* 2007;118:216-224

94. Finkel T, Serrano M, Blasco MA (2007) The common biology of cancer and ageing. *Nature.* 448:767–774

95. Zweier JL, and Hassan Talukder MA. The Role of Oxidants and Free Radicals in Reperfusion Injury. *Cardiovasc Res.* 2006;70:181-190

96. Kobayashi H, Ogawa M, Alford R, et al. New Strategies for Fluorescent Probe Design in Medical Diagnostic Imaging. *Chem Rev.* 2010;110:2620-2640

97. Chang MCY, Pralle A, Isacoff EY, et al. A Selective, Cell-Permeable Optical Probe for Hydrogen Peroxide in Living Cells. *J Am Chem Soc.* 2004;126:15392-15393

98. Miller EW, Albers AE, Pralle A, et al. Boronate-Based Fluorescent Probes for Imaging Cellular Hydrogen Peroxide. *J Am Chem Soc.* 2005;127:16652-16659

99. Miller EW, Tulyathan O, Isacoff EY, et al. Molecular imaging of hydrogen peroxide produced for cell signaling. *Nat Chem Biol.* 2007;3:263-267

100. Dickinson BC, and Chang CJ. A Targetable Fluorescent Probe for Imaging Hydrogen Peroxide in the Mitochondria of Living Cells. *J Am Chem Soc.* 2008;130:11561

101. Abo M, Urano Y, Hanaoka K, et al. Development of a Highly Sensitive Fluorescence Probe for Hydrogen Peroxide. *J Am Chem Soc.* 2011;133:10629-10637

102. Dickinson BC, Huynh C, and Chang CJ. A Palette of Fluorescent Probes with Varying Emission Colors for Imaging Hydrogen Peroxide Signaling in Living Cells. *J Am Chem Soc.* 2010;132:5906-5915

103. Ye Z, Chen J, Wang G, et al. Development of a Terbium Complex-Based Luminescent Probe for Imaging Endogenous Hydrogen Peroxide Generation in Plant Tissues. *Anal Chem.* 2011;83:4163-4169

104. Kim G, Koo Lee YE, Xu H, et al. Nanoencapsulation Method for High Selectivity Sensing of Hydrogen Peroxide Inside Live Cells. *Anal Chem.* 2010;82:2165-2169

105. Panizzi P, Nahrendorf M, Wildgruber M, et al. Oxazine Conjugated Nanoparticle Detects In Vivo Hypochlorous Acid and Peroxynitrite Generation. *J Am Chem Soc.* 2009;131:15739-15744

106. Yang D, Sun ZN, Peng T, et al. Synthetic Fluorescent Probe for Imaging of Peroxynitrite and Hypochlorous Acid in Living Cells. *Methods Mol Biol.* 2010;591:93-103

107. Koide Y, Urano Y, Kenmoku S, et al. Design and Synthesis of Fluorescent Probes for Selective Detection of Highly Reactive Oxygen Species in Mitochondria of Living Cells. *J Am Chem Soc.* 2007;129:10324-10325

108. Yang D, Wang HL, Sun ZN, et al. A Highly Selective Fluorescent Probe for the Detection and Imaging of Peroxynitrite in Living Cells. *J Am Chem Soc.* 2006;128:6004-6005

109. Sun ZN, Wang HL, Liu FQ, et al. BODIPY-Based Fluorescent Probe for Peroxynitrite Detection and Imaging in Living Cells. *Org Lett.* 2009;11:1887-1890

110. Maeda H, Yamamoto K, Nomura Y, et al. A Design of Fluorescent Probes for Superoxide Based on a Nonredox Mechanism. *J Am Chem Soc.* 2005;127:68-69

111. Xu K, Liu X, Tang B, et al. Design of a Phosphinate-Based Fluorescent Probe for Superoxide Detection in Mouse Peritoneal Macrophages. *Chemistry.* 2007;13:1411-1416

112. Maeda H, Yamamoto K, Kohno I, et al. Design of a Practical Fluorescent Probe for Superoxide Based Protection-Deprotection Chemistry of Fluoresceins with Benzenesulfonyl Protecting Group. *Chemistry.* 2007;13:1946-1954

113. Sasaki E, Kojima H, Nishimatsu H, et al. Highly Sensitive Near-Infrared Fluorescent Probes for Nitric Oxide and Their Application to Isolated Organs. *J Am Chem Soc.* 2005;127:3684-3685

114. Lim MH, Xu D, and Lippard SJ. Visualization of nitric oxide in living cells by a copper-based fluorescent probe. *Nat Chem Biol.* 2006, 2:375-380

115. Pluth MD, MCQuade LE, and Lippard SJ. Cell-Trappable Fluorescent Probes for Nitric Oxide Visualization in Living Cells. *Org Lett.* 2010, 12:2318-2321

116. Kenmoku S, Urano Y, Kojima H, et al. Development of a Highly Specific Rhodamine-Based Fluorescence Probe for Hypochlorous Acid and Its Application to Real-Time Imaging of Phagocytosis. *J Am Chem Soc.* 2007;129:7313-7318

117. Sun ZN, Liu FQ, Chen Y, et al. A Highly Specific BODIPY-Based Fluorescent Probe for the Detection of Hypochlorous Acid. *Org Lett.* 2008;10:2171-2174

118. Yang YK, Cho HJ, Lee J, et al. A Rhodamine-Hydroxamic Acid-Based Fluorescent Probe for Hypochlorous Acid and Its Applications to Biological Imagings. *Org Lett.* 2009;11:859-861

119. Manevich Y, Held KD, and Biaglow JE. Coumarin-3-Carboxylic Acid as a Detector for Hydroxyl Radicals Generated Chemically and by Gamma Radiation. *Radiat Res.* 1997;148:580–591

120. Ganea, GM, Kolic PE, El-Zahab B, et al. Ratiometric Coumarin – Neutral Red (CONER) Nanoprobe for Detection of Hydroxyl Radicals. *Anal Chem.* 2011;83:2576-2581

121. Albers AE, Okreglak VS, and Chang CJ. A FRET-Based Approach to Ratiometric Fluorescence Detection of Hydrogen Peroxide. *J Am Chem Soc.* 2006;128:9640-9641

122. Srikun D, Miller EW, Domaille DW, et al. An ICT-Based Approach to Ratiometric Fluorescence Imaging of Hydrogen Peroxide Produced in Living Cells. *J Am Chem Soc.* 2008,130:4596-4597

123. Li C, Hu J, Liu T, et al. Stimuli-Triggered Off/On Switchable Complexation Between a Novel Type of Charge-Generation Polymer (CGP) and Gold Nanoparticles for the Sensitive Colorimetric Detection of Hydrogen Peroxide and Glucose. *Macromolecules.* 2011;44:429-431

124. Belousov VV, Fradkov AF, Lukyanov KA, et al. Genetically Encoded Fluorescent Indicator for Intracellular Hydrogen Peroxide. *Nat Methods.* 2006;3:281-286

125. Wang W, Fang H, Groom L, et al. Superoxide Flashes in Single Mitochondria. *Cell.* 2008;134:279-290

126. Zhao BS, Liang Y, Song Y, et al. A Highly Selective Fluorescent Probe for Visualization of Organic Hydroperoxides in Living Cells. *J Am Chem Soc.* 2010;132:17065-17067

127. Lee D, Khaja S, Velasquez-Castano JC, et al. In Vivo Imaging of Hydrogen Peroxide with Chemiluminescent Nanoparticles. *Nat Mater.* 2007;6:765-769

128. Van de Bittner GC, Dubikovskaya EA, Bertozzi CR, et al. In Vivo Imaging of Hydrogen Peroxide Production in a Murine Tumor Model with a Chemoselective Bioluminescent Reporter. *Proc Nat Acad Sci USA.* 2010;107:21316-21321

129. Imamura H, Huynh Nhat KP, Toqawa H, et al. Visualization of ATP Level Inside Single Living Cells with Fluorescence Resonance Energy Transfer-Based Genetically Encoded Indicators. *Proc Natl Acad Sci USA.* 2009;106:15651-15656

130. Fehr M, Lalonde S, Lager I, et al. In Vivo Imaging of the Dynamics of Glucose Uptake in the Cytosol of COS-7 Cells by Fluorescent Nanosensors. *J Biol Chem* 2003;278:19127-19133

131. Miyawaki A, Llopis, J, Heim R, et al. Fluorescent Indicators for Ca^{2+} Based on Green Fluorescent Proteins and Calmodulin. *Nature.* 1997;388:882-887

132. Vinkenborg JL, Nicolson T, Bellomo EA, et al. Genetically Encoded FRET Sensors to Monitor Zn^{2+} Homeostasis in Single Cells. *Nat Methods.* 2009;6:737-740

133. Vinkenborg JL, van Duijnhoven SMJ, and Merkx M. Reengineering of a Fluorescent Zinc Sensor Protein Yields the First Genetically Encoded Cadmium Probe. *Chem Commun.* 2011;47:11879-11881

134. Shi H, He X, Wang K, et al. Activatable Aptamer Probe for Contrast-Enhanced In Vivo Cancer Imaging Based on Cell Membrane Protein-Triggered Conformation Alternation. *Proc Natl Acad Sci USA.* 2011;108:3900-3905

135. Yeh HY, Yates MV, Mulchandani A, et al. Visualizing the Dynamics of Viral Replication in Living Cells *via* Tat Peptide Delivery of Nuclease-Resistant Molecular Beacons. *Proc Natl Acad Sci USA.* 2008;105:17522–17525

136. Solomon M, Guo K, Sudlow GP, et al. Detection of Enzyme Activity in Orthotopic Murine Breast Cancer by Fluorescence Lifetime Imaging Using a Fluorescence Resonance Energy Transfer-Based Molecular Probe. *J Biomed Opt.* 2011;16:066019

137. Berezin MY, and Achilefu S. Fluorescence Lifetime Measurements and Biological Imaging. *Chem Rev.* 2010;110:2641–2684

138. Razansky D, Vinegoni C, and Ntziachristos V. Multispectral Photoacoustic Imaging of Fluorochromes in Small Animals. *Opt Lett.* 2007;32:2891-2893

139. Levi J, Kothapalli SR, Ma TJ, et al. Design, Synthesis, and Imaging of an Activatable Photoacoustic Probe. *J Am Chem Soc.* 2010;132:11264-11269

140. Wang TD, Friedland S, Sahbaie P, et al. Functional Imaging of Colonic Mucosa with a Fibered Confocal Microscope for Real-time In Vivo Pathology. *Clin Gastroenterol Hepatol.* 2007;5:1300-1305

141. Zysk AM, Nguyen FT, Oldenburg AL, et al. Optical Coherence Tomography: A Review of Clinical Development from Bench to Bedside. *J Biomed Opt.* 2007;12:051403

142. Wallace MB, and Kiesslich R. Advances in Endoscopic Imaging of Colorectal Neoplasia. *Gastroenterology.* 2010;138:2140–2150

143. Strijkers GJ, and Nicolay K. Relaxivity of Nanoparticles for Magnetic Resonance Imaging. *Handbook of Nanophysics.* 2010, 7 vol, 350 chapters

144. Caravan P, Ellison JJ, McMurry TJ, et al. Gadolinium(III) Chelates as MRI Contrast Agents: Structure, Dynamics, and Applications. *Chem Rev.* 1999;99:2293-2352

145. Tu C, Osborne EA, and Louie AY. Activatable T_1 and T_2 Magnetic Resonance Imaging Contrast Agents. *Ann Biomed Eng.* 2011;39:1335-1348

146. Bonnet CS, and Toth E. Smart MR Imaging Agents Relevant to Potential Neurologic Applications. *Am J Neuroradiol.* 2010;31:401-409

147. Moats RA, Fraser SE, Meade TJ. A Smart Magnetic Resonance Imaging Agent That Reports on Specific Enzymatic Activity. *Angew Chem Int Ed.* 1997;36:726-728

148. Urbanczyk-Pearson LM, Femia FJ, Smith J, et al. Mechanistic Investigation of β-Galactosidase-Activated MR Contrast Agents. *Inorg Chem.* 2008;47:56-68

149. Li W, Fraser SE, and Meade TJ. A Calcium-Sensitive Magnetic Resonance Imaging Contrast Agent. *J Am Chem Soc.* 1999;121:1413-1414

150. Hanaoka K, Kikuchi K, and Urano Y. Design and Synthesis of a Novel Magnetic Resonance Imaging Contrast Agent for Selective Sensing of Zinc Ion. *Chem Biol.* 2002;9:1027-1032

151. Aime S, Barge A, Botta M, et al. Dependence of the Relaxivity and Luminescence of Gadolinium and Europium Amino-Acid Complexes on Hydrogencarbonate and pH. *Chem Commun.* 1999;11:1047-1048

152. Aime S, Botta M, Crich SG, et al. A Macromolecular Gd(III) Complex as pH-Responsive Relaxometric Probe for MRI applications. *Chem Commun.* 1999;16:1577-1578

153. Zhang S, Wu K, and Sherry AD. A Novel pH-Sensitive MRI Contrast Agent. *Angew Chem Int Ed.* 1999;38:3192-3194

154. Løkling K, Skurtveit R, Bjørnerud A, et al. Novel pH-Sensitive Paramagnetic Liposomes With Improved MR Properties. *Magn Res Med.* 2004;51:688-696

155. Torres E, Mainini F, Napolitano R, et al. Improved Paramagnetic Liposomes for MRI Visualization of pH Triggered Release. *J Cont Release.* 2011;154:196-202

156. Langereis S, de Lussanet QG, van Genderen MHP, et al. Multivalent Contrast Agents Based on Gd-DTPA-terminated Poly(Propylene Imine) Dendrimers for Magnetic Resonance Imaging. *Macromolecules.* 2004;37:3084-3091

157. Nivorozhkin AL, Kolodziej AF, Caravan P, et al. Enzyme-Activated Gd^{3+} Magnetic Resonance Imaging Contrast Agents with a Prominent Receptor-Induced Magnetization Enhancement. *Angew Chem Int Ed.* 2001;40:2903-2906

158. Hanaoka K, Kikuchi K, Terai T, et al. A Gd^{3+}-Based Magnetic Resonance Imaging Contrast Agent Sensitive to β-Galactosidase Activity Utilizing a Receptor-Induced Magnetization Enhancement (RIME) Phenomenon. *Chem-Eur J.* 2008;14:987-995

159. Anelli PL, Bertini I, Fragai M, et al. Sulfonamide-Functionalized Gadolinium-DTPA Complexes as Possible Contrast Agents for MRI: A Relaxometric Investigation. *Eur J Inorg Chem.* 2000;4:625-630

160. Chang YT, Cheng CM, Su YZ, et al. Synthesis and Characterization of a New Bioactivated Paramagnetic Gadolinium(III) Complex [Gd(DOTA-FPG)(H2O)] for Tracing Gene Expression. *Bioconjug Chem.* 2007;18:1716-1727

161. Querol M, Chen JW, Weissleder R, et al. DTPA-bisamide-Based MR Sensor Agents for Peroxidase Imaging. *Org Lett.* 2005;7:1719-1722

162. Nahrendorf M, Sosnovik D, Chen JW, et al. Activatable Magnetic Resonance Imaging Agent Reports Myeloperoxidase Activity in Healing Infarcts and Noninvasively Detects the Antiinflammatory Effects of Atorvastatin on Ischemia-Reperfusion Injury. *Circulation.* 2008;117:1153-1160

163. Bogdanov A, Matuszewski L, Bremer C, et al. Oligomerization of Paramagnetic Substrates Result in Signal Amplification and Can Be Used for MR Imaging of Molecular Targets. *Mol Imaging.* 2002;1:16-23

164. Querol M, Chen JW, and Bogdanov A. A Paramagnetic Contrast Agent with Myeloperoxidase-sensing Properties. *Org Biomol Chem.* 2006;4:1887-1895

165. Rodriguez E, Nilges M, Weissleder R, Chen JW, et al. Activatable Magnetic Resonance Imaging Agents for Myeloperoxidase Sensing: Mechanism of Activation, Stability, and Toxicity. *J Am Chem Soc.* 2010;132:168-177

166. Thorek DLJ, Chen AK, Czupryna J, et al. Superparamagnetic Iron Oxide Nanoparticle Probes for Molecular Imaging. *An Biomed Eng.* 2006;34:23-38

167. Perez JM, Simeone FJ, Tsourkas A, et al. Peroxidase Substrate Nanosensors for MR Imaging. *Nano Lett.* 2004;4:119-122

168. Harris TJ, von Maltzahn G, Derus A, et al. Proteolytic Actuation of Nanoparticle Self-Assembly. *Angew Chem Int Ed.* 2006;45:3161-3165

169. von Maltzahn G, Harris TJ, Park JH, et al. Nanoparticle Self-Assembly Gated by Logical Proteolytic Triggers. *J Am Chem Soc.* 2007;129:6064-6065

170. Schellenberger E, Rudloff F, Warmuth C, et al. Protease-Specific Nanosensors for Magnetic Resonance Imaging. *Bioconjug Chem.* 2008;19:2440-2445

171. Atanasijevic T, Shusteff M, Fam P, et al. Calcium-Sensitive MRI Contrast Agents Based on Superparamagnetic Iron Oxide Nanoparticles and Calmodulin. *Proc Natl Acad Sci USA.* 2006;103:14707-14712

172. Perez JM, Josephson L, O'Loughlin T, et al. Magnetic Relaxation Switches Capable of Sensing Molecular Interactions. *Nat Biotechnol.* 2002;20:816-820

173. Zhao M, Josephson L, Tang Y, et al. Magnetic Sensors for Protease Assays. *Angew Chem Int Ed.* 2003;42:1375-1378

174. Perez JM, O'Loughin T, Simeone FJ, et al. DNA-based Magnetic Nanoparticle Assembly Acts as a Magnetic Relaxation Nanoswitch Allowing Screening of DNA-cleaving agents. *J Am Chem Soc.* 2002;124:2856-2857

175. Viswanathan S, Kovacs Z, Green KN, et al. Alternatives to Gadolinium-Based Metal Chelates for Magnetic Resonance Imaging. *Chem Rev.* 2010;110:2960-3018

176. Chauvin T, Durand P, Bernier M, et al. Detection of Enzymatic Activity by PARACEST MRI: A General Approach to Target a Large Variety of Enzymes. *Angew Chem Int Ed.* 2008;47:4370-4372

177. Aime S, Barge A, Castelli DD, et al. Paramagnetic Lanthanide(III) Complexes as pH-Sensitive Chemical Exchange Saturation Transfer (CEST) Contrast Agents for MRI Applications. *Magn Reson Med.* 2002;47:639–648

178. Mikawa M, Miwa N, Brautigan M, et al. A pH-Sensitive Contrast Agent for Functional Magnetic Resonance Imaging (MRI). *Chem Lett.* 1998;27:693–694

179. Hovland R, Gløgrd C, Aasen AJ, et al. Preparation and In Vitro Evaluation of a Novel Amphiphilic GdPCTA-12 Derivative; A Micellar MRI Contrast Agent. *Org Biomol Chem.* 2003;1:644–647

180. Aime S, Castelli DD, and Terreno E. Novel pH-reporter MRI Contrast Agents. *Angew Chem Int Ed.* 2002;41:4334-4336

181. Yoo B, and Pagel MD. A PARACEST MRI Contrast Agent To Detect Enzyme Activity. *J Am Chem Soc.* 2006;128:14032-14033

182. Li Y, Sheth VR, Liu G, et al. A Self-Calibrating PARACEST MRI Contrast Agent that Detects Esterase Enzyme Activity. *Contrast Media Mol Imaging.* 2011, in press

183. Lee S, Park K, Kim K, et al. Activatable Imaging Probes with Amplified Fluorescent Signals. *Chem Commun.* 2008;4250-4260

184. Teesalu T, Sugahara KN, Kotamraju VR, et al. C-end Rule Peptides Mediate Neuropilin-1-Dependent Cell, Vascular, and Tissue Penetration. *Proc Natl Acad Sci USA.* 2009;106:16157–16162

185. Sugahara KN, Teesalu T, Karmali PP, et al. Tissue-Penetrating Delivery of Compounds and Nanoparticles into Tumors. *Cancer Cell.* 2009;16:510–520

186. Jaffer FA, Tung CH, Wykrzykowska JJ, et al. Molecular Imaging of Factor XIIIa Activity in Thrombosis Using a Novel, Near-Infrared Fluorescent Contrast Agent That Covalently Links to Thrombi. *Circulation.* 2004;110:170-176

187. Kim DE, Schellingerhout D, Jaffer FA, et al. Near-Infrared Fluorescent Imaging of Cerebral Thrombi and Blood-Brain Barrier Disruption in a Mouse Model of Cerebral Venous Sinus Thrombosis. *J Cereb Blood Flow Metab.* 2005;25:226–233

188. Miserus RJHM, Herias V, Prinzen L, et al. Molecular MRI of Early Thrombus Formation Using a Bimodal α2-Antiplasmin-Based Contrast Agent. *JACC Cardiovasc Imag.* 2009;2:987-996

189. Nahrendorf M, Hu K, Frantz S, et al. Factor XIII Deficiency Causes Cardiac Rupture, Impairs Wound Healing, and Aggravates Cardiac Remodeling in Mice With Myocardial Infarction. *Circulation.* 2006;113:1196-1202

190. Nahrendorf M, Aikawa E, Figueiredo JL, et al. Transglutaminase Activity in Acute Infarcts Predicts Healing Outcome and Left Ventricular Remodelling: Implications for FXIII Therapy and Antithrombin Use in Myocardial Infarction. *Eur Heart J.* 2008;29:445-454

191. Gao GH, Lee JW, Nguyen MK, et al. pH-Responsive Polymeric Micelle Based on PEG-Poly(β-Aminoester)/(Amido Amine) as Intelligent Vehicle for Magnetic Resonance Imaging in Detection of Cerebral Ischemic Area. *J Cont Release.* 2011;155:11-17

192. Andreev OA, Dupuy AD, Segala M, et al. Mechanism and Uses of a Membrane Peptide that Targets Tumors and Other Acidic Tissues In Vivo . *Proc Natl Acad Sci USA.* 2007;104:7893–7898

193. Vävere AL, Biddlecombe GB, Spees WM, et al. A Novel Technology for the Imaging of Acidic Prostate Tumors by Positron Emission Tomography. *Cancer Res.* 2009;69:4510-4516

194. Pauwels EK, Ribeiro MJ, Stoot JH, et al. FDG Accumulation and Tumor Biology. *Nucl Med Biol.* 1998;25:317-322

195. Tjuvajev JG, Doubrovin M, Akhurst T, et al. Comparison of Radiolabeled Nucleoside Probes (FIAU, FHBG, and FHPG) for PET imaging of HSV1-tk Gene Expression. *J Nucl Med.* 2002;43:1072-1083

196. Choi SR, Zhuang ZP, Chacko AM, et al. SPECT Imaging of Herpes Simplex Virus Type1 Thymidine Kinase Gene Expression by [(123}I]FIAU(1). *Acad Radiol.* 2005;12:798-805

197. Bauer C, Bauder-Wuest U, Mier W, et al. 131I-labeled peptides as caspase substrates for apoptosis imaging. *J Nucl Med.* 2005;46:1066–1074

198. Suzuki H, Sato M, and Umezawa Y. Accurate Targeting of Activated Macrophages Based on Synergistic Activation of Functional Molecules Uptake by Scavenger Receptor and Matrix Metalloproteinase. *ACS Chem Biol.* 2008;3:471-479

199. Breurken M, Lempens EHM, and Merkx M. Protease-Activatable Collagen Targeting Based on Protein Cyclization. *ChemBioChem.* 2010;11:1165-1168

200. Lepage M, Dow WC, Melchior M, et al. Noninvasive Detection of Matrix Metalloproteinase Activity In Vivo Using a Novel MRI Contrast Agent with a Solubility Switch. *Mol Imaging.* 2007;6:393–403

201. Lebel R, Jastrzebska B, Therriault H, et al. Novel Solubility-Switchable MRI Agent Allows the Noninvasive Detection of Matrix Metalloproteinase-2 Activity In Vivo in a Mouse Model. *Mag Res Med.* 2008;60:1056-1065

202. Jastrzebska B, Lebel R, Therriault H, et al. New Enzyme-Activated Solubility-Switchable Contrast Agent for Magnetic Resonance Imaging: From Synthesis to In Vivo Imaging. *J Med Chem.* 2009;52:1576-1581

203. Chuang CH, Chuang KH, Wang HE, et al. In Vivo Positron Emission Tomography Imaging of Protease Activity by Generation of a Hydrophobic Product from a Noninhibitory Protease Substrate. *Clin Cancer Res.* 2012 ;18 :238-247

204. Jiang T, Olson ES, Nguyen QT, et al. Tumor Imaging by Means of Proteolytic Activation of Cell-Penetrating Peptides. *Proc Nat Acad Sci USA.* 2004;101:17867-17872

205. Aguilera TA, Olson ES, Timmers MM, et al. Systemic In Vivo Distribution of Activatable Cell Penetrating Peptides is Superior to that of Cell Penetrating Peptides. *Integr Biol (Camb).* 2009;1:371-381

206. Olson ES, Aguilera TA, Jiang T, et al. In Vivo Characterization of Activatable Cell Penetrating Peptides for Targeting Protease Activity in Cancer. *Integr Biol (Camb).* 2009;1:382-393

207. Olson ES, Jiang T, Aguilera TA, et al. Activatable Cell Penetrating Peptides Linked to Nanoparticles as Dual Probes for In Vivo Fluorescence and MR Imaging of Proteases. *Proc Nat Acad Sci USA.* 2010;107:4311-4316

208. Nguyen QT, Olson ES, Aguilera TA, et al. Surgery with Molecular Fluorescence Imaging Using Activatable Cell-Penetrating Peptides Decreases Residual Cancer and Improves Survival. *Proc Nat Acad Sci USA.* 2010;107:4317-4322

209. Nakase I, Niwa M, Takeuchi T, et al. Cellular Uptake of Arginine-Rich Peptides: Roles for Macropinocytosis and Actin Rearrangement. *Mol Ther.* 2004;10:1011-1022

210. Kaplan IM, Wadia JS, and DowdySF. Cationic TAT Peptide Transduction Domain Enters Cells by Macropinocytosis. *J Cont Release.* 2005;102:247-253

211. Van den Berg A, and Dowdy SF. Protein Transduction Domain Delivery of Therapeutic Macromolecules. *Curr Opin Biotech.* 2011;22:1-6

212. Goun EA, Shinde R, Dehnert KW, et al. Intracellular Cargo Delivery by an Octaarginine Transporter Adapted to Target Prostate Cancer Cells through Cell Surface Protease Activation. *Bioconjug Chem.* 2006;17:787-796

213. Yuan X, Lin X, Manorek G, et al. Challenges Associated with the Targeted Delivery of Gelonin to Claudin Expressing Cancer Cells with the Use of Activatable Cell Penetrating Peptides to Enhance Potency. *BMC Cancer.* 2011;11:61-70

214. Whitney M, Crisp JL, Olson ES, et al. Parallel In Vivo and In Vitro Selection Using Phage Display Identifies Protease Dependent Tumor Targeting Peptides. *J Biol Chem.* 2010;285:22532-22541

215. Chen J, Liu TWB, Lo PC, et al. Zipper Molecular Beacons: A Generalized Strategy to Optimize the Performance of Activatable Protease Probes. *Bioconjug Chem.* 2009;20:1836-1842

216. Zhang Y, So MK, and Rao J. Protease-Modulated Cellular Uptake of Quantum Dots. *Nano Lett.* 2006;6:1988-1992

217. Mok H, Bae KH, Ahn CH, et al. PEGylated and MMP-2 Specifically DePEGylated Quantum Dots: Comparative Evaluation of Cellular Uptake. *Langmuir*. 2009;25:1645-1650

218. Zhai XH, Liu M, Guo XJ, et al. SKOV-3 Cell Imaging by Paramagnetic Particles Labeled with Hairpin Cell-Penetrating Peptides. *Chin Med J.* 2011;124:111-117

219. Watkins GA, Jones EF, Shell MS, et al. Development of an Optimized Activatable MMP-14 Targeted SPECT Imaging Probe. *Bioorg Med Chem.* 2009;17:653-659

220. Pan MH, Jones EF, Watkins GA, et al. Biodistribution of an Activatable Cell-Penetrating SPECT Imaging Probe for Prostate Cancer in Mice Study. *J Nucl Med.* 2007;48:315P [abstract]

221. Olson ES, Whitney MA, Friedman B, et al. In Vivo Fluorescence Imaging of Atherosclerotic Plaques with Activatable Cell-Penetrating Peptides Targeting Thrombin Activity. *Integr Biol.* 2012;4:595-605

222. Cobos-Correa A, Trojanek JB, Diemer S, et al. Membrane-Bound FRET Probe Visualizes MMP-12 Activity in Pulmonary Inflammation. *Nat Chem Biol.* 2009;5:628-630

223. Zhao T, Harada H, Teramura Y, et al. A Novel Strategy to Tag Matrix Metalloproteinases-Positive Cells for In Vivo Imaging of Invasive and Metastatic Activity of Tumor Cells. *J Cont Release.* 2010;144:109–114

224. Blankenberg FG. Molecular Imaging: the Latest Generation of Contrast Agents and Tissue Characterization Techniques. *J Cell Biochem.* 2003;90:443-453

Chapter **2**

Characterization of radiolabeled MMP-2/9 activatable cell penetrating peptides *in vitro* and *in vivo* in tumor-bearing mice

Abstract

This Chapter describes the development, *in vitro* and *in vivo* characterization of a matrix metalloproteinase-2 and -9 (MMP-2/9) sensitive activatable cell penetrating peptide (ACPP) for nuclear imaging purposes. The peptide probe showed high sensitivity for MMP-2 and MMP-9, while low to no sensitivity towards other members of the MMP-family. Biodistribution studies displayed a 5-fold higher retention of ACPP in MMP-2/9 positive tumor than in muscle ($p<0.01$) and a 6-fold higher tumor retention relative to a negative control non-ACPP ($p<0.01$). Surprisingly however, the uptake of ACPP was significantly higher in almost all tissues compared to non-ACPP ($p<0.01$). To unravel the activation process of ACPP *in vivo*, we developed dual-isotope ACPP analogs (dACPPs) that allows us to discriminate between uncleaved dACPP and activated dACPP. *In vivo* biodistribution of dACPP indicated that the tissue-associated counts originated from activated dACPP. Interestingly, dACPP administration to healthy mice resulted in a similar dACPP biodistribution compared to MMP-2/9 positive tumor-bearing mice. Furthermore, a radiolabeled cell penetrating peptide (CPP) showed equal tumor-to-tissue ratios as found for ACPP ($p>0.05$). In conclusion, this study demonstrates that tumor targeting of radiolabeled matrix metalloproteinase-2/9 activatable cell penetrating peptides is most likely caused by activation in the vascular compartment rather than tumor specific activation.

Introduction

The matrix metalloproteinases (MMPs), in particular MMP-2 and MMP-9, have been identified as key modulators in the extracellular matrix remodeling, which is a hallmark of pathological conditions such as cancer (1-4). The recognition of MMPs as disease biomarkers has stimulated the development of imaging strategies targeting these proteases, aiming for improved diagnosis or application in image-guided surgery. Commonly used approaches for MMP imaging are based on targeting with antibodies or small molecule ligands (5-9). For example, radiolabeled MMP binding ligands have been developed for the detection of up-regulated MMP levels by means of Single Photon Emission Computed Tomography (SPECT) or Positron Emission Tomography (PET) (10-12). Other strategies for MMP imaging, which do take full advantage of the nature of the target, are directed at the activity of the enzyme and will provide a selective read out of the activated MMP subpopulation and, importantly, will lead to signal amplification since one MMP can continuously activate its substrate (13). The group of Roger Tsien employed a strategy that centered on an activatable cell penetrating peptide (ACPP) that consisted of an MMP-2/9 substrate inserted in between a polyanionic peptide and a polycationic cell penetrating peptide (CPP) conjugated to an imaging label. The cell penetrating property of the polycationic peptide was quenched by electrostatic interactions with the polyanionic domain, preventing cellular uptake of the probe (14). Cleavage of the substrate by MMP-2/9 released the polycationic from the polyanionic domain, thereby triggering cellular adhesion and subsequent uptake of the imaging label-functionalized polycationic peptide. A 3- to 4-fold increase in tumor homing was observed for ACPP compared to MMP-2/9 uncleavable control peptides, accompanied by a 4-fold higher ACPP retention in tumor compared to muscle (14-16). Although ACPPs were successfully used for optical and magnetic resonance imaging of MMP-2/9 (14-18), the use of this concept in nuclear imaging or -therapy has remained largely unexplored. Recently Watkins et al. investigated an MMP-14 activatable analog for SPECT (19). Although *in vitro* activation was observed in cell cultures expressing MMP-14, a control cell line lacking MMP-14 expression also activated the probe, and therefore MMP-14 selectivity could not be demonstrated. In this work, we explored the use of radiolabeled ACPPs (Fig. 2.1) for later application in SPECT or potentially PET imaging of MMP-2/9 expression in tumors. The employed MMP-2/9-selective sequence was earlier used by Tsien and co-workers (14). The polycationic and polyanionic domains consisted of D-amino acids to avoid proteolytic degradation of these domains (20). The cell penetrating peptide domain of ACPP was functionalized with a DOTA chelate and radiolabeled with [177]Lu. The ACPP was studied *in vitro* in MMP-2/9 positive HT-1080 fibrosarcoma cell cultures and *in vivo* in HT-1080 tumor-bearing mice together with a ^{177}Lu-radiolabeled non-activatable cell penetrating peptide (non-ACPP) serving as negative control and a positive control consisting of CPP (without the polyanionic domain) (Fig. 2.1). For further insights in the mode of action of ACPP we also developed dual isotope-labeled analogs for the MMP activatable and non-activatable probes (dACPP and non-dACPP) (Figs. 2.1 and 2.2). The dual isotope approach allows us to discriminate between activated ACPP and uncleaved ACPP as well as a-specific tissue uptake

of the negative control in healthy mice, and in mice bearing either tumors characterized by a high MMP-2/9 expression (HT-1080 fibrosarcoma) or a low MMP-2/9 expression (BT-20 breast carcinoma). Furthermore, a fluorescence resonance energy transfer (FRET) ACPP analog was synthesized for *in vitro* screening applications (Fig. 2.2).
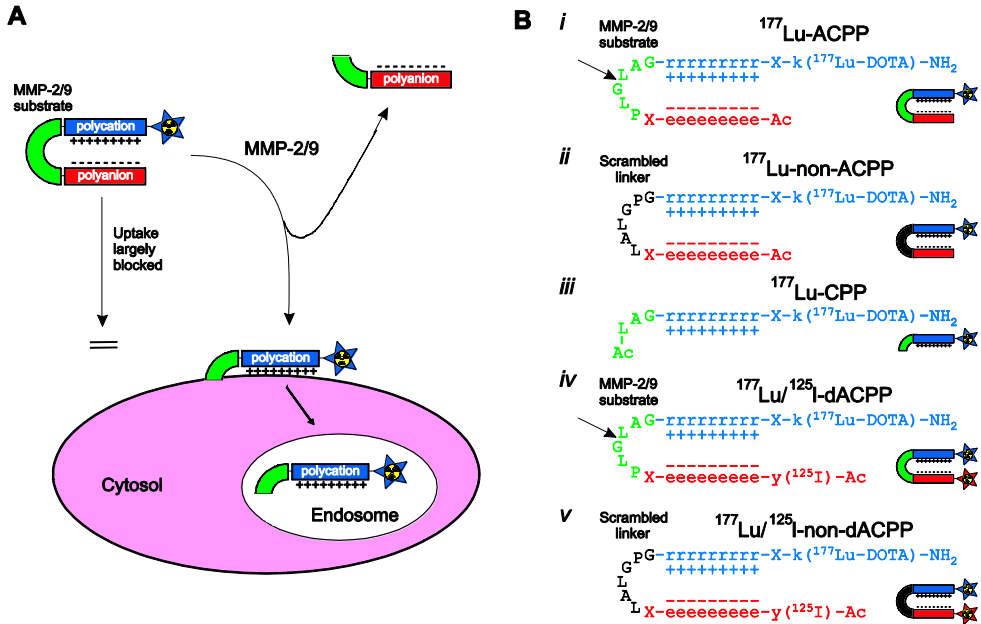
Figure 2.1: *Mechanism and structure of radiolabeled MMP-2/9 activatable ACPPs. (A) The cell penetrating property of a polycationic peptide is masked by a polyanionic peptide. Cleavage of the linker by MMP-2/9 releases the polycationic cell penetrating peptide, which will transfer its radionuclide cargo across the cell membrane. The trapped radioactivity can be imaged by SPECT or PET. (B) Peptide structure of (i) the MMP-2/9-sensitive ^{177}Lu-ACPP, (ii) the negative control ^{177}Lu-non-ACPP containing a scrambled linker, (iii) the positive control ^{177}Lu-CPP, (iv) the MMP-2/9-sensitive dual-isotope radiolabeled ^{177}Lu/^{125}I-dACPP, and (v) the negative control ^{177}Lu/^{125}I-non-dACPP. The MMP-2/9 cleavage site is indicated by the arrow.*
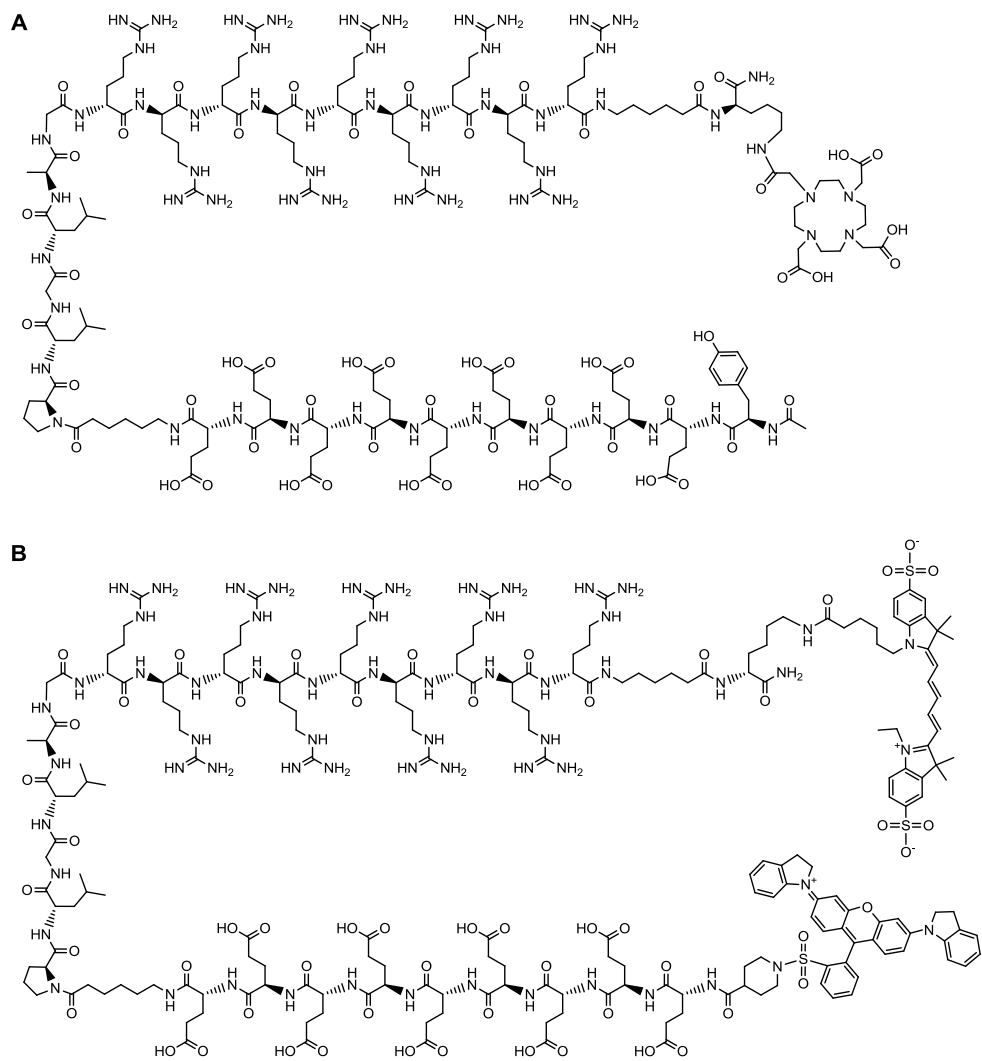
Figure 2.2: *Molecular structures of (A) Ac-y-e₉-x-PLGLAG-r₉-x-k(DOTA)-NH₂ (dACPP) and (B) QSY21-e₉-x-PLGLAG-r₉-x-k(Cy-5)-NH₂ (FRET-ACPP).*

Results

Probe synthesis

The peptides ACPP, dACPP, non-ACPP, non-dACPP, CPP, FRET-ACPP, and FRET-non-ACPP were successfully prepared by Fmoc solid-phase peptide synthesis and purified by reversed phase – HPLC. Liquid chromatography – mass spectrometry (LC-MS) analysis demonstrated >95% pure peptides with molecular masses consistent to their theoretic masses (Fig. 2.3).
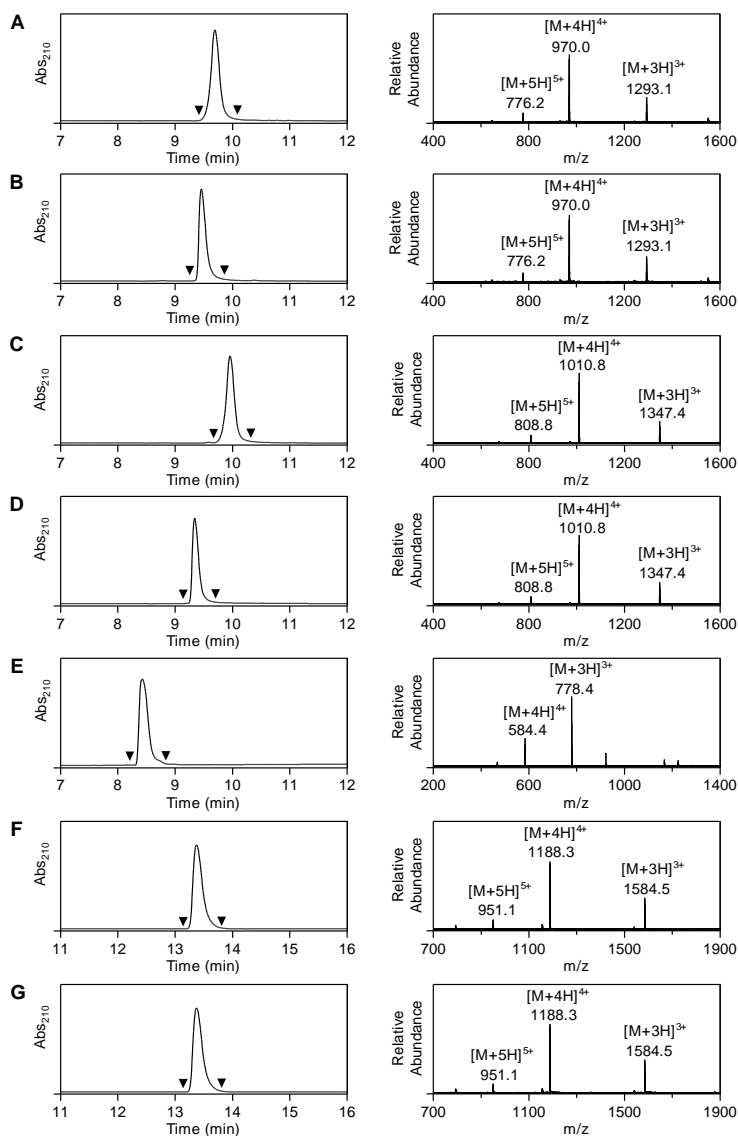
Figure 2.3: *LC-MS characterization of (A) Ac-e$_9$-x-PLGLAG-r$_9$-x-k(DOTA)-NH$_2$ (ACPP, obsd. 3874.1 Da, calcd. 3874.1 Da), (B) Ac-e$_9$-x-LALGPG-r$_9$-x-k(DOTA)-NH$_2$ (non-ACPP, obsd. 3874.1 Da, calcd. 3874.1 Da), (C) Ac-y-e$_9$-x-PLGLAG-r$_9$-x-k(DOTA)-NH$_2$ (dACPP, obsd. 4037.1 Da, calcd. 4037.1 Da), (D) Ac-y-e$_9$-x-LALGPG-r$_9$-x-k(DOTA)-NH$_2$ (non-dACPP, obsd. 4037.1 Da, calcd. 4037.1 Da), (E) Ac-LAG-r$_9$-x-k(DOTA)-NH$_2$ (CPP, obsd. 2332.5 Da, calcd. 2332.4 Da), (F) QSY21-e$_9$-x-PLGLAG-r$_9$-x-k(Cy-5)-NH$_2$ (FRET-ACPP, obsd. 4747.3 Da, calcd. 4747.3 Da), and (G) QSY21-e$_9$-x-LALGPG-r$_9$-x-k(Cy-5)-NH$_2$ (FRET-non-ACPP, obsd. 4747.3 Da, calcd. 4747.3 Da). The left and right graphs show the UV absorbance chromatogram and the mass spectrum of the UV-peak bracketed by the arrowheads, respectively.*

Enzyme assay

The sensitivity of the ACPP structure towards nine different enzymes (MMP-1, MMP-2, MMP-3, MMP-7, MMP-9, MMP-14, urokinase, plasmin, and thrombin) was studied *in vitro*. LC-MS analysis after 1h of incubation showed that ACPP is efficiently cleaved between the glycine and leucine residue by MMP-2, MMP-9, and to a minor extent by MMP-14, while no ACPP cleavage was observed for the other enzymes (Figs. 2.4 and 2.5). To further prove the specificity of ACPP, an ACPP analog was synthesized containing a scrambled linker. Under similar conditions, MMP-2, -9, and -14 were not able to cleave this negative control peptide non-ACPP (Fig. 2.4B).
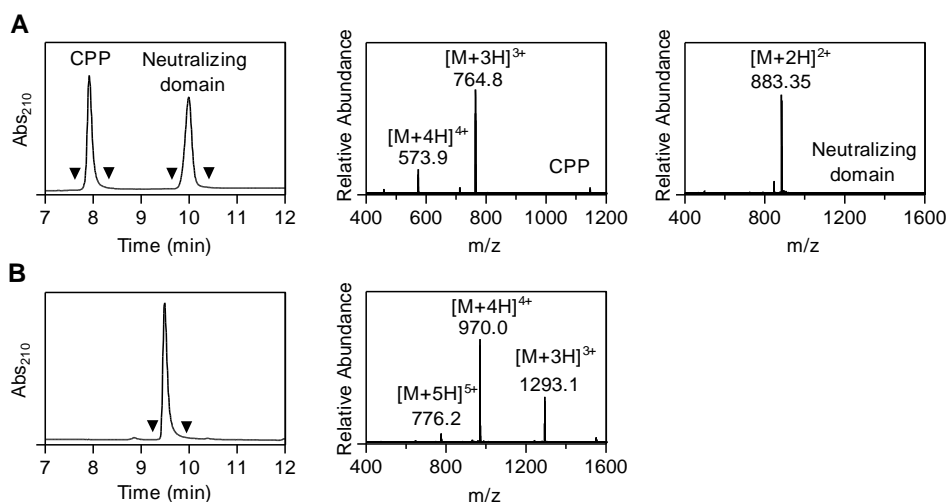
Figure 2.4: *LC-MS characterization of dACPP and non-ACPP (0.1 mM) incubated with MMP-2 (30 nM) for 1h. (A) LC chromatogram (UV) of dACPP (left) and MS spectra of the UV-peaks bracketed by the arrowheads; CPP (obsd. 2290.4 Da, calcd. 2290.4 Da for H_2N-LAG-r_9-x-k(DOTA)-NH_2) and Neutralizing domain (obsd. 1764.7 Da, calcd. 1764.7 Da for Ac-y-e_9-x-PLG-COOH). (B) LC chromatogram (UV) of non-ACPP (left) and MS spectra of the UV-peak bracketed by the arrowheads (obsd. 3874.1 Da, calcd. 3874.1 Da for non-ACPP). Similar results were obtained for non-ACPP incubated with MMP-9 and MMP-14 (data not shown).*

Fluorescence Resonance Energy Transfer (FRET)-ACPP and MMP-2, MMP-9 kinetics

The enzyme kinetics of the ACPP with MMP-2 and MMP-9 was determined using the FRET-ACPP analog. In this probe, a Cy-5 fluorophore and a QSY21 quencher were conjugated to the polycationic and polyanionic domain, respectively (Fig. 2.2B). Cy-5 shows maximal emission at 670 nm when excited at 650 nm. The quenching group QSY21 is not fluorescent and has a wide absorption spectrum from 540 to 730 nm with a peak at 660 nm. For the intact FRET-ACPP, efficient energy transfer between Cy-5 and QSY21 occurred resulting in near-to-complete fluorescence quenching.

A

B

Figure 2.5: *ACPP sensitivity towards nine different enzymes in vitro. (A) LC chromatograms of dACPP (0.1 mM) 1h after incubation with 5 nM of either MMP-1, MMP-2, MMP-3, MMP-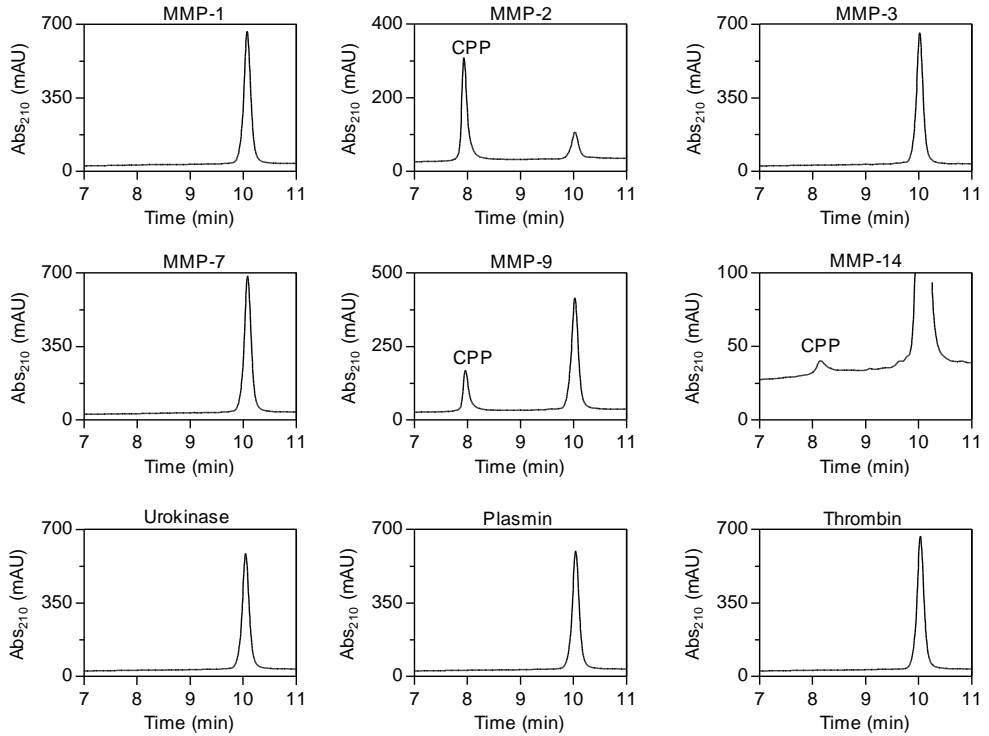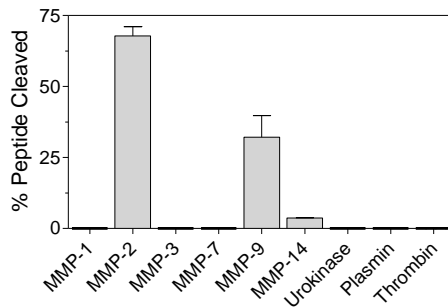7, MMP-9, MMP-14, Urokinase, Plasmin, or Thrombin (representative of three measurements). (B) Percentage cleaved ACPP after 1h incubation. The experiments were performed in triplicate and the data are presented as mean ± SD.*

Incubation of FRET-ACPP with MMP-2 showed a strong increase in Cy-5 fluorescence, while this was not observed for FRET-non-ACPP (Fig. 2.6). Furthermore, MMP-2 mediated probe activation was blocked in the presence of GM6001, a broad-spectrum MMP inhibitor (Fig. 2.6). We observed rapid cleavage of FRET-ACPP by MMP-2 and MMP-9, characterized by catalytic efficiencies (k_{cat}/K_m) of $(4.0 \pm 0.5) \cdot 10^5$ $M^{-1}s^{-1}$ and $(5.2 \pm 0.7) \cdot 10^4$ $M^{-1}s^{-1}$, respectively.
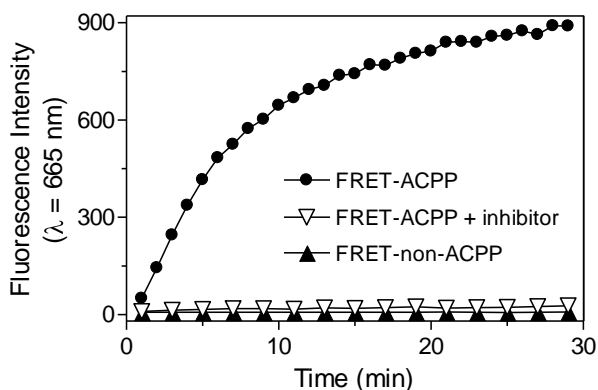
Figure 2.6: *Fluorescence intensity change at λ = 665 nm for FRET-ACPP (with/without 50 µM MMP inhibitor GM6001) and FRET-non-ACPP (1.25 µM) upon incubation with MMP-2 (1.0 nM).*

In vitro cell assay

We radiolabeled the polycationic domain of ACPP, non-ACPP, and CPP with ^{177}Lu with a >98% radiochemical yield (Fig. 2.7) and set out to assess the uptake of ^{177}Lu-ACPP by MMP positive HT-1080 cells. Although these cells secrete MMP-2 and MMP-9 as was evidenced by gelatin zymography (Fig. 2.8), it has been demonstrated that those enzymes become too diluted in two-dimensional cell culture supernatants, resulting in minimal ACPP probe activation and insignificant uptake (15). Therefore, ^{177}Lu-ACPP was pre-cleaved with MMP-2, resulting in 85% activation (Fig. 2.7E), incubated for 3h at 1.25 µM with HT-1080 cells and compared to ^{177}Lu-non-ACPP, uncleaved ^{177}Lu-ACPP, and ^{177}Lu-CPP. The cellular uptake of the activated ACPP was comparable to uptake of the positive control taking the 85% activation of ACPP into account, while uncleaved ACPP displayed negligible cellular uptake (Fig. 2.9C). The localization of the activated probe upon penetration of HT-1080 cells was determined by confocal laser scanning microscopy (CLSM) using a fluorescein labeled analog and showed entrapment of the probe in cytoplasmic vesicles (Fig. 2.10).
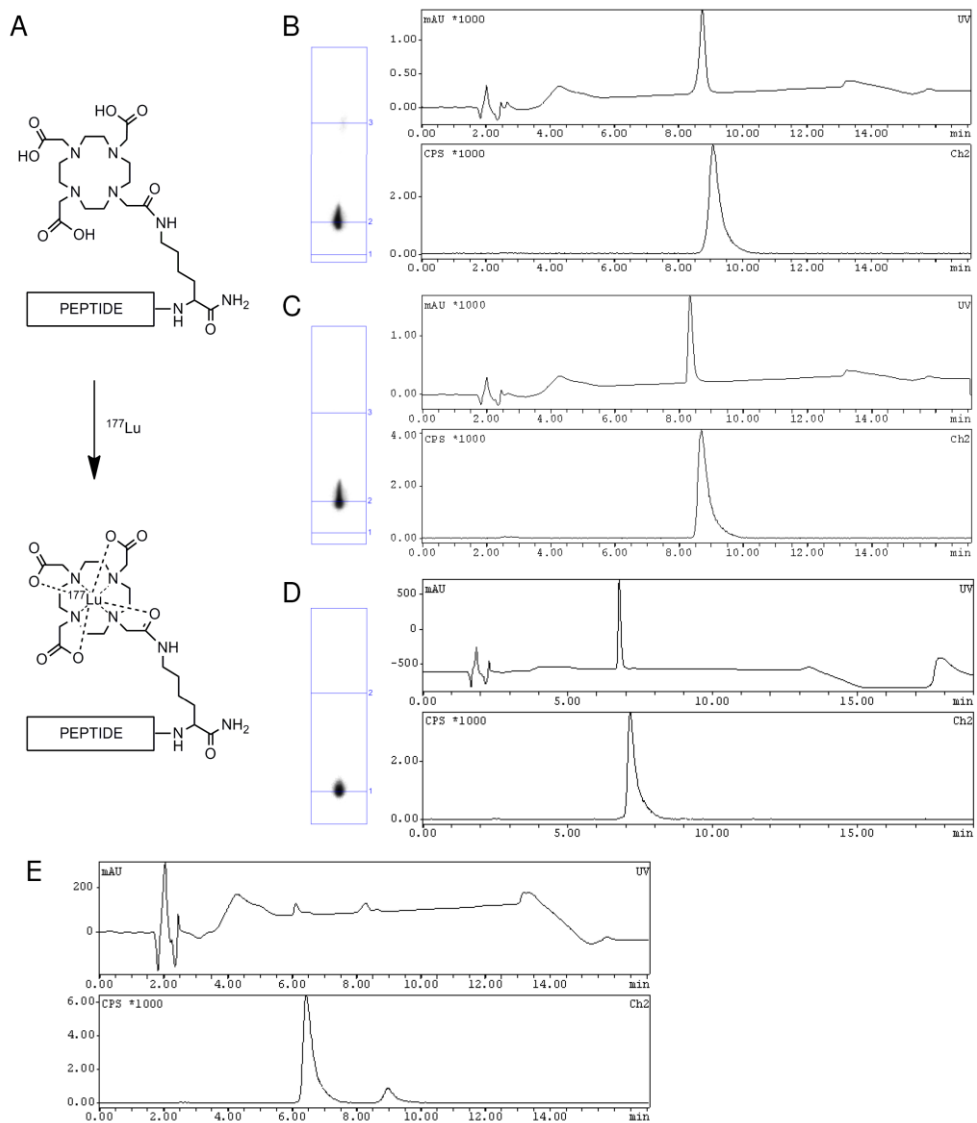
Figure 2.7: *(A)* ^{177}*Lu labeling of DOTA-conjugated peptides. (B-D) Instant silica thin layer chromatography (iTLC) (left) and γ-HPLC spectra (right) of the radiolabeled peptides (B)* ^{177}*Lu-ACPP (>98% radiochemical purity (rp)), (C)* ^{177}*Lu-non-ACPP (>98% rp), and (D)* ^{177}*Lu-CPP (>98% rp).* ^{177}*Lu labeling of peptide analogs lacking the DOTA moiety resulted in <5% rp (data not shown). (E) γ-HPLC spectrum of* ^{177}*Lu-ACPP activated by MMP-2 for 3h yielding 85% activation. For γ-HPLC spectra, the upper panel shows the UV absorbance chromatogram at 212 nm and the lower panel shows the γ-radiation monitored by a γ-detector.*

Figure 2.8: *Gelatin zymography. Analysis of serum-free medium of phorbol 12-myristate 13-acetate stimulated HT-1080 cells (lane 2). Active MMP-2 was loaded as reference (lane 1).*
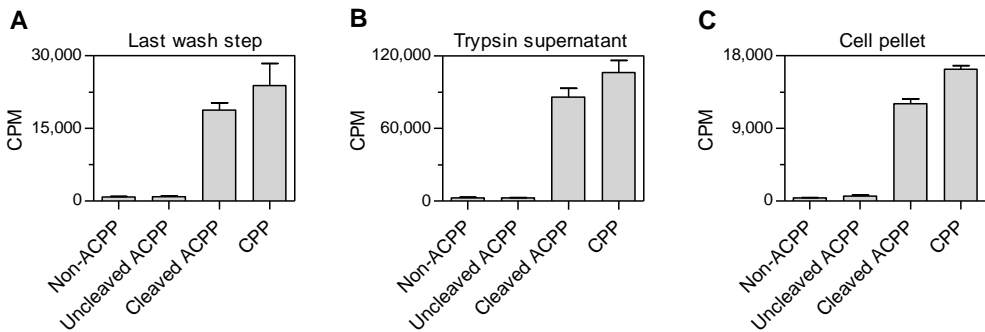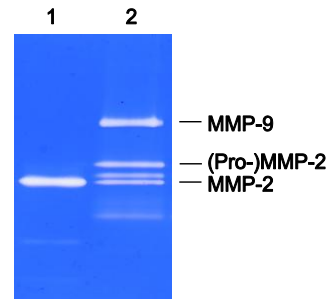
Figure 2.9: *Cell assay showing γ-counting results for (A) last wash fraction, (B) trypsin supernatant, and (C) cell pellet for ^{177}Lu-non-ACPP, uncleaved ^{177}Lu-ACPP, pre-activated ^{177}Lu-ACPP (for 85%), and ^{177}Lu-CPP after 3h incubation. The experiments were performed in triplicate and the data are presented as mean ± SD. For pre-activated ACPP and CPP a substantial amount of radioactivity was detected in the last wash step. Most likely, this observation can be explained by detachment of CPP which was bound to the ECM of the cells and not yet internalized.*
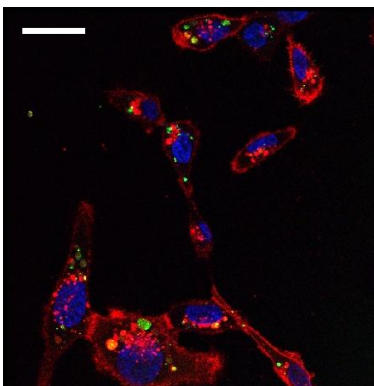
Figure 2.10: *CLSM image of HT-1080 cells incubated with fluorescein-labeled CPP for 4h (green). Nuclei were stained with Hoechst 33342 (blue), and phospholipid bilayer membranes with DiD (red). White bar = 25 μm.*

Probe sensitivity towards trypsin

In the described *in vitro* cell assay, trypsin digestion was used to harvest cells prior to γ-counting. To assess the sensitivity of ACPP, non-ACPP, and CPP towards trypsin, the peptides (0.1 mM) were incubated with trypsin for 5 min. A substantial amount of ACPP (~30%) was cleaved by trypsin, while under similar conditions no cleavage/degradation occurred for non-ACPP and CPP (Fig. 2.11). ACPP was cleaved between the amino acids leucine and alanine present in the MMP-2 cleavable linker PLGLAG.
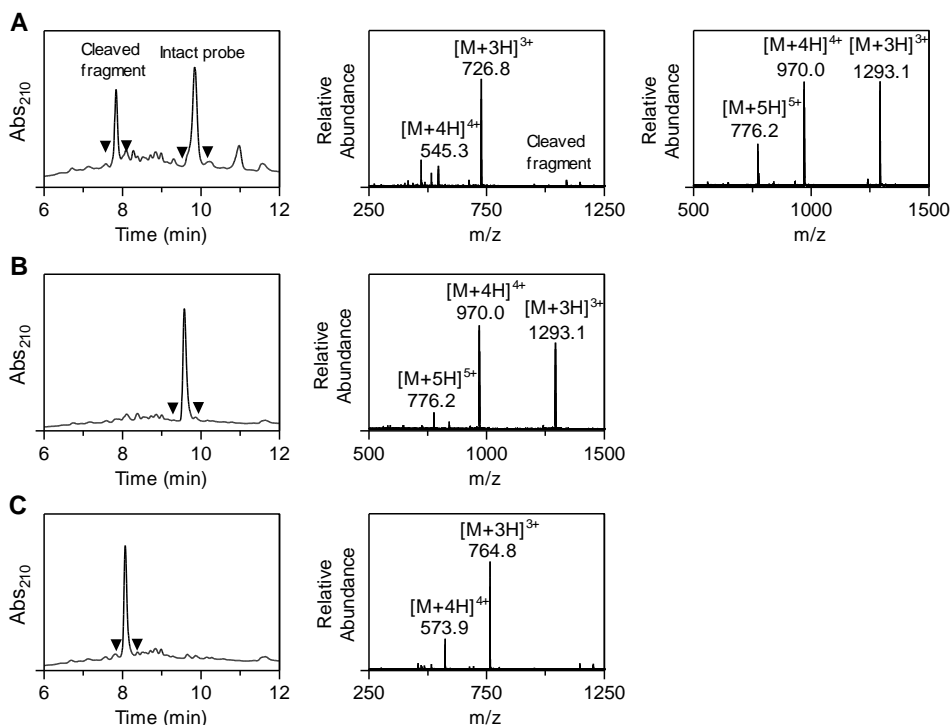
Figure 2.11: *LC-MS characterization of (A) ACPP (obsd. 2177.4 Da for cleaved fragment, calcd. 2177.4 Da for H_2N-AG-r_9-x-k(DOTA)-NH_2, and obsd. 3874.1 Da, ACPP calcd. 3874.1 Da), non-ACPP (obsd. 3874.1 Da, calcd. 3874.1 Da), and (C) CPP (obsd. 2290.4 Da, calcd. 2290.4 Da) 5 min after incubation with trypsin (0.125 w/v%).*

To exclude trypsin-mediated ACPP activation in our *in vitro* cell assay, the cells incubated with the probes were carefully washed 5-times with Dulbecco's PBS before the cells were harvested by trypsin. These wash steps ensured that the soluble probes were removed before trypsin digestion (last wash fraction contained <0.05% radioactivity compared to incubation medium for non-ACPP and intact ACPP). The data showed that the cellular uptake of the negative control and trypsin sensitive intact probe was similar, indicating that there is no significant role of trypsin on ACPP activation in this experiment (Fig. 2.9).

In vivo biodistribution of ACPP and non-ACPP and its dual-isotope labeled analogs

Our investigations continued with *in vivo* biodistribution studies of the radiolabeled ACPP and the negative control peptide non-ACPP (60 nmol, i.v.-injection) in MMP-2/9 positive HT-1080 tumor-bearing mice (Fig. 2.12; Tables 2.1 and 2.2). Table 2.3 shows the statistical analysis of the biodistribution data. The tumor uptake of ^{177}Lu-ACPP was significantly higher compared to its accumulation in muscle as well as the tumor uptake of ^{177}Lu-non-ACPP after 3h, 6h, and 24h, supporting earlier studies proposing ACPP activation by tumoral MMP-2/9 (*14-16*). Surprisingly however, not only the tumor, but also other tissues showed significantly higher retention of ^{177}Lu-ACPP compared to ^{177}Lu-non-ACPP. In muscle and heart the relative difference between ^{177}Lu-ACPP and ^{177}Lu-non-ACPP retention was even higher than that observed for tumor (Table 2.2), although no MMP-2/9 activity was detected by gelatin zymography in these tissues (Fig. 2.13).
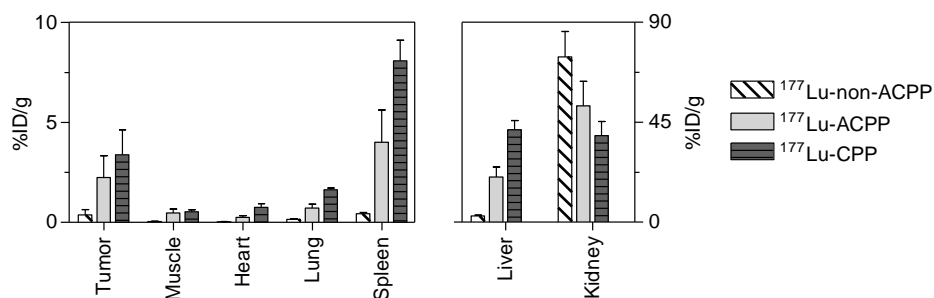
Figure 2.12: *Comparison of the biodistribution of 60 nmol ^{177}Lu-non-ACPP, ^{177}Lu-ACPP, and ^{177}Lu-CPP in HT-1080 tumor-bearing mice (n=6) 24h post-injection. The data are presented as mean ± SD.*

Table 2.1: *Biodistribution results of 60 nmol ^{177}Lu-ACPP and ^{177}Lu-non-ACPP at 3h, 6h, and 24h post injection in HT-1080 tumor-bearing mice. The data are mean %ID/g ± SD.*

HT-1080	^{177}Lu-ACPP			^{177}Lu-non-ACPP		
	3h, n=4	6h, n=3	24h, n=6	3h, n=3	6h, n=3	24h, n=6
Blood	0.46 ± 0.22	0.04 ± 0.02	0.01 ± 0.00	0.02 ± 0.00	0.00 ± 0.00	0.00 ± 0.00
HT-1080 tumor	1.82 ± 0.59	1.90 ± 0.71	2.23 ± 1.09	0.50 ± 0.07	0.31 ± 0.14	0.37 ± 0.27
Muscle	0.55 ± 0.29	0.48 ± 0.18	0.46 ± 0.20	0.03 ± 0.01	0.03 ± 0.01	0.04 ± 0.01
Heart	0.64 ± 0.29	0.33 ± 0.03	0.25 ± 0.08	0.04 ± 0.01	0.04 ± 0.01	0.03 ± 0.01
Lung	1.92 ± 0.67	0.82 ± 0.13	0.70 ± 0.20	0.28 ± 0.11	0.15 ± 0.05	0.15 ± 0.03
Spleen	2.85 ± 0.35	2.79 ± 0.39	4.00 ± 1.62	0.37 ± 0.09	0.36 ± 0.06	0.43 ± 0.06
Liver	12.6 ± 2.30	17.0 ± 2.62	20.3 ± 4.65	2.19 ± 0.43	2.16 ± 0.36	2.89 ± 0.33
Kidney	67.8 ± 10.5	52.2 ± 1.23	52.4 ± 10.9	78.6 ± 22.5	84.7 ± 17.9	74.4 ± 11.5
Fat	0.31 ± 0.13	0.27 ± 0.15	0.23 ± 0.02	0.03 ± 0.01	0.03 ± 0.03	0.04 ± 0.02
Thigh bone	2.67 ± 0.98	2.66 ± 0.20	2.66 ± 0.68	0.69 ± 0.05	0.50 ± 0.07	0.67 ± 0.21
Brain	0.04 ± 0.01	0.01 ± 0.00	0.01 ± 0.00	0.00 ± 0.00	0.00 ± 0.00	0.00 ± 0.00

Table 2.2: *Organ ratio ^{177}Lu-ACPP/^{177}Lu-non-ACPP at 3h, 6h, and 24h post-injection in HT-1080 tumor-bearing mice.*

ACPP/ non-ACPP	3h	6h	24h
Blood	26.6	8.1	1.9
HT-1080 tumor	3.7	6.1	6.0
Muscle	16.7	14.0	12.0
Heart	16.2	9.1	7.6
Lung	6.9	5.5	4.6
Spleen	7.8	7.8	9.3
Liver	5.8	7.9	7.0
Kidney	0.9	0.6	0.7

Table 2.3: *Statistical analysis of biodistribution data (24h) comparing means of ^{177}Lu-ACPP and ^{177}Lu-non-ACPP.*

24h	Welch's t-test	Mann Whitney U-test
ACPP vs non-ACPP		
HT-1080 tumor	0.0158	0.0022
Muscle	0.0036	0.0022
Heart	0.0016	0.0022
ACPP		
HT-1080 tumor vs muscle	0.0114	0.0022
HT-1080 tumor vs heart	0.0068	0.0022
non-ACPP		
HT-1080 tumor vs muscle	0.0036	0.0022
HT-1080 tumor vs heart	0.0034	0.0022
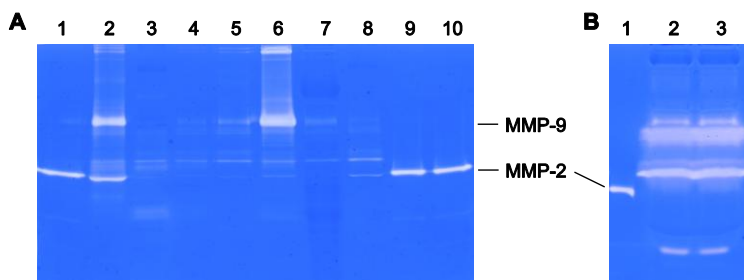
Figure 2.13: *Gelatin zymography. (A) Analysis of tissue homogenates (representative of three mice). Lane 1 = active MMP-2, lanes 2-8 = HT-1080 tumor, muscle, heart, lung, spleen, liver, bladder, respectively. Lanes 9 and 10 = active MMP-2 (0.13 ng). (B) Analysis of mouse serum. Lane 1 = active MMP-2, lanes 2 and 3 = serum from tumor-free and HT-1080 tumor-bearing mice, respectively.*

Furthermore, ^{177}Lu-non-ACPP displayed a significantly higher HT-1080 tumor retention compared to muscle and heart. A high liver, spleen, and kidney retention was observed for ^{177}Lu-ACPP, while ^{177}Lu-non-ACPP accumulated mainly in the kidneys, indicating that the probes are excreted via different pathways. As CPPs have been reported to mainly distribute to the liver (15,21), the altered biodistribution may have been caused by enzymatic conversion of ^{177}Lu-ACPP into ^{177}Lu-CPP. The biodistribution data obtained with ACPP do however not allow discrimination between retention of uncleaved ACPP and the MMP cleavage product CPP. In principle, the differences found in the tissue accumulation of ACPP and non-ACPP could originate from a-specific accumulation instead of tumoral MMP-related activation. In order to address this open question and to unravel the activation process of ACPP (i.e. does ACPP activation takes place and, if so, where), we developed dual-isotope radiolabeled analogs (dACPPs) (Fig. 2.1B), in which the polycationic cell penetrating peptide and the polyanionic peptide were labeled with the orthogonal radio isotopes ^{177}Lu (E_γ = 208 keV) and ^{125}I (E_γ = 35 keV), respectively (Fig. 2.14). A large ratio of ^{177}Lu over ^{125}I would indicate cleavage of the probe and subsequent retention of the ^{177}Lu-radiolabeled CPP. The *in vivo* biodistribution of the dual isotope probe ^{177}Lu/^{125}I-dACPP 24h post i.v.-injection showed a ~10- to 50-fold higher retention of ^{177}Lu in tumor, muscle, heart, lung, and spleen compared to ^{125}I (Fig. 2.15A, Table 2.5), while for ^{177}Lu/^{125}I-non-dACPP the tissue retention of ^{177}Lu was only slightly higher, i.e. ~2- to 3-fold, than for ^{125}I (Fig. 2.15B). Furthermore, the biodistribution of ^{177}Lu/^{125}I-dACPP showed a high accumulation of ^{177}Lu in the liver, while ^{125}I retention was minimal. No significant higher ^{177}Lu-to-^{125}I ratio was observed in tumor compared to muscle, heart, lung, and spleen at both 3h and 24h post-injection (Tables 2.4 and 2.5).

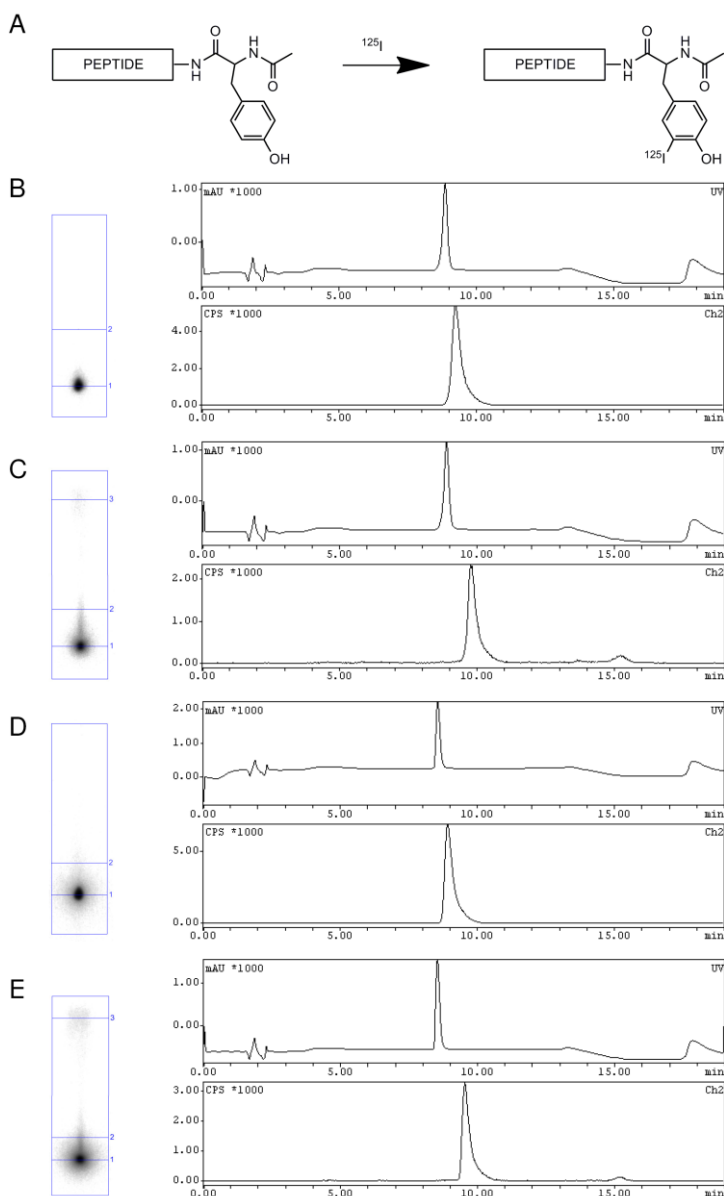**Figure 2.14:** *(A) ^{125}I labeling of tyrosine containing peptides. (B-E) iTLC (left) and γ-HPLC spectra (right) of the radio labeled peptides (B) ^{177}Lu-dACPP (>98% rp), (C) ^{125}I-dACPP (>96% rp), (D) ^{177}Lu-non-dACPP (>98% rp), and (E) ^{125}I-non-dACPP (>96% rp). ^{125}I labeling of peptides lacking the tyrosine residue (i.e. ACPP and non-ACPP) resulted in <5% rp (data not shown).*

Table 2.4: *Biodistribution results of 60 nmol ^{177}Lu/^{125}I-dACPP and ^{177}Lu/^{125}I-non-dACPP in HT-1080 tumor-bearing mice 3h post-injection (n=3). The data are presented as mean ± SD.*

HT-1080 3h	^{177}Lu/^{125}I-dACPP			^{177}Lu/^{125}I-non-dACPP		
	^{177}Lu (%ID/g)	^{125}I (%ID/g)	Ratio ^{177}Lu/^{125}I	^{177}Lu (%ID/g)	^{125}I (%ID/g)	Ratio ^{177}Lu/^{125}I
Blood	0.64 ± 0.23	0.52 ± 0.10	1.3 ± 0.8	0.01 ± 0.00	0.34 ± 0.42	ND
HT-1080 tumor	3.36 ± 0.18	0.65 ± 0.28	6.0 ± 2.8	0.32 ± 0.11	0.44 ± 0.36	0.9 ± 0.3
Muscle	0.59 ± 0.09	0.16 ± 0.08	4.2 ± 1.8	0.04 ± 0.00	0.12 ± 0.11	0.5 ± 0.3
Heart	0.69 ± 0.11	0.21 ± 0.04	3.3 ± 1.2	0.03 ± 0.00	0.19 ± 0.23	0.4 ± 0.3
Lung	1.90 ± 0.26	0.41 ± 0.08	4.8 ± 1.5	0.36 ± 0.09	0.38 ± 0.39	1.5 ± 0.8
Spleen	3.18 ± 0.36	0.38 ± 0.05	8.4 ± 0.8	0.28 ± 0.05	0.29 ± 0.14	1.1 ± 0.5
Liver	12.5 ± 0.31	0.51 ± 0.01	24.3 ± 0.8	1.85 ± 0.12	0.81 ± 0.02	2.3 ± 0.2
Kidney	59.9 ± 16.7	24.4 ± 6.17	2.5 ± 0.2	95.1 ± 9.18	70.3 ± 22.6	1.4 ± 0.4
Fat	0.29 ± 0.04	0.09 ± 0.02	3.5 ± 1.4	0.03 ± 0.00	0.10 ± 0.10	0.4 ± 0.3
Thigh bone	3.12 ± 0.19	0.94 ± 0.19	3.4 ± 0.5	0.61 ± 0.14	0.55 ± 0.11	1.1 ± 0.1
Brain	0.04 ± 0.01	0.03 ± 0.00	1.2 ± 0.5	ND	ND	ND

Table 2.5: *Biodistribution results of 60 nmol ^{177}Lu/^{125}I-dACPP and ^{177}Lu/^{125}I-non-dACPP in HT-1080 tumor-bearing mice 24h post-injection (n=6). The data are presented as mean ± SD.*

HT-1080 24h	^{177}Lu/^{125}I-dACPP			^{177}Lu/^{125}I-non-dACPP		
	^{177}Lu (%ID/g)	^{125}I (%ID/g)	Ratio ^{177}Lu/^{125}I	^{177}Lu (%ID/g)	^{125}I (%ID/g)	Ratio ^{177}Lu/^{125}I
Blood	0.01 ± 0.02	0.01 ± 0.00	ND	0.01 ± 0.00	0.01 ± 0.01	ND
HT-1080 tumor	1.65 ± 0.66	0.13 ± 0.03	13.4 ± 6.2	0.52 ± 0.25	0.18 ± 0.06	2.9 ± 1.9
Muscle	0.47 ± 0.18	0.02 ± 0.01	22.1 ± 3.8	0.05 ± 0.02	0.03 ± 0.01	1.4 ± 0.3
Heart	0.23 ± 0.07	0.02 ± 0.00	10.6 ± 4.4	0.04 ± 0.00	0.03 ± 0.00	1.3 ± 0.1
Lung	0.61 ± 0.25	0.05 ± 0.01	11.4 ± 3.3	0.21 ± 0.04	0.06 ± 0.01	3.6 ± 0.1
Spleen	3.23 ± 1.63	0.07 ± 0.02	46.2 ± 18.2	0.54 ± 0.09	0.14 ± 0.01	3.8 ± 0.7
Liver	18.4 ± 3.67	0.25 ± 0.05	77.5 ± 25.8	3.50 ± 0.60	0.68 ± 0.11	5.2 ± 0.8
Kidney	47.5 ± 7.70	17.0 ± 2.97	2.8 ± 0.4	84.0 ± 14.3	50.5 ± 8.84	1.7 ± 0.0
Fat	0.26 ± 0.15	0.02 ± 0.01	ND	0.08 ± 0.09	0.06 ± 0.07	ND
Bladder	0.46 ± 0.24	0.29 ± 0.25	ND	0.11 ± 0.03	0.16 ± 0.02	ND
Thigh bone	2.57 ± 0.38	0.55 ± 0.11	4.8 ± 1.3	0.87 ± 0.19	0.58 ± 0.09	1.5 ± 0.2
Brain	0.01 ± 0.00	0.00 ± 0.00	ND	0.00 ± 0.00	0.00 ± 0.00	ND
Stomach, full*	0.12 ± 0.03	0.06 ± 0.02	ND	0.03 ± 0.02	0.04 ± 0.02	ND
Intestine, full*	0.63 ± 0.24	0.11 ± 0.01	ND	0.13 ± 0.06	0.11 ± 0.06	ND
Thyroid*	0.12 ± 0.03	1.51 ± 0.45	ND	0.00 ± 0.00	0.78 ± 0.35	ND

* expressed in %ID

An *in vivo* biodistribution study of ^{177}Lu/^{125}I-dACPP in tumor-free healthy mice and BT-20 tumor-bearing mice was also carried out, which showed the same 10- to 50-fold higher retention levels of ^{177}Lu relative to ^{125}I in various tissues as was observed in HT-1080 tumor-bearing mice (Fig. 2.15, Tables 2.6 and 2.7). No significant difference was found for ^{177}Lu/^{125}I ratios between BT-20 tumors and HT-1080 tumors at both 3h and 24h post injection (p>0.05). Furthermore, ^{177}Lu-dACPP uptake was in a comparable range for both tumor types at 3h and 24h. Gelatin zymography analysis of tissue homogenates, however, showed significant lower gelatinase expression of BT-20 tumors compared to HT-1080 tumors (Fig. 2.16, p<0.05), suggesting that the dACPP activation is not caused by tumor-associated MMP-2/9.

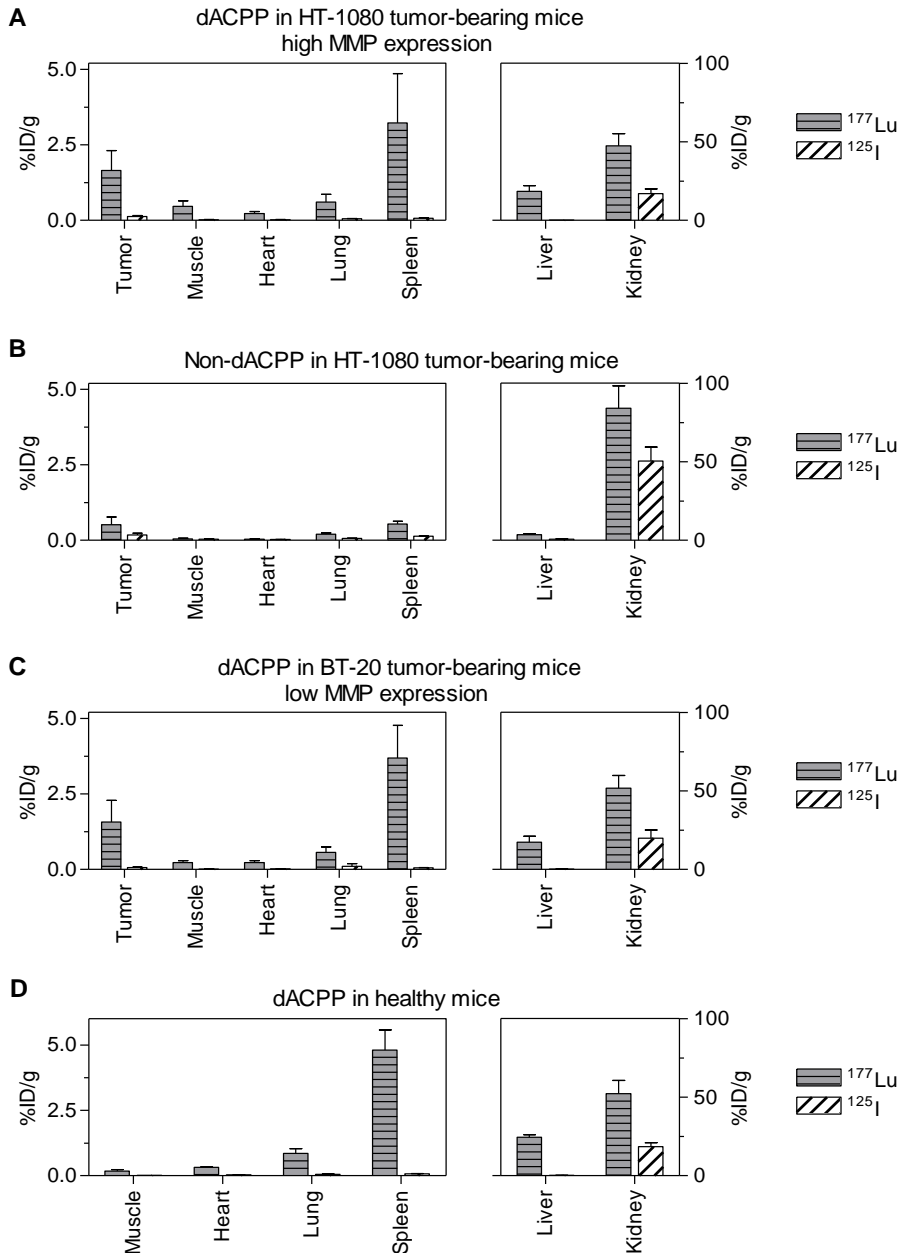**Figure 2.15:** *(A) Comparison of the in vivo biodistribution of (A) ^{177}Lu/^{125}I-dACPP (60 nmol, n=6), and (B) ^{177}Lu/^{125}I-non-dACPP (60 nmol, n=6) in HT-1080 tumor-bearing mice, and ^{177}Lu/^{125}I-dACPP (60 nmol, n=4) (C) in BT-20 tumor bearing-mice and (D) in tumor-free healthy mice 24h post-injection. The data are presented as mean ± SD.*

Table 2.6: *Biodistribution results of 60 nmol ^{177}Lu/^{125}I-dACPP in BT-20 tumor-bearing mice at 3h (n=3) and 24h (n=4) post-injection. The data are presented as mean ± SD.*

BT-20 3h & 24h	^{177}Lu/^{125}I-dACPP, 3h			^{177}Lu/^{125}I-dACPP, 24h		
	^{177}Lu (%ID/g)	^{125}I (%ID/g)	Ratio ^{177}Lu/^{125}I	^{177}Lu (%ID/g)	^{125}I (%ID/g)	Ratio ^{177}Lu/^{125}I
Blood	0.48 ± 0.22	0.16 ± 0.08	3.2 ± 1.4	0.00 ± 0.00	0.01 ± 0.00	ND
BT-20 tumor	5.26 ± 2.59	0.25 ± 0.20	25.5 ± 14.1	1.57 ± 0.72	0.06 ± 0.02	27.2 ± 5.6
Muscle	0.41 ± 0.14	0.04 ± 0.02	12.5 ± 3.4	0.24 ± 0.06	0.01 ± 0.01	18.3 ± 8.0
Heart	0.56 ± 0.11	0.07 ± 0.03	8.6 ± 3.5	0.23 ± 0.06	0.02 ± 0.00	13.2 ± 4.5
Lung	1.93 ± 0.38	0.28 ± 0.07	6.9 ± 0.9	0.57 ± 0.18	0.10 ± 0.09	8.8 ± 5.5
Spleen	3.68 ± 0.48	0.18 ± 0.08	22.1 ± 6.2	3.69 ± 1.08	0.05 ± 0.01	69.8 ± 22.1
Liver	9.71 ± 1.39	0.32 ± 0.07	30.6 ± 4.2	17.4 ± 3.77	0.19 ± 0.10	116 ± 59.4
Kidney	62.4 ± 7.82	30.9 ± 4.19	2.0 ± 0.2	51.8 ± 8.14	19.8 ± 5.40	2.7 ± 0.5
Fat	0.26 ± 0.10	0.05 ± 0.02	5.7 ± 0.3	0.18 ± 0.07	0.02 ± 0.01	12.4 ± 2.1
Thigh bone	2.75 ± 0.54	0.56 ± 0.16	5.1 ± 1.1	2.03 ± 0.46	0.26 ± 0.20	11.8 ± 7.3
Brain	0.03 ± 0.01	0.02 ± 0.01	ND	0.01 ± 0.00	0.00 ± 0.00	ND

Table 2.7: *Biodistribution results of 60 nmol ^{177}Lu/^{125}I-dACPP in tumor-free mice (n=4) at 24h post-injection. The data are presented as mean ± SD.*

Tumor-free 24h	^{177}Lu/^{125}I-dACPP		
	^{177}Lu (%ID/g)	^{125}I (%ID/g)	Ratio ^{177}Lu/^{125}I
Blood	0.02 ± 0.01	0.01 ± 0.00	ND
Muscle	0.18 ± 0.06	0.01 ± 0.00	12.9 ± 2.9
Heart	0.32 ± 0.04	0.03 ± 0.00	11.8 ± 1.5
Lung	0.86 ± 0.18	0.05 ± 0.01	16.6 ± 0.8
Spleen	4.81 ± 0.77	0.08 ± 0.01	58.3 ± 12.2
Liver	24.6 ± 1.51	0.19 ± 0.04	130.7 ± 15.2
Kidney	52.1 ± 8.61	18.5 ± 2.46	2.8 ± 0.2
Fat	0.31 ± 0.11	0.02 ± 0.01	ND
Thigh bone	2.75 ± 0.17	0.61 ± 0.13	4.6 ± 0.8
Brain	0.01 ± 0.00	0.00 ± 0.00	ND
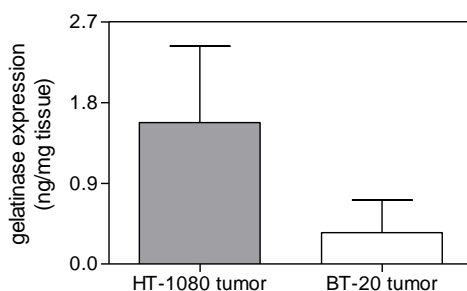
Figure 2.16: *Gelatinase expression levels of HT-1080 tumors (n=3) and BT-20 tumors (n=5). The data are presented as mean ± SD.*

In vivo biodistribution of radiolabeled CPP

The *in vivo* biodistribution of ^{177}Lu-CPP (Fig. 2.10; Table 2.8), the activated cell penetrating peptide domain of ACPP serving as positive control, revealed significantly higher tumor retention levels compared to muscle and heart in both HT-1080 and BT-20 tumors (p<0.05). Comparison of the tumor-to-tissue ratios for ^{177}Lu-ACPP and ^{177}Lu-CPP showed no significant differences for both tumor types at both 3h and 24h post-injection (p >0.05, Fig. 2.17 and Table 2.9), indicating that ACPP was most likely activated in the vascular compartment.
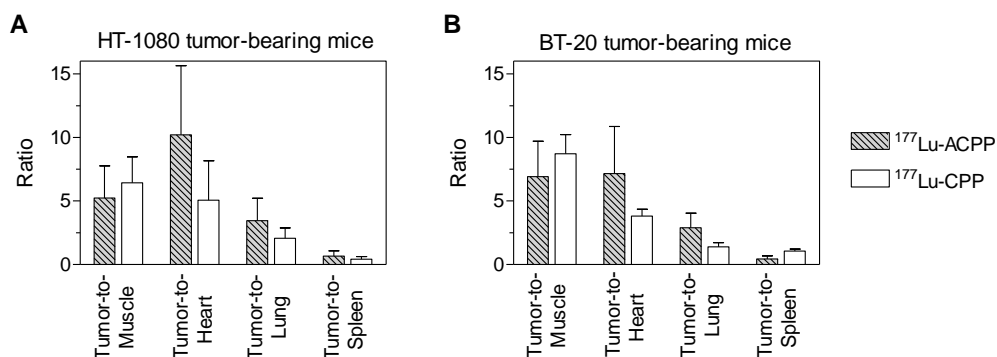
Figure 2.17: *Tumor-to-tissue ratios for 60 nmol ^{177}Lu-ACPP and 60 nmol ^{177}Lu-CPP in (A) HT-1080 and (B) BT-20 tumor-bearing mice at 24h post injection. The data are presented as mean ± SD.*

Table 2.8: *Biodistribution results of 60 nmol ^{177}Lu-ACPP at 3h, and 24h post-injection in HT-1080 and BT-20 tumor-bearing mice. The data are mean %ID/g ± SD.*

HT-1080	^{177}Lu-CPP		BT-20	^{177}Lu-CPP	
	3h, n=4	24h, n=6		3h, n=3	24h, n=3
Blood	0.75 ± 0.13	0.03 ± 0.01	Blood	0.91 ± 0.12	0.00 ± 0.00
HT-1080 tumor	3.98 ± 0.61	3.37 ± 1.26	BT-20 tumor	6.57 ± 1.54	1.78 ± 0.43
Muscle	0.84 ± 0.08	0.53 ± 0.10	Muscle	0.76 ± 0.05	0.21 ± 0.07
Heart	1.71 ± 0.18	0.74 ± 0.18	Heart	1.83 ± 0.35	0.55 ± 0.06
Lung	5.41 ± 0.56	1.63 ± 0.08	Lung	5.10 ± 1.26	1.15 ± 0.15
Spleen	6.53 ± 0.21	8.07 ± 1.03	Spleen	6.50 ± 0.55	5.93 ± 0.67
Liver	24.9 ± 2.08	41.6 ± 4.21	Liver	24.3 ± 0.63	31.3 ± 1.62
Kidney	41.6 ± 6.71	39.0 ± 6.39	Kidney	41.2 ± 5.28	26.5 ± 6.56
Fat	0.61 ± 0.15	0.51 ± 0.20	Fat	0.88 ± 0.51	0.91 ± 1.05
Thigh bone	4.37 ± 0.42	3.81 ± 0.33	Thigh bone	4.52 ± 0.63	2.22 ± 0.18
Brain	0.06 ± 0.00	0.03 ± 0.00	Brain	0.19 ± 0.23	0.02 ± 0.00

Table 2.9: *Tumor-to-muscle ratios for ^{177}Lu-ACPP and ^{177}Lu-CPP 3h, and 24h post-injection in HT-1080 and BT-20 tumor-bearing mice. The data are presented as mean ± SD.*

Ratio	^{177}Lu-ACPP 3h	^{177}Lu-ACPP 24h	^{177}Lu-CPP 3h	^{177}Lu-CPP 24h
HT-1080 tumor/muscle	4.1 ± 2.0	5.2 ± 2.5	4.8 ± 0.8	6.4 ± 2.1
BT-20 tumor/muscle	13.7 ± 7.3	6.9 ± 2.8	8.7 ± 1.5	9.5 ± 4.6

Blood kinetic profiles

^{177}Lu/^{125}I-dACPP showed a faster blood clearance of ^{177}Lu compared to ^{125}I in HT-1080 tumor-bearing mice, pointing to dACPP activation and subsequent tissue trapping of ^{177}Lu-CPP, while comparable blood clearance rates were observed for ^{177}Lu and ^{125}I for HT-1080 tumor-bearing mice injected with ^{177}Lu/^{125}I-non-ACPP (Fig. 2.18). We observed a 30- and 10-fold higher blood concentration for ^{177}Lu-CPP and ^{177}Lu-ACPP respectively, compared to ^{177}Lu-non-ACPP 3h post-injection, indicating the presence of activated CPP in blood for ^{177}Lu-ACPP at this time-point (Fig. 2.18). After 6h, both ACPP and non-ACPP were essentially cleared from circulation (Table 2.1). Blood half-lives for ^{177}Lu were calculated to be ~19 min for the negative control probes, ~25 min for the ACPP probes, and 84 min for CPP. The partial activation of the ACPP probes in the vasculature has most likely resulted in the presence of the CPP and intact ACPP in the blood. Therefore, both intact ACPP (*i.e.* non-ACPP) and activated ACPP (*i.e.* CPP) will have contributed to the half-life of the ACPP probe, explaining why the observed half-life for the ACPP probes is in between the half-lives of the non-ACPP probes and CPP.

Determination of volume-of-distribution

The volume-of-distribution (V_D) calculated from the blood clearance measurements for ^{177}Lu is in the range of $0.27 < V_D < 0.36$ L/kg bodyweight (V_D values in L/kg are for ACPP: 0.36 ± 0.19; non-ACPP: 0.32 ± 0.05; dACPP: 0.27 ± 0.17; and non-dACPP: 0.29 ± 0.08). This points toward a rapid distribution of these probes throughout the extracellular fluids in the whole-body without cell membrane crossing but with some binding to compounds and cell surfaces in the extracellular, extravascular space (22). The volume of distribution for ^{177}Lu-CPP was found to be 4-fold higher (V_D = 1.28 ± 0.21 L/kg), suggesting that a significant amount of the highly positively charged polypeptide directly binds to cells in the extravascular, extracellular space and endothelial cells in the vascular space. In this respect, CPP will probably have a high tendency to bind to circulating cells as well, which would explain the relatively high blood levels of CPP observed at later time points (Fig. 2.18D). Furthermore, CPPs consisting of oligoarginine sequences display affinity for serum proteins, which may increase the circulation time (23). Alternatively, a slow desorption of the polycationic peptide and subsequent transport back into the circulation is a reasonable explanation for the observed prolonged blood clearance profile (15).
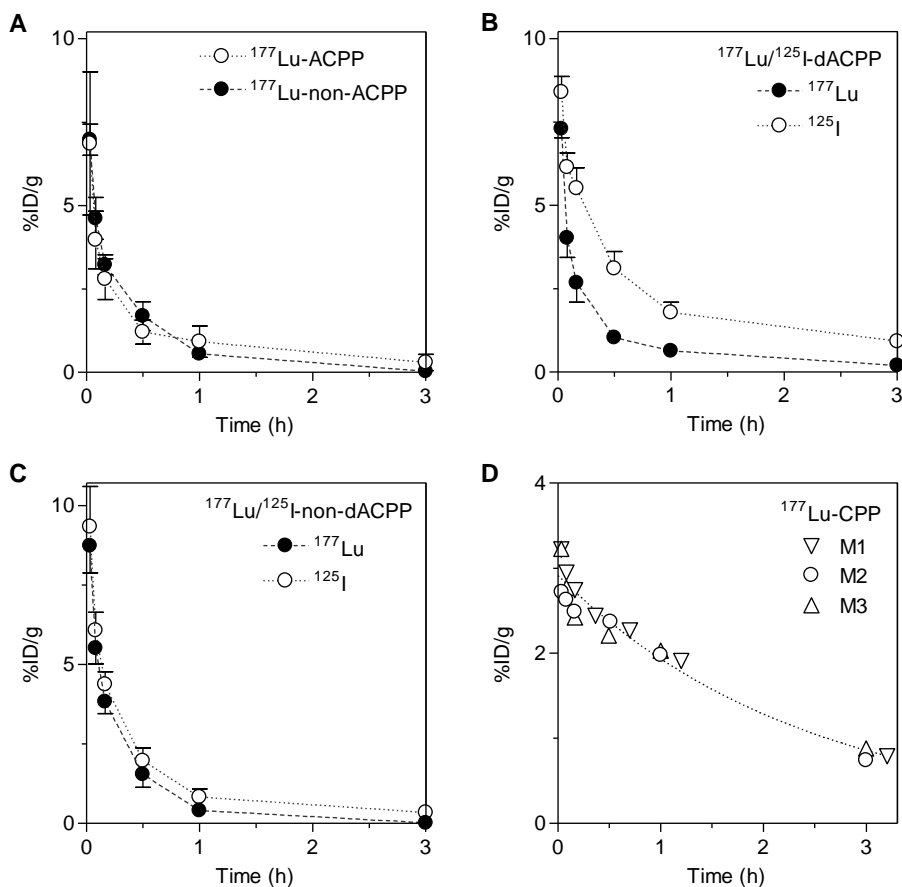
Figure 2.18: *Blood kinetic profiles of 60 nmol (A) ^{177}Lu-ACPP (open circle) and ^{177}Lu-non-ACPP (filled circle), (B) ^{177}Lu/^{125}I-dACPP, (C) ^{177}Lu/^{125}I-non-dACPP, and (D) ^{177}Lu-CPP in HT-1080 tumor-bearing mice (n=3). The data are presented as mean ± SD.*

Discussion

The use of activatable cell penetrating imaging probes has been advocated as a promising general strategy for the *in vivo* imaging of proteolytic activity, in particular in tumors (14, 24). Several recent reports have asserted that tumors can be visualized via optical and magnetic resonance imaging of MMP-2/9 activity using ACPPs (14-18). An analogous radiolabeled ACPP probe for Positron Emission Tomography or Single Photon Emission Computed Tomography would allow clinical translation to sensitive whole-body diagnostic imaging, while avoiding potential toxicity risks associated with Gd-uptake and retention in cells and organs. Therefore, we set our sights on the development of radiolabeled ACPPs consisting of an MMP-2/9 sensitive peptide linker. In accordance with the results for a Cy-5 conjugated MMP-2/9 cleavable ACPP (14,15), we showed that the radiolabeled ACPPs can

efficiently be activated by MMP-2/9 *in vitro* (Figs. 2.5 and 2.9), followed by cellular uptake in endosomes (Fig. 2.10). For the application of ACPPs in molecular imaging, the observed entrapment of the activated probe in the cytoplasmic vesicles is acceptable. However, the potential application of ACPPs as vehicles for intracellular drug delivery is hampered if the activated domain is not efficiently transported to the nucleus or released into the cytoplasm. The *in vivo* biodistribution of a ^{177}Lu radiolabeled ACPP and a negative control non-ACPP containing a scrambled linker was assessed in mice bearing HT-1080 tumors with high MMP-2/9 expresion (Fig. 2.12; Tables 2.1-2.3). We found for the ACPP a high uptake in the tumor compared to muscle or heart, however an even higher uptake in spleen, liver, and kidney. For the tumor, ACPP exhibited a 6-fold higher retention than for non-ACPP, which is slightly more than reported by Tsien and co-workers for their optical probes (14-16). At a first glance this seems to support ACPP sensitivity towards tumoral MMP-2/9, but surprisingly, retention ratios of ACPP over non-ACPP were in many tissues higher compared to HT-1080 tumors. For example, the ACPP retention in muscle is 12-fold higher compared to non-ACPP despite the fact that MMP-2/9 activity in muscle was not detected by gelatin zymography (Fig. 2.13). Dual-isotope-labeled ACPPs, in which the polycationic CPP was labeled with ^{177}Lu and the polyanionic domain was labeled with ^{125}I, revealed similar ^{177}Lu-to-^{125}I tissue ratios in tumor, muscle, heart, lung, and spleen after 3h and 24h post-injection, which indicated that ACPP got activated and subsequently retained in all tissues as ^{177}Lu-CPP (Fig. 2.15; and Tables 2.4 and 2.5). Similar ^{177}Lu-to-^{125}I ratios were observed in muscle, heart, lung, and spleen when dACPP was administrated to healthy mice or mice bearing BT-20 tumors, characterized by low MMP-2/9 expression (Tables 2.6 and 2.7). The negative control on the other hand showed very modest ^{177}Lu-to-^{125}I tissue ratios of 2 to 3 at 24h post-injection, which may have been caused by activation by a-specific proteolytic degradation of the linker around one of the flexible glycine residues. The iodinated probes were not subject to significant dehalogenation as evidenced by the low amount of ^{125}I measured in thyroids and the stomach (Table 2.5). At 3h post injection, absolute ^{177}Lu-to-^{125}I ratios were lower in all tissues compared to 24h post injection, which is most likely caused by contribution of background signal from the blood in these tissues due to the uncomplete clearance of the ^{177}Lu/^{125}I labeled probe from the circulation at this time point.

The biodistribution and blood clearance experiments for the various probes compellingly show that the employed ACPP is taken up and retained in all tissues in its activated form, even in the absence of an MMP expressing tumor (Fig. 2.15C). These findings do not support tumor-associated MMP-2/9 cleavage of ACPP as the main mechanism for ACPP activation and subsequent tumor accumulation. Instead, the higher retention of the activated ACPP in both MMP-positive HT-1080 and MMP-reduced BT-20 tumors compared to muscle is most likely due to tissue a-specific ACPP activation, resulting in increased accumulation of the activated probe in the tumors promoted by the enhanced permeability and retention (EPR) effect in combination with high vascularisation (26). Further evidence for this assertion comes from the similar biodistribution profiles observed for ^{177}Lu-ACPP and the positive control ^{177}Lu-CPP (Fig. 2.17). Passive uptake due to tumor-leakiness will likely occur for any probe with a high free volume-of-distribution, including our negative control peptide non-ACPP, explaining the

significantly higher tumor uptake of non-ACPP compared to muscle and the smaller relative difference in uptake between ACPP and non-ACPP in tumor compared to muscle.

Interestingly, it was recently demonstrated that tumor retention of nanoparticles by the EPR effect can be further increased by MMP-2/9-sensitive ACPP functionalization of the nanoparticles (17). The latter study also showed that significantly higher muscle uptake was obtained for MMP-2-sensitive ACPP-labeled nanoparticles compared to non-ACPP-labeled nanoparticles, which is consistent with an activation of the nanoparticles in the vascular system and subsequent tissue a-specific uptake. The tumor-to-muscle ratio for this MMP activatable nanoparticle was ~6, slightly higher than observed for the low molecular weight MMP activatable peptides (16,17), indicating that the EPR effect may play out favourably for larger-sized activatable probes.

Attempts have been undertaken to analyze the stability of ACPP in mouse serum, but for various reasons these experiments proved not to be valuable. For example, the high tendency of the (radiolabeled) ACPP probes, in particular of CPP, to bind to serum proteins complicated HPLC analysis enormously (23,26) (data not shown). On the other hand, Size Exclusion Chromatography (SEC) was not helpful, because of the almost similar elution times of radiolabeled CPP and ACPP (data not shown). As last alternative, we incubated the FRET-ACPP analog with mouse serum and measured changes in Cy-5 fluorescence in real time. An increase in Cy-5 fluorescence was observed for FRET-ACPP (Fig. 2.19). In the presence of GM6001, a broad spectrum MMP inhibitor, the activation of FRET-ACPP in serum was diminished marginally, suggesting a minor role of MMP-mediated activation. However, also FRET-non-ACPP showed a strong change in Cy-5 fluorescence in mouse serum overtime (Fig. 2.19), while *in vivo* activation of the radiolabeled non-ACPP analog was basically not observed. Therefore, these *in vitro* studies could not be used as a reliable model for the *in vivo* experiments.
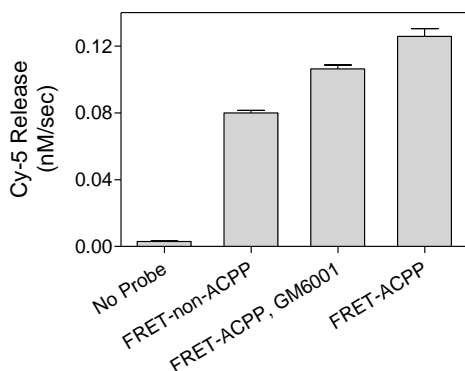

Figure 2.19: *Cy-5 release (nM/s) for serum samples containing no probe, FRET-non-ACPP, FRET-ACPP + GM6001 MMP-inhibitor, and FRET-ACPP respectively. The data are presented as mean ± SD.*

Conclusion

In summary, we have reported the first *in vivo* studies exploring the use of radiolabeled activatable cell penetrating peptides for the detection of MMP activity in tumors. Activation of the radiolabeled ACPP indeed resulted in a strong enhancement of tumor retention *in vivo*, showing that the concept of activatable cell penetrating peptides can be translated to nuclear applications. However, dual isotope-labeled ACPPs and control experiments in healthy and tumor-bearing mice revealed that the activation of ACPP was tumor independent. Most likely, probe activation occurred already in the vasculature followed by non-specific tumor uptake. Therefore, several challenges need to be addressed to achieve clinical translation of ACPPs. Firstly, the protease-sensitive linker should be carefully chosen to prevent a-specific cleavage. Secondly, highly specific accumulation in the tissue of interest may be achieved by ACPPs that are exclusively sensitive to cell membrane bound enzymes, *e.g.* MMP-14, that do not shed into the vasculature, thereby avoiding ACPP activation in blood. In Chapter 5 the development and characterization of such MMP-14 specific ACPPs is described.

Acknowledgements

Materials and methods

Materials

All reagents and solvents were obtained from commercial sources (Sigma-Aldrich, and Biosolve) and used without further purification. 9-fluorenylmethyloxycarbonyl (Fmoc)-protected amino acids and Rink amide resin were purchased from either Novabiochem (Merck) or Bachem. DOTA succinimidyl ester, QSY21 succinimidyl ester, and Cy-5 succinimidyl ester were obtained from Macrocyclics, Invitrogen, and GE Healthcare, respectively. Human recombinant enzymes were purchased from Calbiochem (Merck), Sigma, or R&D Systems. The enzymes were activated according to vendor's protocols if needed. The labeling buffers were treated with Chelex-100 resin (BioRad Laboratories) overnight and filtered through 0.22 µm. Iodogen iodination tubes were purchased from Pierce Protein Research (Thermo Fischer Scientific). Tablets to prepare phosphate buffered saline (PBS) pH 7.4 were acquired from Calbiochem (Merck).

Animal studies

All animal procedures were approved by the ethical review committee of the Maastricht University Hospital (The Netherlands), and were performed according to the principles of laboratory animal care (NIH publication 85-23, revised 1985), and the Dutch national law "Wet op Dierproeven" (Stb 1985, 336). Six-week old athymic female mice (CD-1 nu/nu, body weight 22-30g, Charles River Labs) were housed in an enriched environment under standard conditions: 23-25 °C, 50-60% humidity, and 12h-lightdark-cycles for >1 week. Food and water were freely available.

Probe synthesis

Peptides Ac-e_9-x-PLGLAG-r_9-x-k(Mtt)-resin, Ac-e_9-x-LALGPG-r_9-x-k(Mtt)-resin, Ac-y-e_9-x-PLGLAG-r_9-x-k(Mtt)-resin, Ac-y-e_9-x-LALGPG-r_9-x-k(Mtt)-resin, Ac-LAG-r_9-x-k(Mtt)-resin, QSY21-e_9-x-PLGLAG-r_9-x-k-resin, and QSY21-e_9-x-LALGPG-r_9-x-k-resin were synthesized on an automatic synthesizer (Prelude, Protein Technologies Inc.) by Fmoc solid-phase peptide synthesis (SPPS) using Rink amide resin (0.1 mmol), HBTU as the activating reagent, and N,N-Diisopropylethylamine (DIPEA) as base. D-amino acids are denoted in lower case and x represents 6-aminohexanoic acid. The Mtt protecting group was selectively removed by incubating the peptides on resin with 1.8% v/v trifluoroacetic acid (TFA) in dichloromethane with 2.0% v/v tri-isopropylsilane (TIS) as scavenger for 10 x 3 min after which DOTA succinimidyl ester or fluorescein succinimidyl ester (1.5 equiv) in NMP was added to the peptide resins and was reacted overnight in the presence of DIPEA. The peptides were cleaved from the resin by a mixture of 96.0% v/v trifluoroacetic acid (TFA), 2.0% v/v tri-isopropyl silane (TIS), and 2.0% v/v MilliQ (Millipore) water for 4h, filtered, and precipitated in ice cold diethylether. The peptide pellets were dissolved in MilliQ water and purified by preparative reversed-phase high pressure liquid chromatography (RP-HPLC) using an Agilent 1200 apparatus, equipped with a C18 Zorbax column (length = 150 mm, diameter = 21.2 mm, particle size = 5.0 μm). The elution gradient was set from 5 to 30% of buffer B (0.1% TFA in acetonitrile) over 100 min, where buffer A was 0.1% TFA in MilliQ (Millipore) water. The UV wavelength was preset at 210 and 254 nm. All peptides structures were analyzed by LC-MS on an Agilent 1200 apparatus, equipped with a C18 Eclipse plus-column (length = 100 mm, diameter = 2.1 mm, particle size = 3.5 μm) and an electrospray mass spectrometer (Agilent Technologies 6210, Time-of-Flight LC/MS). Cy-5-succinimidyl ester (2.0 equiv) was conjugated to QSY21-e_9-x-PLGLAG-r_9-x-k-NH_2, and QSY21-e_9-x-LALGPG-r_9-x-k-NH_2 in NMP overnight in the presence of triethylamine (TEA), purified by RP-HPLC and analyzed by LC-MS.

Found masses: 3874.1 Da for Ac-e_9-x-PLGLAG-r_9-x-k(DOTA)-NH_2 (ACPP, Calcd. 3874.1 Da, 11.0 μmol), 3874.1 Da for Ac-e_9-x-LALGPG-r_9-x-k(DOTA)-NH_2 (non-ACPP, Calcd. 3874.1, 11.9 μmol), 4037.2 Da for Ac-y-e_9-x-PLGLAG-r_9-x-k(DOTA)-NH_2 (dACPP, Calcd. 4037.1 Da, 10.4 μmol), 4037.2 Da for Ac-y-e_9-x-LALGPG-r_9-x-k(DOTA)-NH_2 (non-dACPP, Calcd. 4037.1 Da, 7.2 μmol), 2332.5 Da for Ac-LAG-r_9-x-k(DOTA)-NH_2 (CPP, Calcd. 2332.4 Da, 37.8 μmol), 2304.4 Da for Ac-LAG-r_9-x-k(fluorescein)-NH_2 (fluorescein-CPP, Calcd. 2304.3 Da, 34.4 μmol), 4747.3 Da for QSY21-e_9-x-PLGLAG-r_9-x-k(Cy-5)-NH_2 (FRET-ACPP, MW 4747.3 Da, 3.8 μmol), and 4747.3 Da for QSY21-e_9-x-LALGPG-r_9-x-k(Cy-5)-NH_2 (FRET-non-ACPP, MW 4747.3 Da, 5.8 μmol).

Enzyme ACCP cleavage assay

dACPP or non-ACPP (0.1 mM) were incubated in triplicate with 5.0 nM of either human recombinant MMP-1, MMP-2, MMP-3, MMP-7, MMP-9, MMP-14, thrombin, plasmin, or urokinase in a mixture of 50 mM Tris, 200 mM NaCl, 10 mM $CaCl_2$ and 10 µM $ZnCl_2$ at pH 7.5 at 700 rpm and 37 °C. After 1h, the enzymes were quenched by the addition of TFA (10% v/v). To determine the percentage cleaved peptide, the formation of the activated cell penetrating peptide domain was monitored by LC-MS and compared to a 100% cleaved reference sample (0.1 mM dACPP incubated with 30 nM MMP-2 for 1h).

Trypsin digestion

ACPP, non-ACPP, and CPP (0.1 mM) were incubated in a mixture of 50% v/v Dulbecco's PBS and 50% v/v trypsin-EDTA (0.25% w/v) at 37 °C. After 5 min, TFA (10% v/v) was added to quench tryptic activity and samples were analyzed by LC-MS.

In vitro FRET-ACPP activation and enzyme kinetics

In buffer: FRET-ACPP, and FRET-non-ACPP (1.25 µM) were incubated with 1.0 nM MMP-2 in the presence or absence of 50 µM GM6001 (from a 50 mM stock in DMSO) in a mixture of 50 mM Tris, 200 mM NaCl, 10 mM $CaCl_2$ and 10 µM $ZnCl_2$ at pH 7.5 at 37 °C. Changes in Cy5-fluorescence intensity were measured at 665 nm (excitation 649 nm) using a LS55 fluorescence spectrometer (PerkinElmer) for 30 min.

In serum: FRET-ACPP, at 7.64 µM in a buffer of 50 mM Tris, 200 mM NaCl, 10 mM $CaCl_2$ and 10 µM $ZnCl_2$ at pH 7.5, was incubated in triplicate in a 96-well black plate at 50:50% v/v with mouse serum (Innovative Research) containing 1.0 uL GM6001 in DMSO (50 µM final concentration) or blank DMSO. Changes in Cy5-fluorescence intensity were measured at 670 nm (excitation at 612 nm) using a FLUOstar OPTIMA plate reader (BMG LABTECH) at 37 °C. The plate was set to stir 5 seconds prior to measurement and every 20 seconds a measurement was performed for 30 min. As controls, mouse serum was incubated with FRET-non-ACPP, or without peptide probe under similar conditions as for FRET-ACPP. The reaction rate v (µM/s) was calculated using Cy-5-succinimidyl ester (0.01, 0.02, 0.04, 0.08, 0.16, 0.32 µM) as calibration.

Enzyme kinetics: FRET-ACPP, at several concentrations (0.64, 0.91, 1.28, 1.81, 2.56, and 3.62 µM), was incubated in triplicate in a 96-well black plate with 5.0 nM MMP-2 or MMP-9 in a mixture of 50 mM Tris, 200 mM NaCl, 10 mM $CaCl_2$ and 10 µM $ZnCl_2$ at pH 7.5 at 37 °C. Changes in Cy5-fluorescence intensity were measured at 670 nm (excitation at 612 nm) using a plate reader. The plate was set to stir 5 seconds prior to measurement and every 20 seconds a measurement was performed for 30 min. The reaction rate v (µM/s) was determined for every FRET-ACPP concentration, using Cy-5-succinimidyl ester (0.01, 0.02, 0.04, 0.08, 0.16, 0.32 µM) as calibration. The enzyme kinetic data was fitted to the Michaelis-Menten equation: $v = (V_{max} * [S]) / (K_m + [S])$, where V_{max} (µM/s) is the maximum cleavage rate, [S] (µM) is the concentration FRET-ACPP, and K_m (µM) is the FRET-ACPP concentration at which the reaction rate is half of V_{max}. k_{cat} (s^{-1}), the number of substrate molecules cleaved per enzyme molecule per second, was calculated using the equation: $k_{cat} = V_{max} / [E]$, where [E] (µM) is the enzyme concentration. The constant k_{cat}/K_m ($M^{-1}s^{-1}$) was subsequently derived.

Radiolabeling

For in vitro cell assay: ^{177}LuCl$_3$ (PerkinElmer) in 0.05 M HCl (20.0 µL, 10.0 MBq) was mixed with ACPP, non-ACPP, or CPP in MilliQ water (33.4 µL, 25.8 nmol), and 0.2 M Tris-HCl at pH 7.4 (346 µL) for 20 min, at 300 rpm and 90 °C.

For in vivo studies:

^{177}Lu-ACPP and ^{177}Lu-non-ACPP. ^{177}LuCl$_3$ in 0.05 M HCl (5.0 µL, 5.0 MBq) was mixed with ACPP or non-ACPP in MilliQ water (38.8 µL, 300 nmol), and metal-free 0.9% NaCl (450 µL) for 20 min, at 300 rpm and 90 °C.

^{177}Lu/^{125}I-dACPP and ^{177}Lu/^{125}I-non-dACPP. ^{177}LuCl$_3$ in 0.05 M HCl (5.0 µL, 10.0 MBq) was mixed with dACPP or non-dACPP in MilliQ water (38.8 µL, 300 nmol), and metal-free 0.9% NaCl (450 µL) for 20 min, at 300 rpm and 90 °C. ^{125}I (PerkinElmer) in 1 mM NaOH (5.0 µL, 2.5 MBq) was mixed with dACPP or non-dACPP in MilliQ water (38.8 µL, 300 nmol), and PBS (225 µL) in an Iodogen iodination tube for 7 min, at 300 rpm and 25 °C, and transferred to a siliconized 1.5 mL tube together with 250 µL 0.9% NaCl.

^{177}Lu-CPP. ^{177}LuCl$_3$ in 0.05 M HCl (5.0 µL, 5.0 MBq) was mixed with CPP in MilliQ water (31.5 uL, 300 nmol), and metal-free 0.9% NaCl (450 µL) for 20 min, at 300 rpm and 90 °C.

The ^{177}Lu and ^{125}I labeling yields were determined by radio-TLC, using iTLC-SG strips (Pall) eluted with 200 mM EDTA in 0.9% NaCl and 20 mM citric acid at pH 5.2, respectively, imaged on a phosphor imager (FLA-7000, Fujifilm) and quantified with AIDA Image Analyzer software. Analytical radio-HPLC was carried out on an Agilent 1100 system equipped with a C18 Eclipse XBD-column (length = 150 mm, diameter = 4.6 mm, particle size = 5.0 µm) and a Gabi radioactive detector (Raytest). The radiochemical purities were 95% or higher, and typically at least 98%. ^{177}Lu-labeled dACPP was mixed with ^{125}I-labeled dACPP in a 1:1 molar ratio.

Cell culture

HT-1080 fibrosarcoma and BT-20 breast carcinoma cells acquired from the American Type Culture Collection (ATCC) were maintained under standard culture conditions in Eagle's Minimal Essential Medium (MEM) supplemented with 10% heat inactivated fetal bovine serum (Gibco), penicillin (100 U/mL), streptomycin (100 µg/mL), and 2 mM Glutamax (Gibco).

***In vitro* cell incubation with radiolabeled ACPP probes**

^{177}Lu-ACPP was activated prior to cell incubation with recombinant human MMP-2 (10 pmol) for 3h in 50 mM Tris, 200 mM NaCl, 10 mM CaCl$_2$ and 10 µM ZnCl$_2$ at pH 7.5, as was assessed by RP-HPLC. HT-1080 cells were cultured in poly-D-lysine coated 12-well plates. At 80% confluency, cells were washed 2x with Dulbecco's PBS (Gibco) and 1x with serum-free medium and subsequently incubated in triplicate with 1.25 µM ^{177}Lu-non-ACPP, 1.25 µM uncleaved ^{177}Lu-ACPP, 1.25 µM pre-cleaved ^{177}Lu-ACPP, and 1.25 µM ^{177}Lu-CPP (19.3 µL/1.25 nmol probe, 0.5 MBq ^{177}Lu) respectively in serum-free medium (981 uL). After 3h of incubation, cells were washed 5x with Dulbecco's PBS and harvested by trypsination (0.25% w/v trypsin-EDTA (Gibco)). The trypsin activity was inhibited by addition of MEM, after which the cells were isolated by centrifugation (1,000 rpm, 10 min, RT). Cell pellets and all wash fractions were analyzed for ^{177}Lu radioactivity (115-270 keV) by a γ-counter (Wizard 1480, PerkinElmer).

Confocal laser scanning microscopy

Sterile glass coverslips (Menzel-Gläser) were coated in 100 µg/mL poly-D-lysine solution for 15 min at room temperature, dried for 2h, and subsequently seeded with HT-1080 cells in poly-D-lysine coated 24-well plates. Cells were cultured till 80% confluency in MEM, followed by incubation with 1.25 µM fluorescein-CPP. After 4h, the cells were rinsed with fresh MEM, and phospholipid bilayer membranes and cell nuclei were respectively stained with Vybrant DiD cell-labeling solution (Invitrogen) at 5.0 µL/mL MEM and Hoechst 33342 (Invitrogen) at 0.2 µg/mL MEM for 10 min. The staining medium was aspirated; the cells were incubated with MEM for another 10 min, and subsequently washed 3x with phenol-red free MEM. The coverslips were mounted with diamond power shield (Essence) on Menzel-Gläser slides.

Confocal fluorescence images were recorded at room temperature on a Leica TSC SP5 spectral confocal laser scanning microscope using a 100X oil-immersion objective. Hoechst 33342 staining of nuclei was visualized by excitation using a 405 nm Diode. The fluorescence emission of fluorescein was recorded after excitation using a 488 nm Argon laser. DiD was excited using the 633 nm line of a HeNe laser.

HT-1080 fibrosarcoma / BT-20 breast carcinoma model

HT-1080 or BT-20 cells at 80-90% confluency were harvested by trypsination. The trypsin activity was inhibited by addition of MEM, after which cells were isolated by centrifugation. The cells were washed 1x with sterile Dulbecco's PBS and concentrated to 3.0×10^7 HT-1080 cells/mL or 6.0×10^7 BT-20 cells/mL in sterile Dulbecco's PBS. BT-20 cells were diluted once to 3.0×10^7 BT-20 cells/mL by addition of ice-cold matrigel. Approximately 3.0×10^6 HT-1080 or BT-20 cells were injected per mouse, subcutaneously on the left flank. The tumor sizes were determined by a ruler every two days and their volumes were calculated using the formula: ½ x l x b x h. When tumors reached a size of 8-50 mm^3 (typically 1-2 weeks and 3-5 weeks after s.c. injection of HT-1080 and BT-20 cells, respectively), the mice were used for *in vivo* studies.

Biodistribution experiments

Biodistribution experiments were performed on HT-1080 tumor-bearing mice (n=3-4), BT-20 tumor-bearing mice (n=3-4), or tumor-free healthy mice (n=4) by i.v.-injection of ^{177}Lu-ACPP (60 nmol/100 µL, ca. 1.0 MBq), ^{177}Lu-non-ACPP (60 nmol/100 µL, ca. 1.0 MBq), ^{177}Lu/^{125}I-dACPP (60 nmol/100 µL, ca. 1.0 MBq ^{177}Lu, ca. 0.25 MBq ^{125}I), ^{177}Lu/^{125}I-non-dACPP (60 nmol/100 µL, ca. 1.0 MBq ^{177}Lu, ca. 0.25 MBq ^{125}I), or ^{177}Lu-CPP (60 nmol/100 µL, ca. 1.0 MBq). The mice were anesthetized with isoflurane 3h, 6h, or 24h after i.v.-injection, subjected to cardiac puncture, and sacrificed by cervical dislocation. Organs and tissues of interest were harvested and weighed, after which the radioactivity of the samples was measured in a γ-counter along with standards to determine the injected dose per gram (%ID/g). The energy windows were set to 10-80 keV for ^{125}I and 155-380 keV for ^{177}Lu.

Blood kinetic measurements + biodistribution experiments

HT-1080 tumor-bearing mice (n=3) were i.v.-injected with ^{177}Lu-ACPP (60 nmol/100 µL, ca. 1.0 MBq), ^{177}Lu-non-ACPP (60 nmol/100 µL, ca. 1.0 MBq), ^{177}Lu/^{125}I-dACPP (60 nmol/100 µL, ca. 1.0 MBq ^{177}Lu, ca. 0.25 MBq ^{125}I), ^{177}Lu/^{125}I-non-dACPP (60 nmol/100 µL, ca. 1.0 MBq ^{177}Lu, ca. 0.25 MBq ^{125}I), or ^{177}Lu-CPP (60 nmol/100 µL, ca. 1.0 MBq). At selected time points (2, 5, 10, 30 min,

1h, and 3h) blood samples were withdrawn from the vena saphena, weighed and diluted to 1 mL with MilliQ water. The mice were anesthetized with isoflurane 24h after i.v.-injection, subjected to cardiac puncture, and sacrificed by cervical dislocation. Organs and tissues of interest were harvested and weighed, after which the radioactivity was measured of all samples in a γ-counter along with standards to determine the %ID/g. The probe concentration at t=0 (C_0) was calculated by fitting the blood clearance curves to a 2-phase exponential decay function $Y = span_1 \cdot exp(-K_1 \cdot X) + span_2 \cdot exp(-K_2 \cdot X) + Plateau$ for ^{177}Lu-ACPP , ^{177}Lu-non-ACPP, ^{177}Lu-dACPP, ^{177}Lu-non-dACPP was fitted, while ^{177}Lu-CPP was fitted to a 1-phase exponential decay function $Y = span_1 \cdot exp(-K_1 \cdot X) + Plateau$ using GraphPad Prism. The area under the curve (AUC) was determined for the fitted blood kinetic profiles for all probes. The half-lives, the time points at which the AUC reaches 50% of the total AUC, was subsequently derived using MatLab. The volume of distribution per mouse was calculated using the formula $V_D = Dose / (Body\ weight * C_0)$ [L/kg].

Sample preparation for gelatin zymography

Cell assays. Confluent HT-1080 cells were washed with Dulbecco's PBS and incubated in serum-free MEM containing 20 nM phorbol 12-myristate 13-acetate (PMA) for 48h. The medium was centrifuged (1,000 rpm, 5 min) and supernatant was stored at -80 °C until zymography analysis. Typically, 20 μL supernatant was used per analysis.

Tissue homogenates. After γ-counting, tissue samples were homogenized in 20 volumes of 50 mM Tris, 200 mM NaCl, 10 mM $CaCl_2$, and 10 μM $ZnCl_2$ at pH 7.5 at 4 °C at 30 Hz for 5 min using a tissue lyser (Qiagen), mixed for 4h at 4 °C and centrifuged at 10,000 rpm for 5 min. The supernatants were aliquoted and stored at -80 °C until zymography analysis. Typically, 11.2 μL tissue supernatant (from 0.53 mg tissue) was used per analysis.

Blood samples. Fresh mouse blood (50 μL from vena saphena) was centrifuged at 5000 rpm for 5 min. Serum was pipetted off and stored at -80 °C until zymography analysis. Typically, 2.0 μL serum was used per analysis.

Gelatin zymography

Samples were analyzed on 10% SDS-PAGE gel containing 0.1% (w/v) gelatin (Biorad). Active MMP-2 (0.21 ng) was loaded as an internal standard used to normalize activities between gels. After running the gel at 150V, it was washed with MilliQ water, incubated for 3 × 20 min in 2.5% Triton-X (60 rpm) to remove SDS, washed with MilliQ water, and incubated in 50 mM Tris, 200 mM NaCl, 5 mM $CaCl_2$, 0.1% (w/v) NaN_3, and 0.02% (w/v) Brij-35 at pH 7.6 at 37 °C for 2 days. Gels were stained for 2h with 0.25% Coomassie Blue in 60% (v/v) MilliQ water, 30% (v/v) Methanol, 10% (v/v) Acetic acid, and destained for >24h with 67.5% (v/v) MilliQ water, 25% (v/v) Methanol, 7.5% (v/v) Acetic acid. Gelatinatic activity showed up as clear bands against a dark background. Zymograms were imaged (Epson Perfection V700 Photo scanner) and band intensities were quantified using ImageJ.

Statistical methods

Quantitative data were expressed as mean ± SD. Comparisons between the means of the groups were performed by the parametric Welch's t-test (27). Due to the relatively small sample sizes per

group (n=3-6), the non-parametric Mann Whitney U test was also performed. All tests were two-tailed, and P-values of less than 0.05 indicate significant differences. GraphPad Prism was used for all statistical calculations.

References

1. Davidson B, Goldberg I, Kopolovic J, et al. MMP-2 and TIMP-2 expression correlates with poor prognosis in cervical carcinoma - a clinicopathologic study using immunohistochemistry and mRNA in situ hybridization. *Gynecol Oncol.* 1999;73:372-382

2. Kanayama H, Yokota K, Kurokawa Y, et al. Prognostic values of matrix metalloproteinase-2 and tissue inhibitor of metalloproteinase-2 expression in bladder cancer. *Cancer.* 1998;82:1359-1366

3. Sakakibara M, Koizumi S, Saikawa Y, et al. Membrane-type matrix metalloproteinase-1 expression and activation of gelatinase A as prognostic markers in advanced pediatric neuroblastoma. *Cancer.* 1999;85:231-239

4. Jezierska A, and Motyl T. Matrix metalloproteinase-2 involvement in breast cancer progression: a mini-review. *Med Sci Monit.* 2009;15:RA32-40

5. Pieper-Furst U, Kleuser U, Stocklein WF, et al. Detection of subpicomolar concentrations of human matrix metalloproteinase-2 by an optical biosensor. *Anal Biochem.* 2004;332:160-167

6. Ardito CM, Briggs CD, and Crawford HC. Targeting of extracellular proteases required for the progression of pancreatic cancer. *Expert Opin Ther Targets.* 2008;12:605-619

7. Faust A, Waschkau B, Waldeck J, et al. Synthesis and Evaluation of a Novel Hydroxamate Based Fluorescent Photoprobe for Imaging of Matrix Metalloproteinases. *Bioconjug Chem.* 2009;20:904-912

8. Park B-H, Chang Y, Lee Y-J, et al. Targeting of membrane type1-matrix metalloproteinase (MT1-MMP) using superparamagnetic nanoparticles in human liver cancer cells. *Colloids Surface A.* 2008;313-314:647-650

9. Schäfers M, Schober O, and Hermann S. Matrix-metalloproteinases as imaging targets for inflammatory activity in atherosclerotic plaques. *J Nucl Med.* 2010;51:663-666

10. Breyholz HJ, Wagner S, Faust A, et al. Radiofluorinated pyrimidine-2,4,6-triones as molecular probes for noninvasive MMP-targeted imaging. *ChemMedChem.* 2010;5:777-789

11. Wagner S, Breyholz HJ, Holtke C, et al. A new 18F-labelled derivative of the MMP inhibitor CGS 27023A for PET: radiosynthesis and initial small-animal PET studies. *Appl Radiat Isot.* 2009;67:606-610

12. Ohshima S, Petrov A, Fujimoto S, et al. Molecular imaging of matrix metalloproteinase expression in atherosclerotic plaques of mice deficient in apolipoprotein e or low-density-lipoprotein receptor. *J Nucl Med.* 2009;50:612-617

13. Law B, and Tung CH. Proteolysis: a biological process adapted in drug delivery, therapy, and imaging. *Bioconjug Chem.* 2009;20:1683-1695

14. Jiang T, Olson ES, Nguyen QT, et al. Tumor imaging by means of proteolytic activation of cell-penetrating peptides. *Proc Nat Acad Sci USA.* 2004;101:17867-17872

15. Aguilera TA, Olson ES, Timmers MM, et al. Systemic in vivo distribution of activatable cell penetrating peptides is superior to that of cell penetrating peptides. *Integr Biol (Camb).* 2009;1:371-381

16. Olson ES, Aguilera TA, Jiang T, et al. In vivo characterization of activatable cell penetrating peptides for targeting protease activity in cancer. *Integr Biol (Camb).* 2009;1:382-393

17. Olson ES, Jiang T, Aguilera TA, et al. Activatable cell penetrating peptides linked to nanoparticles as dual probes for in vivo fluorescence and MR imaging of proteases. *Proc Nat Acad Sci USA.* 2010;107:4311-4316

18. Nguyen QT, Olson ES, Aguilera TA, et al. Surgery with molecular fluorescence imaging using activatable cell-penetrating peptides decreases residual cancer and improves survival. *Proc Nat Acad Sci USA.* 2010;107:4317-4322

19. Watkins GA, Jones EF, Scott Shell M, et al. Development of an optimized activatable MMP-14 targeted SPECT imaging probe. *Bioorg Med Chem.* 2009;17:653-659

20. Elmquist A, and Langel U. In vitro uptake and stability study of pVEC and its all-D analog. *Biol Chem.* 2003;384:387–393

21. Lee HJ, and Pardridge WM. Pharmacokinetics and delivery of tat and tat-protein conjugates to tissues in vivo. *Bioconjug Chem.* 2001;12:995-999

22. Durbin PW, Jeung N, Kullgren B, et al. Gross composition and plasma and extracellular water volumes of tissues of a reference mouse. *Health Physics.* 1992;63:427-442

23. Kosuge M, Takeuchi T, Nakase I, et al. Cellular internalization and distribution of arginine-rich peptides as a function of extracellular peptide concentration, serum, and plasma membrane associated proteoglycans. *Bioconjug Chem.* 2008;19:656–664

24. Goun EA, Shinde R, Dehnert KW, et al. Intracellular cargo delivery by an octaarginine transporter adapted to target prostate cancer cells through cell surface protease activation. *Bioconjug Chem.* 2006;17:787-796

25. Duncan R. The dawning era of polymer therapeutics. *Nat Rev Drug Discov.* 2003;2:347-360

26. Sarko D, Beijer B, Boy RG, et al. The pharmacokinetics of cell-penetrating peptides. *Mol Pharmaceuticals.* 2010;7:2224-2231

27. Ruxton GD. The unequal variance t-test is an underused alternative to Student's t-test and the Mann-Whitney U test. *Behavioral Ecology.* 2006;17:688-690

Chapter **3**

Detection of cardiac remodeling using a dual-isotope radiolabeled MMP-2/9 activatable cell penetrating imaging probe

Abstract

The role of matrix metalloproteinases (MMPs) in pathological conditions such as adverse left ventricular (LV) remodeling after myocardial infarction (MI) has stimulated the development of imaging probes targeting these proteases. It was demonstrated that non-invasive imaging of the temporal and spatial patterns of MMP-2/9 abundance in myocardial remodeling holds great promise to predict cardiac function post MI. Here, we tested a radiolabeled cell-penetrating imaging probe (dACPP) activatable by matrix metalloproteinase-2 and -9 (MMP-2/9) for the detection of active MMPs, and determined the dACPP biodistribution *in vivo* in a mouse model of myocardial infarction. dACPP showed a significant higher uptake in infarcted than in remote myocardium, and in muscle in mice 10 days post MI. The biodistribution for a dual-isotope dACPP, which allowed us to discriminate between uncleaved dACPP and activated dACPP, showed increased retention of the activated probe in infarcted compared to remote myocardium. This correlated to MMP-2 levels determined by gelatin zymography, while no correlation was found for an MMP-2/9 insensitive negative control non-dACPP. In addition, the infarct-to-remote ratios found for dACPP were significantly higher than those for the positive control, CPP. In conclusion, these data show a significant contribution of infarct associated dACPP activation to infarct targeting of dACPP, most likely due to MMPs.

Introduction

Myocardial infarction (MI) is commonly followed by maladaptive remodeling of the myocardial extracellular matrix (ECM) resulting in congestive heart failure (1). The matrix metalloproteinases (MMPs), a family of extracellular matrix degrading enzymes, are involved in this remodeling process (2,3). In particular, two soluble species of MMPs, the gelatinases MMP-2 and MMP-9, are increased in activity and abundance, and act as crucial modulators in adverse cardiac remodeling (4-7). MMP-9 predominantly plays a role in the early wound healing and inflammation response shortly after MI, while MMP-2 is mainly involved in the cardiac ECM remodeling phases (2). In a recent study, it was illustrated that a non-invasive methodology to image the temporal and spatial levels of MMP-2/9 in myocardial remodeling holds great promise to predict cardiac function post MI in a pig model (8). The MMP level was visualized by Single Photon Emission Computed Tomography (SPECT) using a radiolabeled MMP-inhibitor and this showed correlation to the cardiac function measured by Magnetic Resonance Imaging (MRI). We hypothesized that imaging of the MMP catalytic activity instead of MMP abundance will further improve the monitoring of the myocardial remodeling process. Chen et al. have demonstrated that a quenched near-infrared fluorescent (NIRF) probe can successfully be used to monitor MMP-2/9 activity in MI-mice (9). However, in the human heart NIRF imaging would only be feasible by invasively monitoring the activation of the fluorescent probe by real-time intravascular catheter detection (10). Here, we tested a dual-isotope radiolabeled activatable cell penetrating molecular imaging probe (dACPP, Chapter 2) that is sensitive to the proteolytic activity of MMP-2 and -9 (11) for later application in non-invasive SPECT or Positron Emission Tomography (PET) of myocardial remodelling (Fig. 3.1). In these probes, the polycationic cell-penetrating peptide domain and the polyanionic peptide domain were labeled with the orthogonal radioisotopes ^{177}Lu (energy of the γ-ray emitted by isotope is $E_γ = 208$ keV) and ^{125}I ($E_γ = 35$ keV), respectively. A large ratio of ^{177}Lu over ^{125}I would indicate cleavage of the probe and subsequent retention of the ^{177}Lu-radiolabeled CPP, thereby facilitating a direct read-out of the relative level of MMP activity. We provide data demonstrating a correlation between elevated MMP-2 levels and increased uptake of the activated ACPP in the infarcted areas of the heart in MI-mice, suggesting that the ACPP can be used to detect active MMPs in left ventricular remodelling after MI.
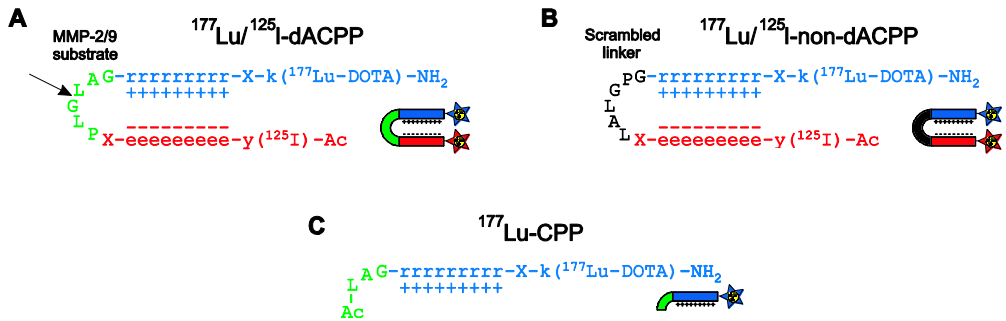
Figure 3.1: *Peptide structure of (A) MMP-2/9 sensitive $^{177}Lu/^{125}I$-dACPP, (B) the negative control $^{177}Lu/^{125}I$-non-dACPP, and (C) the positive control ^{177}Lu-CPP. The MMP-2/9 cleavage site is indicated by the arrow.*

Results

In vivo distribution of dACPP and non-dACPP in MI- and sham-mice at 20h post-injection.

Following successful synthesis and radiolabeling (Chapter 2), $^{177}Lu/^{125}I$-dACPP and $^{177}Lu/^{125}I$-non-dACPP were studied in mice 10 days after induction of a myocardial infarction (MI) or 10 days after sham-surgery. Table 3.1 shows the biodistribution data for $^{177}Lu/^{125}I$-dACPP in MI- and sham-mice. Absolute ^{177}Lu-dACPP uptake was significantly higher in infarct than in remote myocardium, and in muscle in MI-mice and in hearts of sham-mice (Fig. 3.2, $p<0.001$). In addition, autoradiography of ^{177}Lu-dACPP biodistribution in MI-hearts revealed a comparable 6-fold higher probe retention in infarct compared to remote (Fig. 3.3). Furthermore, ^{177}Lu-dACPP showed a significantly higher uptake in infarct compared to the negative control ^{177}Lu-non-dACPP (Tables 3.1 and 3.2, $p<0.001$).

While for sham-mice MMP-2 in the heart was nearly undetectable by gelatin zymography analysis, MMP-2 levels were highly increased in infarcted myocardium and slightly elevated in remote myocardium in MI-mice (Fig. 3.4A). Quantification of gelatin zymograms revealed a significant higher MMP-2 level in infarcted heart tissue compared to remote heart tissue and sham-hearts (Fig. 3.4B, $p<0.001$). Figures 3.3C and 3.3D show respectively the intra-experimental (per mouse) and inter-experimental correlation between MMP-2 level and ^{177}Lu-dACPP uptake in infarcted, border, and remote myocardium ($p<0.005$). Strong linear dependencies were found for the intra-experimental data (Pearson correlation coefficients *r* of 0.84-0.95) and inter-experimental data ($r = 0.78$) (Table 3.3).
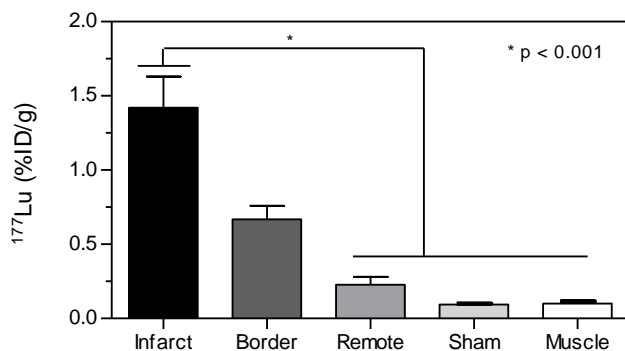
Figure 3.2: *^{177}Lu-biodistribution of 10 nmol ^{177}Lu/^{125}I-dACPP in infarct, border, remote myocardium and muscle of MI-mice (n=5) and in hearts of sham-mice (n=4) at 20h post injection. Data are mean ± SD.*

Table 3.1: *Biodistribution results of 10 nmol ^{177}Lu/^{125}I-dACPP in MI-mice and sham-mice 20h post injection. The data are presented as mean ± SD.*

| 20h - dACPP	MI-mice (n=5)			sham-mice (n=4)		
	^{177}Lu (%ID/g)	^{125}I (%ID/g)	Ratio ^{177}Lu/^{125}I	^{177}Lu (%ID/g)	^{125}I (%ID/g)	Ratio ^{177}Lu/^{125}I
Blood	0.01 ± 0.00	0.01 ± 0.00	1.4 ± 0.4	0.01 ± 0.00	0.01 ± 0.00	1.5 ± 0.8
Heart, infarct	1.43 ± 0.21	0.09 ± 0.06	22.2 ± 13.4	-	-	-
Heart, border	0.67 ± 0.09	0.05 ± 0.02	14.0 ± 4.3	-	-	-
Heart, remote	0.23 ± 0.05	0.04 ± 0.02	6.2 ± 0.8	0.09 ± 0.01	0.02 ± 0.01	5.0 ± 1.5
Muscle	0.10 ± 0.02	0.01 ± 0.00	9.0 ± 1.4	0.11 ± 0.02	0.01 ± 0.00	9.8 ± 2.1
Lung	0.43 ± 0.28	0.06 ± 0.04	7.5 ± 0.9	0.43 ± 0.09	0.06 ± 0.01	7.2 ± 0.7
Spleen	2.50 ± 0.70	0.14 ± 0.07	20.9 ± 9.6	2.84 ± 1.02	0.15 ± 0.03	19.1 ± 3.2
Liver	20.4 ± 4.23	0.40 ± 0.16	55.9 ± 16.5	19.0 ± 2.80	0.48 ± 0.07	40.2 ± 7.6
Kidney	75.0 ± 10.4	34.8 ± 6.63	2.2 ± 0.1	77.8 ± 10.0	39.6 ± 4.34	2.0 ± 0.2
Fat	0.12 ± 0.07	0.04 ± 0.04	4.2 ± 1.9	0.12 ± 0.08	0.02 ± 0.01	6.1 ± 0.7
Thigh bone	1.52 ± 0.39	0.64 ± 0.54	3.5 ± 2.1	1.63 ± 0.30	0.15 ± 0.05	11.4 ± 4.2
Brain	0.01 ± 0.00	0.00 ± 0.00	ND	0.01 ± 0.00	0.00 ± 0.00	ND
Stomach, full*	0.07 ± 0.03	0.05 ± 0.03	ND	0.06 ± 0.01	0.08 ± 0.07	ND
Intestine, full*	0.44 ± 0.18	0.17 ± 0.08	ND	0.45 ± 0.10	0.28 ± 0.31	ND
Thyroid*	0.04 ± 0.05	0.08 ± 0.12	ND	0.03 ± 0.03	0.47 ± 0.55	ND

* expressed in %ID
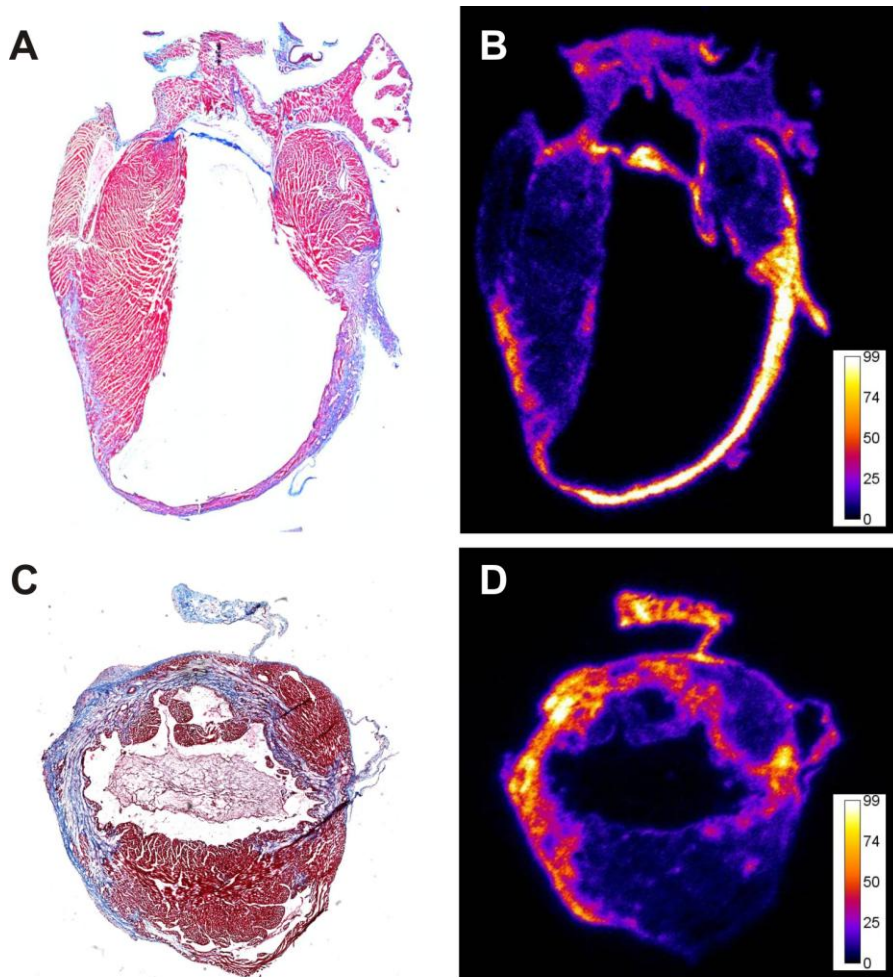
Figure 3.3: *Histology and autoradiography of hearts 20h post-injection of 10 nmol ^{177}Lu-dACPP in mice 10 days post MI. Representative azan staining of (A) a coronal section and (C) a transversal section showing the infarct scar in blue, and remote myocardium in red. (B,D) Autoradiography showing distribution of ^{177}Lu-dACPP in adjacent sections.*

Table 3.2: *Biodistribution results of 10 nmol $^{177}Lu/^{125}I$-non-dACPP and ^{177}Lu-CPP in MI-mice 20h post injection. The data are presented as mean ± SD.*

20h	$^{177}Lu/^{125}I$-non-dACPP (n=5)			^{177}Lu-CPP (n=5)
	^{177}Lu (%ID/g)	^{125}I (%ID/g)	Ratio $^{177}Lu/^{125}I$	^{177}Lu (%ID/g)
Blood	0.01 ± 0.00	0.01 ± 0.00	0.6 ± 0.2	0.01 ± 0.00
Heart, infarct	0.27 ± 0.13	0.20 ± 0.11	1.4 ± 0.1	2.49 ± 0.69
Heart, border	0.15 ± 0.07	0.13 ± 0.08	1.3 ± 0.1	1.59 ± 0.55
Heart, remote	0.08 ± 0.02	0.06 ± 0.02	1.2 ± 0.2	0.66 ± 0.17
Muscle	0.03 ± 0.01	0.02 ± 0.01	1.1 ± 0.1	0.24 ± 0.66
Lung	0.33 ± 0.22	0.16 ± 0.19	2.7 ± 0.8	1.24 ± 0.65
Spleen	0.55 ± 0.05	0.26 ± 0.05	2.2 ± 0.2	5.71 ± 2.88
Liver	3.69 ± 1.02	1.33 ± 0.63	2.9 ± 0.5	38.0 ± 10.0
Kidney	100.6 ± 21.3	69.2 ± 16.8	1.5 ± 0.1	6.22 ± 2.28
Fat	0.05 ± 0.05	0.04 ± 0.03	1.2 ± 0.2	0.33 ± 0.13
Thigh bone	0.70 ± 0.39	1.00 ± 0.81	1.1 ± 0.6	2.16 ± 0.98
Brain	0.00 ± 0.00	0.00 ± 0,00	ND	0.02 ± 0.00
Stomach, full*	0.11 ± 0.12	0.14 ± 0.13	ND	0.19 ± 0.05
Intestine, full*	0.14 ± 0.04	0.20 ± 0.10	ND	1.39 ± 0.49
Thyroid*	0.02 ± 0.02	0.25 ± 0.23	ND	0.08 ± 0.07

* expressed in %ID
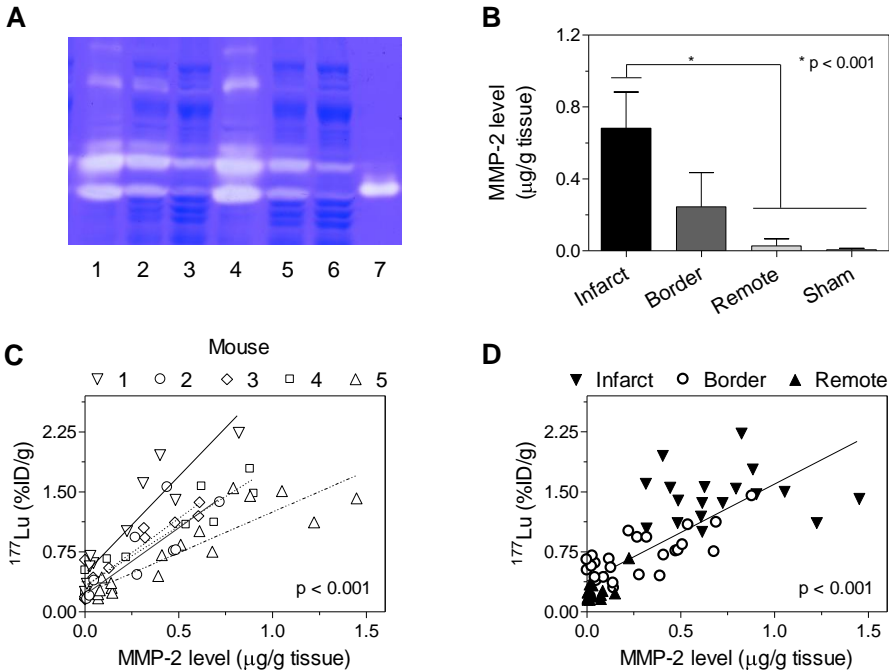
Figure 3.4: *(A) Representative gelatin zymogram of heart homogenates. Lane 1 and 4 = infarcted myocardium, 2 and 5 = border myocardium, 3 and 6 = remote myocardium, and 7 = active MMP-2 (0.21 ng). (B) MMP-2 expression in MI-hearts (n=5) and sham-hearts (n=4). Data are mean ± SD. (C) Intra-experimental correlation and (D) inter-experimental correlation between ^{177}Lu-biodistribution of 10 nmol $^{177}Lu/^{125}I$-dACPP (n=5) and MMP-2 levels in mice 10 days post MI. The resulting best fit parameters are shown in Table 3.3.*

Table 3.3: *Best fit parameters for linear regression analysis between ^{177}Lu uptake for $^{177}Lu/^{125}I$-dACPP (n=5) and MMP-2 levels in hearts of mice 10 days post MI. Parameters slope (%ID/g · (ug/g)$^{-1}$) and Pearson correlation coefficient r are listed.*

20h	Intra-experimental						Inter-experimental
	Mouse 1	Mouse 2	Mouse 3	Mouse 4	Mouse 5		N=5
Pearson *r* Slope	0.93 2.4 ± 0.3	0.84 1.7 ± 0.4	0.94 1.7 ± 0.2	0.95 1.5 ± 0.2	0.90 1.0 ± 0.1		0.78 1.2 ± 0.1

^{177}Lu-to-^{125}I ratios for dACPP and non-dACPP.

The dual-isotope–labeled $^{177}Lu/^{125}I$-dACPP and $^{177}Lu/^{125}I$-non-dACPP probes enabled us to study the *in vivo* probe activation in more detail. In MI-mice, which received $^{177}Lu/^{125}I$-dACPP, infarcted heart tissue showed a significantly higher ^{177}Lu-to-^{125}I ratio compared to remote myocardium (Fig. 3.5, Table 3.1, p<0.05) and this points toward a higher degree of probe activation in the infarct zone. Furthermore, the ^{177}Lu-to-^{125}I ratio was significantly elevated in infarcted myocardium compared to muscle of MI-mice and heart tissue of sham-mice (p<0.05). In animals injected with the negative control $^{177}Lu/^{125}I$-non-dACPP, the ^{177}Lu-to-^{125}I ratio was near to unity and similar in infarcted, and remote myocardium and muscle (Fig. 3.5, Table 3.2, p>0.05). A significant linear dependency was found between the ^{177}Lu-to-^{125}I ratios for dACPP and MMP-2 levels in MI-hearts (p<0.001), while no correlation was found for non-dACPP (Fig 3.5B, p>0.05).

In vivo biodistribution of $^{177}Lu/^{125}I$-dACPP in post-MI mice at 5h post-injection.

We also have determined the biodistribution of $^{177}Lu/^{125}I$-dACPP 5h post injection (Table 3.4). At this time point circulating dACPP was rarely observed. A detailed blood kinetic experiment for dACPP in MI-mice is presented in Chapter 4. We found higher absolute uptake levels for ^{177}Lu and ^{125}I at 5h compared to 20h post injection in MI-hearts (Tables 3.1 and 3.4). Furthermore, an impressive 10-fold higher ^{177}Lu uptake in infarcted compared to remote myocardium was observed at 5h post injection (Fig. 3.6, p<0.001), while a 6-fold difference was detected at 20 h post injection (Fig. 3.2). At 5h and 20h post probe injection, the uptake of ^{177}Lu as well as the ^{177}Lu-to-^{125}I ratios for $^{177}Lu/^{125}I$-dACPP in MI-hearts showed a linear dependency with the observed MMP-2 levels (Figs. 3.5 and 3.6, p<0.001). But importantly, the correlation coefficients for the 5h post injection data were stronger compared to the coefficients for the 20h post injection data.
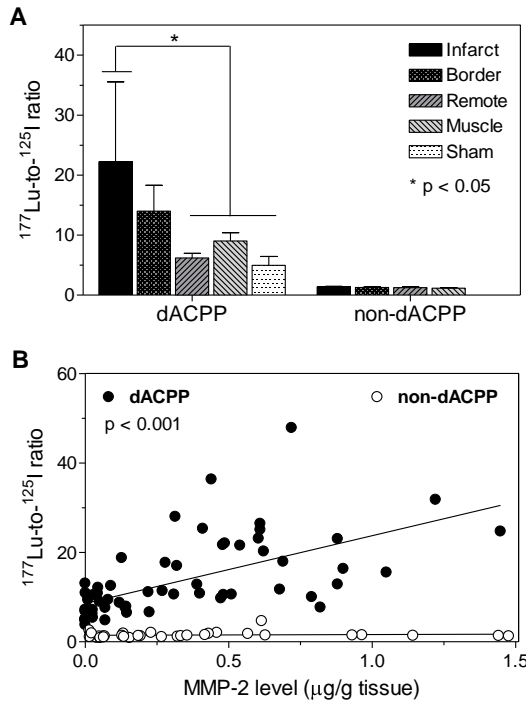
Figure 3.5: *(A) ^{177}Lu-to-^{125}I ratios for $^{177}Lu/^{125}I$-dACPP (n=5) and $^{177}Lu/^{125}I$-non-dACPP (n=5) in infarcted, border, and remote myocardium, muscle in MI-mice and heart tissue of sham-mice 20h post injection. Data are mean ± SD. (B) Correlation between MMP-2 levels and ^{177}Lu-to-^{125}I ratios for $^{177}Lu/^{125}I$-dACPP (n=5) and $^{177}Lu/^{125}I$-non-dACPP (n=4). Slope: 15.1 ± 2.6, and Pearson r: 0.60 for $^{177}Lu/^{125}I$-dACPP. Slope 0.18 ± 0.31, and Pearson r: 0.10 for $^{177}Lu/^{125}I$-non-dACPP.*

Table 3.4: *Biodistribution results of 10 nmol $^{177}Lu/^{125}I$-dACPP in MI-mice (n=3) 5h post injection. The data are presented as mean ± SD.*

5h	$^{177}Lu/^{125}I$-dACPP		
	^{177}Lu (%ID/g)	^{125}I (%ID/g)	Ratio $^{177}Lu/^{125}I$
Blood	0.09 ± 0.03	0.11 ± 0.04	0.9 ± 0.5
Heart, infarct	3.60 ± 0.68	0.28 ± 0.03	13.0 ± 2.7
Heart, border	1.18 ± 0.31	0.16 ± 0.02	7.3 ± 1.4
Heart, remote	0.35 ± 0.13	0.13 ± 0.02	2.6 ± 0.7
Muscle	0.48 ± 0.14	0.19 ± 0.21	5.7 ± 4.3
Lung	1.09 ± 0.30	0.28 ± 0.11	4.1 ± 1.1
Spleen	2.72 ± 1.48	0.14 ± 0.05	18.3 ± 4.6
Liver	28.5 ± 5.33	0.51 ± 0.08	56.0 ± 13.1
Kidney	59.9 ± 8.10	37.0 ± 8.11	1.7 ± 0.3
Fat	0.33 ± 0.08	0.08 ± 0.02	4.1 ± 0.6
Thigh bone	2.47 ± 1.02	0.64 ± 0.64	6.2 ± 4.8
Brain	0.02 ± 0.00	0.01 ± 0.00	ND
Stomach, full*	0.10 ± 0.03	1.13 ± 1.71	ND
Intestine, full*	0.83 ± 0.24	2.45 ± 3.31	ND
Thyroid*	0.09 ± 0.02	0.35 ± 0.06	ND

* expressed in %ID
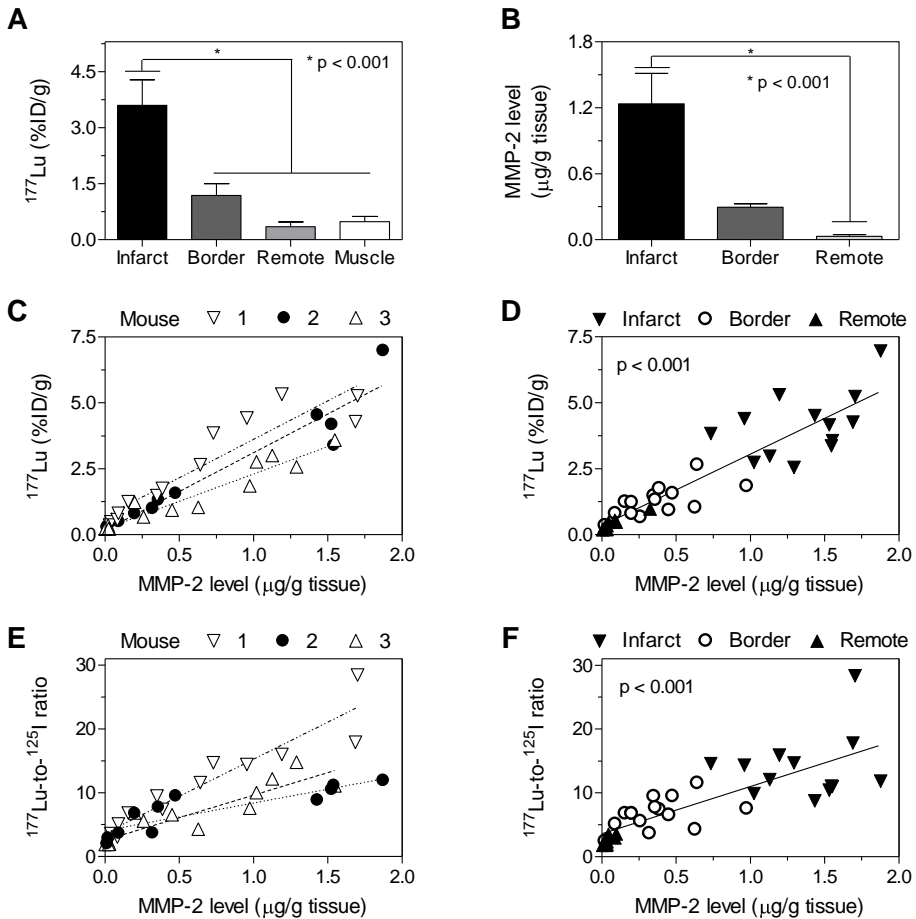
Figure 3.6: *(A) ^{177}Lu-biodistribution of 10 nmol ^{177}Lu/^{125}I-dACPP (n=3) in MI-mice at 5h post injection. Data are mean ± SD. (B) MMP-2 levels in MI-hearts of the same mice (n=3). Data are mean ± SD. (C) Intra-experimental and (D) inter-experimental correlation between MMP-2 levels and ^{177}Lu uptake. (E) Intra-experimental and (F) inter-experimental correlation between MMP-2 levels and ^{177}Lu-to-^{125}I ratios. Best fit parameters are shown in Table 3.5.*

Table 3.5: *Best fit parameters for linear regression analysis between MMP-2 levels and ^{177}Lu uptake, and between MMP-2 levels and ^{177}Lu/^{125}I ratios for ^{177}Lu/^{125}I-dACPP (n=5) in hearts of MI-mice 5h post injection. Parameters slope and Pearson correlation coefficient r are listed.*

5h		Intra-experimental				Inter-experimental
		Mouse 1	Mouse 2	Mouse 3		(n=3)
^{177}Lu	Pearson *r* Slope	0.93 2.9 ± 0.3	0.96 2.1 ± 0.2	0.96 2.9 ± 0.3		0.92 2.7 ± 0.2
^{177}Lu/^{125}I-ratio	Pearson *r* Slope	0.94 11.6 ± 1.2	0.90 7.0 ± 1.0	0.87 4.3 ± 0.8		0.80 7.4 ± 0.9

Discussion

The *in vivo* visualization of elevated levels of MMPs in heart disease has been demonstrated by Sinusas and coworkers to correlate to cardiac dysfunction (8). In that study, a radiolabeled MMP targeted tracer was studied in pigs with a myocardial infarction and a 3-4 fold higher tracer uptake was observed in infarcted myocardium compared to remote myocardium. To extend the tool box for *in vivo* monitoring of MMP levels, we focused on the detection of MMP catalytic activity instead of MMP levels. Here, we employed a dual-isotope radiolabeled peptide probe that is cleavable by MMP-2/9 and subsequently is trapped in the tissue. This probe consisted of an MMP-2/9 substrate inserted in between a polycationic cell penetrating peptide (CPP) and a polyanionic peptide that were labeled with the orthogonal radioisotopes ^{177}Lu (energy of the γ-ray emitted by isotope is E_γ = 208 keV) and ^{125}I (E_γ = 35 keV), respectively. The cell penetrating property of the polycationic peptide was quenched by electrostatic interactions with the polyanionic domain, preventing tissue association of the probe. Activation of the probe would result in efficient tissue retention of the ^{177}Lu-labeled polycationic peptide, while the ^{125}I labeled counterpart would be cleared by the kidneys. Therefore, a large ratio of ^{177}Lu over ^{125}I would indicate cleavage of the probe and subsequent retention of the ^{177}Lu-radiolabeled CPP, thereby facilitating a direct read-out of the relative level of MMP activity.

Here, we tested this dual-isotope radiolabeled MMP-2/9 sensitive activatable CPP (dACPP) in a mouse model of myocardial infarction (MI) to detect elevated tissue levels of MMP activity. Both autoradiography of MI-hearts and biodistribution studies showed a 6-fold increased uptake of the peptide-based probe in infarcted regions of the heart compared to remote areas 20h post injection. At 5h post injection an impressive 10-fold higher uptake in infarcted myocardium was observed compared to remote myocardium, which is a >2 fold larger difference than reported for radiolabeled MMP targeted tracers in pig and mice 1 week post MI (8,12), and for a fluorescent activatable probe in mice 1 week post MI (9). We also found increased MMP-2 levels in infarcted myocardium compared to remote myocardium and the MMP-2 levels showed a linear dependency with both the ^{177}Lu uptake as well as ^{177}Lu-to-^{125}I ratios for ^{177}Lu/^{125}I-dACPP at 5h and 20h post injection (Figs. 3.4-3.6). For the MMP-2/9 insensitive negative control ^{177}Lu/^{125}I-non-dACPP, the ^{177}Lu-to-^{125}I ratios were nearly to unity and similar in both infarct (1.4 ± 0.1) and remote (1.2 ± 0.2). These data point toward MMP-specific activation of the cleavable probe in the MI-hearts. Next to gelatin zymography, histology was performed on MI-hearts to assess levels of MMP activity, and macrophages. Unfortunately, bad tissue quality limited qualitative histological analysis of MMP-2, MMP-9, and macrophage levels, as high background signals were observed (data not shown). Nevertheless, these data seem to indicate elevated levels of active MMP-2, -9, and macrophages in areas of increased ^{177}Lu-dACPP uptake.

We recently showed that dACPP and the positive control peptide CPP are characterized by a similar biodistribution pattern in tumor-bearing mice, suggesting that dACPP activation in the vascular compartment was the main mechanism for the observed elevated probe uptake in tumoral tissue (11). Here, we found a significant higher ^{177}Lu infarct-to-remote (p<0.01) and ^{177}Lu infarct-to-muscle (p<0.05) ratio for dACPP compared to the positive control CPP (Fig.

3.7, Tables 3.2 and 3.3), indicating a significant degree of infarct-specific activation of dACPP.
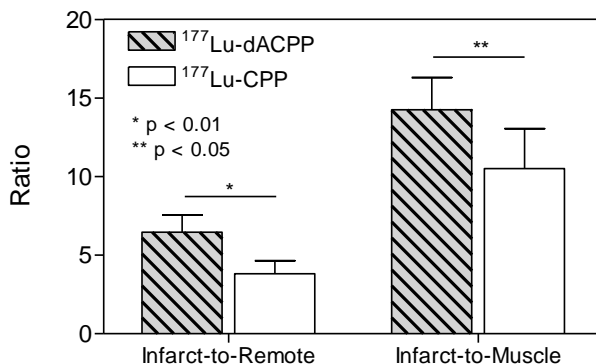

Figure 3.7: *Infarct-to-remote and infarct-to-muscle ratios for 10 nmol of ^{177}Lu-dACPP and 10 nmol of ^{177}Lu-CPP in MI-mice 20h after injection (n=5). Data are mean ± SD.*

The absolute higher uptake levels of ^{177}Lu-dACPP in infarcted myocardium (3.60 ± 0.68 %ID/g at 5h post injection) in comparison to MMP-2/9 expressing tumors (1.90 ± 0.71 %ID/g at 6h post injection) also point toward infarct-specific retention of dACPP. In this respect it is important to point out that tumors are characterized by a high tissue perfusion and an enhanced permeability and retention (EPR) compared to heart tissue, which is associated with a higher unspecific accumulation of the ^{177}Lu-ACPP probe in tumors, as was observed in tumor-bearing mice (1.90 ± 0.71 %ID/g in tumor vs 0.33 ± 0.03 %ID/g in heart). The higher local uptake in infarcted myocardium compared to tumors is therefore exciting and is most likely due to infarct specific activation. Yet, no significant difference in MMP-2 levels were observed for HT-1080 tumors and myocardial infarcted tissue by gelatin zymography (Fig. 2.16 vs Figs. 3.4B and 3.6B). Even though the MMP-2 levels were similar, the MMP-2 activity may have been different in both models. Namely, the *in vivo* MMP-2 activity is controlled by the family of tissue inhibitors of metalloproteinases (TIMPs). It would be valuable to determine the TIMPs levels for both models.

Despite infarct-specific activation, the biodistribution data of [77]Lu/^{125}I-dACPP in MI-mice also suggest a degree of background dACPP activation in the vasculature, indicated by ^{177}Lu-to-^{125}I ratios > 1 in various tissues that show low levels of MMP expression, e.g. sham-hearts (^{177}Lu/^{125}I ratio = 5.0 ± 1.5) and remote myocardium (^{177}Lu/^{125}I ratio = 6.2 ± 0.8). Probe activation in the vasculature has resulted in a strong accumulation of the activated domain, ^{177}Lu-CPP, in the liver (20.4 ± 4.2 %ID/g), an organ adjacent to the heart. Therefore, an ACPP-based activatable imaging probe that is activated in the infarct without activation in the vasculature is highly valuable. Such a probe may display reduced background liver uptake as observed for non-dACPP (3.7 ± 1.0 %ID/g), an ACPP analog that showed no detectable cleavage in the vasculature, while the local infarct-specific activation may still result in relatively high target uptake. Hereby, an improvement of the signal-to-noise ratios

may be achieved. In Chapter 5, the development of these infarct-specific sensitive ACPPs is subject of research.

The biodistribution data for 5h and 20h post injection, suggest probe wash-out from the MI-hearts overtime. As mentioned earlier, we found linear dependencies between MMP-2 expression on one hand and probe uptake (^{177}Lu uptake) and probe activation (^{177}Lu-to-^{125}I ratio) on the other hand at both time points. Stronger Pearson correlation coefficients (r) were observed at 5h post-injection due to higher variation for the 20h post injection biodistribution data. The observed probe clearance from the target tissue overtime most likely has contributed to this larger variation. A blood kinetic experiment revealed a blood half life of ~17 min (see Chapter 4, Table 4.1). For imaging of dACPP biodistribution in MI-mice, the best time point would be 2.5h post injection. At this time point, the background signal from the blood is sufficiently low (~0.1% ID/g).

In this study, myocardial infarction was induced via surgery, which often is associated with an inflammatory response, scar tissue formation and potential MMP expression in the surgical wound area. This area is relatively close to the infarcted myocardium. In the biodistribution studies, the hearts were carefully excised from the euthanized animal to minimize presence of surrounding tissue. For a follow-up study, a different animal model of heart disease without the need for surgery and accompanying risk for infections and scar tissue formation, *e.g.* a spontaneous heart failure model, may be valuable to assess dACPP biodistribution with regard to MMP detection in heart disease.

Conclusion

We demonstrated a significant contribution of infarct-associated ACPP activation to infarct targeting of dACPP, most likely due to MMPs. An impressive 10-fold higher probe uptake was observed in infarcted tissue compared to remote myocardium. Future research should address whether dACPP can be used for *in vivo* nuclear imaging of MMPs in heart disease.

Acknowledgements

Methods

Probe synthesis

Peptides Ac-y-e$_9$-*x*-PLGLAG-r$_9$-*x*-k(DOTA)-NH$_2$ (dACPP), Ac-y-e$_9$-*x*-LALGPG-r$_9$-*x*-k(DOTA)-NH$_2$ (non-dACPP), and Ac-LAG-r$_9$-*x*-k(DOTA)-NH$_2$ (CPP), wherein x denotes amino-hexanoic acid, were synthesized as previously described (Chapter 2).

Animal studies

All animal procedures were approved by the ethical review committee of the Maastricht University Hospital (The Netherlands), and were performed according to the principles of laboratory animal care (NIH publication 85-23, revised 1985) (13), and the Dutch national law "Wet op Dierproeven" (Stb 1985, 336). Male Swiss mice (body weight >25g, Charles River Labs) were housed in an enriched environment under standard conditions: 21-23 °C, 50-60% humidity, and 12h-lightdark-cycles for >1 week. Food and water were freely available.

Myocardial infarction (MI) model

MI was induced by permanent ligation of the left anterior descending coronary artery (LAD) using published procedures (14). In short, animals were subcutaneously injected with buprenorphine (0.1 mg/kg) and 30 min later anesthetized with isoflurane. Animals were intubated and ventilated with 100% oxygen with a rodent respirator. After left thoracotomy between ribs four and five, the LAD was ligated with a 6-0 prolene suture. The chest and skin were closed with 5-0 silk sutures. The animal's temperature was continuously measured rectally and maintained at 36.5–37.5 °C during surgery. Sham-operated animals underwent the same procedure, except that the 6-0 prolene suture was passed through the myocardium without ligating the LAD, and served as controls. After surgery, animals were allowed to recover at 30 °C overnight. Ten days post MI, the animals were used for biodistribution studies.

Radiolabeling

The labeling buffers were treated with Chelex-100 resin (BioRad Laboratories) overnight and filtered through 0.22 μm. *^{177}Lu/^{125}I-dACPP and ^{177}Lu/^{125}I-non-dACPP.* ^{177}LuCl$_3$ in 0.05 M HCl (4.0 μL, 20.0 MBq) was mixed with dACPP or non-dACPP in MilliQ water (3.7 μL, 25 nmol), and metal-free 0.9% NaCl (242.3 μL) for 20 min, at 600 rpm and 90 °C. ^{125}I (PerkinElmer) in phosphate buffered saline (PBS) pH 7.4 (7.0 μL, 12.5 MBq) was mixed with dACPP or non-dACPP in MilliQ water (3.7 μL, 25 nmol), and PBS (239.3 μL) in a Pierce iodination tube (Thermo Fischer Scientific) for 20 min, at 600 rpm and 23 °C, and transferred to a siliconized 1.5 mL tube. *^{177}Lu-CPP.* ^{177}LuCl$_3$ in 0.05 M HCl (2.0 μL, 10.0 MBq) was mixed with CPP in MilliQ water (3.0 uL, 25 nmol), and metal-free 0.9% NaCl (245 μL) for 20 min, at 600 rpm and 90 °C.

The ^{177}Lu and ^{125}I labeling yields were determined by radio-TLC, using iTLC-SG strips (Pall) eluted with 200 mM EDTA in 0.9% NaCl and 20 mM citric acid at pH 5.2, respectively, imaged on a phosphor imager (FLA-7000, Fujifilm) and quantified with AIDA Image Analyzer software. Analytical radio-HPLC was carried out on an Agilent 1100 system equipped with a C18 Eclipse XBD-column (length = 150 mm, diameter = 4.6 mm, particle size = 5.0 μm) and a Gabi radioactive detector (Raytest). The radiochemical purities were 95% or higher, and typically at least 97%.

^{177}Lu-labeled dACPP/non-dACPP was mixed with ^{125}I-labeled dACPP/non-dACPP in a 1:1 molar ratio.

Biodistribution experiments

Biodistribution experiments were performed on MI-mice (n=3-5 per probe) or sham-mice (n=4) by i.v.-injection of ^{177}Lu/^{125}I-dACPP (10 nmol/100 µL, ca. 4.0 MBq ^{177}Lu, ca. 2.5 MBq ^{125}I), ^{177}Lu/^{125}I-non-ACPP (10 nmol/100 µL, ca. 4.0 MBq ^{177}Lu, ca. 2.5 MBq ^{125}I), or ^{177}Lu-CPP (10 nmol/100 µL, ca. 4.0 MBq). The mice were anesthetized with isoflurane 5h or 20h after i.v.-injection, subjected to 2% (w/v) Evans Blue i.v.-injection (50 mg/kg) and sacrificed 2 min later by cervical dislocation. Organs and tissues of interest were harvested and weighed, after which the radioactivity of the samples was measured in a γ-counter (Wizard 1480; PerkinElmer) along with standards to determine the injected dose per gram (%ID/g). The energy windows were set to 10-80 keV for ^{125}I and 155-380 keV for ^{177}Lu. The hearts were cooled to 4 °C, cut in 1 mm slices from apex to base. Randomly heart slices were incubated in 1.0% (w/v) 2,3,5-triphenyltetrazolium chloride (TTC) in PBS at 37°C, 300 rpm for 20 min to prove consistency between *in vivo* Evans Blue and *ex vivo* TTC staining (Fig. 3.8). Infarct, border, and remote areas were isolated based on Evans Blue staining, and %ID/g for ^{125}I and ^{177}Lu was determined by a γ-counter. TTC-stained slices were excluded for γ-counting due to wash-out of the radiolabeled probes during the incubation.
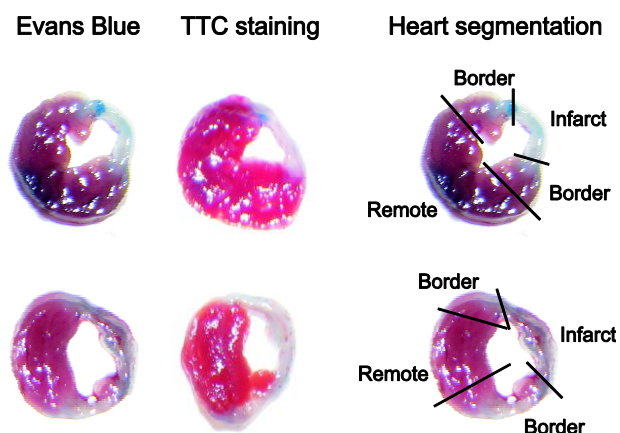
Figure 3.8: *Representative photographs of in vivo Evans Blue stained and subsequent ex vivo TTC stained 1 mm transversal heart slices of different mice showing consistency in infarct/remote identification. On the right, representative assignments of the infarcted, border, and remote myocardium is shown for the Evans Blue stained slices.*

Sample preparation, tissue homogenates.

After γ-counting, tissue samples were homogenized in 20 volumes of 50 mM Tris, 200 mM NaCl, 10 mM $CaCl_2$, and 10 µM $ZnCl_2$ at pH 7.5 at 4 °C at 25 Hz for 2 × 5 min and subsequently mixed at 5 Hz for 2 × 15 min using a tissue lyser (Qiagen), and then centrifuged at 5,000 rpm for 5 min at 4 °C. The supernatants were aliquoted and stored at -80 °C until zymography analysis. Typically, 14 µL tissue supernatant (from 0.7 mg tissue homogenate) was used per analysis.

Gelatin zymography

Samples were analyzed on 10% SDS-PAGE gel containing 0.1% (w/v) gelatin (Biorad). MMP-2 (Calbiochem, Merck) (0.21 ng) was loaded as an internal standard used to normalize activities between gels. Electrophoresis was performed at 150V for 1.5h, after which the gels were washed with MilliQ water, incubated for 3 × 20 min in 2.5% Triton-X (50 rpm) to remove SDS, washed with MilliQ water, and incubated in 50 mM Tris, 200 mM NaCl, 5 mM $CaCl_2$, 0.1% (w/v) NaN_3, and 0.02% (w/v) Brij-35 at pH 7.6 and 37 ^{o}C for 2 days. Gels were stained for 2h with 0.25% Coomassie Blue in 60% (v/v) MilliQ water, 30% (v/v) Methanol, 10% (v/v) Acetic acid, and destained for > 24h with 67.5% (v/v) MilliQ water, 25% (v/v) Methanol, 7.5% (v/v) Acetic acid. Gelatinatic activity showed up as clear bands against a dark background. Zymograms were imaged (Epson Perfection V700 Photo scanner) and band intensities were quantified using ImageJ.

Autoradiography and histology

MI-mice (n=4) were injected i.v. with ^{177}Lu-dACPP (10 nmol/100 μL, ca. 20.0 MBq ^{177}Lu). The mice were anesthetized with isoflurane 20h after i.v.-injection, and tissue perfusion fixation was performed with 4% PFA in sterile PBS. The hearts were excised and incubated in 4% PFA at 4 °C for 2h, washed with ice-cold PBS, and incubated in 15% sucrose in PBS for 16-48h. The hearts were cut in half (either in coronal or transversal direction), and sliced into sections with a cryomicrotome (repetitions of 1 x 40 μm and 10 x 10 μm sections for autoradiography and histology, respectively). Autoradiography was performed for max. 80 h using a MicroImager (BioSpace Lab). The radioactivity within each region of interest (ROI) was quantified by ImageJ. Azan staining was performed using standard procedures.

Statistical methods

Quantitative data were expressed as mean ± SD. Standard one-way or repeated measures ANOVA, with Bonferroni's post hoc testing, was used for multiple group comparisons. Single groups were compared with the one-tailed unpaired Welch's t test (15). Groups with $p < 0.05$ were considered significantly different. Linear regression was performed to assess linear relationship between MMP expression levels and ^{177}Lu-uptake for dACPP and between MMP expression and ^{177}Lu-to-^{125}I ratios for dACPP and non-dACPP. GraphPad Prism was used for all statistical calculations.

References

1. Deschamps AM, and Spinale FG. Pathways of matrix metalloproteinase induction in heart failure: Bioactive molecules and transcriptional regulation. *Cardiovasc Res.* 2006;69:666-676
2. Vanhoutte D, Schellings M, Pinto Y, et al. Relevance of matrix metalloproteinases and their inhibitors after myocardial infarction: a temporal and spatial window. *Cardiovasc Res.* 2006;69:604-613
3. Zavadzkas JA, Plyler RA, Bouges S, et al. Cardiac-restricted overexpression of extracellular matrix metalloproteinase inducer causes myocardial remodeling and dysfunction in aging mice. *Am J Physiol Heart Circ Physiol.* 2008;295:H1394-H1402
4. Mukherjee R, Mingoia JT, Bruce JA, et al. Selective spatiotemporal induction of matrix metalloproteinase-2 and matrix metalloproteinase-9 transcription after myocardial infarction. *Am J Physiol Heart Circ Physiol.* 2006;291:H2216-H2228

5. Hayashidani S, Tsutsui H, Ikeuchi M, et al. Targeted deletion of MMP-2 attenuates early LV rupture and late remodeling after experimental myocardial infarction. *Am J Physiol Heart Circ Physiol.* 2003;285:H1229–H1235

6. Ducharme A, Frantz S, Aikawa M, et al. Targeted deletion of matrix metalloproteinase-9 attenuates left ventricular enlargement and collagen accumulation after experimental myocardial infarction. *J Clin Invest*. 2000;106:55–62

7. Bergman MR, Teerlink JR, Mahimkar R, et al. Cardiac matrix metalloproteinase-2 expression independently induces marked ventricular remodeling and systolic dysfunction. *Am J Physiol Heart Circ Physiol.* 2007;292:H1847-H1860

8. Sahul ZH, Mukherjee R, Song J, et al. Targeted imaging of spatial and temporal variation of matrix metalloproteinase activity in porcine model of post-infarct remodeling: relationship to myocardial dysfunction. *Circ Cardiovasc Imaging.* 2011;4:381-391

9. Chen J, Tung C-H, Allport JR, et al. Near-infrared fluorescent imaging of matrix metalloproteinase activity after myocardial infarction. *Circulation.* 2005;111:1800-1805

10. Jaffer FA, Vinegoni C, John MC, et al. Real-time catheter molecular sensing of inflammation in proteolytically active atherosclerosis. *Circulation.* 2008;118:1802-1809

11. van Duijnhoven SMJ, Robillard MS, Nicolay K, et al. Tumor targeting of MMP-2/9 activatable cell-penetrating imaging probes is caused by tumor-independent activation. *J Nucl Med.* 2011;52:279-286

12. Su H, Spinale FG, Dobrucki LW, et al. Noninvasive targeted imaging of matrix metalloproteinase activation in a murine model of postinfarction remodeling. *Circulation.* 2005;112:3157-3167

13. *Guide for the Care and Use of Laboratory Animals*. Washington, DC: Government Printing Office; 1985. NIH publication 86-23

14. Lutgens E, Daemen M, de Muinck ED, et al. Chronic myocardial infarction in the mouse: cardiac structural and functional changes. *Cardiovasc Res.* 1999;41:586–593

15. Ruxton GD. The unequal variance t-test is an underused alternative to Student's t-test and the Mann-Whitney U test. *Behav Ecol.* 2006;17:688–690

Chapter **4**

Long-circulating radiolabeled MMP-2/9 activatable cell penetrating peptides

Abstract

A radiolabeled matrix metalloproteinase-2/9 (MMP-2/9) activatable cell penetrating peptide (dACPP) has been shown to be a promising imaging probe for the detection of cardiac remodeling. This peptide-based probe is characterized by a relatively short circulation time ($t_{1/2} \sim 17$ min), thereby limiting the exposure time to the target protease. Here, we developed MMP-2/9 activatable cell penetrating peptides with a prolonged circulation time ($t_{1/2} \sim 90$ min) due to the introduction of low molecular weight albumin binding ligands (i.e. palmitic acid (Palm), or deoxycholic acid (DOCA)) into the probes. We have called these imaging probes AlbACPPs. In the presence of human serum albumin, *in vitro* cleavage of AlbACPP-PEG-DOCA by MMP-2 occurred at a comparable rate as observed for the parent dACPP probe, while the cleavage rate for AlbACPP-PEG-Palm was significantly lower. *In vivo* biodistribution studies in a mouse model of myocardial infarction pointed towards local activation of AlbACPP-PEG-DOCA in areas of cardiac remodelling. Despite the increased circulation time of this probe, the infarct-to-remote ratios and absolute probe uptake in infarcted areas of the heart was comparable to dACPP.

Introduction

Short circulating imaging probes are clinically advantageous as diagnostic imaging can be performed within a few hours after probe administration limiting hospitalization time. Although a rapid blood clearance results in low background signals, it also minimizes the exposure time of the probe to its protein target that may result in a hampered accumulation at the target site. In Chapter 3, we showed that a short circulating radiolabeled low molecular weight activatable cell penetrating peptide (dACPP) ($t_{1/2}$ ~ 17 min) cleavable by the proteolytic activity of matrix metalloproteinases-2/9 (MMP-2/9) was locally activated in mouse heart tissue undergoing cardiac remodeling. We demonstrated that the level of activation of the ACPP imaging probes correlated significantly with the expression levels of MMP-2/9. Unfortunately however, this probe displayed a relatively low absolute uptake. In that respect, further improvements of the ACPP imaging platform may be achieved by ACPP imaging probes with a longer circulation, thereby increasing the exposure time to the target proteases.

Several strategies have been reported to increase the circulation time of peptide probes including PEGylation (MW_{PEG} > 2 kDa) of the probes (1), loading the probes on or into macromolecular carriers (2,3), or covalent or non-covalent binding of the probes to the transporter protein albumin (4-7). In general, PEGylation results in a stealth character of the imaging probe that may reduce probe-target interaction. Alternatively, covalent coupling of the low molecular weight peptides to high molecular weight carriers such as albumin is aimed to reduce renal clearance as these probe conjugates are too large to be excreted by the kidneys (5). However, covalent coupling of ACPP to these carriers will mainly restrict the bioavailability of the ACPP-conjugate to the blood pool, while free ACPP displayed distribution to the extravascular extracellular space (8). We therefore focused on the development of low molecular weight MMP-2/9 ACPP probes which can reversibly bind to albumin upon intravenous administration and still allows the extravasation of the unbound compound. We hypothesized that the imaging probe may be able to dissociate from albumin and distribute into the extravascular extracellular space to be activated in the extracellular matrix subjected to remodelling. It has to be noted that the infarcted myocardium may show signs of a hyperpermeable damaged microvasculature (9). Therefore, the albumin-ACPP conjugate may display some enhanced retention in the infarcted region. Furthermore, albumin is not only present in the intravascular space, but also in the interstitial space (10). In that respect, we aimed for albumin-ACPP conjugates wherein the ACPP probe retains its MMP-2/9 sensitivity once bound to albumin.

Albumin is the most abundant protein in the circulation (7). Binding pockets on the surface of the protein enable strong association of a variety of compounds such as bile, and long-chain fatty acids. Functionalization of peptides or MRI imaging agents with several types of albumin-binding compounds has resulted in long-circulating peptides (4-7) or blood pool MRI contrast enhancing agents (11-14). Here we focused on the conjugation of the MMP-2/9 ACPP imaging probe to a high affinity albumin ligand, palmitic acid (Palm) with a equilibrium binding constant (K_a) of 2.2 × 10^8 M^{-1} (15), or to an intermediate affinity albumin ligand,

deoxycholic acid (DOCA) with a K_a of 7.6×10^4 M^{-1} (16). The ligands were coupled to ACPP via a γ-Glu linker, which has been reported to further improve the affinity for albumin (6), most probably by direct interaction with charged amino acids on the surface of albumin. Peptide probes with and without a poly(ethyleneglycol) (PEG) linker between the ACPP peptide and the albumin ligand were synthesized to study steric hindrance effects around the MMP cleavable linker, potentially induced by the bulky albumin protein. To enable dual isotope studies, a DOTA chelate (for ^{177}Lu labeling) was coupled to the cell penetrating peptide domain and a 3-(4-hydroxyphenyl)propionic acid (SHPP) residue (for ^{125}I conjugation) was introduced at the N-terminal region of the neutralizing domain. The molecular structures of the MMP-2/9 activatable probes AlbACPP-PEG-DOCA, AlbACPP-DOCA, AlbACPP-PEG-Palm and AlbACPP-Palm are shown in Figure 4.1. The blood kinetics and biodistribution profiles of ^{177}Lu/^{125}I-AlbACPP-PEG-DOCA and ^{177}Lu/^{125}I-AlbACPP-PEG-Palm and the corresponding negative controls were determined in a mouse model of myocardial infarction.

Results

Probe synthesis

The MMP-2/9 sensitive peptide-based probes dACPP (synthesis described in Chapter 2), AlbACPP-PEG-DOCA, AlbACPP-DOCA, AlbACPP-PEG-Palm and AlbACPP-Palm were successfully prepared by Fmoc solid-phase peptide synthesis. Deoxycholic acid was activated using n-hydroxy succininimidyl ester (NHS), purified and subsequently conjugated to the N-terminus of the peptide probe on the solid phase. Similarly, palmitic acid-NHS was coupled to the N-terminus of the peptide probe on the solid phase. Subsequently, DOTA-NHS was conjugated to the C-terminal lysine residue upon site-specific deprotection of the Mtt-protected ε-amino group. Following peptide cleavage, all probes were purified by reversed phase – HPLC. In the final step, SHPP-NHS was conjugated to the N-terminal lysine of AlbACPP-PEG-DOCA and AlbACPP-PEG-Palm and the peptide based probes were purified. The negative control probes non-AlbACPP-PEG-DOCA and non-AlbACPP-PEG-Palm, containing the MMP-2/9 insensitive LALGPG peptide substrate, were synthesized by employing the same strategy. Liquid chromatography – mass spectrometry (LC-MS) analysis demonstrated pure peptides with molecular masses consistent to their theoretic masses (Fig. 4.2).

A

B

C
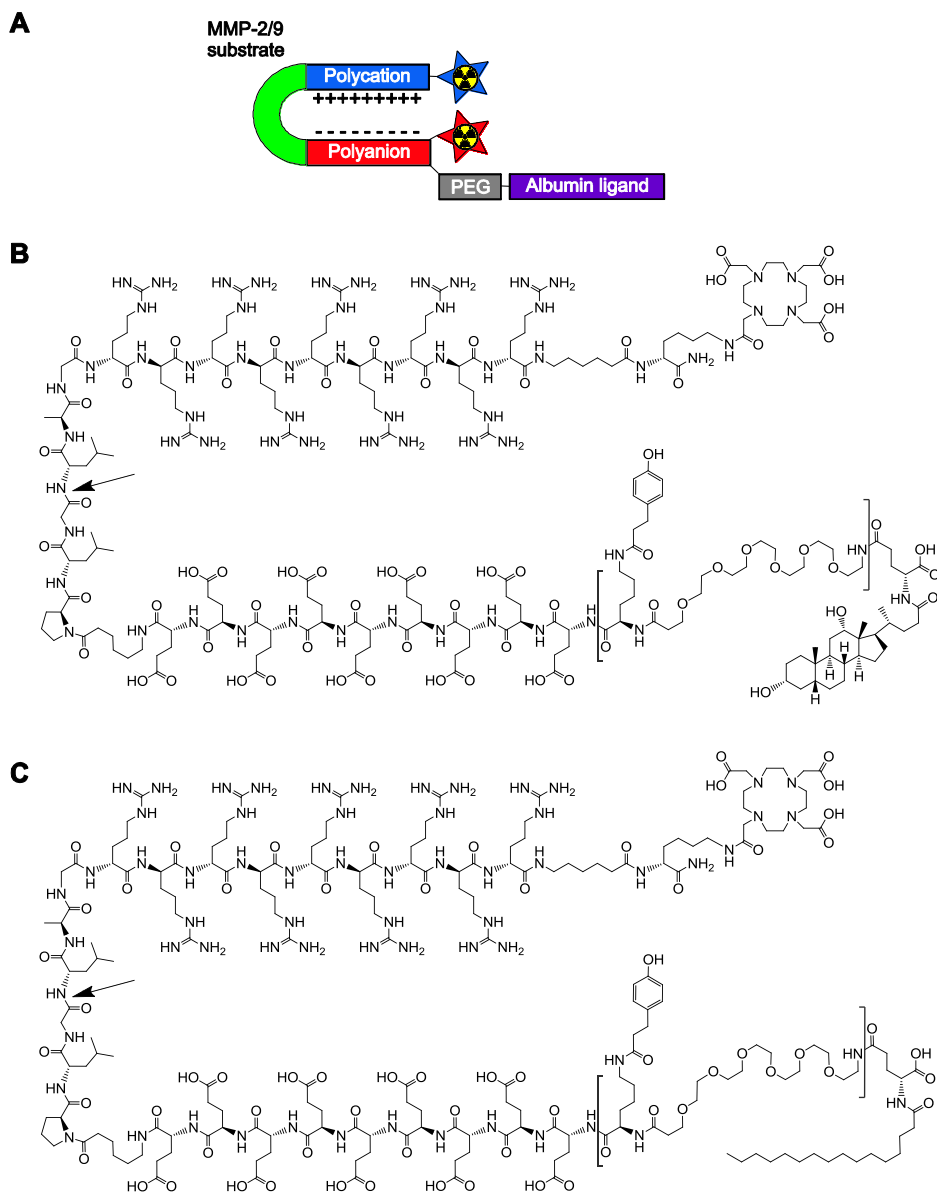
Figure 4.1: *(A) Schematic of an MMP-2/9 sensitive albumin binding dual-isotope labeled AlbACPP. Molecular structure of (B) DOCA-e*-PEG$_6$-k(SHPP)-e$_9$-x-PLGLAG-r$_9$-x-k(DOTA)-NH$_2$ (AlbACPP-PEG-DOCA) and (C) Palm-e*-PEG$_6$-k(SHPP)-e$_9$-x-PLGLAG-r$_9$-x-k(DOTA)-NH$_2$ (AlbACPP-PEG-Palm). The MMP-2/9 cleavage site is indicated by the arrow. The domain that is surrounded by brackets is not present in the probes AlbACPP-DOCA and AlbACPP-Palm. For the negative control probes non-AlbACPP-PEG-DOCA and non-AlbACPP-PEG-Palm, the MMP-2/9 substrate PLGLAG was replaced by MMP-2/9 insensitive scrambled linker LALGPG.*
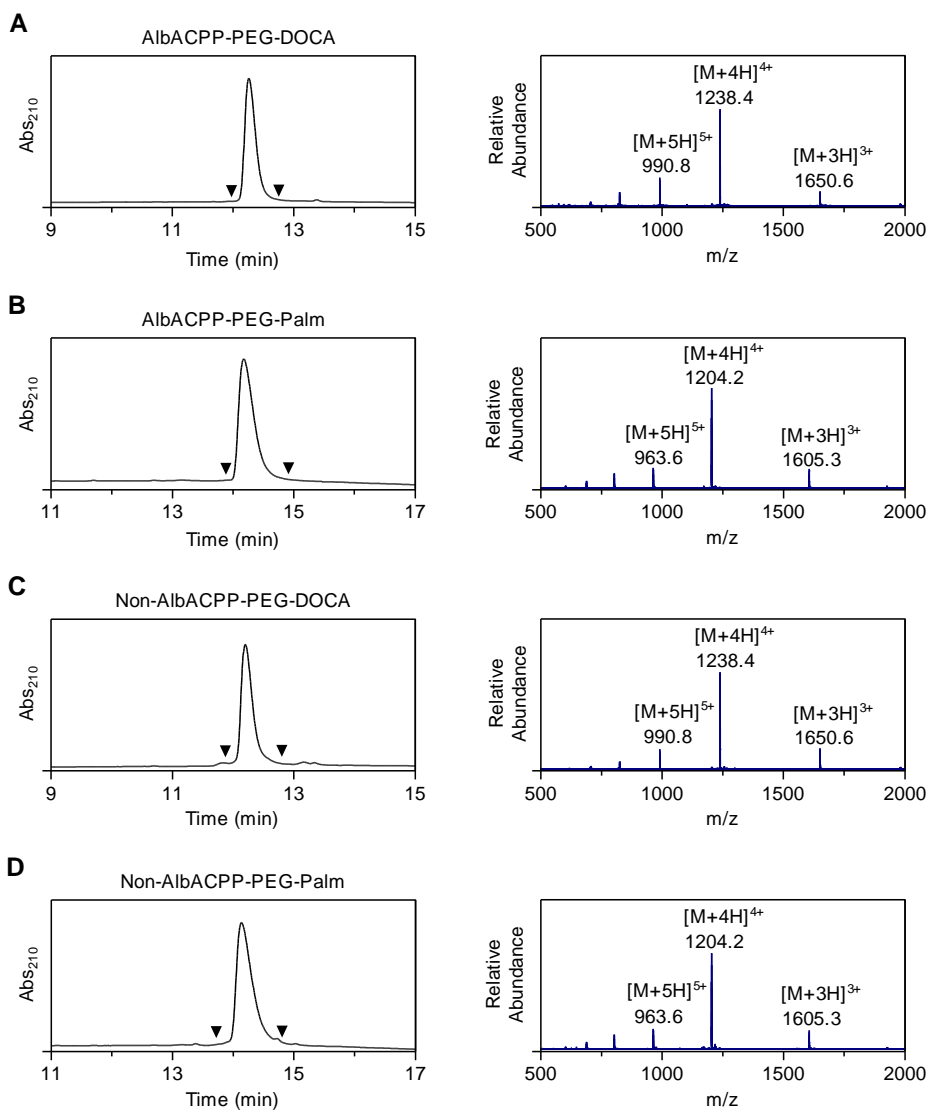
Figure 4.2: *LC-MS characterization of (A) DOCA-e*-PEG$_6$-k(SHPP)-e$_9$-x-PLGLAG-r$_9$-x-k(DOTA)-NH$_2$ (AlbACPP-PEG-DOCA, obsd. 4946.8 Da, calcd. 4946.7 Da), (B) Palm-e*-PEG$_6$-k(SHPP)-e$_9$-x-PLGLAG-r$_9$-x-k(DOTA)-NH$_2$ (AlbACPP-PEG-Palm, obsd. 4810.8 Da, calcd. 4810.7 Da), (C) DOCA-e*-PEG$_6$-k(SHPP)-e$_9$-x-LALGPG-r$_9$-x-k(DOTA)-NH$_2$ (Non-AlbACPP-PEG-DOCA, obsd. 4946.8 Da, calcd. 4946.7 Da), and (D) Palm-e*-PEG$_6$-k(SHPP)-e$_9$-x-LALGPG-r$_9$-x-k(DOTA)-NH$_2$ (Non-AlbACPP-PEG-Palm, obsd. 4810.8 Da, calcd. 4810.7 Da). The left and right graphs show the UV absorbance chromatogram and the mass spectrum of the UV-peak bracketed by the arrowheads, respectively.*

MMP-2 sensitivity of AlbACPPs in presence of albumin

Binding of AlbACPPs to albumin may reduce ACPP sensitivity for MMP-2/9 due to steric hindrance around the MMP-2/9 cleavable site of ACPP, induced by the bulky albumin protein. To investigate this possible effect, the MMP-2 sensitivity of dACPP, AlbACPP-PEG-DOCA, AlbACPP-DOCA, AlbACPP-PEG-Palm and AlbACPP-Palm was assessed in the presence of 4.5% w/v human serum albumin (HSA). All probes were radiolabeled with ^{177}Lu, incubated with MMP-2, and the release of ^{177}Lu-CPP was measured by γ-HPLC overtime (Figs. 4.3 and 4.4). dACPP, AlbACPP-PEG-DOCA, and AlbACPP-DOCA showed a similar ^{177}Lu-CPP release after 1h and 4h incubation (p>0.05), while AlbACPP-PEG-Palm and AlbACPP-Palm showed a significant reduced CPP release at the same time points (p<0.05). In addition, the CPP release for AlbACPP-Palm probe was significantly lower at 4h compared to AlbACPP-PEG-Palm (p<0.05). This suggests that PEGylation improved accessibility around the MMP-2/9 cleavable site for AlbACPP-PEG-Palm, but may be further enhanced by application of a longer PEG-chain.

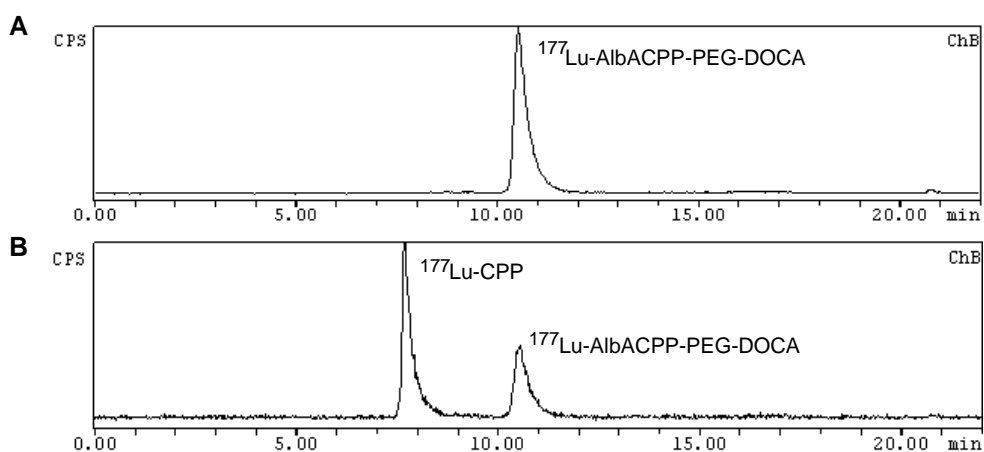**Figure 4.3:** *γ-HPLC analysis of ^{177}Lu-AlbACPP-PEG-DOCA (25.0 μM) (A) before and (B) 60 min after incubation with MMP-2 (18.0 nM) in the presence of 4.5% HSA. The panel shows the γ-radiation monitored by a γ-detector (CPS = counts per second).*
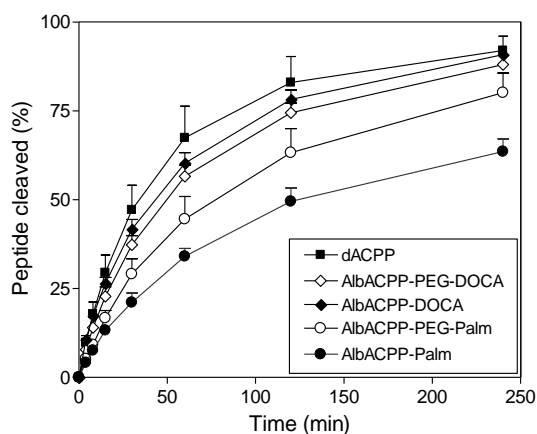
Figure 4.4: ^{177}Lu-CPP release (%) from ^{177}Lu-dACPP, ^{177}Lu-AlbACPP-PEG-DOCA, ^{177}Lu-AlbACPP-DOCA, ^{177}Lu-AlbACPP-PEG-Palm, and ^{177}Lu-AlbACPP-Palm (25 µM), respectively, upon incubation with MMP-2 (18 nM) in the presence of 4.5% HSA. The experiments were performed in duplicate for ^{177}Lu-AlbACPP-Palm and in triplicate for the other peptide probes. The data are presented as mean ± SD.

Bloodkinetics and in vivo biodistribution

The blood kinetics of $^{177}Lu/^{125}I$-dACPP, $^{177}Lu/^{125}I$-AlbACPP-PEG-DOCA, and $^{177}Lu/^{125}I$-AlbACPP-PEG-Palm and the negative control probes $^{177}Lu/^{125}I$-non-AlbACPP-PEG-DOCA, and $^{177}Lu/^{125}I$-non-AlbACPP-PEG-Palm were studied in a mouse model of myocardial infarction (11 day-old infarcts). All peptides displayed biphasic elimination from the circulation, but a strong increase in circulation time was observed for the albumin binding probes compared to dACPP (Fig. 4.5, Table 4.1). Specifically, the ^{177}Lu half lives were 17 min for $^{177}Lu/^{125}I$-dACPP, 87 min for $^{177}Lu/^{125}I$-AlbACPP-PEG-DOCA, and 95 min for $^{177}Lu/^{125}I$-AlbACPP-PEG-Palm. The calculated volume of distribution (V_D) was 0.16 L/kg for dACPP, 0.12 L/kg for AlbACPP-PEG-DOCA, and 0.08 L/kg for AlbACPP-PEG-Palm. This suggests an extracellular extravascular biodistribution for dACPP, as was earlier observed in tumor-bearing mice (Chapter 2), a restricted extracellular extravascular biodistribution for AlbACPP-PEG-DOCA, and no extravascular distribution for AlbACPP-PEG-Palm (17,18).

The blood kinetics of ^{177}Lu and ^{125}I for $^{177}Lu/^{125}I$-AlbACPP-PEG-DOCA follow different trends, with a 2.4-fold faster clearance of ^{177}Lu compared to ^{125}I (half lives of 87 min and 207 min, respectively), which would suggest probe activation and tissue entrapment of the activated CPP domain. Further evidence for this assertion comes from the $^{177}Lu/^{125}I$ ratios in the analyzed tissues, displaying a higher uptake for ^{177}Lu than that for ^{125}I (Table 4.3). $^{177}Lu/^{125}I$-AlbACPP-PEG-Palm showed a 1.9-fold faster clearance of ^{177}Lu compared to ^{125}I (half lives of 95 min and 185 min, respectively) and $^{177}Lu/^{125}I$ ratios were reduced in all tissues compared to $^{177}Lu/^{125}I$-AlbACPP-PEG-DOCA, suggesting a lower *in vivo* sensitivity of this probe for proteolytic degradation (Table 4.4). This corresponds well with the results obtained in the *in vitro* MMP-2 sensitivity assay. AlbACPP-PEG-DOCA and non-AlbACPP-PEG-DOCA showed a high uptake by the kidneys, while AlbACPP-PEG-Palm and non-AlbACPP-PEG-Palm accumulate preferentially in the liver.
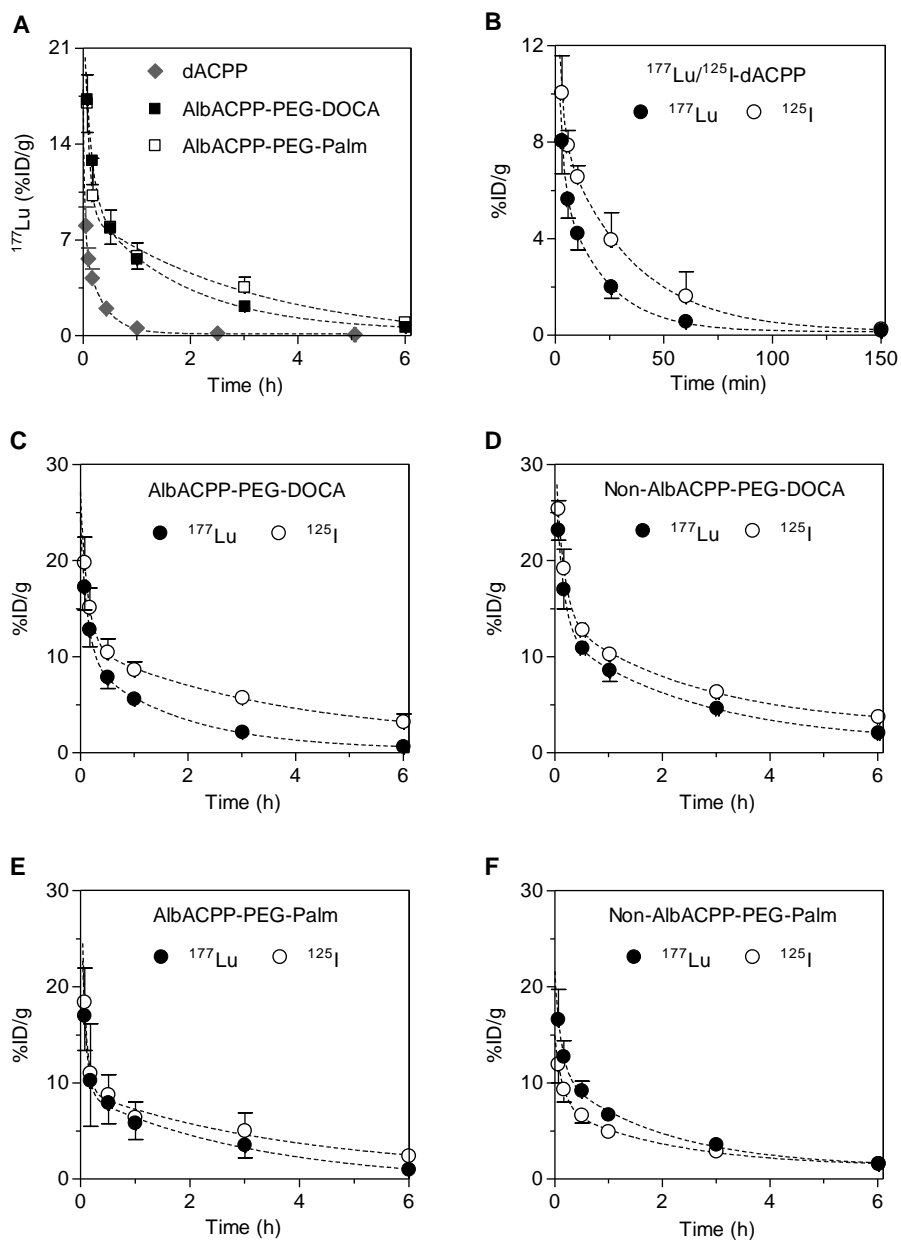
Figure 4.5: *Blood kinetic profiles of 10 nmol (A) ^{177}Lu-dACPP, ^{177}Lu-AlbACPP-PEG-DOCA, and ^{177}Lu-AlbACPP-PEG-Palm, (B) ^{177}Lu/^{125}I-dACPP (n=3), (C) ^{177}Lu/^{125}I-AlbACPP-PEG-DOCA (n=3), (D) ^{177}Lu/^{125}I-non-AlbACPP-PEG-DOCA (n=2), (E) ^{177}Lu/^{125}I-AlbACPP-PEG-Palm (n=3), and (F) ^{177}Lu/^{125}I-non-AlbACPP-PEG-Palm (n=2) in MI-mice. The data are presented as mean %ID/g ± SD. Blood kinetics were fitted with a 2-phase exponential decay function (see Table 4.1).*

Table 4.1: *Parameters for ^{177}Lu and ^{125}I blood kinetic profiles for $^{177}Lu/^{125}I$-dACPP, $^{177}Lu/^{125}I$-AlbACPP-PEG-DOCA, $^{177}Lu/^{125}I$-AlbACPP-PEG-Palm, $^{177}Lu/^{125}I$-non-AlbACPP-PEG-DOCA, and $^{177}Lu/^{125}I$-non-AlbACPP-PEG-Palm in mice 11 days post MI. Blood kinetics were fitted with the 2-phase exponential decay function $Y = span_1 \cdot exp(-K_1 \cdot X) + span_2 \cdot exp(-K_2 \cdot X) + Plateau$. The half-life is the time point at which the area under the fitted curved (AUC) reached 50% of the total AUC.*

	$Span_1$ (%ID/g)	K_1 (h^{-1})	$Span_2$ (%ID/g)	K_2 (h^{-1})	half-life (min)
^{177}Lu					
dACPP (n=3)	6.63	2.94	11.2	32.0	17
AlbACPP-PEG-DOCA (n=3)	9.51	0.57	14.6	7.68	87
AlbACPP-PEG-Palm (n=3)	9.26	0.31	24.4	14.0	95
Non-AlbACPP-PEG-DOCA (n=2)	11.5	0.39	18.1	7.16	150
Non-AlbACPP-PEG-Palm (n=2)	9.64	0.50	10.8	8.04	169
^{125}I					
dACPP (n=3)	8.63	1.85	9.30	30.0	25
AlbACPP-PEG-DOCA (n=3)	9.82	0.27	16.0	7.36	207
AlbACPP-PEG-Palm (n=3)	8.52	0.26	26.5	13.5	185
Non-AlbACPP-PEG-DOCA (n=2)	11.6	0.39	18.3	6.75	230
Non-AlbACPP-PEG-Palm (n=2)	6.22	0.48	7.44	6.64	220

Distribution in MI-hearts

A significantly higher uptake of ^{177}Lu-AlbACPP-PEG-DOCA was observed in infarcted areas (1.68 ± 0.34 %ID/g) of the heart compared to remote regions (0.25 ± 0.02 %ID/g) at 50h post-injection (p<0.01, Table 4.3). For the non-albumin binding probe ^{177}Lu-dACPP, a comparable biodistribution pattern was observed in infarct and remote areas at 20h post-injection; 1.43 ± 0.21 %ID/g and 0.23 ± 0.05 %ID/g, respectively (Chapter 3). Correspondingly, the infarct-to-remote ratios for both probes were in the similar range (6.5 ± 1.1 vs 6.6 ± 1.3 for ^{177}Lu-dACPP and ^{177}Lu-AlbACPP-PEG-DOCA, respectively). The negative control probe, ^{177}Lu-non-AlbACPP-PEG-DOCA (n=2), showed a 2.5-fold lower uptake in the infarcted region (0.66 ± 0.09 %ID/g) compared to ^{177}Lu-AlbACPP-PEG-DOCA (p<0.05), while for dACPP and non-dACPP, a 5.3-fold difference was observed. Analysis of the $^{177}Lu/^{125}I$ ratios revealed a significantly higher ratio in the infarcted area (3.5 ± 0.9) compared to remote areas (0.8 ± 0.1) for $^{177}Lu/^{125}I$-AlbACPP-PEG-DOCA (p<0.05). Furthermore, ^{177}Lu uptake and $^{177}Lu/^{125}I$ ratios for $^{177}Lu/^{125}I$-AlbACPP-PEG-DOCA correlated significantly with the MMP-2 levels (Fig. 4.6, Table 4.2), suggesting MMP mediated local activation of $^{177}Lu/^{125}I$-AlbACPP-PEG-DOCA in infarcted heart tissue. Interestingly, the observed $^{177}Lu/^{125}I$ ratios are several folds lower than observed for $^{177}Lu/^{125}I$-dACPP in both infarct and remote (22.2 ± 13.4 and 6.2 ± 0.8, respectively). For animals injected with $^{177}Lu/^{125}I$-AlbACPP-PEG-Palm (n=3), the hearts from two animals did not contain an infarct. The biodistribution results for these animals and for animals injected with the negative control $^{177}Lu/^{125}I$-non-AlbACPP-PEG-Palm (n=2) can be found in Table 4.4, but statistical analysis of these data was not be performed.
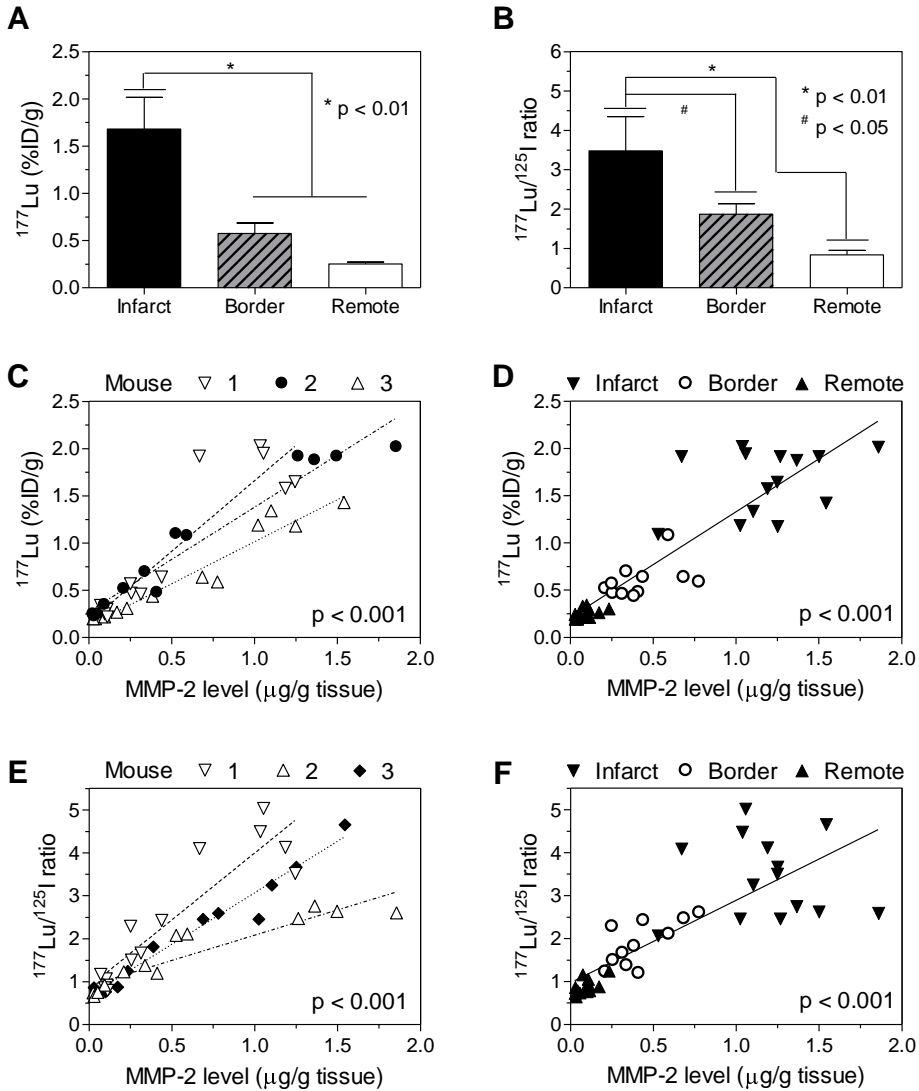
Figure 4.6: *(A) ^{177}Lu-biodistribution and (B) ^{177}Lu/^{125}I ratios of 10 nmol ^{177}Lu/^{125}I-AlbACPP-PEG-DOCA (n=3) in MI-mice at 50h post injection. Data are mean ± SD. (C) Intra-experimental and (D) inter-experimental correlation between MMP-2 level and ^{177}Lu uptake. (E) Intra-experimental and (F) inter-experimental correlation between MMP-2 level and ^{177}Lu-to-^{125}I ratios. Best fit parameters are shown in Table 4.2.*

Table 4.2: *Best fit parameters for linear regression analysis between MMP-2 levels and ^{177}Lu uptake, and between MMP-2 levels and ^{177}Lu/^{125}I ratios for ^{177}Lu/^{125}I-AlbACPP-PEG-DOCA (n=3) in hearts of MI-mice 5h post injection. Parameters slope and Pearson correlation coefficient r are listed.*

AlbACPP-PEG-DOCA	Intra-experimental				Inter-experimental
	Mouse 1	Mouse 2	Mouse 3		(n=3)
^{177}Lu					
Pearon r	0.97	0.92	0.97		0.82
Slope	0.89 ± 0.07	1.49 ± 0.19	1.10 ± 0.08		1.12 ± 0.09
^{177}Lu/^{125}I-ratio					
Pearson r	0.98	0.92	0.93		0.81
Slope	2.40 ± 0.15	3.12 ± 0.39	1.17 ± 0.14		1.92 ± 0.23

Table 4.3: *Biodistribution results of 10 nmol ^{177}Lu/^{125}I-AlbACPP-PEG-DOCA (n=3) and ^{177}Lu/^{125}I-non-AlbACPP-PEG-DOCA (n=2) in MI-mice 50h post injection. Data are presented as mean ± SD.*

50h	^{177}Lu/^{125}I-AlbACPP-PEG-DOCA (n=3)			^{177}Lu/^{125}I-non-AlbACPP-PEG-DOCA		
	^{177}Lu (%ID/g)	^{125}I (%ID/g)	Ratio ^{177}Lu/^{125}I	^{177}Lu (%ID/g)	^{125}I (%ID/g)	Ratio ^{177}Lu/^{125}I
Blood	0.01 ± 0.00	0.06 ± 0.01	0.19 ± 0.04	0.04 ± 0.04	0.10 ± 0.03	0.40 ± 0.33
Heart, infarct	1.68 ± 0.34	0.51 ± 0.21	3.48 ± 0.87	0.66 ± 0.09	0.65 ± 0.08	1.02 ± 0.00
Heart, border	0.58 ± 0.11	0.32 ± 0.11	1.87 ± 0.27	0.24 ± 0.01	0.29 ± 0.05	0.85 ± 0.09
Heart, remote	0.25 ± 0.02	0.30 ± 0.03	0.84 ± 0.11	0.19 ± 0.00	0.27 ± 0.01	0.70 ± 0.04
Muscle	0.30 ± 0.19	0.14 ± 0.05	2.12 ± 0.78	0.09 ± 0.00	0.10 ± 0.01	0.91 ± 0.61
Lung	0.54 ± 0.18	0.30 ± 0.06	1.74 ± 0.23	0.60 ± 0.45	0.54 ± 0.38	1.07 ± 0.09
Spleen	2.20 ± 1.24	0.37 ± 0.22	6.18 ± 1.93	0.72 ± 0.11	1.04 ± 0.31	0.70 ± 0.10
Liver	23.2 ± 3.22	3.13 ± 0.60	7.46 ± 0.57	6.96 ± 0.40	5.22 ± 0.33	1.33 ± 0.01
Kidney	66.0 ± 21.5	5.03 ± 2.23	13.8 ± 2.51	119.7 ± 28.7	15.9 ± 2.34	7.48 ± 0.71
Fat	0.27 ± 0.13	0.25 ± 0.12	1.11 ± 0.01	0.20 ± 0.11	0.29 ± 0.22	0.74 ± 0.19
Thigh bone	2.29 ± 0.38	0.55 ± 0.35	4.96 ± 2.02	0.40 ± 0.01	0.27 ± 0.04	1.49 ± 0.18
Brain	0.01 ± 0.00	0.01 ± 0.00	ND	0.01 ± 0.00	0.01 ± 0.00	ND
Stomach, full*	0.10 ± 0.02	0.15 ± 0.05	ND	0.06 ± 0.01	0.24 ± 0.05	ND
Intestine, full*	0.28 ± 0.02	0.25 ± 0.03	ND	0.14 ± 0.01	0.44 ± 0.11	ND
Thyroid*	0.06 ± 0.04	0.79 ± 0.69	ND	0.02 ± 0.01	1.25 ± 1.72	ND

* expressed in %ID

Table 4.4: *Biodistribution results of 10 nmol ^{177}Lu/^{125}I-AlbACPP-PEG-Palm (n=3) and ^{177}Lu/^{125}I-non-AlbACPP-PEG-Palm (n=2) in MI-mice 50h post injection. Data are presented as mean ± SD.*

50h	^{177}Lu/^{125}I-AlbACPP-PEG-Palm			^{177}Lu/^{125}I-non-AlbACPP-PEG-Palm		
	^{177}Lu (%ID/g)	^{125}I (%ID/g)	Ratio ^{177}Lu/^{125}I	^{177}Lu (%ID/g)	^{125}I (%ID/g)	Ratio ^{177}Lu/^{125}I
Blood	0.01 ± 0.00	0.08 ± 0.02	0.16 ± 0.00	0.02 ± 0.01	0.11 ± 0.02	0.19 ± 0.03
Heart, infarct#	1.04	0.75	1.40	0.95 ± 0.43	0.52 ± 0.25	1.83 ± 0.05
Heart, remote	0.37 ± 0.04	0.40 ± 0.04	0.92 ± 0.05	0.33 ± 0.04	0.24 ± 0.05	1.42 ± 0.14
Muscle	0.20 ± 0.06	0.16 ± 0.03	1.18 ± 0.18	0.14 ± 0.01	0.09 ± 0.02	1.51 ± 0.15
Lung	0.50 ± 0.07	0.39 ± 0.03	1.25 ± 0.10	1.75 ± 1.74	3.14 ± 3.30	0.59 ± 0.07
Spleen	2.92 ± 0.56	2.21 ± 0.35	1.32 ± 0.06	5.80 ± 2.59	10.5 ± 1.17	0.54 ± 0.19
Liver	35.0 ± 1.88	18.4 ± 2.27	1.91 ± 0.12	35.6 ± 5.49	22.1 ± 3.55	1.61 ± 0.01
Kidney	21.0 ± 2.61	6.95 ± 1.42	3.06 ± 0.24	25.8 ± 2.91	4.32 ± 1.23	6.32 ± 2.47
Fat	0.34 ± 0.20	0.35 ± 0.18	0.95 ± 0.09	0.66 ± 0.68	0.36 ± 0.34	1.67 ± 0.32
Thigh bone	1.27 ± 0.18	0.62 ± 0.07	2.06 ± 0.07	1.53 ± 0.04	1.21 ± 0.29	1.29 ± 0.28
Brain	0.01 ± 0.00	0.01 ± 0.00	ND	0.01 ± 0.00	0.01 ± 0.00	ND
Stomach, full*	0.11 ± 0.03	0.19 ± 0.07	ND	0.14 ± 0.04	0.18 ± 0.07	ND
Intestine, full*	0.74 ± 0.28	0.60 ± 0.17	ND	0.52 ± 0.01	0.35 ± 0.09	ND
Thyroid*	0.04 ± 0.02	1.35 ± 1.57	ND	0.03 ± 0.01	0.04 ± 0.03	ND

* expressed in %ID, # n = 1

Discussion

The present study focused on the development of long-circulating activatable peptide probes for the detection of MMP-2/9 in cardiac remodeling *in vivo*. In Chapter 3, an MMP-2/9 activatable cell penetrating imaging probe (dACPP) was characterized that displayed a short blood half life of ~17 min. To further improve the retention of the imaging probe in infarcted regions, we aimed for a longer exposure time of the probe to its target protease by introducing albumin binding ligands into the peptide probes. Albumin, the most abundant protein in serum, is too large to be cleared by the kidneys and functions as a carrier for a wide-range of molecules *in vivo*. Albumin-targeted probes have been reported to show enhanced circulation times. Here, we aimed for imaging probes that display non-covalent albumin binding, thereby enabling dissociation of these probes from albumin and potential extravasation from the vasculature into areas of extracellular matrix remodeling. Two albumin binding MMP-2/9 sensitive ACPPs (AlbACPP-PEG-DOCA and AlbACPP-PEG-Palm) were developed, containing either an intermediate affinity albumin ligand, deoxycholic acid (DOCA), or a high affinity albumin ligand, palmitic acid (Palm).

In vitro, AlbACPP-PEG-DOCA showed a similar cleavage rate for MMP-2 as dACPP in the presence of human serum albumin, while the cleavage rate of AlbACPP-PEG-Palm was significantly lower. In these experiments, the albumin unbound probe fractions were determined to be <0.01% for AlbACPP-PEG-Palm, and 2.0% for AlbACPP-PEG-DOCA. Above calculations are based on the albumin concentration and reported equilibrium binding constants of palmitic acid and deoxycholic acid for bovine serum albumin. Notably, it has been reported that the binding affinity of albumin ligands for serum albumins is species dependent (19). In the *in vitro* and *in vivo* experiments, human serum albumin and mouse serum albumin were respectively the albumin species of interest, and this may have influenced the unbound probe fraction. Albumin consists of respectively four and seven high affinity binding pockets for deoxycholic acid and palmitic acid (20,21) and as such different pockets may be involved in binding. Therefore, the accessibility of the MMP-2/9 cleavable site may be different for both probes once bound to albumin. Experiments comparing AlbACPP-PEG-Palm and AlbACPP-Palm, showed a higher MMP-2 sensitivity for AlbACPP-PEG-Palm, which suggest an improved accessibility of the MMP-2/9 cleavage site as a result of the introduction of the PEG$_6$ linker.

In vivo experiments in a mouse model of myocardial infarction showed that both AlbACPPs are characterized by a more than 5-fold enhancement in blood half life compared to dACPP. The elongated blood circulation time is most likely caused by a reduction in renal clearance due to albumin binding. Another property of the albumin ligands, that is micelle formation in aqueous solutions, is not expected to have influenced the circulation time as the initial blood concentration of the AlbACPP probes is >1000-fold below the critical micelle concentration (2-5 mM range) for bile acid derivatives and palmitic acid (20,22). AlbACPP-PEG-Palm showed a slightly longer blood half life compared to AlbACPP-PEG-DOCA. Furthermore, the calculated volume of distributions suggest that extravasation from the vasculature did not occur for AlbACPP-PEG-Palm, but did happen for AlbACPP-PEG-DOCA to a certain extent. Due to its high molecular weight of 66 kDa, albumin by itself shows a low transfer rate from

plasma to interstitial compartments (21). Calculation of the *in vivo* albumin unbound probe fraction revealed percentages of <0.01% for AlbACPP-PEG-Palm, and 3.3% for AlbACPP-PEG-DOCA. The differences in albumin affinity and corresponding unbound probe fraction, and also the higher proteolytic degradation for AlbACPP-DOCA, will likely have contributed to the differences observed in circulation time and free volume-of-distribution for AlbACPP-PEG-Palm and AlbACPP-PEG-DOCA.

The strong affinity of palmitic acid for albumin leads to severely limited extravascular biodistribution of this probe. Modification of the albumin targeting residue in AlbACPP-PEG-Palm may allow optimization of the balance between albumin dissociation and potential extravasation on one hand and circulation time on the other hand. For example, leaving out the γ-Glu spacer and/or decreasing the length of the acyl chain will result in a decreased albumin affinity (6).

Although ^{177}Lu-AlbACPP-PEG-DOCA showed a prolonged circulation time compared to ^{177}Lu-dACPP, the accumulation of these probes in infarcted myocardium is comparable. In this respect, the restricted extravasation from the circulation of AlbACPP-PEG-DOCA as suggested by its volume of distribution, may have reduced the effective concentration of this probe in the remodeling myocardium, resulting in a lower degree of MMP-2/9 facilitated activation. Nevertheless, the ^{177}Lu-to-^{125}I ratio for AlbACPP-PEG-DOCA in infarcted myocardium was higher compared to remote myocardium, suggesting infarct specific activation. Another notable observation is the higher uptake in the infarcted myocardium of the negative control probe ^{177}Lu-non-AlbACPP-PEG-DOCA compared to ^{177}Lu-non-dACPP, whereas the uptake for ^{177}Lu-AlbACPP-PEG-DOCA and ^{177}Lu-dACPP were similar. Moreover, the AlbACPP probes showed a higher level of ^{125}I in most tissues and lower ^{177}Lu-to-^{125}I ratios compared to dACPP. Following extravasation into the interstitial space the AlbACPP probes may have bound to interstitial albumin, resulting in the entrapment of the ^{125}I label in all tissues. Alternatively, next to binding to albumin, palmitic acid and deoxycholic acid can directly interact with cellular membranes potentially leading to (endothelial) cellular tagging that may result in accumulation of the imaging probe in all tissues (23). Specifically, probe activation in the vasculature or ECM will result in the release of the ^{177}Lu-CPP fragment that is expected to penetrate the cells. For AlbACPPs the released ^{125}I labeled fragment will maintain its tissue retention and/or cellular tagging property due to the presence of the albumin ligand whereas the released ^{125}I labeled fragment for dACPP showed strong tissue clearance and subsequent kidney accumulation. Furthermore, changes in microvascular integrity may have facilitated albumin-probe leakage from the circulation into the infarcted myocardium. Myocardial infarction typically results in myocyte necrosis and subsequent damage to the microvasculature leading to enhanced vascular permeability (9). These properties may explain both the high levels of ^{125}I in all tissues and increased uptake of the negative control in infarcted myocardium.

Unfortunately, the hearts from two animals injected with ^{177}Lu/^{125}I-AlbACPP-PEG-Palm, did not contain an infarct. Therefore, more experiments are needed to discuss the biodistribution of this particular probe in the MI-heart.

The *in vivo* biodistribution experiments further demonstrated high liver uptake of AlbACPP-PEG-Palm, while AlbACPP-PEG-DOCA showed strong accumulation in the kidneys. Both palmitic acid and bile acids such as deoxycholic acid are known to be efficiently taken up by hepatocytes (24-26). The observed discrepancy might be caused by the conjugation of a relatively large ACPP peptide to the albumin ligands. It has been suggested that bile acid transporters display a strongly reduced efficiency in cellular uptake of bile acid – peptide conjugates containing more than five amino acids (22), which may explain the reduced liver uptake of AlbACPP-PEG-DOCA. Alternatively, in its albumin unbound form, the probes are expected to be filtered from the circulation by the kidneys. The higher unbound probe fraction for AlbACPP-PEG-DOCA compared to AlbACPP-PEG-Palm may suggest a more effective kidney uptake/excretion of this probe.

Conclusion

The circulation time of ACPP peptide probes was efficiently enhanced via *in vivo* protein binding using the albumin ligands deoxycholic acid or palmitic acid. *In vitro* experiments demonstrated a reduced protease sensitivity for AlbACPP-PEG-Palm, but not for AlbACPP-PEG-DOCA compared to the parent dACPP probe. Despite the increased circulation time, biodistribution in MI-hearts did not show improvements for AlbACPP-PEG-DOCA compared to dACPP. Therefore, dACPP, characterized by a short circulation time, is favored over AlbACPPs for imaging studies.

Materials and methods

Materials

All reagents and solvents were obtained from commercial sources (Sigma-Aldrich, and Biosolve) and used without further purification. 9-fluorenylmethyloxycarbonyl (Fmoc)-protected amino acids and Rink amide resin were purchased from either Novabiochem (Merck) or Iris Biotech. DOTA succinimidyl ester was obtained from Macrocyclics. Human recombinant MMP-2 was purchased from Calbiochem (Merck).
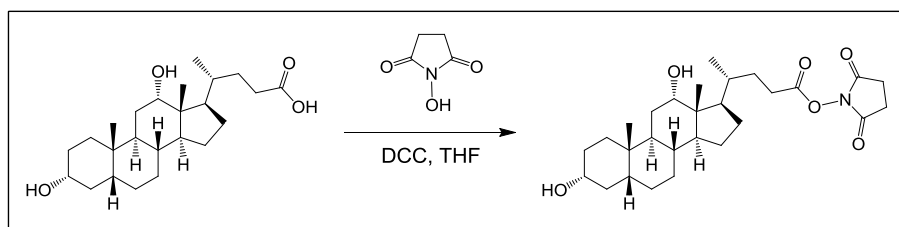
Scheme 4.1: *Synthesis of deoxycholate succinimidyl ester*

Synthesis of deoxycholate succinimidyl ester (Scheme 4.1).

Deoxycholate (1.0 g, 2.54 mmol) and N-Hydroxysuccinimide (292 mg, 2.54 mmol) were dissolved in anhydrous Tetrahydrofuran (THF, 50 mL) and N,N'-Dicyclohexylcarbodiimide (DCC, 520 mg, 2.54 mmol) was added at 4 °C and stirred for 30 min. The mixture was subsequently reacted at room temperature for 20h under nitrogen, after which the precipitated dicyclohexylurea was removed by filtration. Deoxycholate succinimidyl ester (DOCA-NHS) was obtained by flash silica gel column chromatography of the filtrate in a yield of 68% (850 mg, 1.74 mmol) and stored at -20 °C under nitrogen.

Probe synthesis

Peptides Fmoc-e*-e$_9$-*x*-PLGLAG-r$_9$-*x*-k(Mtt)-resin, Fmoc-e*-PEG$_6$-k(Boc)-e$_9$-*x*-PLGLAG-r$_9$-*x*-k(Mtt)-resin, and Fmoc-e*-PEG$_6$-k(Boc)-e$_9$-*x*-LALGPG-r$_9$-*x*-k(Mtt)-resin were synthesized on an automatic synthesizer (Prelude, Protein Technologies Inc.) by Fmoc solid-phase peptide synthesis (SPPS) using Rink amide resin (0.1 mmol), HBTU as the activating reagent, and N,N-Diisopropylethylamine (DIPEA) as base. D-amino acids are denoted in lower case, *x* represents 6-aminohexanoic acid, and Fmoc-d-Glu-OtBu was used as building block for e*. The peptides were splitted 50%:50%, incubated in 20% piperidine for 2x 5 min to remove the N-terminal Fmoc and subsequently reacted with Palmitic acid-NHS (3.0 equiv) and DOCA-NHS (3.0 equiv), respectively, in NMP overnight in the presence of DIPEA. The Mtt protecting group was selectively removed by incubating the peptides on resin with 1.8% v/v trifluoroacetic acid (TFA) in dichloromethane with 2.0% v/v tri-isopropylsilane (TIS) as scavenger for 10 x 3 min after which DOTA succinimidyl ester (4.0 equiv) in NMP was added to the peptide resins and was reacted for 1.5h in the presence of DIPEA. The peptides were cleaved from the resin by a mixture of 96.0% v/v trifluoroacetic acid (TFA), 2.0% v/v tri-isopropyl silane (TIS), and 2.0% v/v MilliQ (Millipore) water for 4h, filtered, and precipitated in ice cold diethylether. The peptide pellets were dissolved in MilliQ water and purified by preparative reversed-phase high pressure liquid chromatography (RP-HPLC) using an Agilent 1200 apparatus, equipped with a C18 Zorbax column (length = 150 mm, diameter = 21.2 mm, particle size = 5.0 µm). The UV wavelength was preset at 210 and 254 nm. All peptides structures were analyzed by LC-MS on an Agilent 1200 apparatus, equipped with a C18 Eclipse plus-column (length = 100 mm, diameter = 2.1 mm, particle size = 3.5 µm) and an electrospray mass spectrometer (Agilent Technologies 6210, Time-of-Flight LC/MS). Peptides DOCA-e*-PEG$_6$-k-e$_9$-*x*-PLGLAG-r$_9$-*x*-k(DOTA)-NH$_2$, DOCA-e*-PEG$_6$-k-e$_9$-*x*-LALGPG-r$_9$-*x*-k(DOTA)-NH$_2$, Palm-e*-PEG$_6$-k-e$_9$-*x*-PLGLAG-r$_9$-*x*-k(DOTA)-NH$_2$, and Palm-e*-PEG$_6$-k-e$_9$-*x*-LALGPG-r$_9$-*x*-k(DOTA)-NH$_2$ were reacted with 3-(4-hydroxyphenyl)propionic acid (SHPP) *N*-hydroxysuccinimide ester (10 equiv) in

DMF in the presence of DIPEA overnight, after which the peptides were purified by RP-HPLC, and analyzed by LC-MS.

Found masses: 4335.4 Da for DOCA-e*-e$_9$-x-PLGLAG-r$_9$-x-k(DOTA)-NH$_2$ (AlbACPP-DOCA, Calcd. 4335.4 Da), 4946.8 Da for DOCA-e*-PEG$_6$-k(SHPP)-e$_9$-x-PLGLAG-r$_9$-x-k(DOTA)-NH$_2$ (AlbACPP-PEG-DOCA, Calcd. 4946.7 Da, 2.7 µmol), 4946.8 Da for DOCA-e*-PEG$_6$-k(SHPP)-e$_9$-x-LALGPG-r$_9$-x-k(DOTA)-NH$_2$ (non-AlbACPP-PEG-DOCA, Calcd. 4946.7 Da, 2.0 µmol), 4199.4 Da for Palm-e*-e$_9$-x-PLGLAG-r$_9$-x-k(DOTA)-NH$_2$ (ACPP-Palm, Calcd. 4199.3 Da), 4810.8 Da for Palm-e*-PEG$_6$-k(SHPP)-e$_9$-x-PLGLAG-r$_9$-x-k(DOTA)-NH$_2$ (AlbACPP-PEG-Palm, Calcd. 4810.7 Da, 5.4 µmol), and 4810.8 Da for Palm-e*-PEG$_6$-k(SHPP)-e$_9$-x-LALGPG-r$_9$-x-k(DOTA)-NH$_2$ (non-AlbACPP-PEG-Palm, Calcd. 4810.7 Da, 4.7 µmol).

Animal studies

All animal procedures were approved by the ethical review committee of the Maastricht University Hospital (The Netherlands), and were performed according to the principles of laboratory animal care (NIH publication 85-23, revised 1985) (27), and the Dutch national law "Wet op Dierproeven" (Stb 1985, 336). Male Swiss mice (body weight >25g, Charles River Labs) were housed in an enriched environment under standard conditions: 21-23 °C, 50-60% humidity, and 12h-lightdark-cycles for >1 week. Food and water were freely available.

Myocardial infarction (MI) model

MI was induced by permanent ligation of the left anterior descending coronary artery (LAD) using published procedures (28). In short, animals were subcutaneously injected with buprenorphine (0.1 mg/kg) and 30 min later anesthetized with isoflurane. Animals were intubated and ventilated with 100% oxygen with a rodent respirator. After left thoracotomy between ribs four and five, the LAD was ligated with a 6-0 prolene suture. The chest and skin were closed with 5-0 silk sutures. The animal's temperature was continuously measured rectally and maintained at 36.5–37.5 °C during surgery. After surgery, animals were allowed to recover at 30 °C overnight. 11 days post myocardial infarction, the animals were used for *in vivo* studies.

Radiolabeling

For in vitro studies: ^{177}LuCl$_3$ (PerkinElmer) in 0.05 M HCl (2.0 µL, 10.0 MBq) was mixed with dACPP, AlbACPP-PEG-DOCA, AlbACPP-PEG-Palm, AlbACPP-DOCA, or AlbACPP-Palm in MilliQ water (~3.0 µL, 23 nmol) and metal-free 0.9% NaCl for 20 min at 600 rpm and 90°C (final volume 80.0 µL). *For in vivo studies:* ^{177}LuCl$_3$ in 0.05 M HCl (3.0 µL, 15.0 MBq) was mixed with AlbACPP-PEG-DOCA, AlbACPP-PEG-Palm, non-AlbACPP-PEG-DOCA, or non-AlbACPP-PEG-Palm in MilliQ water (2.4 µL, 15 nmol) and metal-free 0.9% NaCl (144.6 µL) for 20 min at 600 rpm and 90°C. ^{125}I (PerkinElmer) in 1 mM NaOH (3.0 µL, 6.0 MBq) was mixed with AlbACPP-PEG-DOCA, AlbACPP-PEG-Palm, non-AlbACPP-PEG-DOCA, or non-AlbACPP-PEG-Palm in MilliQ water (2.4 µL, 15 nmol) and PBS (144.6 µL) in an IODOGEN iodination tube for 20 min at 600 rpm and 23°C and transferred to a siliconized 1.5-mL tube. The ^{177}Lu and ^{125}I labeling yields were determined by radio-thin layer chromatography, using instant thin-layer chromatography silica gel strips (Pall) eluted with 200 mM EDTA in 0.9% NaCl and 20 mM citric acid at pH 5.2, respectively, and imaged on a phosphor imager (FLA-7000; Fujifilm) and quantified with AIDA Image Analyzer software. Analytic radio-HPLC was performed on an Agilent 1100 system equipped with a C18 Eclipse XBD column (length

= 150 mm, diameter = 4.6 mm, particle size = 5.0 μm) and a Gabi radioactive detector (Raytest). The radiochemical purities were 95% or higher. The ^{177}Lu-labeled peptides were mixed with the ^{125}I-labeled peptides in a 1:1 molar ratio.

In vitro MMP-2 sensitivity in presence of human serum albumin

[177]Lu-dACPP, ^{177}Lu-AlbACPP-PEG-DOCA, ^{177}Lu-AlbACPP-DOCA, ^{177}Lu-AlbACPP-PEG-Palm, and ^{177}Lu-AlbACPP-Palm (21.8 μL) were mixed in triplicate with 5.0% w/v human serum albumin, 50 mM Tris, 200 mM NaCl, 10 mM $CaCl_2$ and 10 μM $ZnCl_2$ (225 μL) at pH 7.5 at 600 rpm and 37 °C. After 20 min, 3.2 μL human recombinant MMP-2 was added (final conditions: 25.0 μM peptide, 18.0 nM MMP-2, 4.5% w/v HSA (0.67 mM) in 250 uL). At seven different time points (4, 8, 15, 30, 60, 120, and 245 min) 28 μL of the reaction mixtures was incubated with 2.0 μL GM6001 (from 50 mM stock in DMSO) to block MMP-2 activity, and subsequently analyzed by γ-HPLC to determine the percentage cleaved peptide.

Because of the >25-fold lower concentrations of the AlbACPP probes relative to HSA and the presence of multiple binding sites per protein molecule (20,21), it was assumed that the binding capacity of albumin was far from saturated. Therefore, the unbound probe fraction, α, was calculated from $α = 1/(1 + C_a \cdot K_a)$, where C_a is the total concentration of albumin and K_a is the equilibrium binding constant (14,15).

Blood kinetic measurements and biodistribution experiments

Blood kinetic and biodistribution experiments were performed on MI-mice by i.v.-injection of ^{177}Lu/^{125}I-dACPP (n=3), ^{177}Lu/^{125}I-AlbACPP-PEG-DOCA (n=3), ^{177}Lu/^{125}I-AlbACPP-PEG-Palm (n=3), ^{177}Lu/^{125}I-non-AlbACPP-PEG-DOCA (n=2), or ^{177}Lu/^{125}I-non-AlbACPP-PEG-Palm (n=2) (10 nmol/100 μL, ca. 5.0 MBq ^{177}Lu, ca. 2.0 MBq ^{125}I). At selected time points (2, 5, 10, 30, 60, and 150 min for dACPP, and 4, 10, 30, 60, 180, and 360 min for the other probes), blood samples were withdrawn from the vena saphena, weighed, and diluted to 1 mL with MilliQ water. The mice were anesthetized with isoflurane 5h or 50h after i.v.-injection, subjected to 2% (w/v) Evans Blue i.v.-injection (50 mg/kg) and sacrificed 2 min later by cervical dislocation. Organs and tissues of interest were harvested and weighed, after which the radioactivity of the samples was measured in a γ-counter (Wizard 1480; PerkinElmer) along with standards to determine the injected dose per gram (%ID/g). The energy windows were set to 10-80 keV for ^{125}I and 155-380 keV for [177]Lu. The blood clearance data was fitted to a 2-phase exponential decay: $Y = span_1 \cdot exp(-K_1 \cdot X) + span_2 \cdot exp(-K_2 \cdot X) + Plateau$ using GraphPad Prism. The area under the curve (AUC) was determined for the fitted ^{177}Lu blood kinetic profiles for all probes. The half-lives, the time points at which the AUC reaches 50% of the total AUC, was subsequently derived using MatLab. The volume of distribution per probe was calculated using the formula $V_D = dose/(mean body weight \cdot C_0)$ [L/kg]. Because of the ~100-fold lower concentrations of AlbACPP-PEG-Palm and AlbACPP-PEG-DOCA (~3-4 μM) relative to mouse serum albumin (0.4 mM (29)) and the presence of multiple binding sites per protein molecule (19,20), it was assumed that the binding capacity of albumin was far from saturated. Therefore, the unbound probe fraction, α, was calculated from $α = 1/(1 + C_a \cdot K_a)$, where C_a is the total concentration of albumin and K_a is the equilibrium binding constant (14,15).

The hearts were cooled to 4 °C, cut in 1 mm slices from apex to base. Infarct, border, and remote areas were isolated based on Evans Blue staining, and %ID/g for ^{125}I and ^{177}Lu was determined by

a γ-counter. The hearts from two animals injected with $^{177}Lu/^{125}I$-AlbACPP-PEG-Palm, did not contain an infarct, but only a local infection area, as was assessed by ex vivo analysis.

Sample preparation, tissue homogenates.

After γ-counting, tissue samples were homogenized in 20 volumes of 50 mM Tris, 200 mM NaCl, 10 mM $CaCl_2$, and 10 µM $ZnCl_2$ at pH 7.5 at 4 °C at 25 Hz for 2 × 5 min and subsequently mixed at 5 Hz for 2 × 15 min using a tissue lyser (Qiagen), and then centrifuged at 5,000 rpm for 5 min at 4 °C. The supernatants were aliquoted and stored at -80 °C until zymography analysis. Typically, 14 µL tissue supernatant (from 0.7 mg tissue homogenate) was used per analysis.

Gelatin zymography

Samples were analyzed on 10% SDS-PAGE gel containing 0.1% (w/v) gelatin (Biorad). MMP-2 (Calbiochem, Merck) (0.21 ng) was loaded as an internal standard used to normalize activities between gels. Electrophoresis was performed at 150V for 1.5h, after which the gels were washed with MilliQ water, incubated for 3 × 20 min in 2.5% Triton-X (50 rpm) to remove SDS, washed with MilliQ water, and incubated in 50 mM Tris, 200 mM NaCl, 5 mM $CaCl_2$, 0.1% (w/v) NaN_3, and 0.02% (w/v) Brij-35 at pH 7.6 and 37 °C for 2 days. Gels were stained for 2h with 0.25% Coomassie Blue in 60% (v/v) MilliQ water, 30% (v/v) Methanol, 10% (v/v) Acetic acid, and destained for > 24h with 67.5% (v/v) MilliQ water, 25% (v/v) Methanol, 7.5% (v/v) Acetic acid. Gelatinatic activity showed up as clear bands against a dark background. Zymograms were imaged (Epson Perfection V700 Photo scanner) and band intensities were quantified using ImageJ.

Statistical methods

Quantitative data were expressed as mean ± SD. The means of the groups were compared by the parametric Welch's t test. All tests were one-tailed, and P values of less than 0.05 indicate significant differences. GraphPad Prism was used for all statistical calculations.

References

1. Roberts MJ, Bentley MD, and Harris JM. Chemistry for Peptide and Protein PEGylation. *Adv Drug Del Rev.* 2002;54:459-476

2. Liu J, Liu J, Chu L, et al. Novel Peptide-Dendrimer Conjugates as Drug Carriers for Targeting Nonsmall Cell Lung Cancer. *Int J Nanomedicine* 2011;6:59-69

3. Woodle MC, Storm G, Newmann MS, et al. Prolonged Systemic Delivery of Peptide Drugs by Long-Circulating Liposomes: Illustration with Vasopressin in the Brattleboro Rat. *Pharm Res.* 1992;9:260-265

4. Kurtzhals P, Havelund S, Jonassen I, et al. Albumin Binding of Insulins Acylated with Fatty Acids: Characterization of the Ligand-Protein Interaction and Correlation Between Binding Affinity and timing of the Insulin Effect in Vivo. *Biochem J.* 1995;312:725-731

5. Koehler MFT, Zobel K, Beresini MH, et al. Albumin Affinity Tags Increase Peptide Half-life in Vivo. *Bioorg Med Chem Lett.* 2002;12:2883-2886

6. Madsen K, Knudsen LB, Agersoe H, et al. Structure-Activity and Protraction Relationship of Long-Acting Glucagon-like Peptide-1 Derivatives: Importance of Fatty Acid Length, Polarity, and Bulkiness. *J Med Chem.* 2007;50:6126-6132

7. Ahrén B, and Burke B. Using Albumin to Improve the Therapeutic Properties of Diabetec Treatments. *Diabetes Obes Metab.* 2012;14:121-129

8.   van Duijnhoven SMJ, Robillard MS, Nicolay K, et al. Tumor Targeting of MMP-2/9 Activatable Cell-Penetrating Imaging Probes Is Caused by Tumor-Independent Activation. *J Nucl Med.* 2011;52:279-286

9.   Kloner RA, Rude RE, Carlson N, et al. Ultrastructural evidence of microvascular damage and myocardial cell injury after coronary artery occlusion: which comes first? *Circulation*. 1980;62:945–952

10.   Ballmer PE. Causes and mechanisms of hypoalbuminaemia. *Clin Nutr.* 2001;20:271-273

11.   Martin VV, Ralston WH, Hynes MR, et al. Gadolinium(III) Di- and Tetrachelates Designed for in Vivo Noncovalent Complexation with Plasma Proteins: A Novel Molecular Design for Blood Pool MRI Contrast Enhancing Agents. *Bioconjug Chem.* 1995;6:616-623

12.   de Häen C, Anelli PL, Lorusso V, et al. Gadocoletic Acid Trisodium Salt (B22956/1): A New Blood Pool Magnetic Resonance Contrast Agent With Application in Coronary Angiography. *Inv Radiol.* 2006;41:279-291

13.   Caravan P, Parigi G, Chasse JM, et al. Albumin Binding, Relaxivity, and Water Exchange Kinetics of the Diastereoisomers of MS-325, a Gadolinium(III)-Based Magnetic Resonance Angiography Contrast Agent. *Inorg Chem.* 2007;46:6632-6639

14.   Wallace RA, Haar JP Jr, Miller DB, et al. Synthesis and Preliminary Evaluation of MP-2269: A Novel, Nonaromatic Small-Molecule Blood-Pool MR Contrast Agent. *Magn Reson Med.* 1998;40:733-739

15.   Elmadhoun BM, Wang GQ, Templeton JF, et al. Binding of [^{3}H]palmitate to BSA. *Am J Physiol Gastrointest Liver Physiol.* 1998;275:G638-644

16.   Pond SM, Davis CKC, Bogoyevitch MA, et al. Uptake of palmitate by hepatocyte suspensions: facilitation by albumin? *Am J Physiol Gastrointest Liver Physiol.* 1992;262:G883-G894

17.   Riches AC, Sharp JG, Brynmor Thomas D, et al. Blood Volume Determination in the Mouse. *J Physiol.* 1973;228:279-284

18.   Durbin PW, Jeung N, Kullgren B, et al. Gross Composition and Plasma and Extracellular Water Volumes of Tissues of a Reference Mouse. *Health Phys.* 1992;63:427–442

19.   Basken NE, Mathias CJ, Lipka AE, et al. Species dependence of [^{64}Cu]Cu-Bis(thiosemicarbazone) radiopharmaceutical binding to serum albumins. *Nucl Med Biol.* 2008;35:281-286

20.   Makino S, Reynolds JA, and Tanford C. The binding of deoxycholate and triton-X-100 to proteins. *J Biol Chem.* 1973;248:4926-4932

21.   van de Vusse, GJ. Albumin as fatty acid transporter. *Drug Metab Pharmacokinet.* 2009;24:300-307

22.   Swaan PW, Hillgren KM, Szoka FC, et al. Enhanced transepithelial transport of peptides by conjugation to cholic acid. *Bioconjug Chem.* 1997;8:520-525

23.   Cobos-Correa A, Trojanek JB, Diemer S, et al. Membrane-Bound FRET Probe Visualizes MMP12 Activity in Pulmonary Inflammation. *Nat Chem Biol.* 2009;5:628-630

24.   Dawson PA, Lan T, and Rao A. Bile acid transporters. *J Lipid Res.* 2009;50:2340-2357

25.   Accattino L, and Simon FR. Identification and characterization of a bile acid receptor in isolated liver surface membranes. *J Clin Invest.* 1976;57:496-508

26.   Weisiger R, Gollan J, and Ockner R. Receptor for albumin on the liver cell surface may mediate uptake of fatty acids and other albumin-bound substances. *Science.* 1981;211:1048-1051

27.   *Guide for the Care and Use of Laboratory Animals*. Washington, DC: Government Printing Office; 1985. NIH publication 86-23

28.   Lutgens E, Daemen M, de Muinck ED, et al. Chronic myocardial infarction in the mouse: cardiac structural and functional changes. *Cardiovasc Res.* 1999;41:586–593

29.   Peeples ES, Schopfer LM, Duysen EG, et al. Albumin, a new biomarker of organophosphorus toxicant exposure, identified by mass spectrometry. *Tox Sci.* 2005;83:303-312

Chapter **5**

Development of radiolabeled matrix metalloproteinase-14 activatable cell penetrating peptides

Abstract

Matrix metalloproteinase-14 (MMP-14 or MT1-MMP) belongs to the membrane-type (MT) MMP subfamily, and plays an important role in adverse cardiac remodelling. Here, we aimed to develop radiolabeled activatable cell penetrating peptides (ACPP) sensitive to MMP-14 for the detection of elevated MMP-14 levels in adverse cardiac remodelling. Three ACPP analogs were synthesized and the most effective ACPP analog was selected using MMP-14 sensitivity and enzyme specificity assays. This ACPP, called ACPP-14B, showed high sensitivity towards MMP-14, soluble MMP-2, and MT2-MMP, while limited sensitivity was measured for other members of the MMP family. In *in vitro* cell assays, radiolabeled ACPP-14B showed efficient cellular uptake upon activation. A pilot *in vivo* study showed increased uptake of the radiolabeled probe in regions of infarcted myocardium compared to remote myocardium.

Introduction

The cell membrane-associated matrix metalloproteinase-14 (MMP-14 or MT1-MMP), a member of the membrane-type (MT) MMP subfamily, is involved in several protein modification and biological signaling pathways (1,2). Specifically, MMP-14 has been shown to convert the MMP-2 pro-enzyme into its active form, thereby facilitating extracellular matrix proteolysis (2,3). Furthermore, MMP-14 has been recognized to play an important role in the profibrotic cascade by activation of the transforming growth factor-beta (TGF) pathway and subsequent induction of fibrillar collagens (2,3). As such, MMP-14 is involved in a variety of physiological, but also pathological tissue remodeling processes. For example in cancer, MMP-14 plays a significant role in tumor growth and metastasis (4-6). In atherosclerosis, MMP-14 is directly linked to pathogenesis of plaque vulnerability (7). Furthermore, MMP-14 expression and activity is increased in pressure overload hypertrophy and in left-ventricular remodelling after cardiac ischemia-reperfusion injury or myocardial infarction, contributing to cardiac dysfunction (2,8-11). In this respect, MMP-14 upregulation holds great promise as an early biomarker for a variety of diseases. Several groups have reported on the development and/or application of MMP-14 molecular imaging probes. MMP-14 probes based on binding to the active site used peptide ligands or antibodies and were applied in near infrared fluorescence imaging, magnetic resonance imaging, or SPECT imaging (12-15). Furthermore, MMP-14 activatable molecular imaging probes have been developed for near infrared fluorescence imaging and SPECT imaging. Spinale and coworkers used an MMP-14 specific fluorogenic substrate for MMP-14 detection following cardiac ischemia-reperfusion injury (2,8). Ouyang *et al.* developed a genetically encoded fluorescence resonance energy transfer (FRET) imaging probe by flanking the MMP-14 cleavage domain in the pro-peptide sequence of MMP-2 by the fluorescent proteins ECFP and YPet (16). This genetically encoded biosensor was further optimized by employing an MMP-14 substrate, CRPAH-LRDSG, with enhanced sensitivity for MMP-14 (17). Watkins *et al.* investigated the use of an MMP-14 activatable cell penetrating peptide (ACPP) for SPECT imaging by inserting the MMP-14 peptide substrate SGRIGF-LRTA between a radiolabeled polycationic and polyanionic peptide domain (18,19). In the latter approach, *in vitro* activation was observed in cell cultures expressing MMP-14, but a control cell line lacking MMP-14 expression also activated the probe, and therefore MMP-14 selectivity could not be demonstrated. *In vivo* studies for this latter probe have not been reported so far. In a recent study, the similar substrate GRIGF-LRTA was demonstrated to possess high sensitivity for MMP-14, but also for the membrane-type matrix metalloproteinases MMP-15 and MMP-16, while the sensitivity towards MMP-2 and MMP-9 was low (20). By flanking the substrate GRIGF-LRTA with a Cy-5.5 fluorescent dye and a BHQ-3 quencher an organic FRET imaging probe was obtained, which was successfully used for the *in vivo* detection of membrane-type matrix metalloproteinase activity by optical imaging (20).

Here, we aimed to develop radiolabeled MMP-14 ACPPs by using three MMP-14 substrates different from the study of Watkins and colleagues (Figs. 5.1 and 5.2). These substrates include the MMP-14 cleavage domain in the pro-peptide sequence of MMP-2, CPKESCN-

LFVLKD and the more MMP-14 sensitive CRPAH-LRDSG substrate, which previously have been applied in the development of MMP-14 genetically encoded fluorescence resonance energy transfer (FRET) probes (16,17). Furthermore, the peptide PLA-C_{mob}WAR, which has been successfully used in an organic FRET probe for the monitoring of MMP-14 in heart disease, was employed as MMP-14-selective sequence (9). The polycationic and polyanionic domains consisted of D-amino acids to avoid proteolytic degradation of these domains. The cell penetrating peptide domain of the ACPPs was functionalized with a DOTA chelate to enable radiolabeling with ^{177}Lu. A dual-isotope radiolabeled MMP-2/9 ACPP approach recently showed valuable in the discrimination between intact and activated probe in *in vivo* biodistribution studies (21). Accordingly, we set out to develop MMP-14 sensitive dual-isotope radiolabeled ACPPs using the orthogonal radio-isotopes ^{177}Lu and ^{125}I. To introduce the radiolabel ^{125}I in the polyanionic inhibitory domain, either a tyrosine was introduced in the polyanionic inhibitory domain for direct radiolabeling, or ^{125}I can be introduced specifically to the N-terminus via coupling of a ^{125}I labelled 3-(4-hydroxyphenyl)propionic acid (SHPP) residue. The ACPPs were then studied for their MMP-14 sensitivity and specificity (Fig. 5.2). The best performing ACPP was studied *in vivo* in a pilot study in a mouse model of myocardial infarction.
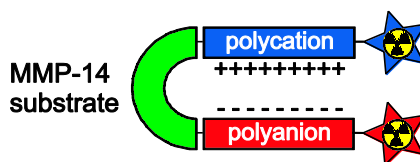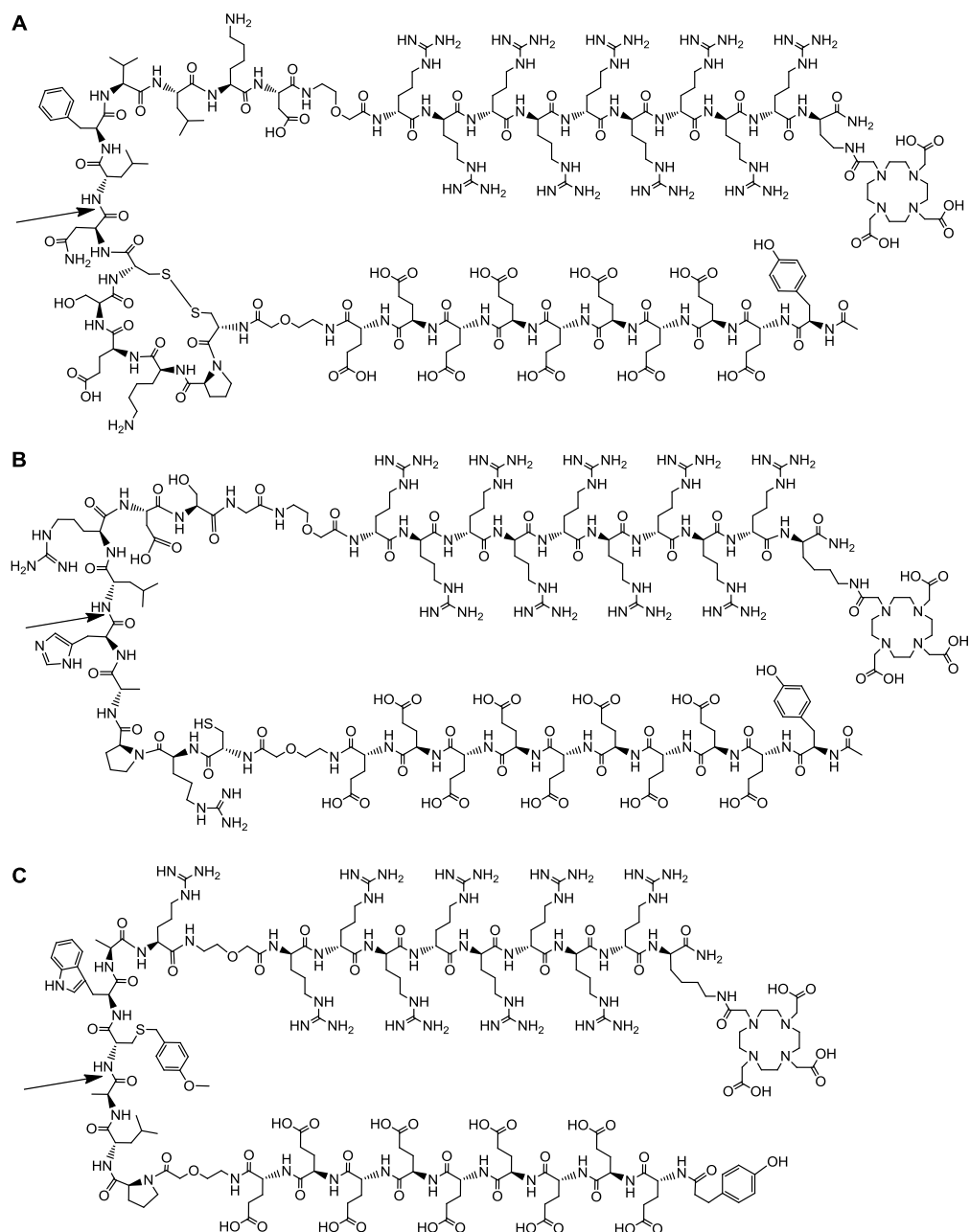

Figure 5.1: *Schematic of an MMP-14 sensitive dual-isotope labeled activatable cell penetrating peptide imaging probe.*

Results

Probe synthesis
The peptides ACPP-14A, ACPP-14B, and ACPP-14C (Fig. 5.2) were successfully prepared by Fmoc solid-phase peptide synthesis and in-solution coupling strategies, and purified by reversed phase – HPLC. Liquid chromatography – mass spectrometry (LC-MS) analysis demonstrated >95% pure peptides with molecular masses consistent to their theoretic masses (Fig. 5.3).
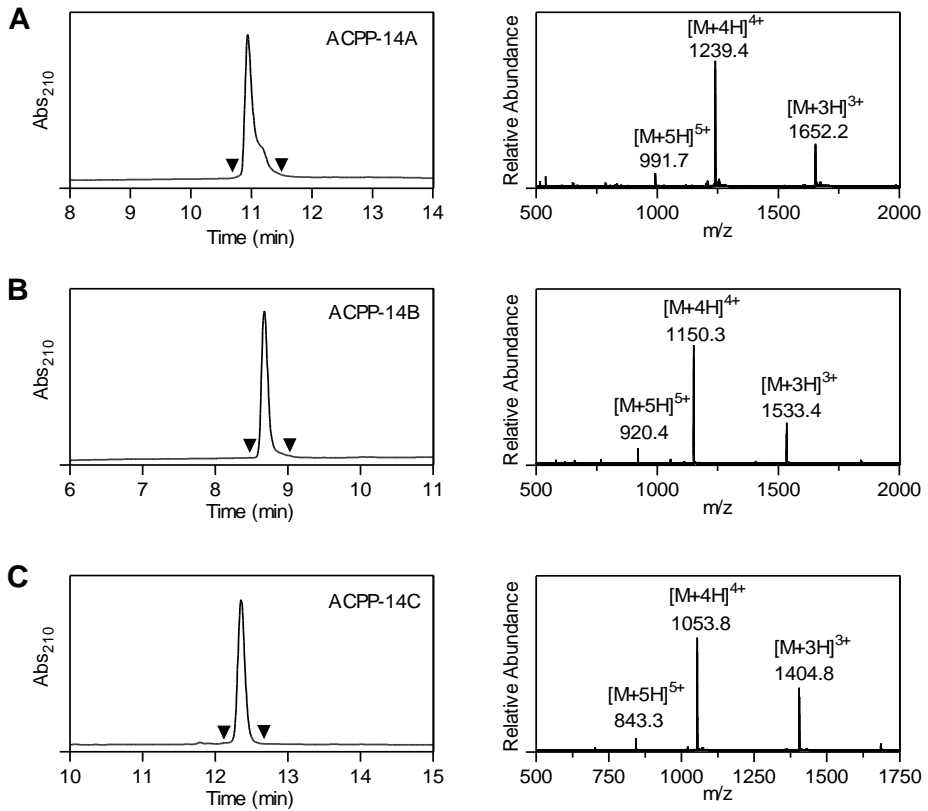
Figure 5.2: *Molecular structure of (A) Ac-y-e₉-X-C*PKESC*NLFVLKD-X-r₉-dab(DOTA)-NH₂ (ACPP-14A), (B) Ac-y-e₉-X-CRPAHLRDSG-X-r₉-k(DOTA)-NH₂ (ACPP-14B), and (C) SHPP-e₉-X-PLACₘₒᵦWAR-X-r₈-k(DOTA)-NH₂ (ACPP-14C). The arrows indicate the MMP-14 cleavage sites. In ACPP-14A, the two cysteines, indicated by C*, form an intramolecular disulfide bridge.*

Figure 5.3: *LC-MS characterization of (A) Ac-y-e$_9$-X-C*PKESC*NLFVLKD-X-r$_9$-dab(DOTA)-NH$_2$ (ACPP-14A, obsd. 4951.4 Da, calcd. 4951.4 Da), (B) Ac-y-e$_9$-X-CRPAHLRDSG-X-r$_9$-k(DOTA)-NH$_2$ (ACPP-14B, obsd. 4597.3 Da, calcd. 4597.3 Da), and (C) SHPP-e$_9$-X-PLAC$_{mob}$WAR-X-r$_8$-k(DOTA)- NH$_2$ (ACPP-14C, obsd. 4209.1 Da, calcd. 4209.1 Da). The left and right graphs show the UV absorbance chromatogram and the mass spectrum of the UV-peak bracketed by the arrowheads, respectively.*

MMP-14 sensitivity of ACPP-14 probes

The peptides ACPP-14A, ACPP-14B, and ACPP-14C (without SHPP functionality) were screened for MMP-14 sensitivity by incubating the peptides (0.1 mM) with MMP-14 (0.13 µM) for 60 min. For ACPP-14A, a small fraction (<5%) of the peptide was cleaved between the asparagine and leucine residue (Fig. 5.4A). In contrast, ACPP-14B and ACPP-14C were efficiently cleaved by MMP-14 (Figs. 5.4B and C). Due to the low MMP-14 sensitivity of ACPP-14A, this peptide probe was excluded from further analysis.
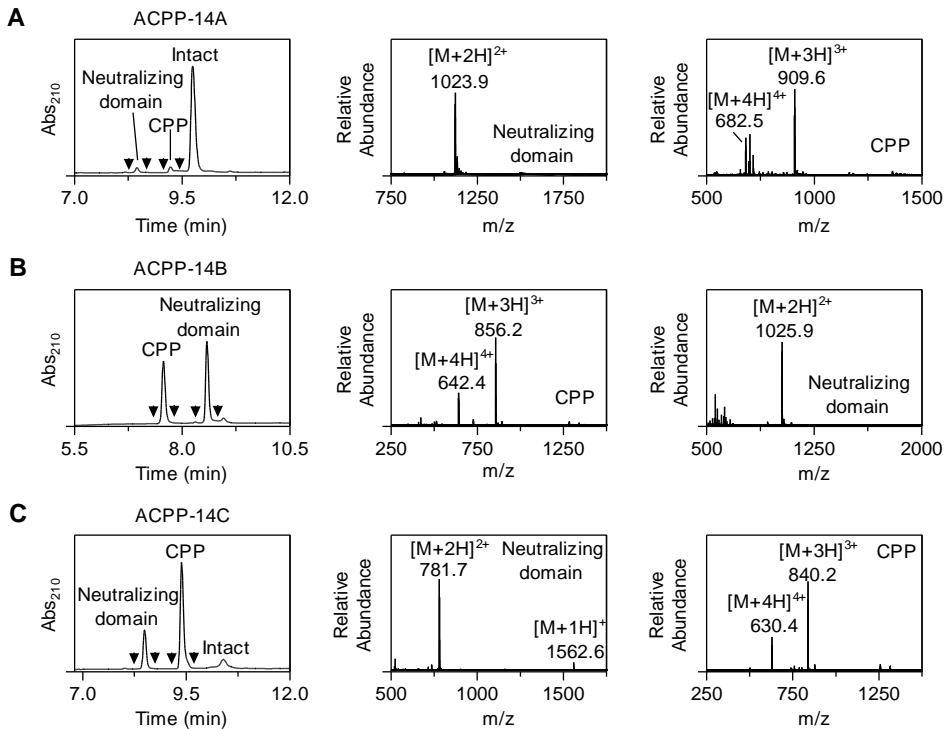
Figure 5.4: *LC-MS characterization of ACPP-14A, ACPP-14B, and ACPP-14C (0.1 mM) incubated with MMP-14 (0.13 µM) for 60 min. The left and right graphs show the UV absorbance chromatogram and the mass spectra of the UV-peaks bracketed by the arrowheads, respectively. (A) ACPP-14A; MS spectra of Neutralizing domain (obsd. 2244.8 Da, calcd. 2244.8 Da for Ac-y-e$_9$-X-C*PKESC*N-COOH), and CPP (obsd. 2724.7 Da, calcd. 2724.7 Da for H$_2$N-LFVLKD-X-r$_9$-dab(DOTA)-NH$_2$). (B) ACPP-14B; MS spectra of CPP (obsd. 2565.5 Da, calcd. 2565.5 Da for H$_2$N-LRDSG-X-r$_9$-k(DOTA)-NH$_2$), and Neutralizing domain (obsd. 2049.8 Da, calcd. 2049.8 Da for Ac-y-e$_9$-X-CRPAH-COOH). (C) ACPP-14C (without SHPP functionality); MS spectra of Neutralizing domain (obsd. 1561.5 Da, calcd. 1561.5 Da for e$_9$-x-PLA-COOH), and CPP (obsd. 2517.4 Da, calcd. 2517.4 Da for H$_2$N-C$_{mob}$WAR-X-r$_8$-k(DOTA)-NH$_2$).*

Enzyme specificity of ACPP-14B and ACPP-14C

ACPP-14B and ACPP-14C were incubated with twelve different enzymes, including the soluble matrix metalloproteinases MMP-1, MMP-2, MMP-3, MMP-7, and MMP-9, and the catalytic domains of the membrane-type matrix metalloproteinases MMP-14, MMP-15, and MMP-16. The sensitivity of the probes was also tested for the catalytic domain of ADAM-17, a desintegrin and metalloproteinase that is upregulated in heart failure. Finally, the sensitivity was determined towards enzymes present in the circulation, i.e. urokinase, plasmin, and thrombin. LC-MS analysis after 1h of incubation showed that ACPP-14B is efficiently cleaved between the histidine and leucine residue by MMP-2, MMP-14, and MMP-16. The other members of the MMP family effected minor degradation of ACPP-14B, while negligible

cleavage was observed for ADAM-17 and no cleavage was observed for thrombin, plasmin, and urokinase (Fig. 5.5A). ACPP-14C was efficiently cleaved, between the alanine and C_{mob} residue, by MMP-1, MMP-14, MMP-15, MMP-16, and to a modest extent by MMP-2, -3, -7, and -9, while no ACPP-14C cleavage was observed for ADAM-17, thrombin, plasmin, and urokinase (Fig. 5.5B). In conclusion, both ACPP-14B and ACPP-14C showed improved membrane-type MMP specificity compared to the MMP-2/9 dACPP probe described in Chapter 2 (Fig. 2.5B). ACPP-14B was selected for further *in vitro* and *in vivo* analysis as it showed the most MMP-14 specificity.
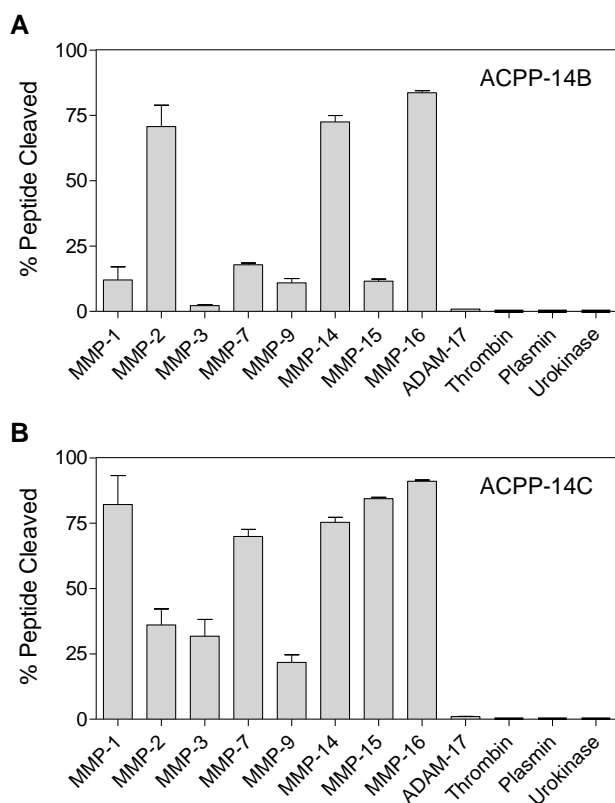

Figure 5.5: *The percentage of released CPP from (A) ACPP-14B and (B) ACPP-14C (0.1 mM) after 1h incubation with twelve different enzymes (20 nM) in vitro. The experiments were performed in triplicate and the data are presented as mean ± SD. Note: ACPP-14C was incubated with 67 nM MMP-7 instead of 20 nM.*

In vitro cell assay ACPP-14B

The uptake of ACPP-14B by HT-1080 cells was assessed by employing the same approach as for the MMP-2/9 dACPP (Chapter 2). That means, the cellular uptake was compared between radiolabeled pre-cleaved ^{177}Lu-ACPP-14B, uncleaved ^{177}Lu-ACPP-14B, a negative control and

a positive control (Figs. 5.6 and 5.7). ^{177}Lu-non-ACPP (Chapter 2), which showed no MMP-14 sensitivity, and ^{177}Lu-CPP-14B served as negative and positive control, respectively. CPP-14B was obtained by MMP-14-mediated cleavage of ACPP-14B and subsequent isolation of the polycationic domain by reversed phase-HPLC. After 3h incubation at 1.25 μM, the cellular uptake of the activated ^{177}Lu-ACPP-14B was comparable to uptake of the positive control ^{177}Lu-CPP-14B, and furthermore significantly higher with respect to uncleaved ^{177}Lu-ACPP-14B, and ^{177}Lu-non-ACPP (Fig. 5.7). Although not significant, intact ^{177}Lu-ACPP-14B exhibited a slightly higher uptake and retention compared to the negative control ^{177}Lu-non-ACPP, while this was not observed for ^{177}Lu-ACPP (Chapter 2).
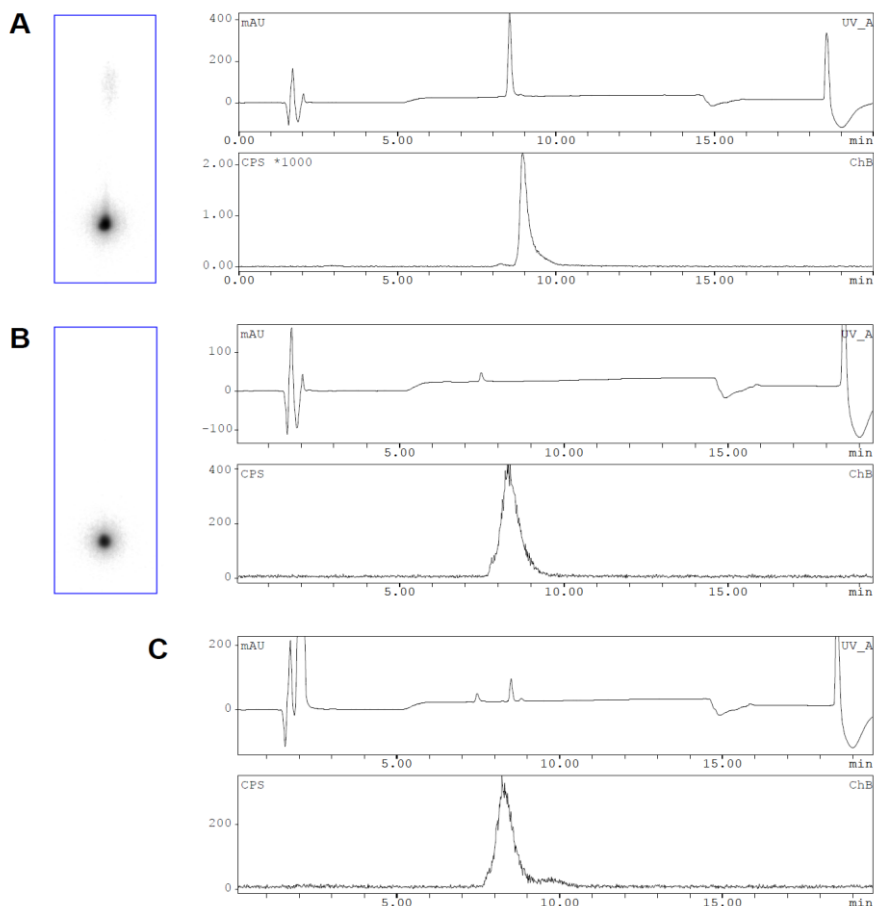

Figure 5.6: *iTLC and γ-HPLC spectra of (A) uncleaved ^{177}Lu-ACPP-14B and (B) ^{177}Lu-CPP-14B, and (C) γ-HPLC spectrum of pre-activated ^{177}Lu-ACPP-14B, showing >95% cleavage. Radiochemical purities were >99% as assessed by iTLC. The upper panel shows the UV absorbance chromatogram at 212 nm and the lower panel shows the γ-radiation monitored by a γ-detector.*

We continued to investigate if the modest uptake of ACPP-14B was mediated through activation by membrane-type MMP-14 and MMP-16 expressed by HT-1080 cells (22). Thereto, the negative control, intact ACPP-14B, and pre-cleaved ACPP-14B were subjected to HT-1080 cell uptake experiments in the presence of a broad-spectrum MMP inhibitor, GM6001. The presence of GM6001 did not affect the cellular uptake of ACPP-14B, and this suggests no MT-MMP mediated activation (data not shown).
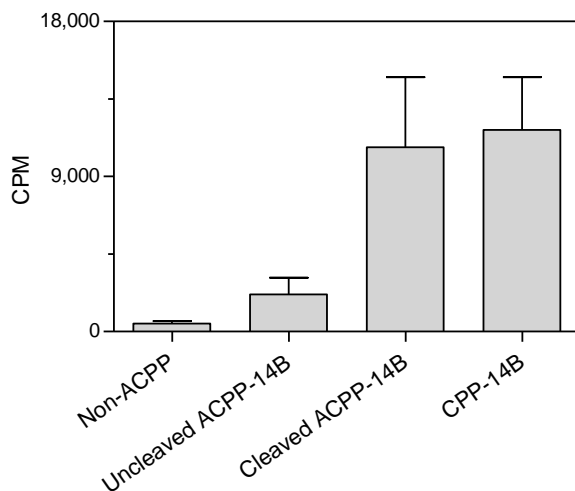

Figure 5.7: *Cellular uptake of ^{177}Lu-non-ACPP, uncleaved ^{177}Lu-ACPP-14B, pre-activated ^{177}Lu-ACPP-14B, and ^{177}Lu-CPP-14B after 3h incubation with HT-1080 cells, assessed by γ-counting.*

In vivo biodistribution

An *in vivo* pilot study was performed to assess the *in vivo* biodistribution of ACPP-14B and CPP-14B, 5h post-injection, in a mouse model of myocardial infarction (MI). For comparison with the MMP-2/9 sensitive probe dACPP (Chapter 2), the biodistribution of this probe was also determined under similar conditions. We aimed to characterize the *in vivo* biodistribution of ACPP-14B using a dual-isotope approach with ^{177}Lu, labeled to the polycationic domain, and ^{125}I, labeled to the polyanionic domain, as orthogonal radiolabels. Although iodination of ACPP-14B resulted in efficient conjugation of ^{125}I to the peptide (Fig. 5.8), the oxidative conditions, needed for activation of ^{125}I, resulted in disulfide formation between cysteine residues, resulting in peptide dimers (Fig. 5.9). An alternative approach, activating ^{125}I in iodination tubes prior to conjugation to ACPP-14B under non-oxidative conditions resulted in ~60% labeling. Unfortunately, a >95% radiochemical purity could not be achieved by solid phase extraction (Fig. 5.8), and desalting strategies to remove ^{125}I could not be applied due to the low molecular weight of the peptide.
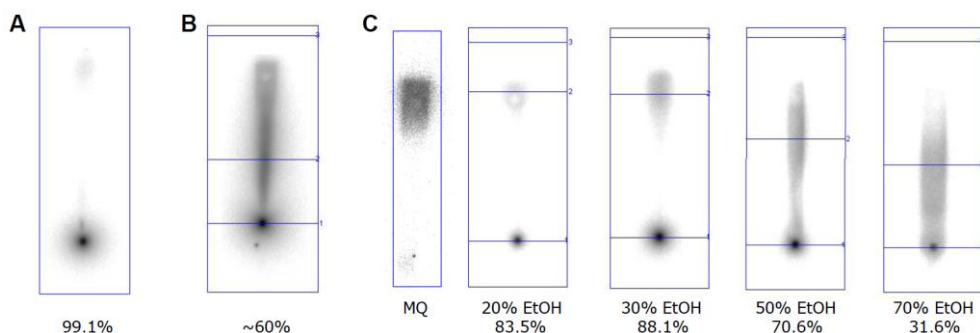
Figure 5.8: *Radio-TLC analysis of ^{125}I iodination of ACPP-14B. (A) Direct iodination of ACPP-14B in an iodination tube results in >95% radiochemical purity, but also in disulfide formation. (B) Prior activation of ^{125}I and subsequent iodination in an siliconized tube resulted in ~60% labeling yields. (C) iTLC results for solid phase extraction fractions of unpure ACPP-14B. Maximum obtained purity was <90%.*
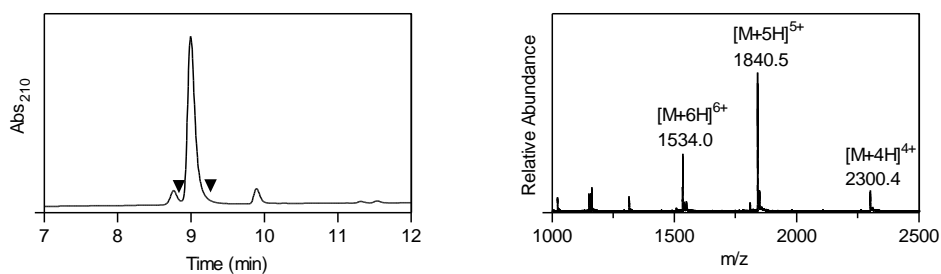

Figure 5.9: *LC-MS characterization of ACPP-14B incubated in PBS in an iodination tube for 5 minutes in the absence of ^{125}I. The left and right graphs show the UV absorbance chromatogram and the mass spectrum of the UV-peak bracketed by the arrowheads, respectively. Found mass corresponded to the calculated mass of an ACPP-14B peptide dimer linked to each other via a disulfide bridge.*

Therefore, only the single isotope labeled probe ^{177}Lu-ACPP-14B was used in this pilot study. The biodistribution studies in 10 day-old MI-mice revealed a higher uptake of both ACPP-14B and CPP-14B in infarcted regions of the heart compared to remote myocardium (Fig. 5.10, Table 5.1). The infarct-to-remote ratio for ACPP-14B seems to be higher compared to CPP-14B (Fig. 5.10) and would suggest infarct-specific activation, but the difference was not statistically significant due to the relatively high variation for ACPP-14B. Evaluation of dACPP in the same mouse model demonstrated a higher uptake of dACPP in the infarcted heart compared to ACPP-14B, but also in other tissues such as remote myocardium, muscle, lung, spleen, and liver, while the accumulation of dACPP in kidney was lower compared to ACPP-14B. These differences suggest a diminished background activation of ACPP-14B in the vasculature compared to dACPP (Chapters 2 and 3), resulting in a lower retention of the

activated probe in most tissues. Specifically, in Chapters 2 and 3 it was shown that the intact probe is mainly trapped in the kidneys while the activated probe, CPP, shows a strong uptake by liver and spleen and increased background uptake in basically all tissues. In addition, the positive control ^{177}Lu-CPP-14B showed a comparably high level of liver and spleen uptake. The blood kinetic profile (Fig. 5.11) shows a rapid elimination of ^{177}Lu-ACPP-14B from the circulation with a blood half-life of ~24 min, similar to dACPP (Fig. 4.5). The calculated volume-of-distribution for ACPP-14B is 0.3 L/kg, which is also in the same range as for dACPP, and indicates that the probe is rapidly distributed throughout the extracellular extravascular space.

Table 5.1: *Biodistribution results of 10 nmol ^{177}Lu-dACPP, ^{177}Lu-ACPP-14B, and ^{177}Lu-CPP-14B 5h post-injection in MI mice (n=3). The data are mean %ID/g ± SD.*

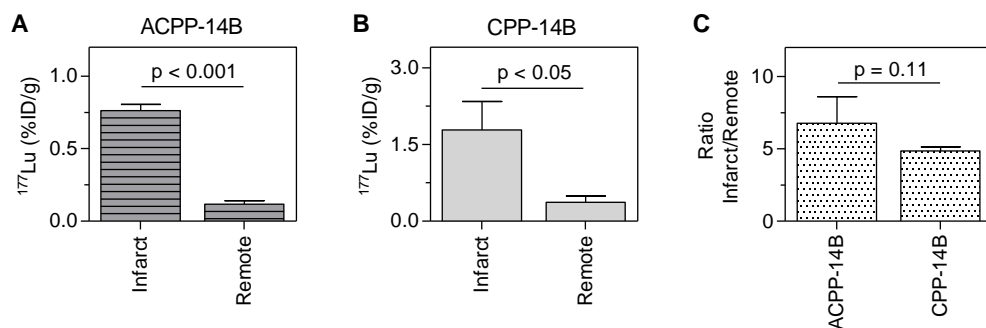|	^{177}Lu-dACPP	^{177}Lu-ACPP-14B	^{177}Lu-CPP-14B
Blood	0.09 ± 0.03	0.09 ± 0.03	0.14 ± 0.08
Heart, infarct	3.60 ± 0.68	0.76 ± 0.04	1.78 ± 0.56
Heart, remote	0.35 ± 0.13	0.12 ± 0.02	0.37 ± 0.12
Muscle	0.48 ± 0.14	0.11 ± 0.09	0.10 ± 0.02
Lung	1.09 ± 0.30	0.42 ± 0.11	0.56 ± 0.21
Spleen	2.72 ± 1.48	0.73 ± 0.13	3.72 ± 0.50
Liver	28.5 ± 5.33	6.41 ± 1.03	31.3 ± 3.22
Kidney	59.9 ± 8.10	92.1 ± 7.26	10.3 ± 1.75
Fat	0.33 ± 0.08	0.55 ± 0.27	0.14 ± 0.08
Thigh bone	2.47 ± 1.02	0.29 ± 0.06	2.58 ± 0.15
Brain	0.02 ± 0.00	0.01 ± 0.01	0.01 ± 0.00

Figure 5.10: *Uptake of (A) ^{177}Lu-ACPP-14B and (B) ^{177}Lu-CPP-14B in infarcted and remote areas in MI-mice (n=3), 5h post-injection. (C) Infarct-to-remote ratios. The data are mean ± SD.*
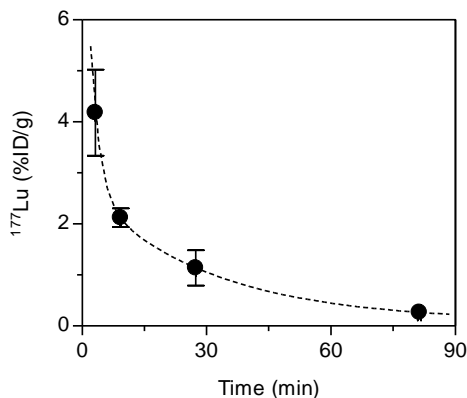
Figure 5.11: *Blood kinetics of ^{177}Lu-ACPP-14B in MI-mice (n=3). The data are mean %ID/g ± SD and fitted to the 2-phase exponential decay function $Y = span_1 \cdot exp(-K_1 \cdot X) + span_2 \cdot exp(-K_2 \cdot X) + Plateau$. $Span_1$ = 2.61 %ID/g, K_1 =1.99 min^{-1}, $Span_2$ = 7.35 %ID/g, K_2= 27.1 min^{-1}.*

Discussion

Recently, we showed that the use of activatable cell penetrating imaging probes is a promising strategy for the *in vivo* detection of proteolytic activity in myocardial remodeling. Besides specific activation in infarcted heart tissue, the MMP-2/9 dACPP also showed a considerable degree of activation in the vascular compartment, leading to background uptake of the activated probe in basically all tissues. Therefore, the development of ACPPs which are only activated in the tissue of interest by tissue-specific enzymes should be the next step in optimization of the ACPP concept. The cell membrane-associated matrix metalloproteinase-14 (MMP-14) has been identified to be such a tissue-specific target showing increased activity and expression in myocardial remodeling in ischemia-reperfusion injury or after myocardial infarction. For that reason, we focused on the development of an MMP-14 ACPP. Three different MMP-14 substrates were inserted in the ACPP platform and tested *in vitro*. Unfortunately, the first variant containing the MMP-14 cleavage site of pro-MMP-2, ACPP-14A, showed a low sensitivity towards MMP-14. ACPP-14A analogs (the linear variant, and a peptide probe lacking the 5-amino-3-oxapentanoic acid linker residues) were also synthesized and tested for MMP-14 sensitivity, showing a similar low degree of degradation (data not shown). Accordingly, a poor response of a genetically encoded MMP-14 biosensor employing the same substrate was recently reported (17). The low MMP-14 sensitivity and the fact that ACPPs are expected to be cleared from the circulation relatively fast (blood half-life times of <30 min) (23), does not hold much promise for significant accumulation of ACPP-14A in MMP-14 expressing tissue, precluding *in vivo* imaging of MMP-14 with this particular probe. Therefore, in-depth analysis of the MMP-14 specificity and *in vivo* characteristics of ACPP-14A was not performed.

Two alternative MMP-14 ACPPs, containing the substrates CRPAH-LRDSG (ACPP-14B) and PLAC$_{mob}$WAR (ACPP-14C) respectively, showed high sensitivity for MMP-14. Because MMP-14

specificity was reported for the substrate PLAC$_{mob}$WAR concatenated between two fluorophores, we were surprised to observe efficient cleavage of ACPP-14C by other MMPs (8). Attachment of the relatively large and charged peptide domains may adversely have affected the cleavage rate for MMP-14 in competition to other MMPs. Due to the broad MMP sensitivity for both tissue-specific and soluble MMPs, ACPP-14C is most likely also activated in the vascular compartment, and, as a result, represents at best only a marginal improvement compared to the MMP-2/9 dACPP with respect to the specific targeting of proteolytic activity involved in myocardial remodeling (Chapter 3).

ACPP-14B showed the highest specificity for tissue-specific MMPs, i.e. MMP-14 and MMP-16. We continued to study ACPP-14B in a cell assay and subsequently, a small pilot study was carried out to compare ACPP-14B with the MMP-2/9 sensitive probe dACPP in a mouse model of myocardial infarction. In the cell assay, intact ACPP-14B seemed to show an increased cellular uptake compared to the negative control non-ACPP. The cellular uptake of ACPP-14B was not reduced in the presence of a broad MMP inhibitor, suggesting that there is no role for transmembrane MMP-mediated activation of intact ACPP-14B. In these experiments, we used the scrambled negative control for the MMP-2/9 ACPP (Chapter 2) that also showed no MMP-14 sensitivity. However, the linkers for ACPP-14B and non-ACPP, O1Pen-CRPAHLRDSG-O1Pen and Ahx-LALGPG respectively, are rather different. A major dissimilarity is that the linker of non-ACPP consists solely of hydrophobic, non-polar amino acids, while the linker of ACPP-14B contains mainly polar amino acids, including three positively charged residues. It might be that the linker of ACPP-14B can interact with proteins/cells via hydrogen bonding mediating some cellular retention. Another difference is that the linker of ACPP-14B consists of 42 bonds versus 25 bonds for the linker in non-ACPP. Therefore, the effective molality (EM) for ACPP-14B, 23 mM, is lower compared to non-ACPP, 49 mM (24), and may be associated with a higher level of dissociation of the polycationic and polyanionic domain and thus less efficient masking of the cell penetrating property of the polycationic peptide in ACPP-14B. Yet, efficient intramolecular hairpin formation and subsequent masking of the cell penetrating property is expected for both probes as the EMs are much higher than the 5.9 µM affinity between the polycationic and polyanionic domain (25).

In an *in vivo* pilot study in a mouse model of myocardial infarction, ACPP-14B was compared with the MMP-2/9 sensitive dACPP. Earlier extensive studies exploring dACPP, non-dACPP, and CPP, revealed that the activated domain of the dACPP imaging probe is efficiently taken up by the liver, while the intact probe is accumulated in the kidney's (Chapters 2 and 3). These experiments showed that an extensive part of dACPP was activated in the vasculature. Here, ACPP-14B was mainly accumulated in the kidneys and this suggests a diminished activation of ACPP-14B in the vasculature, which may be explained by the difference in sensitivity for circulating MMPs. We demonstrated that dACPP is sensitive towards the soluble proteases MMP-2 and MMP-9 (Chapter 2), while ACPP-14B showed *in vitro* sensitivity towards MMP-2, but not for MMP-9.

The retention of ACPP-14B, and CPP-14B in the infarcted areas of the heart was higher compared to remote areas, which was also observed for dACPP and its controls (Chapter 3).

Comparison of the infarct-to-remote ratio for ACPP-14B and CPP-14B showed an increased ratio for ACPP-14B, suggesting local activation. However, the difference was not statistically significant due to the relatively high variation for ACPP-14B. Extended biodistribution studies and, in particular, dual-isotope studies would be valuable to verify if ACPP-14B probe activation occurs *in vivo* and to specify the localization, with a special interest into infarcted and remote areas of the heart. Such studies could further address the question if ACPP-14B will out-perform dACPP in terms of specific targeting of infarcted myocardium. We aimed for the dual-isotope approach in the reported pilot study by labeling ACPP-14B with both ^{177}Lu and ^{125}I. Although iodination of ACPP-14B resulted in efficient conjugation of ^{125}I to the peptide, the oxidative conditions, needed for activation of ^{125}I, resulted in disulfide formation between cysteine residues, resulting in peptide dimers. Therefore, re-design of the ACPP-14B peptide structure, to prevent side-reactions during iodination, may enable dual-isotope studies. Hereto, the cysteine residue can be acetylated, but oxidation of the sulfur atom may still occur. Furthermore, this conversion results in a more hydrophobic residue that may impact the MMP-14 sensitivity of the probe. Substitution of the cysteine by a serine residue will possibly be a more attractive option.

Conclusion

We have successfully developed a series of radiolabeled activatable cell penetrating peptides (ACPP) sensitive to MMP-14. The most effective ACPP analog, ACPP-14B, was selected by MMP-14 sensitivity and enzyme specificity assays. In *in vitro* cell assays, this radiolabeled ACPP showed efficient cellular uptake upon activation. Furthermore, the level of *in vivo* background activation in the vasculature was decreased compared to an earlier well-studied MMP-2/9 ACPP probe, while an increased uptake in infarcted heart tissue was observed compared to remote heart tissue, which warrants further research into the *in vivo* biodistribution and behavior of ACPP-14B.

Materials and methods

Materials

All reagents and solvents were obtained from commercial sources (Sigma-Aldrich, and Biosolve) and used without further purification. 9-fluorenylmethyloxycarbonyl (Fmoc)-protected amino acids and Rink amide resin were purchased from either Novabiochem (Merck) or Iris Biotech. DOTA succinimidyl ester was obtained from Macrocyclics. Human recombinant enzymes were purchased from Calbiochem (Merck), Sigma, or R&D Systems. The enzymes were activated according to vendor's protocols if needed.

Probe synthesis

Peptides Ac-y-e$_9$-X-CPKESCNLFVLKD-X-r$_9$-dab(ivDde)-resin, Ac-y-e$_9$-X-CRPAHLRDSG-X-r$_9$-k(ivDde)-resin, and Fmoc-e$_9$-X-PLAC$_{mob}$WAR-X-r$_8$-k(Mtt)-resin were synthesized on an automatic synthesizer (Prelude, Protein Technologies Inc.) by Fmoc solid-phase peptide synthesis (SPPS) using Chemmatrix rink amide resin (0.1 mmol), HBTU as the activating reagent, and N,N-Diisopropylethyl amine (DIPEA) as base. D-amino acids are denoted in lower case. X and C$_{mob}$ represents 5-amino-3-oxapentanoic acid and 4-methoxybenzyl-L-cysteine, respectively. The ivDde protecting group was selectively removed by incubating Ac-y-e$_9$-X-CPKESCNLFVLKD-X-r$_9$-dab(ivDde)-resin, and Ac-y-e$_9$-X-CRPAHLRDSG-X-r$_9$-k(ivDde)-resin with 5.0% v/v hydrazine-monohydrate in DMF for 10 x 3 min. The Mtt protecting group was selectively removed by incubating Fmoc-e$_9$-X-PLAC$_{mob}$WAR-X-r$_8$-k(Mtt)-resin with 1.8% v/v trifluoroacetic acid (TFA) in dichloromethane with 2.0% v/v tri-isopropylsilane (TIS) as scavenger for 10 x 3 min. DOTA succinimidyl ester (4.0 equiv) in NMP was added to the peptide resins and was reacted for 1h in the presence of DIPEA. After Fmoc removal, the peptides were cleaved from the resin by a mixture of 90.5% v/v trifluoroacetic acid (TFA), 2.0% v/v 1,2-ethanediol (EDT), 5.0% v/v tri-isopropyl silane (TIS), and 2.5% v/v MilliQ (Millipore) water for 4h, filtered, and precipitated in ice cold diethylether. The peptide pellets were dissolved in MilliQ water and purified by preparative reversed-phase high pressure liquid chromatography (RP-HPLC) using an Agilent 1200 apparatus, equipped with a C18 Zorbax column (length = 150 mm, diameter = 21.2 mm, particle size = 5.0 µm). The elution gradient was set from 5 to 30% of buffer B (0.1% TFA in acetonitrile) over 100 min, where buffer A was 0.1% TFA in MilliQ (Millipore) water. The UV wavelength was preset at 210 and 254 nm. All peptides structures were analyzed by LC-MS on an Agilent 1200 apparatus, equipped with a C18 Eclipse plus-column (length = 100 mm, diameter = 2.1 mm, particle size = 3.5 µm) and an electrospray mass spectrometer (Agilent Technologies 6210, Time-of-Flight LC/MS). 80% of peptide Ac-y-e$_9$-X-CPKESCNLFVLKD-X-r$_9$-dab(DOTA)-NH$_2$ was cyclized at 50 rpm in 15% v/v DMSO, 10% v/v acetonitrile, and 75% v/v MilliQ water for 3 days, purified by RP-HPLC, and analyzed by LC-MS. The positive control of Ac-y-e$_9$-X-CRPAHLRDSG-X-r$_9$-k(DOTA)-NH$_2$ was obtained by incubating this peptide (1.0 mM, 0.96 µmol) with 60 nM MMP-14 in a mixture of 50 mM Tris, 200 mM NaCl, 10 mM CaCl$_2$ and 10 µM ZnCl$_2$ at pH 7.5 at 700 rpm and 37 °C for 24h, after which the polycationic domain was isolated by RP-HPLC, and analyzed by LC-MS. 50% of peptide e$_9$-X-PLAC$_{mob}$WAR-X-r$_8$-k(DOTA)-NH$_2$ was reacted with 3-(4-hydroxyphenyl)propionic acid (SHPP) *N*-hydroxysuccinimide ester (10 equiv) in DMF in the presence of DiPEA for 6h, after which the peptide was purified by RP-HPLC, and analyzed by LC-MS.

Found masses: 4953.4 Da for Ac-y-e_9-X-CPKESCNLFVLKD-X-r_9-dab(DOTA)-NH_2 (Calcd. 4953.4 Da, 2.2 µmol), 4951.4 Da for Ac-y-e_9-X-C*PKESC*NLFVLKD-X-r_9-dab(DOTA)-NH_2 (ACPP-14A, Calcd. 4951.4 Da, 1.3 µmol), 4597.3 Da for Ac-y-e_9-X-CRPAHLRDSG-X-r_9-k(DOTA)-NH_2 (ACPP-14B, Calcd. 4597.3 Da, 3.4 µmol), 2565.5 Da for LRDSG-X-r_9-k(DOTA)-NH_2 (CPP-14B, Calcd. 2565.5 Da, 0.62 µmol), 4061.2 Da for e_9-X-PLAC$_{mob}$WAR-X-r_8-k(DOTA)-NH_2 (Calcd. 4061.1 Da, 5.0 µmol), and 4209.1 Da for SHPP-e_9-X-PLAC$_{mob}$WAR-X-r_8-k(DOTA)-NH_2 (ACPP-14C, Calcd. 4209.1 Da, 1.2 µmol).

Design consideration ACPP-14C
Initially ACPP-14C was synthesized on the solid phase with a tyrosine residue at the N-terminus. Incubation of this peptide in PBS in a Pierce iodination tube (Thermo Scientific) resulted in oxidation of the C$_{mob}$ residue as was indicated by LC-MS (+16 Da, and +2*16 Da adducts were observed). To prevent oxidation of C$_{mob}$, ^{125}I was intended to be introduced via an ^{125}I-labeled SHPP-*N*-hydroxysuccinimide ester residue.

MMP-14 sensitivity
ACPP-14A, ACPP-14B, and ACPP-14C (0.1 mM) were incubated with 15 nM MMP-14 in a mixture of 50 mM Tris, 200 mM NaCl, 10 mM $CaCl_2$ and 10 µM $ZnCl_2$ at pH 7.5 at 700 rpm and 37 °C. After 1h, the enzyme was quenched by the addition of TFA (10% v/v), and the reaction mixture was analyzed by LC-MS.

Enzyme assay
ACPP-14B and ACPP-14C were incubated in triplicate with 20 nM of either human recombinant MMP-1, MMP-2, MMP-3, MMP-7, MMP-9, MMP-14, MMP-15, MMP-16, ADAM-17, thrombin, plasmin, or urokinase in a mixture of 50 mM Tris, 200 mM NaCl, 10 mM $CaCl_2$ and 10 µM $ZnCl_2$ at pH 7.5 at 700 rpm and 37 °C. After 1h, the enzymes were quenched by the addition of TFA (10% v/v) and the reaction mixtures were analyzed by LC-MS. The formation of the activated cell penetrating peptide domain was monitored and compared to a 100% cleaved reference sample.

Radiolabeling
For in vitro cell assay: [177]LuCl$_3$ (PerkinElmer) in 0.05 M HCl (2.0 µL, 4.0 MBq) was mixed with ACPP-14B, non-ACPP, or CPP-14B in MilliQ water (2.69-4.60 µL, 20.0 nmol), and metal-free 0.9% NaCl (final volume 100 µL) for 20 min, at 600 rpm and 90 °C.
For in vivo studies: [177]LuCl$_3$ in 0.05 M HCl (6.0 µL, 18.0 MBq) was mixed with ACPP-14B or CPP-14B in MilliQ water (10.4 µL, 45 nmol), and metal-free 0.9% NaCl (433.6 µL) for 20 min, at 600 rpm and 90 °C. The ^{177}Lu labelling yields were determined by radio-TLC, using iTLC-SG strips (Pall) eluted with 200 mM EDTA in 0.9% NaCl, imaged on a phosphor imager (FLA-7000, Fujifilm) and quantified with AIDA Image Analyzer software. Analytical radio-HPLC was carried out on an Agilent 1100 system equipped with a C18 Eclipse XBD-column (length = 150 mm, diameter = 4.6 mm, particle size = 5.0 µm) and a Gabi radioactive detector (Raytest). The radiochemical purities were 95% or higher, and typically at least 98%. The labeling of dACPP has been described in Chapter 3.

Cell culture

HT-1080 fibrosarcoma cells acquired from the American Type Culture Collection (ATCC) were maintained under standard culture conditions in Eagle's Minimal Essential Medium (MEM) supplemented with 10% heat inactivated fetal bovine serum (Gibco), penicillin (100 U/mL), streptomycin (100 μg/mL), and 2 mM Glutamax (Gibco).

In vitro cell incubation with radiolabeled ACPP probes

^{177}Lu-ACPP-14B (50 μM) was activated prior to cell incubation with recombinant human MMP-14 (100 nM) for 2h in 50 mM Tris, 200 mM NaCl, 10 mM $CaCl_2$ and 10 μM $ZnCl_2$ at pH 7.5, as was assessed by RP-HPLC. HT-1080 cells were cultured in 12-well plates. At 95% confluency, cells were washed with Dulbecco's PBS (Gibco) and subsequently incubated in triplicate with 1.25 μM ^{177}Lu-non-ACPP, 1.25 μM uncleaved ^{177}Lu-ACPP-14B, 1.25 μM pre-cleaved ^{177}Lu-ACPP-14B, and 1.25 μM ^{177}Lu-CPP-14B (0.25 MBq ^{177}Lu) respectively in serum-free medium (1 mL). After 3h of incubation, cells were washed 3x with Dulbecco's PBS and harvested by trypsination (0.25% w/v trypsin-EDTA (Gibco)). The trypsin activity was inhibited by addition of MEM, after which the cells were isolated by centrifugation (1,000 rpm, 5 min, RT). Cell pellets and all wash fractions were analyzed for ^{177}Lu radioactivity (115-270 keV) by a γ-counter (Wizard 1480, PerkinElmer).

MMP blocking study: HT-1080 cells were cultured in 12-well plates. At 95% confluency, cells were washed with Dulbecco's PBS (Gibco) and subsequently incubated (n=4) with 1.25 μM ^{177}Lu-non-ACPP, 1.25 μM ^{177}Lu-ACPP-14B, and 1.25 μM pre-cleaved ^{177}Lu-ACPP-14B, respectively in serum-free medium (1 mL) containing 50 μM GM6001. After 4h of incubation, cells were washed 3x with Dulbecco's PBS and harvested by trypsination (0.25% w/v trypsin-EDTA (Gibco)). The trypsin activity was inhibited by addition of MEM, after which the cells were isolated by centrifugation (1,000 rpm, 5 min, RT). Cell pellets and all wash fractions were analyzed for ^{177}Lu radioactivity (115-270 keV) by a γ-counter.

Animal studies

All animal procedures were approved by the ethical review committee of the Maastricht University Hospital (The Netherlands), and were performed according to the principles of laboratory animal care (NIH publication 85-23, revised 1985) (26), and the Dutch national law "Wet op Dierproeven" (Stb 1985, 336). Male Swiss mice (body weight >25g, Charles River Labs) were housed in an enriched environment under standard conditions: 21-23 °C, 50-60% humidity, and 12h-lightdark-cycles for >1 week. Food and water were freely available. 10 days post myocardial infarction, the animals wer used for *in vivo* studies.

Mouse model of myocardial infarction (MI)

MI was induced by permanent ligation of the left anterior descending coronary artery (LAD) using published procedures (27). In short, animals were subcutaneously injected with buprenorphine (0.1 mg/kg) and 30 min later anesthetized with isoflurane. Animals were intubated and ventilated with 100% oxygen with a rodent respirator. After left thoracotomy between ribs four and five, the LAD was ligated with a 6-0 prolene suture. The chest and skin were closed with 5-0 silk sutures. The animal's temperature was continuously measured rectally and maintained at 36.5–37.5 °C during surgery. After surgery, animals were allowed to recover at 30 °C overnight.

Blood kinetics and Biodistribution

Biodistribution experiments were performed on MI-mice (n=3 per probe) by i.v.-injection of ^{177}Lu-dACPP (10 nmol/100 µL, ca. 4.0 MBq ^{177}Lu), ^{177}Lu-ACPP-14B (10 nmol/100 µL, ca. 4.0 MBq ^{177}Lu), or ^{177}Lu-CPP-14B (10 nmol/100 µL, ca. 4.0 MBq ^{177}Lu). For animals injected with ^{177}Lu-ACPP-14B, blood samples were withdrawn from the vena saphena at selected time points (3, 9, 27, and 81 min), weighed, and diluted to 1 mL with MilliQ water. The mice were anesthetized with isoflurane 5h after i.v.-injection, subjected to 2% (w/v) Evans Blue i.v.-injection (50 mg/kg) and sacrificed 2 min later by cervical dislocation. Organs and tissues of interest were harvested and weighed, after which the radioactivity of the samples was measured in a γ-counter (Wizard 1480; PerkinElmer) along with standards to determine the injected dose per gram (%ID/g). The energy window was set to 155-380 keV for [177]Lu. The average probe concentration at time 0 (C_0) was calculated by fitting the blood clearance data to the 2-phase exponential decay function $Y = span_1 \cdot \exp(-K_1 \cdot X) + span_2 \cdot \exp(-K_2 \cdot X) + Plateau$ using GraphPad Prism. The area under the curve (AUC) was determined and the blood half-life, the time point at which the AUC reaches 50% of the total AUC, was subsequently derived using MatLab. The average volume of distribution was calculated using the formula $V_D = dose/(mean\ body\ weight \cdot C_0)$ [L/kg]. The hearts were cooled to 4 °C, cut in 1 mm slices from apex to base. Infarct, border, and remote areas were isolated based on Evans Blue staining, and %ID/g for ^{177}Lu was determined by a γ-counter.

Iodination strategies

Direct labeling in iodination tube: [125]I (PerkinElmer) in PBS (6.0 µL, 11.5 MBq) was mixed with ACPP-14B in MilliQ water (10.4 µL, 45 nmol), and PBS (433.6 µL) in an Iodogen iodination tube (Pierce) for 20 min, at 600 rpm and 23 °C, and transferred to a siliconized 1.5 mL tube. The ^{125}I labeling yield was determined by radio-TLC, using iTLC-SG strips eluted with 20 mM citric acid at pH 5.2. A >95% radiochemical purity was observed. As control, ACPP-14B in MilliQ water (10.4 µL, 45 nmol) was mixed with PBS (433.6 µL) in an Iodogen iodination tube for 5 min, at 600 rpm and 23 °C, followed by LC-MS analysis. Found mass: 9197.7 Da, Calc. MW: 9197.8 Da for ACPP-14B peptide dimer.

Indirect labeling: [125]I (PerkinElmer) in PBS (439.6 µL, 11.5 MBq) was activated in an Iodogen iodination tube for 7 min according to vendor's protocol, and transferred to a siliconized 1.5 mL tube containing ACPP-14B in MilliQ water (10.4 µL, 45 nmol) and mixed for 20 minutes. As control PBS incubated in an Iodogen iodination tube for 7 min was transferred to a siliconized 1.5 mL tube containing ACPP-14B in MilliQ water (10.4 µL, 45 nmol), and mixed for 20 minutes, followed by LC-MS analysis. Found mass: 4597.3 Da, Calc. mass: 4597.3 Da for ACPP-14B.

For this indirect labeling procedure, a ~60% labeling yield was typically observed by radio-TLC as described before. Unpure ^{125}I-ACPP-14B, mixed with 500 uL 0.1% TFA in MilliQ, was purified by solid phase extraction on a light C_8 Sep-Pak cartridge (Waters). Unfortunately, a >95% radiochemical purity could not be achieved. In detail, the cartridge was washed with 5x1 mL 0.1% TFA in MilliQ after peptide loading. Subsequently, the cartridge was washed with 1 mL 20% EtOH in MilliQ, 1 mL 30% EtOH in MilliQ, 1 mL 50% EtOH in MilliQ, 1 mL 70% EtOH in MilliQ, and 1 mL 96% EtOH in MilliQ. All solutions contained 0.1% TFA. Radioactivity (in MBq) of all fractions was determined, followed by radiochemical purity analysis of fractions of interest using radio-TLC.

Statistical methods

Quantitative data were expressed as mean ± SD. The means of the groups were compared by the parametric Welch's t test. All tests were one-tailed, and P values of less than 0.05 indicate significant differences. GraphPad Prism was used for all statistical calculations.

References

1. Strongin AY, Collier I, Bannikov G, et al. Mechanism of Cell Surface Activation of 72-kDa Type IV Collagenase: Isolation of the Activated Form of the Membrane Metalloprotease. *J. Biol. Chem.* 1995;270:5331–5338

2. Dixon JA, Gaillard II WF, Rivers WT, et al. Heterogeneity in MT1-MMP Activity with Ischemia-Reperfusion and Previous Myocardial Infarction: Relation to Regional Myocardial Function. *Am. J. Physiol. Heart Circ. Physiol.* 2010;299:H1947-1958

3. Tatti O, Vehviläinen P, Lehti K, et al. MT1-MMP releases latent TGF-beta1 from endothelial cell extracellular matrix via proteolytic processing of LTBP-1. *Exp. Cell Res.* 2008;314:2501-2514

4. Ogura S, Ohdaira T, Hozumi Y, et al. Metastasis-related Factors Expressed in pT1 pN0 Breast Cancer: Assessment of Recurrence Risk. *J. Surg. Oncol.* 2007;96:46-53

5. Rozanov DV, Savinov AY, Williams R, et al. Molecular Signature of MT1-MMP: Transactivation of the Downstream Universal Gene Network in Cancer. *Cancer Res.* 2008; 68:4086-4096

6. Tsunezuka Y, Kinoh H, Takina T, et al. Expression of Membrane-type Matrix Metalloproteinase 1 (MT1-MMP) in Tumor Cells Enhances Purlmonary Metastasis in an Experimental Metastasis Assay. *Cancer Res.* 1996;56:5678-5683

7. Schneider F, Sukhova GK, Aikawa M, et al. Matrix Metalloproteinase-14 Deficiency in Bone Marrow–derived Cells Promotes Collagen Accumulation in Mouse Atherosclerotic Plaques. *Circulation.* 2008;117:931–939

8. Deschamps AM, Yarbrough WM, Squires CE, et al. Trafficking of the Membrane Type-1 Matrix Metalloproteinase in Ischemia and Reperfusion: Relation to Interstitial Membrane Type-1 Matrix Metalloproteinase Activity. *Circulation*. 2005;111:1166-1174

9. Spinale FG, Escobar GP, Mukherjee R, et al. Cardiac-Restricted Overexpression of Membrane Type-1 Matrix Metalloproteinase in Mice: Effects on Myocardial Remodeling With Aging. *Circ. Heart Fail*. 2009;2:351-360

10. Skavdahl M, Steenbergen C, Clark J, et al. Estrogen Receptor-β Mediates Male-female Differences in the Development of Pressure Overload Hypertrophy. *Am. J. Physiol. Heart Circ. Physiol.* 2005;288:H469–H476

11. Spinale FG, Mukherjee R, Zavadzkas JA, et al. Cardiac Restricted Overexpression of Membrane Type-1 Matrix Metalloproteinase Causes Adverse Myocardial Remodeling following Myocardial Infarction. *J. Biol. Chem.* 2010;285:30316-30327

12. Zhu L, Wang H, Wang L, et al. High-affinity Peptide Against MT1-MMP for In Vivo Tumor Imaging. *J. Cont. Release.* 2011;150:248-255

13. Park B-H, Chang Y, Lee Y, et al. Targeting of Membrane-Type1-Matrix Metalloproteinase (MT1-MMP) using Superparamagnetic Nanoparticles in Human Liver Cells. *Coll. Surf. A: Physicochem. Eng. Aspects.* 2008;313-314:647-650

14. Van Steenkiste M, Oltenfreiter R, Frankenne F, et al. Membrane Type 1 Matrix Metalloproteinase Detection in Tumors, Using the Iodinated Endogenous [123I]-Tissue Inhibitor 2 of Metalloproteinases as Imaging Agent. *Cancer Biother. Radiopharm.* 2010;25:511-520

15. Kuge Y, Takai N, Ogawa Y, et al. Imaging with Radiolabelled Antimembrane Type 1 Matrix Metalloproteinase (MT1-MMP) Antibody: Potentials for Characterizing Atherosclerotic Plaques. *Eur. J. Nucl. Med. Mol. Imaging.* 2010;37:2093-2104

16. Ouyang M, Lu S, Li X-Y, et al. Visualization of Polarized Membrane Type 1 Matrix Metalloproteinase Activity in Live Cells by Fluorescence Resonance Energy Transfer Imaging. *J. Biol. Chem.* 2008;283:17740-17748

17. Ouyang M, Huang H, Shaner NC, et al. Simultaneous Visualization of Protumorigenic Src and MT1-MMP Activities with Fluorescence Resonance Energy Transfer. *Cancer Res.* 2010;70:2204-2212

18. Watkins GA, Jones EF, Scott Shell M, et al. Development of an Optimized Activatable MMP-14 Targeted SPECT Imaging Probe. *Bioorg. Med. Chem.* 2009;17:653-659

19. Kridel SJ, Sawai H, Ratnikov BI, et al. A Unique Substrate Binding Mode Discriminates Membrane Type-1 Matrix Metalloproteinase from Other Matrix Metalloproteinases. *J. Biol. Chem.* 2002;277:23788–23793

20. Zhu L, Zhang F, Ma Y, et al. In Vivo Optical Imaging of Membrane-Type Matrix Metalloproteinase (MT-MMP) Activity. *Mol. Pharm.* 2011;8:2331-2338

21. van Duijnhoven SMJ, Robillard MS, Nicolay K, et al. Tumor Targeting of MMP-2/9 Activatable Cell-Penetrating Imaging Probes is Caused by Tumor-Independent Activation. *J. Nucl. Med.* 2011;52:279-286

22. Giambernardi TA, Grant GM, Taylor GP, et al. Overview of Matrix Metalloproteinase Expression in Cultured Human Cells. *Matrix Biology.* 1998;16:483-496

23. Durbin PW, Jeung N, Kullgren B, et al. Gross Composition and Plasma and Extracellular Water Volumes of Tissues of a Reference Mouse. *Health Phys.* 1992;63:427–442

24. Aguilera TA, Olson ES, Timmers MM, et al. Systemic In Vivo Distribution of Activatable Cell Penetrating Peptides is Superior to That of Cell Penetrating Peptides. *Integr. Biol.* 2009;1:371-381

25. Galli C, and Mandolini L. The Role of Ring Strain on the Ease of Ring Closure of Bifunctional Chain Molecules, *Eur. J. Org. Chem.* 2000;2000:3117–3125

26. *Guide for the Care and Use of Laboratory Animals*. Washington, DC: Government Printing Office; 1985. NIH publication 86-23

27. Lutgens E, Daemen M, de Muinck ED, et al. Chronic Myocardial Infarction in the Mouse: Cardiac Structural and Functional Changes. *Cardiovasc. Res.* 1999;41:586–593

Chapter **6**

Development of a radiolabeled cell penetrating peptide activatable by angiotensin converting enzyme

Abstract

Angiotensin converting enzyme (ACE) plays an important role in adverse cardiac remodelling. Here, we aimed to develop a radiolabeled activatable cell penetrating peptide (ACPP) sensitive to the dipeptidyl-carboxypeptidase ACE for the future detection of elevated ACE levels in cardiac remodelling. Computational chemistry approaches were applied to assist in the design of ACE-sensitive ACPPs. Unfortunately, the tested ACPPs were not cleaved by ACE.

Introduction

The dipeptidyl carboxypeptidase angiotensin converting enzyme (ACE) is a component of the renin-angiotensin system (RAS), a key regulator of blood pressure and fluid and electrolyte homeostasis (1). The main function of ACE is the degradation of Angiotensin I to the biologically active peptide Angiotensin II. Angiotensin II interacts with the Angiotensin II type 1 receptor, thereby mediating a wide variety of biological effects, including vasoconstriction and hypertrophy of the heart vessel (2). ACE is primarily present as a transmembrane protein on the endothelium, epithelium, and sarcolemma (1,3). However, a soluble form is present in plasma as a result of proteolytic shedding of ACE (1). Nevertheless, the tissue ACE activity, but not circulating ACE activity, has been indicated to be responsible for all the essential physiological effects (4). Under normal physiological conditions the lungs are the main site of ACE expression (5). However in the presence of cardiovascular abnormalities, the heart is the predominant organ of ACE expression (6,7). Upregulated heart-associated ACE activity has been observed in the early and late phases of cardiac remodeling in near-to-all cardiovascular diseases, including hypertension, atherosclerosis, myocardial infarction, heart failure, and diabetes and has a potent adverse effect on the heart and the cardiovascular system (8-14). Blocking of ACE by administration of ACE inhibitors has proven to be beneficial in these cardiovascular diseases in most patients (15-21). However, not all patients do benefit from ACE inhibitors, and some of these patients suffered from adverse effects of the therapy (22). Molecular imaging of ACE has been proposed as a valuable method to monitor cardiac remodeling and help clinicians to predict which patients will benefit from ACE inhibitor therapies (7,23,24). Several radiolabeled ACE inhibitors for nuclear imaging purposes have been developed in recent years (25-28). These imaging probes have been successfully applied in the *in vivo* imaging of organs with high ACE concentrations under normal physiological conditions (25,27). Furthermore, a first *ex vivo* study showed great promise for the detection of ACE in infarcted and non-infarcted segments of the heart (28). In addition, fluorescence resonance energy transfer (FRET) ACE-activatable molecular imaging probes have been developed, mainly for application in *in vitro* bioassay screens for drug development (29). Here, we aimed to develop a radiolabeled ACE activatable cell penetrating peptide (ACPP) for molecular imaging of ACE activity (Fig. 6.1).

In contrast to the substrates applied in ACPPs for the endopeptidase MMP-2/9, and MMP-14, discussed in the previous chapters, the substrate for a dipeptidyl-carboxypeptidase ACE ACPP cannot be inserted between the cell penetrating peptide and neutralizing domain in a linear fashion, because ACE is requiring a C-terminal carboxylic acid group for recognition. In a commercially available ACE FRET probes, a fluorophore was conjugated to the ε-amino group of a lysine residue present at the C-terminus in the ACE substrate RPPGFSA-FK-OH (29). In our approach, the same peptide substrate was used for the development of proof-of-concept ACE ACPPs. The polyanionic neutralizing domain was connected to the ε-amino group of the lysine, leaving the C-terminal carboxylic acid intact. The polycationic CPP domain was conjugated to the N-terminus of the ACE-substrate (Fig. 6.1). The ACE catalytic

pocket is deeply embedded in the interior of the enzyme, with only a narrow cleft giving access from two sides. Because of this, the question arises whether an ACE substrate functionalized with the hybridized polycationic and polyanionic domain can enter the active site. It may be necessary to use linker residues between the ACE substrate and the polycationic and polyanionic domains for more flexibility and spacing. In a first experiment, it was assessed if conjugation of polyethylene glycol (PEG) to the C-terminal lysine of the ACE substrate affects the ACE cleavage rate. Then, molecular dynamics simulations were performed in which the ACE substrate was combined with several linkers to identify substrate-linker domains for application in an ACE ACPP. Three different ACE ACPPs were designed, synthesized, and screened *in vitro*.
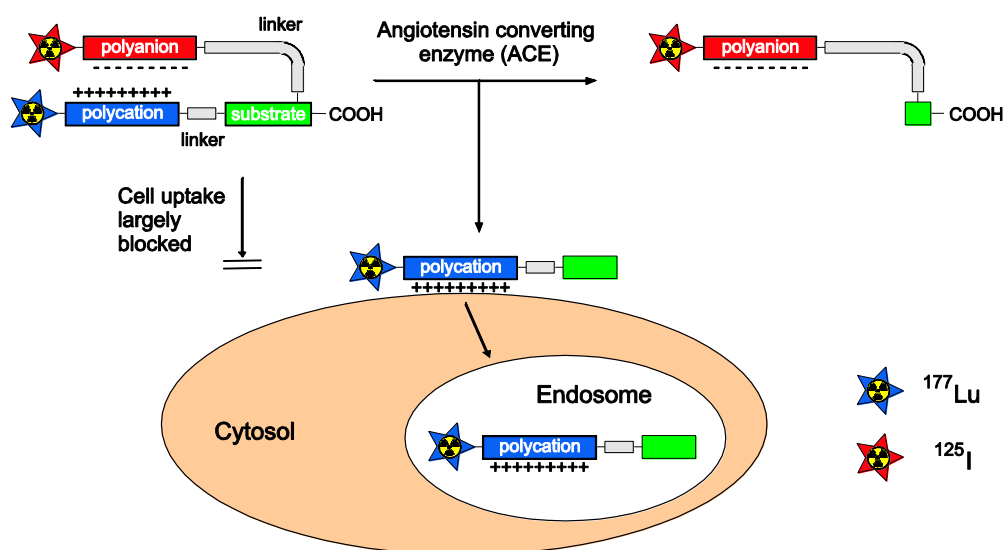
Figure 6.1: *Mechanism and structure of (dual isotope) radiolabeled ACE activatable ACPPs. (A) The cell penetrating property of a polycationic peptide is masked by a polyanionic peptide, which is conjugated to the ε-amino group of the C-terminal lysine of the ACE substrate. Cleavage of the substrate by ACE releases the polycationic cell penetrating peptide, which will transfer the radio-isotope ^{177}Lu across the cell membrane, while the polyanionic domain together with the radio-isotope ^{125}I will be cleared by the kidneys.*

Results

ACE sensitivity of Ac-RPPGFSA−FK(PEG$_8$)-OH

A PEG$_8$ functionalized analog, Ac-RPPGFSAFK(PEG$_8$)-OH, of the commercially available ACE-sensitive FRET probe Mca-RPPGFSAFK(Dnp)-OH was successfully prepared by Fmoc solid-phase peptide synthesis and purified by reversed phase – HPLC (Fig. 6.2). Liquid chromatography – mass spectrometry (LC-MS) analysis demonstrated a >95% pure peptide with a molecular mass consistent to its theoretical mass (Fig. 6.3A). Incubation of this peptide (0.1 mM), as well as the FRET peptide Mca-RPPGFSAFK(Dnp)-OH, with ACE (3.0 nM) yielded near-to-complete cleavage after 20 min and complete cleavage after 1h, indicating efficient cleavage for both peptides (Fig. 6.3). This result suggests that PEG-linkers may be useful for the development of an ACE ACPP.
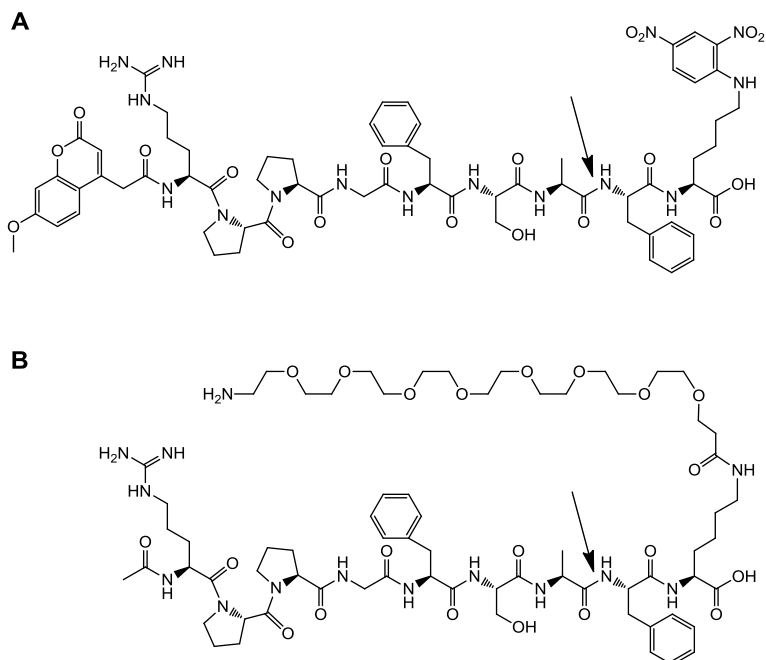
Figure 6.2: *(A) Molecular structure of the FRET ACE probe Mca-RPPGFSAFK(Dnp)-OH. A methoxycoumarin (MCA) fluorophore is present at the N-terminus and the ε-amino group of the C-terminal lysine bears the dinitrophenyl (Dnp) quencher. (B) Molecular structure of Ac-RPPGFSAFK(PEG$_8$)-OH. The arrow indicates the peptide bond that is expected to be cleaved by ACE.*
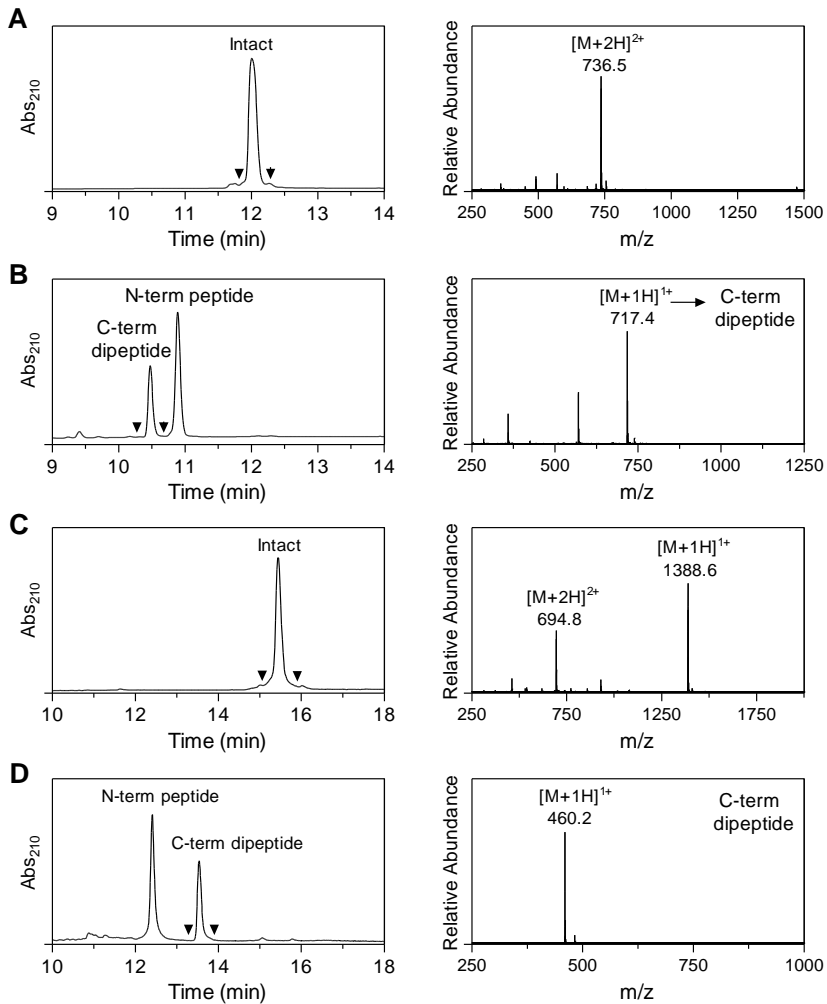
Figure 6.3: *LC-MS characterization of Ac-RPPGFSAFK(PEG$_8$)-OH and Mca-RPPGFSAFK(Dnp)-OH (0.1 mM) before and after incubation with ACE (3.0 nM) for 1h. (A) LC chromatogram (UV) of Ac-RPPGFSAFK(PEG$_8$)-OH and MS spectra of the UV-peak bracketed by the arrowheads (obsd. 1470.8 Da, calcd. 1470.8 Da). (B) LC chromatogram (UV) of Ac-RPPGFSAFK(PEG$_8$)-OH after 1h ACE cleavage and MS spectra of the UV-peak bracketed by the arrowheads (obsd. 716.4 Da, calcd. 716.4 Da for C-term dipeptide). (C) LC chromatogram (UV) of Mca-RPPGFSAFK(Dnp)-OH and MS spectra of the UV-peak bracketed by the arrowheads (obsd. 1387.6 Da, calcd. 1387.6 Da). (D) LC chromatogram (UV) of Mca-RPPGFSAFK(Dnp)-OH after 1h ACE cleavage and MS spectra of the UV-peak bracketed by the arrowheads (obsd. 459.2 Da, calcd. 459.2 Da for C-term dipeptide).*

Molecular modelling

Docking studies were performed to assist in the design of an ACE sensitive ACPP. The starting point of simulations was a structure of the ACE enzyme co-crystallized with a pseudo peptide inhibitor (PDB code 3BKK) from the protein data bank (PDB). As no crystallized structure exists of the enzyme with a substrate, the substrate H_2N-RPPGFSAFK-OH was first docked into the catalytic site with the GOLD docking program (30). Then, PEG linkers were added and optimized with a graphical interface (MOE), as well as the polycationic and polyanionic domains. As mentioned before, the ACE catalytic pocket is deeply embedded in the interior of the enzyme, with only a narrow cleft giving access from two sides. We looked into the design of ACPPs with two different conformations with respect to ACE. In the first conformation, the two charged domains are dissociated and lie on opposite ends of the enzyme. In this configuration, one of the charged domains needs to travel through the narrow cleft to facilitate entering of the substrate into the catalytic site. Secondly, we investigated a conformation wherein both charged domains are associated to each other on the same side of the enzyme, and only the substrate + linker residues have to enter the ACE cavity, while both charged domains remain bound at the exterior on the same side of the cleft. Probes of the first conformation are less promising as the charged domains have to dissociate, which is not favorable, and furthermore one of the charged domains has to pass the narrow cleft.

For the first conformation, it was found that the probe should contain a PEG_6 linker (or longer) on both sides of the ACE substrate. We have called this probe ACE ACPP-1 (Fig. 6.4A). For the second conformation, we found that a PEG_6 linker (or longer) between the N-terminal site of the substrate and the polycationic domain is sufficient, while a PEG_{20} (or longer) linker is needed to bridge the distance between the C-terminal lysine of the substrate and the polyanionic domain (Fig. 6.4B). This probe has been called ACE ACPP-2. Next to these two probes, a non-activatable ACE ACPP was designed (ACE non-ACPP), wherein the polyanionic domain was directly coupled to the C-terminal lysine ε-amino group.

Final probe design

The structures of the designed probes are displayed in Figure 6.5. The polycationic domain consists of nine arginine residues, while the polyanionic domain contains nine glutamic acids. For potential use of ACE ACPP in dual-isotope studies, similar to ^{177}Lu/^{125}I-dACPP described in Chapters 2 and 3, we aimed for conjugation of a DOTA chelate to the polycationic domain for ^{177}Lu labeling and introduction of a tyrosine residue, for ^{125}I conjugation, to the polyanionic domain.
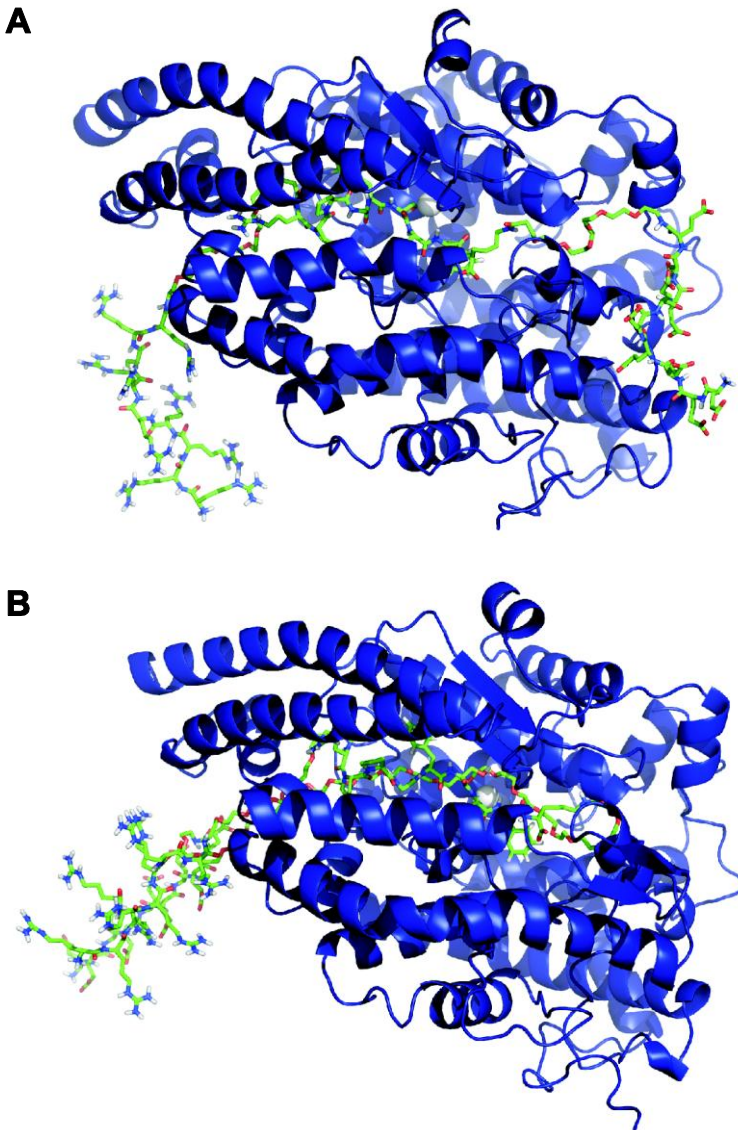
Figure 6.4: *Conformation of ACE ACPP-1 and ACE ACPP-2 peptide within the ACE binding site. ACE is shown as a cartoon, the catalytic zinc ion is shown as a grey sphere in the centre of the enzyme, and the peptide structures are shown as sticks. (A) ACE ACPP-1. The two charged domains are dissociated and lie on opposite ends of the enzyme, enabled by PEG$_6$ linkers on both sides of the ACE substrate. (B) ACE ACPP-2. Both charged domains are associated to each other on the same side of the enzyme. For this latter conformation a PEG$_6$ linker at the N-terminus of the substrate and a PEG$_{20}$ linker conjugated to the C-terminal lysine ε-amino group are required.*

A

B

C
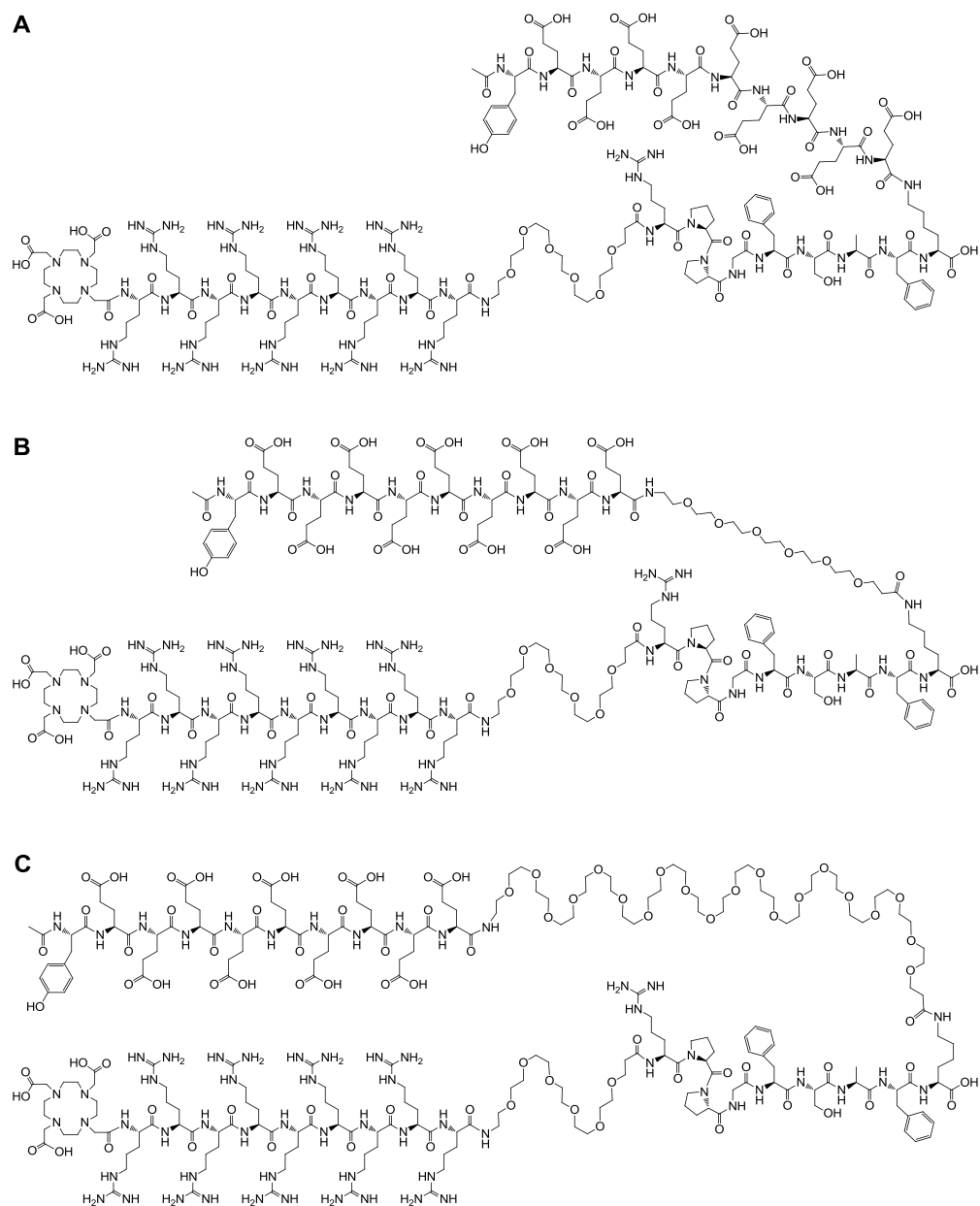
Figure 6.5: *Molecular structures of the designed probes. (A) DOTA-R$_9$-PEG$_6$-RPPGFSAFK(Ac-Y-E$_9$)-OH (ACE non-ACPP*), (B) DOTA-R$_9$-PEG$_6$-RPPGFSAFK(Ac-Y-E$_9$-PEG$_6$)-OH (ACE ACPP-1*), and (C) DOTA-R$_9$-PEG$_6$-RPPGFSAFK(Ac-Y-E$_9$-PEG$_{20}$)-OH (ACE ACPP-2*).*

In vitro ACE assay

The three designed probes (all without the DOTA chelate) were obtained from GenScript and incubated with angiotensin converting enzyme. The negative control, ACE non-ACPP, showed no sensitivity towards ACE as expected. Unfortunately, ACE also did not cleave the other ACE ACPPs (Fig. 6.6), while the FRET probe Mca-RPPGFSAFK(Dnp)-OH was fully cleaved under similar conditions (Fig. 6.6).
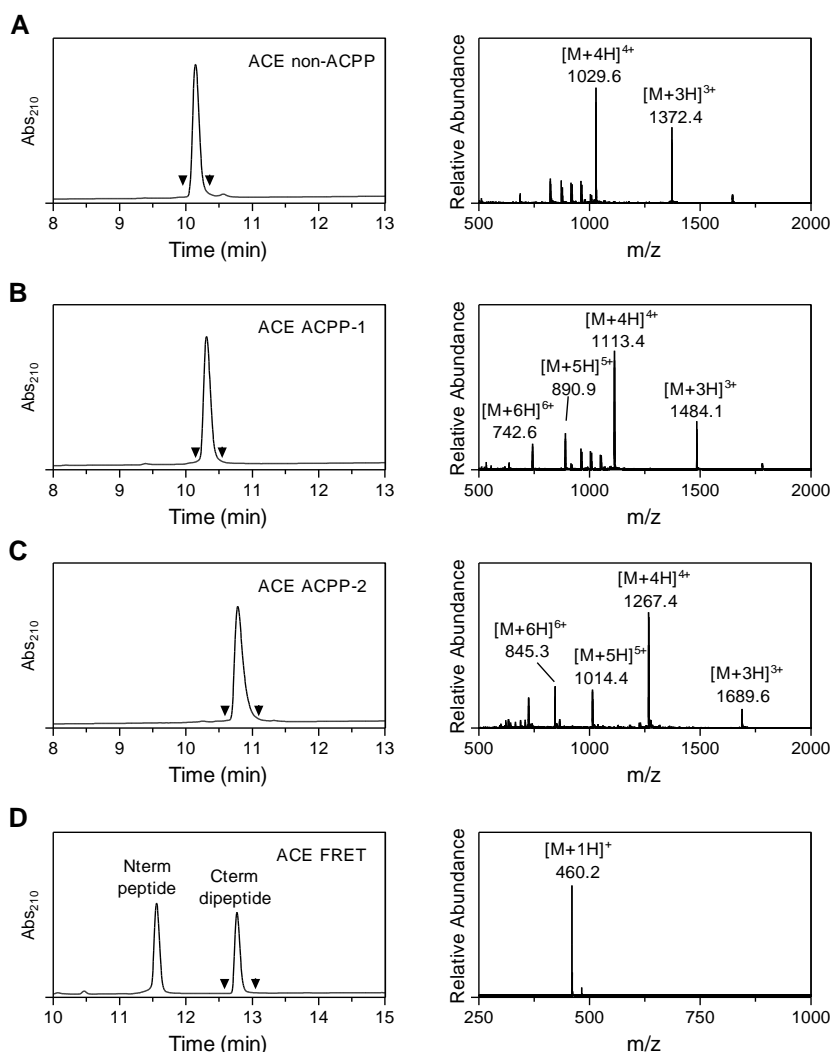

Figure 6.6: *LC-MS characterization of (A) ACE non-ACPP, (B) ACE ACPP-1, (C) ACE ACPP-2, and (D) Mca-RPPGFSAFK(Dnp)-OH (ACE FRET) (0.1 mM) after incubation with ACE (3.0 nM) for 2h. The left and right graphs show the UV absorbance chromatogram and the mass spectrum of the UV-peak bracketed by the arrowheads, respectively.*

Molecular dynamic simulations, carried out with GROMACS (31), suggested that the PEG_{20} chain of ACE ACPP-2 may interfere with the ACE substrate for binding to the zinc ion in the catalytic site (Fig. 6.7). Therefore, ACE ACPP-2 may have entered the ACE catalytic site with masking of the substrate by the PEG-chain. In that case, the probe may possess ACE inhibiting activity. To assess whether ACE ACPP-2 could penetrate the ACE enzyme to act as an ACE inhibitor, a competition experiment was performed, wherein the ACE sensitive peptide Mca-RPPGFSAFK(Dnp)-OH was incubated with ACE in the presence or absence of a 10-fold excess of ACE ACPP-2. The peptide Mca-RPPGFSAFK(Dnp)-OH was cleaved by a similar rate by ACE under both conditions, while ACE ACPP-2 remained intact (Fig. 6.8), suggesting that ACE ACPP-2 did not inhibit ACE activity and could not penetrate the catalytic site.
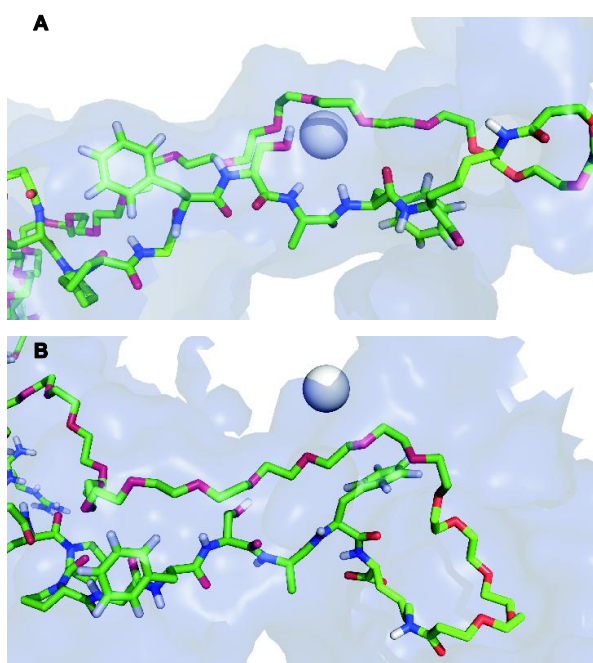

Figure 6.7: *Interaction of ACE ACPP-2 with the catalytic zinc in ACE (A) before and (B) after 1 ns molecular dynamic simulation showing the interference of the PEG_{20}-linker with the zinc ion. For clarity reasons, the structure of ACE is not shown; the surface represents the shape of the binding site cavity.*
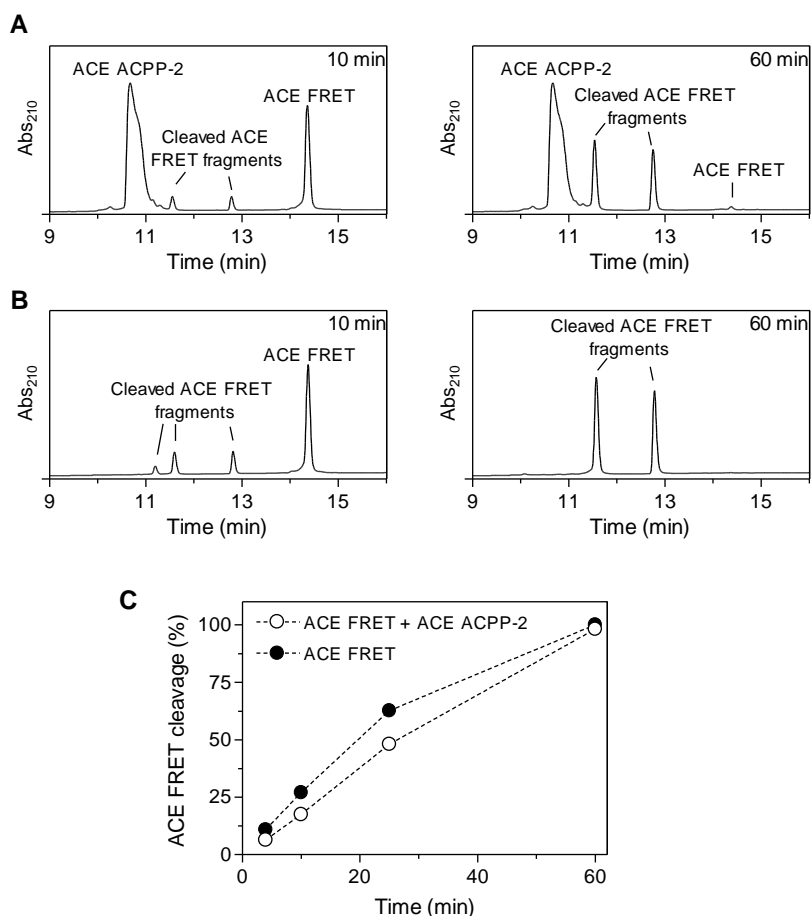
Figure 6.8: *Mca-RPPGFSAFK(Dnp)-OH (ACE FRET) sensitivity towards ACE. LC chromatograms of ACE-FRET (0.1 mM) 10 min and 60 min after incubation with ACE (1.5 nM) in (A) the presence or (B) absence of ACE ACPP-2 (1.0 mM). (C) Percentage cleaved ACE FRET overtime for both conditions.*

Discussion

The present study aimed for the development of radiolabeled activatable cell penetrating peptide probes (ACPPs) for sensing angiotensin converting enzyme (ACE) activity. The development of an ACE ACPP imaging probe was challenging due to two factors. First, the catalytic pocket of ACE is deeply embedded in the interior of the enzyme and therefore linker residues may be necessary between the ACE substrate and the polycationic and polyanionic domain for efficient penetration of the probe into the catalytic site. And second, ACE is a dipeptidyl-carboxypeptidase, which implies that the ACE substrate could not be inserted between the cell penetrating peptide and neutralizing domain in a linear fashion. Inspired by

commercial available ACE FRET probes, we focussed on the conjugation of a polyanionic neutralizing domain to the ε-amino group of a C-terminal lysine present in the ACE substrate, and coupling of the polycationic CPP domain to the N-terminus of the ACE-substrate. The peptide sequence RPPGFSA−FK-OH, containing a C-terminal lysine, was applied as ACE substrate for the development of proof-of-concept ACE ACPPs (Fig. 6.1). In a first study we assessed whether polyethylene glycol (PEG) spacers could be used to link the charged peptide domains to the substrate. In this experiment, a PEG_8 functionalized analog of the FRET probe Mca-RPPGFSAFK(Dnp)-OH was synthesized, Ac-RPPGFSAFK(PEG_8)-OH, and this probe showed a similar cleavage rate by ACE compared to its FRET probe analog. Since modification of the lysine ε-amino group showed to be successful, we continued in the development of an ACE ACPP. Guided by molecular modelling, three different ACE ACPPs were designed. In short, following docking of the substrate into the ACE catalytic site, PEG linkers and the charged polycationic and polyanionic domains were coupled to the substrate to create the ACE ACPPs. The modelling studies revealed two different probes, ACE ACPP-1 and ACE ACPP-2. Both probes fit the catalytic site of ACE, but ACE ACPP-1 requires the dissociation of the polycationic and polyanionic domains, whereas this dissociation is not required for ACE ACPP-2 that consisted of a longer PEG linker between the substrate and the polyanionic domain. In these molecular modelling studies, the substrate was first docked into catalytic site and then extended with PEG chains and the polycationic and polyanionic domains to build the ACE ACPPs. A molecular dynamic simulation assessing whether ACE ACPP-1 and ACE ACPP-2 can enter the catalytic site was not performed. Next to ACE ACPP-1 and ACE ACPP-2, a control probe, ACE non-ACPP, was designed, wherein the polyanionic peptide domain was directly coupled to the lysine ε-amino group. This probe should not fit in the catalytic pocket of ACE. Unfortunately, none of these probes showed any sensitivity to ACE. For ACE ACPP-1, the estimated effective molality E_m is ~10 mM, a ~1000 fold higher than the intermolecular affinity of the two domains and therefore dissociation may not have occured. The extended chain conformation of the PEG_{20} linker required for ACE ACPP-2 to enable the entering of the probe into the catalytic site will be associated with an entropic penalty arising from locking this conformation in place (i.e. preventing more favorable random coil or helical conformations), which may have hampered the probe from entering the catalytic site. Alternatively, the modelling studies suggested that the PEG_{20} chain may interfere with the ACE substrate for binding to the catalytic zinc, thereby masking the ACE substrate. Thereto, we determined if ACE ACPP-2 could penetrate the ACE enzyme and subsequently block the catalytic site by performing a competition experiment between ACE ACPP-2 and the FRET probe Mca-RPPGFSAFK(Dnp)-OH. A comparable cleavage rate was observed for this FRET probe in the absence or presence of a 10-fold excess of ACE ACPP-2. This suggests that ACE ACPP-2 could not enter the ACE catalytic site at all.

Conclusion
Unfortunately, attempts to develop an ACE ACPP did not succeed so far.

Acknowledgements

Materials and methods

Materials

All reagents and solvents were obtained from commercial sources (Sigma-Aldrich, and Biosolve) and used without further purification. 9-fluorenylmethyloxycarbonyl (Fmoc)-protected amino acids and Fmoc-Lys(Mtt)-Wang resin were purchased from either Novabiochem (Merck) or Bachem. Peptides H_2N-R_9-PEG_6-RPPGFSAFK(Ac-Y-E_9)-OH (ACE non-ACPP), H_2N-R_9-PEG_6-RPPGFSAFK(Ac-Y-E_9-PEG_6)-OH (ACE ACPP-1), and H_2N-R_9-PEG_6-RPPGFSAFK(Ac-Y-E_9-PEG_{16})-OH (ACE ACPP-2) were synthesized by GenScript. Peptide Mca-RPPGFSAFK(Dnp)-OH and Angiotensin Converting Enzyme were purchased from R&D Systems.

Probe synthesis

Peptide Ac-RPPGFSAFK$_{Mtt}$-resin was synthesized on an automatic synthesizer (Prelude, Protein Technologies Inc.) by Fmoc solid-phase peptide synthesis (SPPS) using Fmoc-Lys(Mtt)-Wang resin (0.1 mmol), HBTU as the activating reagent, and N,N-Diisopropylethylamine (DIPEA) as base. The Mtt protecting group was selectively removed by incubating Ac-RPPGFSAFK$_{Mtt}$-resin with 1.8% v/v trifluoroacetic acid (TFA) in dichloromethane with 2.0% v/v tri-isopropylsilane (TIS) as scavenger for 10 x 3 min. Fmoc-PEG_8-OH was conjugated to the peptide for 2x20 min in the presence of DIPEA. After Fmoc removal, the peptide was cleaved from the resin by a mixture of 92.5% v/v trifluoroacetic acid (TFA), 5.0% v/v tri-isopropyl silane (TIS), and 2.5% v/v MilliQ (Millipore) water for 2h, filtered, and precipitated in ice cold diethylether. The peptide pellet was dissolved in MilliQ water and purified by preparative reversed-phase high pressure liquid chromatography (RP-HPLC) using an Agilent 1200 apparatus, equipped with a C18 Zorbax column (length = 150 mm, diameter = 21.2 mm, particle size = 5.0 μm). The elution gradient was set from 5 to 30% of buffer B (0.1% TFA in acetonitrile) over 100 min, where buffer A was 0.1% TFA in MilliQ (Millipore) water. The UV wavelength was preset at 210 and 254 nm. All peptides structures were analyzed by LC-MS on an Agilent 1200 apparatus, equipped with a C18 Eclipse plus-column (length = 100 mm, diameter = 2.1 mm, particle size = 3.5 μm) and an electrospray mass spectrometer (Agilent Technologies 6210, Time-of-Flight LC/MS). Found masses: 1470.8 Da for Ac-RPPGFSAFK(PEG_8)-OH (Calcd. 1470.8 Da, 28.1 μmol), 4112.2 Da for H_2N-R_9-PEG_6-RPPGFSAFK(Ac-Y-E_9)-OH (ACE non-ACPP, Calcd. 4112.1 Da), 4447.4 Da for H_2N-R_9-PEG_6-RPPGFSAFK(Ac-Y-E_9-PEG_6)-OH (ACE ACPP-1, Calcd. 4447.3 Da), and 5063.7 Da for H_2N-R_9-PEG_6-RPPGFSAFK(Ac-Y-E_9-PEG_{16})-OH (ACE ACPP-2, Calcd. 5063.7 Da).

In vitro ACE assay Ac-RPPGFSA−FK(PEG$_8$)-OH

Ac-RPPGFSA−FK(PEG$_8$)-OH and Mca-RPPGFSAFK(Dnp)-OH (0.1 mM) were incubated with 3.0 nM ACE in a mixture of 100 mM Tris, 200 mM NaCl, 10 μM ZnCl$_2$, and 0.01% w/v Brij-35 at pH 7.5 at 500 rpm and 37 °C. Samples were taken after 20 min and 1h, ACE was quenched by the addition of TFA (10% v/v), and the samples were analyzed by LC-MS.

In vitro ACE assay ACE ACPPs

ACE non-ACPP, ACE ACPP-1, ACE ACPP-2, and Mca-RPPGFSAFK(Dnp)-OH as control (0.1 mM) were incubated with 3.0 nM ACE in a mixture of 100 mM Tris, 200 mM NaCl, 10 μM ZnCl$_2$, and 0.01% w/v Brij-35 at pH 7.5 at 500 rpm and 37 °C. Samples were taken after 20 min, 2h and 24h, ACE was quenched by the addition of TFA (10% v/v), and the samples were analyzed by LC-MS.

In vitro competition assay ACE ACPP-2 and Mca-RPPGFSAFK(Dnp)-OH

1.5 nM ACE in a mixture of 100 mM Tris, 200 mM NaCl, 10 μM ZnCl$_2$, and 0.01% w/v Brij-35 at pH 7.5, was incubated with ACE ACPP-2 (in MQ, 20% v/v, 1.0 mM) or MQ (20% v/v) at 500 rpm and 37 °C. After 5 min, Mca-RPPGFSAFK(Dnp)-OH (0.1 mM) was added to both mixtures and samples were taken at 4, 10, 25, and 60 min. ACE was quenched by the addition of TFA (10% v/v), and the samples were analyzed by LC-MS.

References

1. Turner AJ, and Hooper NM. The angiotensin-converting enzyme gene family: genomics and pharmacology. *Trends Pharmacol. Sci*. 2002;23:177–183

2. Dzau VJ. Theodore Cooper Lecture: Tissue angiotensin and pathobiology of vascular disease: a unifying hypothesis. *Hypertension*. 2001;37:1047–1052

3. Dell'Italia L, Meng Q, Balcells E, et al. Compartmentalization of angiotensin II generation in the dog heart. Evidence for independent mechanisms in intravascular and interstitial spaces. *J. Clin. Invest.* 1997;100:253–258

4. Esther C, Marino E, Howard T, et al. The critical role of tissue angiotensin-converting enzyme as revealed by gene targeting in mice. *J. Clin. Invest.* 1997;99:2375–2385

5. Ryan JW, Ryan US, Schultz DR, et al. Subcellular localization of pulmonary angiotensin-converting enzyme (kininase II). *Biochem. J.* 1975;146:497–499

6. Gaertner R, Prunier F, Philippe M, et al. Scar and pulmonary expression and shedding of ACE in rat myocardial infarction. *Am. J. Physiol. Heart. Circ. Physiol.* 2002;283:H156–H164

7. Chandrashekhar Y, and Narula J. Exposing ACE up the Sleeve… *J. Nucl. Med.* 2007;48: 173-174

8. Okamura T, Miyazaki M, Inagami T, Toda N. Vascular reninangiotensin system in two-kidney, one-clip hypertensive rats. *Hypertension*. 1986;8:560–565

9. Hoshida S, Kato J, Nishino M, et al. Increased angiotensin-converting enzyme activity in coronary artery specimens from patients with acute coronary syndrome. *Circulation.* 2001; 103:630–633

10. Ruzicka M, Yuan B, Harmsen E, et al. The renin-angiotensin system and volume overload-induced cardiac hypertrophy in rats. Effects of angiotensin-converting enzyme inhibitor versus angiotensin II receptor blocker. *Circulation.* 1993;87:921–930

11. Falkenhahn M, Franke F, Bohle RM, et al. Cellular distribution of angiotensin-converting enzyme after myocardial infarction. *Hypertension.* 1995;25:219–226

12. Studer R, Reinecke H, Muller B, et al. Increased angiotensin-I converting enzyme gene expression in the failing human heart. Quantification by competitive RNA polymerase chain reaction. *J. Clin. Invest.* 1994;94:301–310

13. Hirsch A, Talsness C, Schunkert H, et al. Tissue-specific activation of cardiac angiotensin-converting enzyme in experimental heart failure. *Circ. Res.* 1991;69:475–482

14. Szelachowska M, Kretowski A, and Zdrojewicz Z. The increased activity of angiotensin-converting enzyme in patients with diabetes and nephropathy. *Horm. Metab. Res.* 1996;28:250–251

15. Pfeffer MA, Braunwald E, Moye LA, et al. Effect of captopril on mortality and morbidity in patients with left ventricular dysfunction after myocardial infarction. Results of the Survival And Ventricular Enlargement trial. The SAVE Investigators. *N. Engl. J. Med.* 1992;327:669–677

16. The SOLVD Investigators. Effect of enalapril on survival in patients with reduced left ventricular ejection fractions and congestive heart failure. *N. Engl. J. Med.* 1991;325:293–302

17. Hansson L, Lindholm L, Niskanen L, et al. Effect of angiotensinconverting-enzyme inhibition compared with conventional therapy on cardiovascular morbidity and mortality in hypertension: the Captopril Prevention Project (CAPPP) randomised trial. *Lancet.* 1999;353: 611–616

18. Yusuf S, Sleight P, Pogue J, et al. Effects of an angiotensin-converting-enzyme inhibitor, ramipril, on cardiovascular events in high-risk patients. The Heart Outcomes Prevention Evaluation Study Investigators. *N. Engl. J. Med.* 2000;342:145–153

19. Lapointe N, and Rouleau JL. Activation of vascular tissue angiotensin-converting enzyme (ACE) in heart failure: Effects of ACE inhibitors. *J. Am. Cell. Cardiol.* 2002;39:776-779

20. Fox KM. Efficacy of perindopril in reduction of cardiovasculare events among patiens with stable coronary artery disease: randomized, double-blind, placebo-controlled, multicentre trial (the EUROPA study). *Lancet.* 2003;362:782-788

21. Leuschner F, Panizzi P, Chico-Calero I, et al. Angiotensin-converting enzyme inhibition prevents the release of monocytes from their splenic reservoir in mice with myocardial infarction. *Circ. Res.* 2010;107:1364-1373

22. The PEACE Trial Investigators. Angiotensin converting-enzyme inhibition in stable coronary artery disease. *N. Engl. J. Med.* 2004;351:2058–2068

23. Shirani J, Narula J, Eckelman WC, et al. Early imaging in heart failure: Exploring novel molecular targets. *J. Nucl. Cardiol.* 2007;14:100-110

24. Aras O, Messina SA, Shirani J, et al. The role and regulation of cardiac angiotensin-converting enzyme for noninvasive molecular imaging in heart failure. *Curr. Cardiol. Rep.* 2007;9:150-158

25. Hwang DR, Eckelman WC, Mathias CJ, et al. Positron-labeled angiotensin-converting enzyme (ACE) inhibitor: fluorine-18-fluorocaptopril—probing the ACE activity in vivo by positron emission tomography. *J. Nucl. Med.* 1991;32:1730–1737

26. Lee YHC, Kiesewetter DO, Lang L, et al. Synthesis of 4-[18F]fluorobenzoyl lisinopril: a radioligand for angiotensin converting enzyme (ACE) imaging with positron emission tomography. *J. Labelled Compds. Radiopharm.* 2001;44:S268–S270

27. Femia FJ, Maresca KP, Hillier SM, et al. Synthesis and evaluation of a series of $^{99m}Tc(CO)_3^+$ lisinopril complexes for in vivo imaging of angiotensin-converting enzyme expression. *J. Nucl. Med.* 2008;49:970-977

28. Dilsizian V, Eckelman WC, Loredo ML, et al. Evidence for tissue angiotensin-converting enzyme in explanted hearts of ischemic cardiomyopathy using targeted radiotracer technique. *J. Nucl. Med.* 2007;48:182-187

29.   Joyner JC, Hocharoen L, and Cowan JA. Targeted catalytic inactivation of angiotensin converting enzyme by lisinopril-coupled transition-metal chelates. *J. Am. Chem. Soc.* 2012;134: 3396-3410

30.   Jones G, Willet P, and Glen RC. Molecular recognition of receptor sites using a genetic algorithm with a description of desolvation. *J. Mol. Biol.* 1995;245:43-53

Chapter **7**

Towards the development of radiolabeled activatable cell penetrating peptides to sense oxidative stress *in vivo*

Abstract

Increased levels of reactive oxygen and nitrogen species (RONS), and subsequent oxidative stress, has been shown to significantly contribute to the pathogenesis of several diseases. This important role of excess production of RONS in disease has stimulated the development of in particular fluorescent molecular imaging probes. Here, a research project is proposed to develop a radiolabeled activatable cell penetrating peptide (ACPP) sensitive to the RONS hydrogen peroxide (H_2O_2) for the *in vivo* detection and imaging of oxidative stress. In the proposed RONS ACPP probe, the cell penetrating property of a polycationic peptide is masked by a polyanionic peptide, and both domains are fused to each other by a H_2O_2 self-immolative linker. Reaction of the ACPP with H_2O_2 will result in self-immolation of the linker and subsequent release and local entrapment of the radiolabeled polycationic cell penetrating peptide (CPP). A H_2O_2 ACPP is currently in development.

Introduction

Reactive oxygen and nitrogen species (RONS) are formed as a natural byproduct of our metabolism and is tightly controlled by a defense system of antioxidants. Under physiological conditions, about 1-3% of the consumed oxygen is transformed into superoxide ($O_2^{-\cdot}$), followed by further conversion into other RONS such as hydrogen peroxide (H_2O_2), hydroxyl radical ($\cdot OH$), and peroxynitrite ($ONOO^-$) (1,2). The efficient defense system of antioxidants rapidly scavenges most RONS. However during oxidative stress, there is a cellular mismanagement in the balance between the defense system and production of RONS by mitochondria and endothelial enzymes as xanthine oxidase and NADPH oxidase. As a consequence, the levels of ROS and RNS are typically upregulated resulting in the oxidative damage of vital cell and tissue structures (3,4). For example in heart failure, oxidative stress has been associated with the apoptosis of cardiomyocytes and subsequent contractile dysfunction (5-8). Furthermore, oxidative stress has been linked to the activation and increased expression of matrix metalloproteinases (MMPs), enzymes that play a pivotal role in the adverse cardiac remodeling (9,10). In particular, hydrogen peroxide (H_2O_2) is a major ROS byproduct and a common biomarker for oxidative stress (8). Increased levels of H_2O_2 have been observed during the adverse cardiac remodelling as a result of cardiac hypertrophy or myocardial infarction (11,12).

Despite the important role of H_2O_2 and other RONS in disease, studies describing the *in vivo* molecular imaging of oxidative stress for diagnosis and staging are few (13-15). The short half-lifes of most RONS has challenged researchers over the past decade. The relative long half-life of H_2O_2 and its capability to cross cell-membranes, has made H_2O_2 of special interest as target for molecular imaging of oxidative stress. Currently, most molecular imaging approaches have been focused on the visualization of RONS production in single cells in *in vitro* settings using fluorescenctly activatable probes. In these approaches as reviewed in Chapter 1, RONS-specific triggers are conjugated to fluorophores thereby inducing a strong fluorophore-silencing effect. Upon reaction with a specific RONS, the fluorescence will be restored (Scheme 1.1). The first *in vivo* imaging study of oxidative stress employed nanoparticles formulated from peroxalate esters and fluorescent dyes (13). Reaction of the peroxalate esters with hydrogen peroxide resulted in high-energy dioxetanedione intermediates that subsequently facilitated excitation of the encapsulated dye. This probe was used to detect hydrogen peroxide in the peritoneal cavity of mice during a lipopolysaccharide-induced inflammatory response. Hydrogen peroxide production was also visualized in tumor-bearing mice using an activatable bioluminescent probe (Scheme 7.1) (14). This probe was studied in firefly luciferase expressing tumor-bearing mice and showed tumor-specific activation.
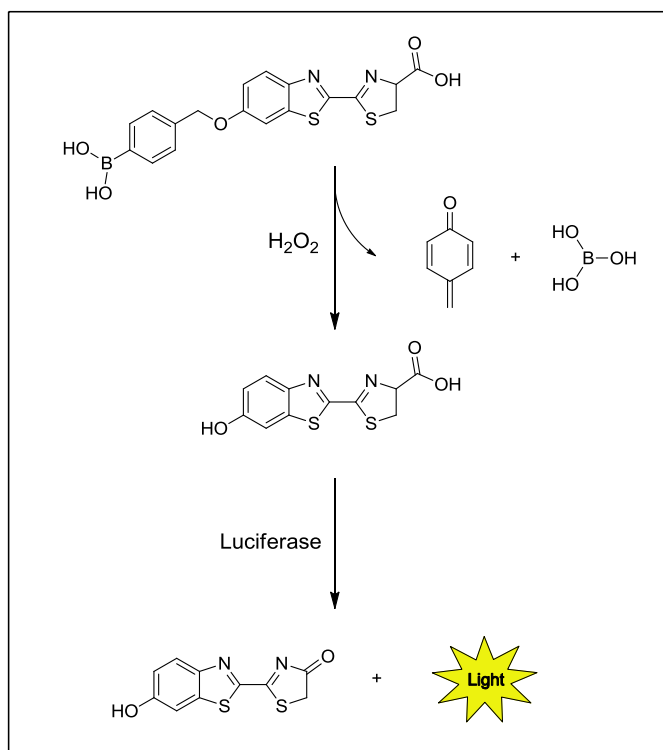
Scheme 7.1: *H$_2$O$_2$ activatable luminescent probe. Reaction of the probe with hydrogen peroxide will release firely luciferin that subsequently will be oxidized by firefly luciferase resulting in a luminescent signal (14).*

Panizzi et al. developed a RONS nanoparticle to which quenched oxazine reporters were conjugated (15). Release of the oxazine reporters by RONS interaction, in particular peroxynitrite and hypochlorous acid, resulted in restoration of its fluorescence. This nanoparticle was studied in a mouse model of myocardial infarction and showed enhancement of oxazine fluorescence in the infarcted areas of the heart. These three papers show that RONS can be detected *in vivo* in small animals, like mice. As reviewed in Chapter 1, fluorescent/bioluminescent imaging probes have limited use for image-based whole-body *in vivo* diagnostics due to the short penetration depth of light. In that respect, molecular imaging probes suitable for magnetic resonance imaging or nuclear imaging would be especially valuable for the future non-invasive detection of oxidative stress in cardiac patients. In this Chapter, we report on the design of a radiolabeled activatable cell penetrating probe (ACPP) for the detection of extracellular levels of H$_2$O$_2$. Subsequently, preliminary results on the synthesis of this probe will be addressed.

Design of a H_2O_2 ACPP for nuclear imaging

In previous chapters ^{177}Lu/^{125}I-dual isotope ACPP probes have been described and developed for enzymatic targets. In these probes, the cell penetrating polycationic peptide and inhibitory polyanionic peptide were conjugated to each other by peptide substrates cleavable by the enzymes of interest. No peptide substrate has however been identified that can be cleaved upon reaction with H_2O_2. Nevertheless, several types of alternative H_2O_2 sensitive domains have been reported that may be applied in the H_2O_2 ACPP imaging probe (16-22) (Fig. 7.1). These domains typically consist of self-immolative building blocks, conjugated to a H_2O_2 specific trigger, that undergo a self-immolative release cascade after reaction with H_2O_2. Scheme 7.2 shows the decomposition for an aniline wedge – H_2O_2 trigger combination and a hemithioaminal spacer – H_2O_2 trigger combination.
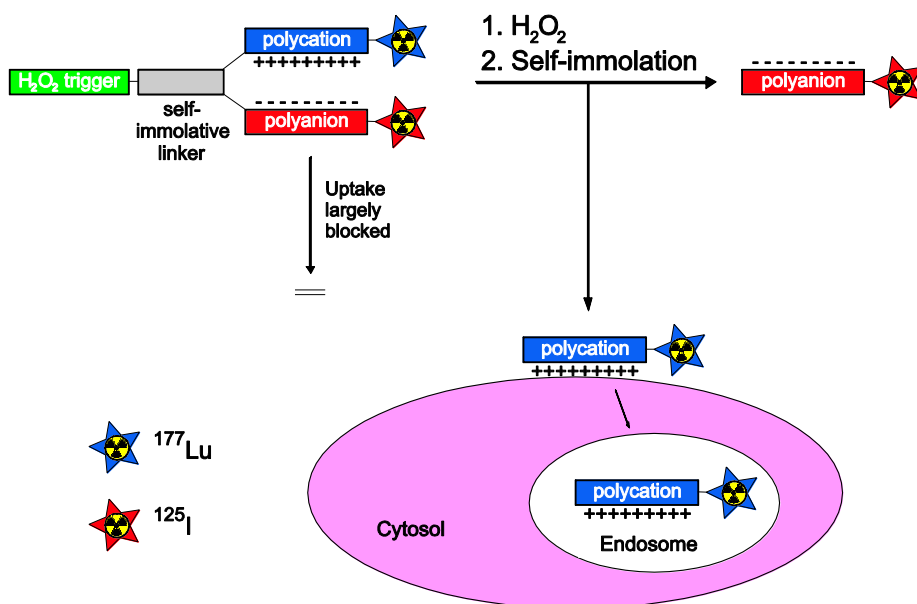
Figure 7.1: *Mechanism of a H_2O_2 activatable cell penetrating probe. The cell penetrating property of a polycationic peptide is masked by a polyanionic peptide, which are fused to each other by a H_2O_2 self-immolative linker. H_2O_2-triggering initiates self-decomposition of the linker, and thereby releases the polycationic cell penetrating peptide (CPP). The activated CPP will transfer its radioactive cargo ^{177}Lu across the cell membrane, while the polyanionic peptide together with ^{125}I will be cleared by the kidneys.*

Aryl boronic acid and esters (Scheme 7.3A) have been extensively used as hydrogen peroxide triggers in various applications such as analyte detection, molecular imaging and drug delivery (14,22-26). Upon contact with hydrogen peroxide, these aryl boron compounds undergo a reaction, which cleaves the boron to form the corresponding phenol derivative (27,28). The mechanism of the reaction between the boronic ester and hydrogen peroxide is shown in Scheme 7.3B.
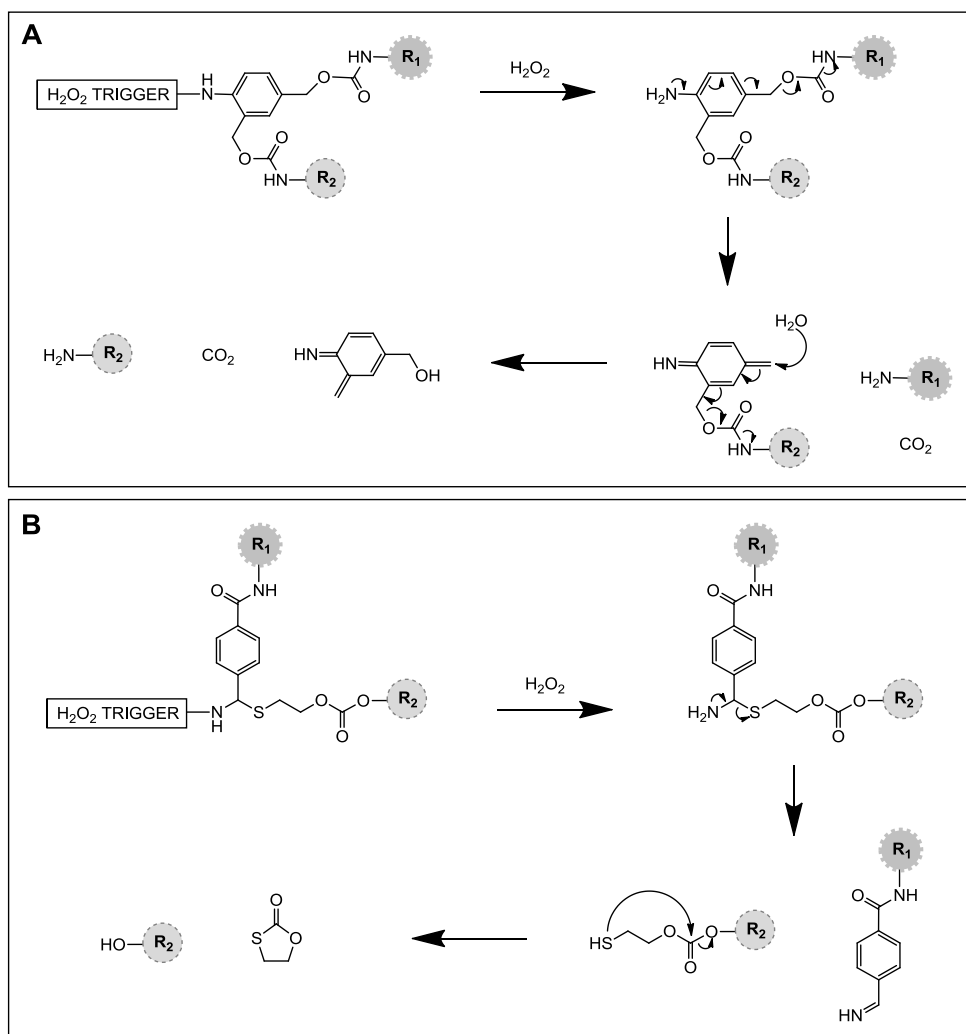
Scheme 7.2: *Mechanism of decomposition of self-immolative linkers. (A) H_2O_2 mediated self-immolation of an aniline wedge – H_2O_2 trigger combination. Reaction with hydrogen peroxide will result in the release of the aniline wedge. In the next step the lone electron pair of the aniline nitrogen initiates an electronic cascade event resulting in the release of the first R-group and carbon dioxide (18). The formed terminal double bond is then attacked by water and the electrons are pushed towards the second carbamate, which then releases the second R-group together with carbon dioxide. (B) H_2O_2 mediated self-immolation of a hemithioaminal spacer – H_2O_2 trigger combination. Reaction with hydrogen peroxide will result in the release of the hemithioaminal spacer. The lone electron pair of the nitrogen will subsequently initiate an electronic cascade event resulting in the release of the first R-group. Then, spontaneous self-immolation will result in the hydrolysis of the carbonate into a thioalkyl carbonate and the second R-group. R_1 and R_2 represent the polycationic and polyanionic peptide domains.*
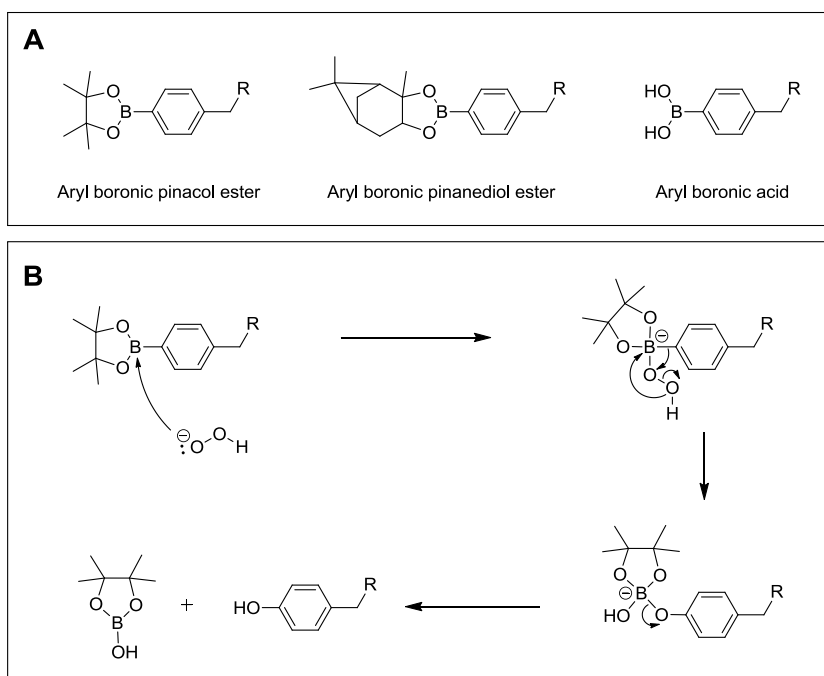
Scheme 7.3: *(A) Molecular structure of aryl boronic pinacol ester, aryl boronic pinanediol ester, and aryl boronic acid. (B) Mechanism of H$_2$O$_2$ mediated deprotection of an aryl boronic pinacol ester into a phenol derivative. Hydrogen peroxide is first activated by a small amount of base to form the peroxide anion, which then attacks the electrophilic boron. Next an aryl shift occurs, where the boron bound oxygen atom inserts into the aryl boron bond. The released hydroxide anion will immediately react with the boron atom resulting in a negatively charged borate anion that subsequently releases the phenol derivative (27,28).*

In various reporter systems, *p*-hydroxy benzyl carbamate linkages are used to conjugate the hydrogen peroxide trigger to the self-immolative wedge functionalized with reporters (22). These carbamate linkages ensure that conversion of the H$_2$O$_2$ trigger into phenol will be followed by a spontaneous self-immolation cascade of the probe (Scheme 7.4). Next to *p*-hydroxy benzyl carbamate, *p*-amino benzyl carbamate (PABC) linkages are well-known self-immolative linkers. For the proposed H$_2$O$_2$ ACPP, we will use a self-immolative strategy for the release of CPP. Various combinations of H$_2$O$_2$ triggers and self-immolative wedges can be applied to generate a family of H$_2$O$_2$ responding ACPPs. Figure 7.2 shows the molecular structure of a potential H$_2$O$_2$ ACPP.
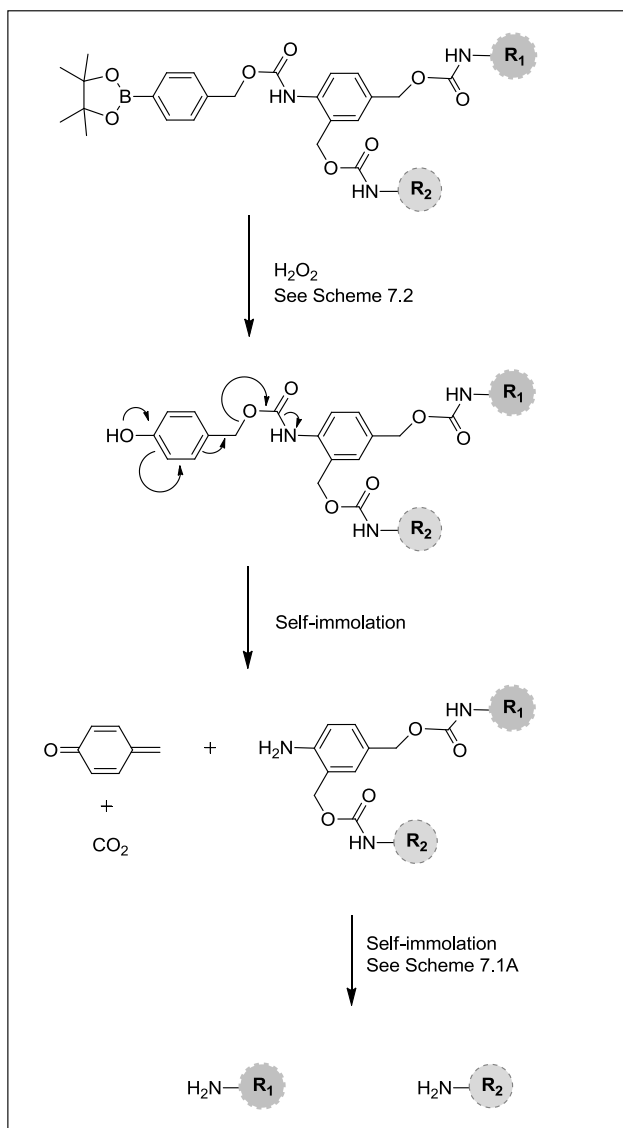
Scheme 7.4: *Proposed mechanism of H_2O_2 mediated self-immolation of an aryl boronic pinacol ester-aniline wedge combination. H_2O_2 will induce the conversion of the aryl boronic pinacol ester into a p-hydroxy benzyl carbamate derivative (Scheme 7.2). One of the free electron pairs of the oxygen then forms a double bond between the oxygen and the aromatic ring, followed by an electronic cascade event resulting in the dissociation of the compound into carbon dioxide and the p-amino benzyl carbamate based aniline wedge. Self-immolation of the aniline moiety will result in the release of the two R-groups (Scheme 7.1A). R_1 and R_2 represent the polycationic and polyanionic peptide domains.*
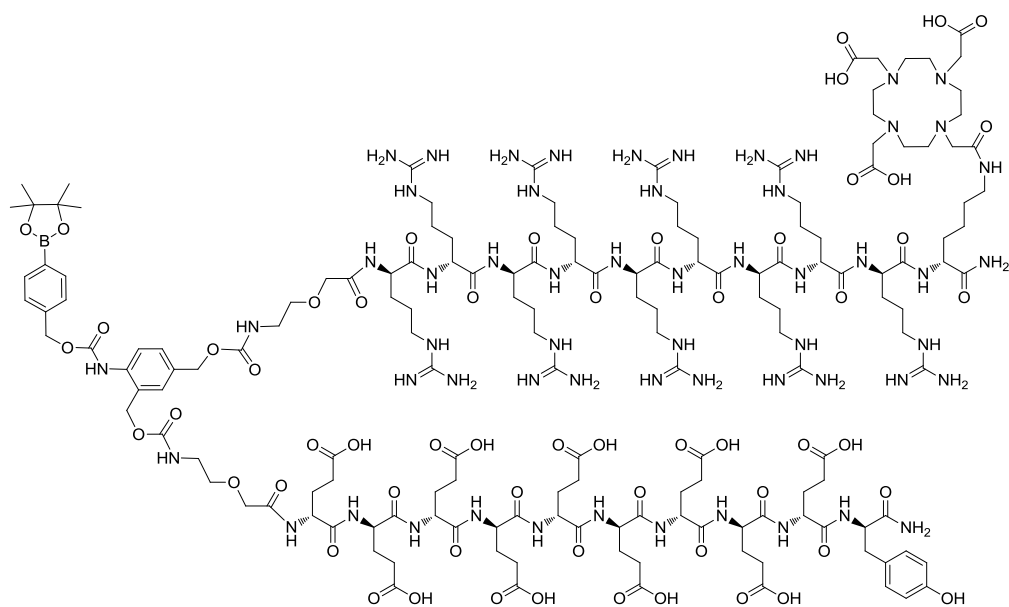
Figure 7.2: *Molecular structure of a potential H₂O₂ ACPP. The probe consists of an aryl boronic pinacol ester conjugated to a self-immolative aniline wedge via a benzyl carbamate linkage. The wedge is functionalized with a DOTA-functionalized polycationic d-peptide, and a tyrosine-polyanionic d-peptide conjugate via p-amino benzyl carbamate linkages. The DOTA chelate can be used for radiolabeling with e.g. ^{177}Lu, while ^{125}I can be conjugated to the tyrosine amino acid, to enable dual-isotope studies. Reaction of this probe with H₂O₂ will result in the release and dissociation of both peptide domains and subsequent local retention of the polycationic peptide.*

Considerations:

-Aryl boronic acid/esters respond to H_2O_2 selectively over other RONS such as nitrix oxide (˙NO), superoxide ($O_2^{-\cdot}$), and lipid peroxides (14). However, recent studies have shown that aryl boronic acids and esters are also highly sensitive towards the RONS peroxynitrite ($ONOO^-$) (29,30), which is mainly produced intracellularly by the reaction of nitric oxide (˙NO) with superoxide ($O_2^{-\cdot}$) (31). Although predominantly present in the cytosol, peroxynitrite is able to cross cell membranes (31) and, therefore, may also contribute to the activation of the proposed ACPP in the extracellular space of tissues subjected to oxidative stress.

-According to several recent papers, aryl boronic acid is more reactive towards H_2O_2 than aryl boronic pinacol ester (32,33). However, Sikora et al. showed a similar second-order rate constant for both H_2O_2 triggers (30).

Short description of performed synthesis so far

We aim for the synthesis of the H$_2$O$_2$ ACPP displayed in Figure 7.2 by coupling the two peptide domains to an aryl boronic pinacol ester-aniline wedge combination. The polycationic peptide domain H$_2$N-O1Pen-r$_9$-k(tri-allyl-DOTA)-NH$_2$, the polyanionic peptide domain H$_2$N-O1Pen-e(allyl)$_9$-y(allyl)-NH$_2$, and the aryl boronic pinacol ester-aniline wedge combination have been successfully synthesized. The coupling of the peptide domains, with side chain protecting groups, to the wedge is subject of current research. Here, the synthesis of the aryl boronic pinacol ester-aniline wedge combination is described briefly.

Synthesis of aryl boronic pinacol ester-aniline wedge

The aryl boronic pinacol ester-aniline wedge combination (**3**) was created by reaction of an aniline wedge (**1**) with boronic pinacol ester (**2**) as shown in Scheme 7.5, following a slightly modified strategy that has been used previously for similar reactions (34,35). The only modification is the use of triphosgene instead of phosgene. Compounds **1** and **2** were synthesized according to reported procedures described in reference (35) and (36), respectively.
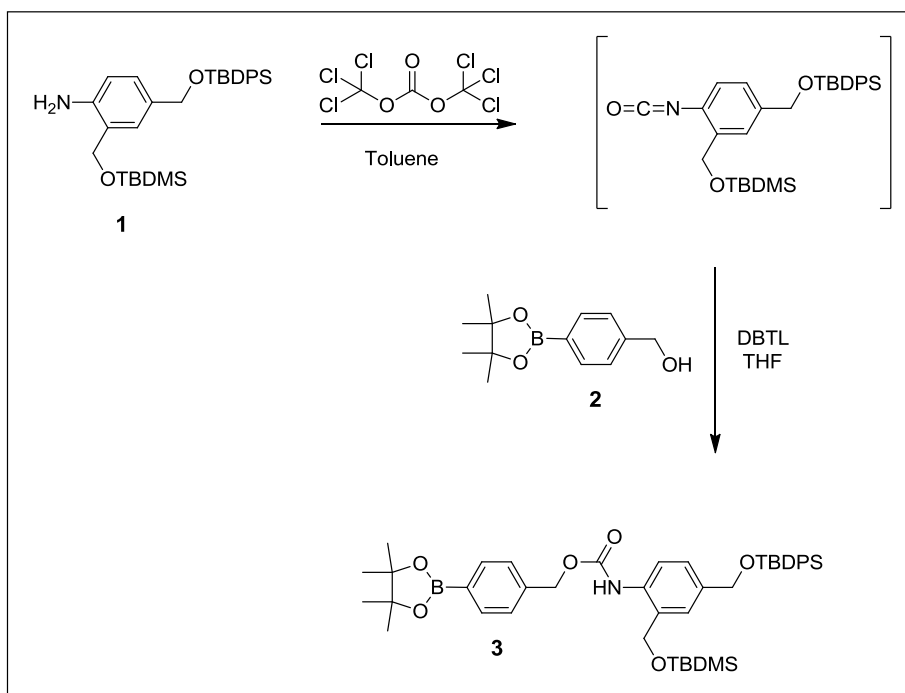
Scheme 7.5: *Synthesis of **3** via activation of **1** with triphosgene and subsequent conjugation to **2** in the presence of catalyst dibutyltin dilaurate (DBTL). Overall yield was 66%. TBDMS and TBDPS are abbreviations for tert-butyldimethylsilyl and tert-butyldiphenylsilyl and function as orthogonal protecting groups for the alcohol moieties.*

Current research is focused on the coupling of the polycationic and polyanionic peptide domains to **3.** The TBDMS group in **3** can be selectively deprotected as previously reported (35), resulting in the alcohol derivative. To form the carbamate bond between the alcohol and the primary N-terminal amine of the peptide domain as shown in Figure 7.2, triphosgene was used to either activate the alcohol or the amine, but in both cases the desired product was not observed (Scheme 7.6A and B). The activation of the alcohol with *p*-nitrophenyl chloroformate and subsequent peptide coupling was not successful either (Scheme 7.6B). The application of other coupling strategies is in progress, *e.g.* the formation of carbamate linkages between compound **3** and small spacers, containing azide or succinimidyl ester (NHS) functionalities, followed by coupling of the peptide domains using click or NHS chemistry.
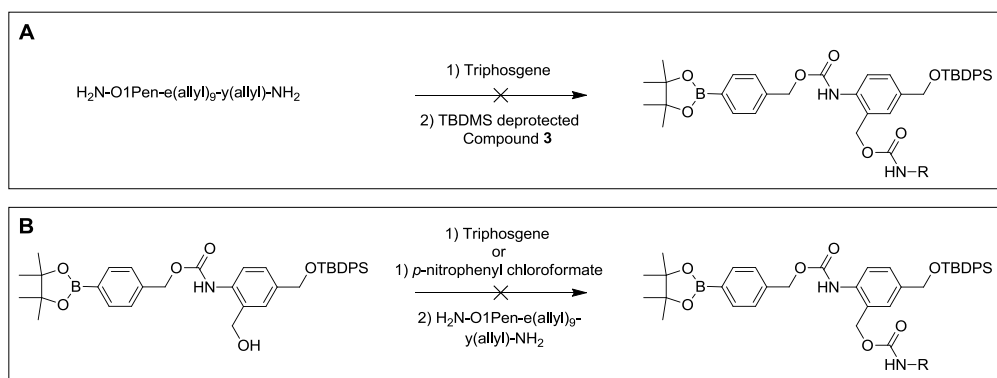
Scheme 7.6: *(A) Reaction scheme of the activation of the peptide and subsequently attachment of the alcohol of TBDMS deprotected compound **3**. (B) Reaction scheme for thriphosgene of p-nitrophenyl chloroformate activation of the alcohol of TBDMS deprotected compound **3** and subsequent coupling of the peptide. R represents peptide O1Pen-e(allyl)$_9$-y(allyl)-NH$_2$.*

Conclusion

Here, a research project is proposed to develop radiolabeled activatable cell penetrating peptide (ACPP) sensitive to the RONS hydrogen peroxide (H$_2$O$_2$) for the *in vivo* detection and imaging of oxidative stress. A H$_2$O$_2$ ACPP, consisting of a H$_2$O$_2$ sensitive self-immolative trigger fusing the polycationic and polyanionic domains, is currently in development.

Materials and methods

Materials

Chemicals and solvents were obtained from commercial sources and used without further purification.

Instrumentation

Column chromatography was performed on a Combiflash Companion automated apparatus equipped with a Teledyne Isco fractions collector, using GraceResolvTM Silica Flash Cartridges. Thin layer chromatography was performed on Merck precoated TLC Silica gel 60 F254 plates. Visualization was accomplished with UV lights and staining with potassium permanganate (0.5 g/100 mL 1M NaOH). ^{1}H NMR spectra were recorded on a Brucker Avance III 300 spectrometer. All spectra were processed with Bruker 1D WIN-NMR software. MALDI-TOF measurements were done on an Applied Biosciences | MDS Sciex, 4800 MALDI TOF/TOF Analyzer. LC-MS was performed on an Agilent 1200 apparatus, equipped with a C18 Eclipse plus-column (length = 100 mm, diameter = 2.1 mm, particle size 3.5 μm) and an electrospray mass spectrometer (Agilent Technologies 6210, Time-of-Flight LC/MS).

Synthesis of compound 3

Toluene (10 mL) was brought to reflux (35). Next, a solution of triphosgene (2.4 g; 8 mmol) in 10 mL toluene and a solution of compound **1** (1.98 mmol) in toluene (8 mL) were added and the resulting mixture was stirred at reflux temperature for 1 hour. The mixture was concentrated to a syrup and a solution of compound **2** (610 mg; 2.6 mmol) in THF (10 mL) and DBTL (100 μL) were added. The resulting mixture was stirred for 2 hours, after which the solvents were evaporated. The crude product was purified using flash silica gel column chromatography (5 % EtOAc/heptane) to obtain the product as a colorless oil (1.0 g; 1.3 mmol; 66%). R_f= 0.28 (10% EtOAc/heptane).

MALDI-TOF MS: m/z = 788.39 [M+Na]$^+$; 804.36 [M+K]$^+$

^{1}H NMR (300 MHz, CDCl$_3$) δ= 0.07 (s, 6H, Si(CH$_3$)$_2$), 0.89 (s, 9H, (CH$_3$)$_2$SiC(C$\underline{H}_3$)$_3$), 1.07 (s, 9H, (C$_6$H$_5$)$_2$SiC(C$\underline{H}_3$)$_3$), 1.35 (s, 12H, BOC(C$\underline{H}_3$)$_2$C(C$\underline{H}_3$)$_2$), 4.70 (s, 4H, CH$_2$OTBDMS, CH$_2$OTBDPS), 5.23 (s, 2H, CH$_2$OC(O)), 7.04 (m, 1H, NHC$_6\underline{H}_3$), 7.21-7.26 (m, 1H, NHC$_6\underline{H}_3$), 7.33-7.46 (m, 8H, BC$_6$H$_4$, Si(C$_6$H$_5$)$_2$), 7.65-7.69 (m, 4H, Si(C$_6$H$_5$)$_2$), 7.79-7.83 (d, J = 8.0 Hz, 2H, BC$_6$H$_4$), 7.98 (br d, 1H, NHC$_6\underline{H}_3$), 8.40 (br s, 1H, NH)

Peptide synthesis

Peptides Fmoc-O1Pen-r_9-k(Mtt)-resin and Fmoc-O1Pen-e(allyl)$_9$-y(allyl)-resin were synthesized on an automatic synthesizer (Prelude, Protein Technologies Inc.) by Fmoc solid-phase peptide synthesis (SPPS) using Rink amide resin (0.1 mmol), HBTU as the activating reagent, and N,N-Diisopropylethylamine (DIPEA) as base. D-amino acids are denoted in lower case and O1Pen represents 5-amino-3-oxapentanoic acid. The Mtt protecting group was selectively removed by incubating Fmoc-O1Pen-r_9-k(Mtt)-resin with 1.8% v/v trifluoroacetic acid (TFA) in dichloromethane with 2.0% v/v tri-isopropylsilane (TIS) as scavenger for 10 x 3 min after which tri-allyl DOTA (2.0 equiv, synthesized according to (37)) in NMP was added to the peptide resins and was reacted overnight in the presence of HBTU and DIPEA. After coupling, the Fmoc group was removed and both peptides were cleaved from the resin by a mixture of 95.0% v/v trifluoroacetic acid (TFA), 2.5% v/v tri-isopropyl silane (TIS), and 2.5% v/v MilliQ (Millipore) water for 4h, filtered, and precipitated in ice cold diethylether. The peptide pellets for H_2N-O1Pen-r_9-k(tri-allyl-DOTA)-NH_2 and H_2N-O1Pen-e(allyl)$_9$-y(allyl)-NH_2 were dissolved in MilliQ water and DMF, respectively, and purified by preparative reversed-phase high pressure liquid chromatography (RP-HPLC) using an Agilent 1200 apparatus, equipped with a C18 Zorbax column (length = 150 mm, diameter = 21.2 mm, particle size = 5.0 μm). The elution gradient was set from 5 to 30% of buffer B (0.1% TFA in acetonitrile) over 100 min for H_2N-O1Pen-r_9-k(tri-allyl-DOTA)-NH_2, and from 35% to 60% of buffer B over 100 min for H_2N-O1Pen-e(allyl)$_9$-y(allyl)-NH_2, where buffer A was 0.1% TFA in MilliQ (Millipore) water. The UV wavelength was preset at 210 and 254 nm. Purified peptides were analyzed by LC-MS.

Found masses: 2157.5 Da for H_2N-O1Pen-r_9-k(tri-allyl-DOTA)-NH_2 (Calcd. 2157.4 Da, 31.8 μmol), and 1842.9 Da for H_2N-O1Pen-e(allyl)$_9$-y(allyl)-NH_2 (Calcd. 1842.8 Da, 21.9 μmol).

References

1. Seifried HE, Anderson DE, Fisher EI, et al. A review of the interaction among dietary antioxidants and reactive oxygen species. *J Nutr Biochem.* 2007;18:567-579

2. Nadege B, Patrick L, Rodrigue R. Mitochondria: from bioenergetics to the metabolic regulation of carcinogenesis. *Front Bioscience.* 2009;14:4015-4034

3. Dalle-Donne I, Rossi R, Colombo R, et al. Biomarkersof oxidative damage in human disease. *Clin Chem.* 2006;52:601-623

4. Valko M, Leibfritz D, Moncol J, et al. Free radicals and antioxidants in normal physiological functions and human disease. *Int J Biochem Cell Biol.* 2007;39:44-84

5. Giordano FJ. Oxygen, oxidative stress, hypoxia, and heart failure. *J Clin Invest.* 2005;115:500-508

6. Dhalla NS, Elmoselhi AB, Hata T, et al. Status of myocardial antioxidants in ischemia-reperfusion injury. *Cardiovasc Res.* 2000;47:446-456

7. Siwik DA, Tzortzis JD, Pimental DR, et al. Inhibition of copper-zinc superoxide dismutase induces cell growth, hypertrophic phenotype, and apoptosis in neonatal rat cardiac myocytes in vitro. *Circ Res.* 1999;85:147–153

8. Rabkin SW, and Kong J. Nitroprusside induces cardiomyocyte death: interaction with hydrogen peroxide. *Am J Physiol Heart Circ Physiol.* 2000;279:H3089-H3100

9. Berry CE, and Hare JM. Xanthine oxidoreductase and cardiovascular disease: molecular mechanisms and pathophysiological implications. *J Physiol.* 2004;555:589-606

10. Tsutsui H, Kinugawa S, and Matsushima S. Oxidative stress and heart failure. *Am J Physiol Heart Circ Physiol.* 2011;301:H2181-H2190

11. Essick EE, Ouchi N, Wilson RM, et al.Adiponectin mediates cardioprotection in oxidative stress-induced cardiac myocyte remodeling. *Am J Physiol Heart Circ Physiol.* 2011;301:H984-H993

12. Shibata R, Izumiya Y, Sato K, et al. Adiponectin protects against the development of systolic dysfunction following myocardial infarction. *J Mol Cell Cardiol.* 2007;42:1065-1074

13. Lee D, Khaja S, Velasquez-Castano JC, et al. In vivo imaging of hydrogen peroxide with chemiluminescent nanoparticles. *Nat Mater.* 2007;6:765-769

14. Van de Bittner GC, Dubikovskaya EA, Bertozzi CR, et al. In vivo imaging of hydrogen peroxide production in a murine tumor model with a chemoselective bioluminescent reporter. *Proc Nat Acad Sci USA.* 2010;107:21316-21321

15. Panizzi P, Nahrendorf M, Wildgruber M, et al. Oxazine conjugated nanoparticle detects in vivo hypochlorous acid and peroxynitrite generation. *J Am Chem Soc.* 2009;131:15739-15744

16. Amir RJ, Pessah N, Shamis M, et al. Self-immolative dendrimers. *Angew. Chem. Int. Ed.* 2003;42:4494–4499

17. Avital-Shmilovici M, and Shabat D. Self-immolative dendrimers: a distinctive approach to molecular amplification. *Soft Matter* 2010;6:1073–1080

18. Erez R, and Shabat D. The azaquinone-methide elimination: comparison study of 1,6- and 1,4-eliminations under physiological conditions. *Org Biomol Chem.* 2008;6:2669–2672

19. Meyer Y, Richard J, Massonneau M, et al. Development of a new nonpeptidic self-immolative spacer. Application to the design of protease sensing fluorogenic probes. *Org Lett.* 2008;10:1517-1520

20. Meyer Y, Richard J, Delest B, et al. A comparative study of the self-immolation of para-aminobenzylalcohol and hemithioaminal-based linkers in the context of protease-sensitive fluorogenic probes. *Org Biomol Chem.* 2010;8:1777-1780

21. Perry-Feigenbaum R, Baran PS, and Shabat D. The pyridinone-methide elimination. *Org Biomol Chem.* 2009;7:4825-4828

22. Sella E, and Shabat D. Self-immolative dendritic probe for direct detection of triacetone triperoxide. *J. Am. Chem. Soc.* 2009, *131*, 9934–9936

23. Sella E, Lubelski A, Klafter J, et al. Two-component dendritic chain reactions: experiment and theory. *J Am Chem Soc.* 2010;132:3945-3952

24. Dickinson BC, and Chang CJ. A targetable fluorescent probe for imaging hydrogen peroxide in the mitochondria of living cells. *J Am Chem Soc.* 2008;130:9638-9639

25. Srikun D, Albers AE, and Chang CJ. A dendrimer-based platform for simultaneous dual fluorescence imaging of hydrogen peroxide and pH gradients produced in living cells. *Chem Sci.* 2011;2:1156-1165

26. Major Jourden JL, and Cohen SM. Hydrogen peroxide activated matrix metalloproteinase inhibitors: a prodrug approach. *Angew Chem Int Ed.* 2010;49:6795-6797

27. Kuivila HG, and Armour AG. Electrophilic displacement reactions IX. Effects of substituents on rates of reactions between hydrogen peroxide and benzeneboronic acid. *J Am Chem Soc.* 1957;79:5659-5662

28. Lippert AR, Van de Bittner GC, and Chang CJ. Boronate oxidation as a bioorthogonal reaction approach for studying the chemistry of hydrogen peroxide in living systems. *Acc Chem Res.* 2011;44:793-804

29. Zielonka J, Sikora A, Joseph J, et al. Peroxynitrite is the major species formed from different flux ratios of Co-generated nitrix oxide and superoxide. *J Biol Chem.* 2010;285:14210-14216

30. Sikora A, Zielonka J, Lopez M, et al. Direct oxidation of boronates by peroxynitrite: mechanism and implications in fluorescence imaging of peroxynitrite. *Free Rad Biol Med.* 2009;47:1401-1407

31. Pacher P, Beckman JS, and Liaudet L. Nitric oxide and peroxynitrite in health and disease. *Physiol Rev.* 2007;87:315-424

32. Leed MGD, Wolkow N, Pham DM, et al. Prochelators triggered by hydrogen peroxide provide hexadentate iron coordination to impede oxidative stress. *J Inorg Biochem.* 2011;105:1161-1172

33. Major Jourden JL, Daniel KB, and Cohen SM. Investigation of self-immolative linkers in the design of hydrogen peroxide activated metalloprotein inhibitors. *Chem Commun.* 2011;47:7968-7970

34. Sella E, and Shabat D. Self-immolative dendritic probe for direct detection of triacetone triperoxide. *Chem Commun.* 2008;44:5701-5703

35. Erez R, and Shabat D. The azaquinone-methide elimination: comparison study of 1,6- and 1,4-eliminations under physiological conditions. *Org Biomol Chem.* 2008;6:2669-2672

36. Lo LC, and Chu CY. Development of highly selective and sensitive probes for hydrogen peroxide. *Chem Commun.* 2003;21:2728-2729

37. Wängler B, Beck C, Wagner-Utermann U, et al. Application of tris-allyl-DOTA in the preparation of DOTA-peptide conjugates. *Tetrahed Lett.* 2006;47:5985-5988

Chapter **8**

General Discussion

In this thesis, the development of radiolabeled bioresponsive probes for molecular imaging, based on activatable cell penetrating peptides (ACPP), has been described. This Chapter provides some final remarks on three items:

1) Rationale to develop probes based on ACPP concept
2) Optimization of the ACPP probe design
3) ACPP probe development for novel targets

Rationale to develop probes based on ACPP concept

In Chapter 1, the design and *in vivo* application of bioresponsive imaging probes have been reviewed in detail. The term "bioresponsive imaging probes" refers to imaging probes that undergo a molecular change upon interaction with an endogenous target that leads to a change in imaging signal. For example, protease bioresponsive probes have been directed to the active site of the enzymes resulting in the cleavage and activation of the imaging probe offering a read-out of enzyme activity (1), while the conventional imaging probes for protease detection rely on a 1:1 probe-target binding fashion and detect enzyme abundance. Importantly, protease bioresponsive probes display signal amplification since the molecular target can continuously activate the imaging probe.

The bioresponsive imaging probe family can be divided into three major types. The first group consists of bioresponsive optical probes that show direct activation of the optical imaging label from a non-fluorescent state to a fluorescent state upon target interaction (1-5). The second group consists of bioresponsive MRI probes that show a change in relaxivity of the MRI contrast agent upon target interaction (4-8). Besides these two types of imaging probes, which both focus on the activation of the imaging label, the third type of bioresponsive imaging probes function through local retention and accumulation at the site of interaction with a chemical or biological endogenous stimulus (9-12). Importantly, this last type of imaging probes is not limited to one specific imaging modality. Hence, probes have been successfully developed for clinically relevant nuclear imaging strategies as well (13). In this thesis, the goal was to develop novel radiolabeled imaging probes belonging to the third class of bioresponsive imaging probes for future non-invasive detection of endogenous biomarkers in cardiovascular disease and cancer with nuclear imaging. Furthermore, a general imaging probe approach that can facilitate the detection of various biomarkers at the same time, in combination with a multiple isotope approach, is valuable for improved diagnosis. Therefore, we focussed on the development of radiolabeled bioresponsive imaging probes, based on activatable cell penetrating peptides (12). In these probes, the cell penetrating property of a polycationic peptide domain is efficiently masked by a polyanionic inhibitory domain that is conjugated to the polycationic domain by a target-specific substrate. This probe design allows the replacement of the substrate by other substrates, enabling tuning of the target-specificity. Cleavage of the substrate releases the polycationic peptide domain, followed by tissue association and accumulation of this peptide. We have developed a radiolabeled MMP-2/9 sensitive ACPP, containing a PLGLAG peptide

substrate, and this probe was studied in tumor-bearing mice (Chapter 2). Despite this probe showed an increased tumor uptake compared to muscle uptake, specific probe activation by MMPs in the tumor could not be shown. Instead the tumor uptake was quite likely due to activation of the probe in the blood and subsequent enhanced retention of the activated probe in the highly vascularized tumor. Therefore, several challenges need to be addressed to achieve clinical translation of ACPPs. Firstly, the protease-sensitive linker should be carefully chosen to prevent a-specific cleavage. Secondly, highly specific accumulation in the tissue of interest may be achieved by ACPPs that are exclusively sensitive to cell membrane bound enzymes that do not shed into the vasculature, thereby avoiding ACPP activation in blood.

Further optimization of the ACPP probe design

The ACPP imaging probes consist of three essential components:
-a cell penetrating domain containing an imaging label;
-a polyanionic inhibitory domain;
-and a target-specific substrate.

Polycationic cell penetrating peptide domain.
In this research, a nona-arginine d-peptide (r_9) was applied as cell penetrating peptide (CPP). This peptide shows efficient cellular uptake via macropinocytosis (14,15). The first step of cellular entry is the association of the guanidine residues of the CPP with sulfated glycans (particularly heparin sulfate) present on the cell membrane. Then, macropinocytotic uptake will lead to entrapment of the probe in intracellular vesicles, typically followed by endosomal escape into the cytoplasm. However, the precise mechanism of this escape remains unclear (16). In Chapter 3, it was demonstrated that an MMP-2/9 ACPP probe was locally activated in the infarcted myocardium resulting in probe retention, but with some probe wash-out from the infarcted myocardium overtime. CPPs have been subjected of intensive research over the last decades (16-21) and some other peptide domains, compared to R_9, have been found to show improved cell penetrating properties (19). In that study, ten different L-form CPPs were studied *in vitro* and *in vivo* (19). The peptides that displayed an increased cellular uptake compared to the polycationic R_9 sequence include an amphipathic-based peptide (KLALKLALKALKAALKLA) and an alternative polycationic peptide (RQIKIWFQNRRMKWKK) (19). Recently in another paper, it has been shown that by increasing the distance between arginine amino acids, the cellular uptake of polycationic CPPs is enhanced (20). Furthermore, the cell penetrating property of R_{10} was improved with higher peptide structural rigidity achieved by cyclization of the R_{10} peptide (21). The separation of the guanidinium groups in the cyclic structure was suggested as a critical factor governing the increased cell penetrating efficiency (21). In conclusion, the incorporation of alternative cell penetrating peptides may enhance the tissue retention by reducing probe wash-out of the activated ACPP. Another important aspect that may be taken into account is the *in vivo* biodistribution of cell penetrating peptides. We and others have

demonstrated that the poly-arginine cell penetrating peptide domain displays a strong liver uptake (19,22). Other cell penetrating peptides such as PKKKRKVK displayed a ~25-fold lower liver uptake, and accumulated predominantly in the kidneys (19). Replacement of the CPP r_9 with PKKKRKVK (or its D-peptide analog) in ACPP probes that show some background activation in the vasculature, *e.g.* the MMP-2/9 dACPP presented in Chapter 3, should reduce probe uptake by the liver. This may be valuable for the imaging of molecular targets that are close to the liver, such as MMP-2 and MMP-9 in cardiac remodeling.

Notably, the L-peptide R_9 was shown to be degraded rapidly in serum, which may have led to a loss in cell penetrating efficiency with respect to amphipathic-based CPPs (19). In our studies we employed the D-form based polycationic r_9 sequence, which has been shown to resist proteolysis (23). One may reason that the cellular uptake of D-peptides may be better compared to L-peptides. It was recently shown that the binding affinity of D-peptide r_9 for heparin sulfate (HS) was slightly larger than that for L-peptide R_9 (24). Nevertheless, L-peptide R_9 showed a stronger cellular uptake compared to D-peptide r_9 in HS-rich cell types, indicating that cell internalization is chirality dependent (24). The exact difference in probe recognition and cellular uptake between R_9 and r_9 is unfortunately not yet clarified (24).

For the application of ACPP in molecular imaging, local accumulation is critical, but internalization is not required. However, the potential application of ACPPs as vehicles for intracellular drug delivery is hampered if the activated domain is not efficiently internalized. Moreover, we showed that a fluorescein-conjugated CPP was mainly accumulated in endosomes without release into the cytoplasm (Chapter 2). For drug delivery applications, the attachment of an endosomal escape device to the ACPP probe may, therefore, be necessary to allow cytosolic delivery (25).

Polyanionic inhibitory domain

The function of the polyanionic inhibitory domain is to mask the cell penetrating property. We showed that the cell penetrating property of the polycationic r_9 d-peptide could be efficiently inhibited with a polyanionic e_9 d-peptide (Chapter 2). In the above sections other attractive cell penetrating peptides have been discussed. The potential application of these peptides in future ACPP imaging probes may also require optimization of the molecular structure of the inhibitory domain to ensure efficient masking of the cell penetrating property for the intact probe.

Target-specific substrate/trigger

In the ACPP imaging probes, the cell penetrating peptide and the inhibitory domain are fused by a substrate that is cleaved by the molecular target of interest. The choice of the substrate is directly associated with probe sensitivity and specificity. In many cases, the substrate can be degraded not only by the molecular target of interest, but also by other related molecular targets. For example, the family of matrix metalloproteinases (MMPs) can degrade multiple substrates, with considerable substrate overlap between individual MMPs (26). Given the fact that proteases such as MMPs have redundant functions, one may raise the question which probe type, either selective probes, sensitive to a specific protease, or broad-spectrum

cleavable probes, sensitive to a complete protease family, represent the optimal strategy for monitoring disease progression. In general, specific probes are very valuable firstly to monitor the particular biological role of a certain protease in disease progression and secondly to reveal a disease stage. Broad-spectrum probes may also be valuable to reveal a disease stage as in specific cases multiple members of a protease family are upregulated. Furthermore, broad-spectrum probes are useful for assessing the effect of drug therapy against all members of a protease family (27).

In case of MMP-2 and MMP-9 that show considerable substrate overlap, the development of a specific probe would be valuable. Namely, the overexpression of MMP-2 and MMP-9 in adverse cardiac remodeling after a myocardial infarction (MI) follows different time frames. MMP-9 predominantly plays a role in the early wound healing and inflammation response shortly after MI, while MMP-2 is mainly involved in the cardiac ECM remodeling phases (28). Detection of the individual MMPs would be valuable for staging, but substrates that show 100% specificity for one of these MMPs have not been reported so far. In Chapter 2, the substrate PLGLAG was used that showed sensitivity towards MMP-2, MMP-9 and to a limited extent MMP-14. In Chapter 5, the insertion of MMP-14 sensitive substrates into the ACPP imaging probe resulted in probes that were cleaved by MMP-14, but also by other MMP members. Molecular biology tools, such as phage display maturation screens, may be valuable in the search for more enzyme-specific substrates.

In most approaches, peptides have been applied as substrates to link the polycationic and polyanionic domain resulting in ACPP probes that can sense proteolytic activity. Using a self-immolative strategy as proposed in Chapter 7, the ACPP family may find application in the detection of the activity of non-proteolytic enzymes and detection of the production of molecular targets such as reactive oxygen and nitrogen species.

ACPP probe development for novel targets

In this thesis, the development of a radiolabeled ACPP imaging probe for MMP-2/9 has been described and this probe showed promise in the detection of cardiac remodeling (Chapter 3). A linear dependency was found between probe uptake and MMP-2 expression in heart of mice 10 days post myocardial infarction. An impressive 10-fold higher probe uptake was found in infarcted myocardium compared to remote myocardium. However, the MMP-2/9 sensitive dACPP showed also a strong liver uptake that may hamper the application of this probe in heart disease. Besides specific activation in infarcted heart tissue, the MMP-2/9 dACPP showed a considerable degree of activation in the vascular compartment, leading to the strong background uptake in the liver and other tissues. Therefore, the development of ACPPs which are only activated in the tissue of interest is highly valuable. In Chapter 5, we focused on the development of ACPPs for the cell membrane-associated matrix metalloproteinase-14 (MMP-14) that has been identified to be such a tissue-specific target showing increased activity in heart disease and cancer. In a small pilot study, this probe displayed increased uptake in infarcted heart tissue compared to remote heart tissue, and

this probe will be subject of further research to reveal the *in vivo* biodistribution and behavior in more detail. Next, we focused on the development of ACPP imaging probes for angiotensin converting enzyme (ACE) and hydrogen peroxide (H_2O_2). The designed ACE ACPPs were not activated by ACE and further research into the probe design is needed. A H_2O_2 ACPP, consisting of a H_2O_2 sensitive self-immolative trigger fusing the polycationic and polyanionic domains, is currently in development. Next to these targets, the ACPP imaging concept has been developed by others for the *in vitro* detection of several disease-related enzymes such as urokinase, enterokinase, prostate-specific antigen, elastase, and plasmin (12,29-31) as well as acidic conditions by employing a reduction-sensitive disulfide bridge between the polycationic and polyanionic domain (12). Recently, a fluorescently-labeled ACPP was developed for detection of thrombin in carotid atherosclerotic plaques (32).

With respect to heart disease, the activity of several enzymes has been reported to be elevated, and the non-invasive monitoring of the levels of these biomarkers may be valuable for diagnosis and staging. These biomarkers include aldosterone synthase (33-35) and chymase (36). These enzymes are, next to angiotensin converting enzyme (ACE), involved in the renin-angiotensin-aldosterone system (RAAS). Furthermore, thrombospondin 2 (37), and also members of the ADAM (a disintegrin and metalloprotease) family, *e.g.* ADAM-10, -12, -15 (38), ADAM-17 (39-41), and ADAMTS-1 (41), may be attractive for molecular imaging of heart disease. As mentioned earlier, for the development of successful bioresponsive ACPP-based imaging probes for one or more of the above biomarkers, target-specific substrates/triggers are crucial.

References

1. Mahmood U, and Weissleder R. Near-infrared optical imaging of proteases in cancer. *Mol Cancer Ther.* 2003;2:489-496

2. Law B, and Tung CH. Proteolysis: a biological process adapted in drug delivery, therapy, and imaging. *Bioconjug Chem.* 2009;20:1683-1695

3. Neefjes J, and Dantuma NP. Fluorescent probes for proteolysis: tools for drug discovery. *Nat Rev Drug Dis.* 2004;3:58-69

4. Razgulin A, Ma N, and Rao J. Strategies for in vivo imaging of enzyme activity: an overview and recent advances. *Chem Soc Rev.* 2011;40:4186-4216

5. Elias DR, Thorek DLJ, Chen AK, et al. In vivo imaging of cancer biomarkers using activatable molecular probes. *Cancer Biomarkers.* 2008;4:287-305

6. Tu C, Osborne EA, and Louie AY. Activatable T_1 and T_2 magnetic resonance imaging contrast agents. *Ann Biomed Eng.* 2011;39:1335-1348

7. Bonnet CS, and Toth E. Smart MR imaging agents relevant to potential neurologic applications. *Am J Neuroradiol.* 2010;31:401-409

8. Moats RA, Fraser SE, Meade TJ. A smart magnetic resonance imaging agent that reports on specific enzymatic activity. *Angew Chem Int Ed.* 1997;36:726-728

9. Teesalu T, Sugahara KN, Kotamraju VR, et al. C-end rule peptides mediate neuropilin-1-dependent cell, vascular, and tissue penetration. *Proc Natl Acad Sci USA.* 2009;106:16157–16162

10. Jaffer FA, Tung CH, Wykrzykowska JJ, et al. Molecular imaging of factor XIIIa activity in thrombosis using a novel, near-infrared fluorescent contrast agent that covalently links to thrombi. *Circulation.* 2004;110:170-176

11. Lepage M, Dow WC, Melchior M, et al. Noninvasive detection of matrix metalloproteinase activity in vivo using a novel MRI contrast agent with a solubility switch. *Mol Imaging.* 2007;6:393–403

12. Jiang T, Olson ES, Nguyen QT, et al. Tumor imaging by means of proteolytic activation of cell-penetrating peptides. *Proc Nat Acad Sci USA.* 2004;101:17867-17872

13. Chuang CH, Chuang KH, Wang HE, et al. In vivo positron emission tomography imaging of protease activity by generation of a hydrophobic product from a noninhibitory protease substrate. *Clin Cancer Res.* 2012;18:238-247

14. Nakase I, Niwa M, Takeuchi T, et al. Cellular uptake of arginine-rich peptides: roles for macropinocytosis and actin rearrangement. *Mol Ther.* 2004;10:1011-1022

15. Kaplan IM, Wadia JS, and DowdySF. Cationic TAT peptide transduction domain enters cells by macropinocytosis. *J Cont Release.* 2005;102:247-253

16. Van den Berg A, and Dowdy SF. Protein Transduction domain delivery of therapeutic macromolecules. *Curr Opin Biotech.* 2011;22:1-6

17. Walrant A, Bechara C, Alves ID, et al. Molecular partners for interaction and cell-internalization of cell-penetrating peptides: how identical are they? *Nanomedicine.* 2012;7:133-143

18. Wender PA, Galliher WC, Goun EA, et al. The design of guanidinium-rich transporters and their internalization mechanisms. *Adv Drug Deliv Rev.* 2008;60:452-472

19. Sarko D, Beijer B, Boy RG, et al. The pharmacokinetics of cell-penetrating peptides. *Mol Pharm.* 2010;7:2224-2231

20. Rothbard JB, Kreider E, VanDeusen CL, et al. Arginine-rich molecular transporters for drug delivery: role of backbone spacing in cellular uptake. *J Med Chem.* 2002;45:3612–3618

21. Lättig-Tünnemann G, Prinz M, Hoffmann D, et al. Backbone rigidity and static presentation of guanidinium groups increases cellular uptake of arginine-rich cell-penetrating peptides. *Nat Commun.* 2011;2:453

22. van Duijnhoven SMJ, Robillard MS, Nicolay K, et al. Tumor targeting of MMP-2/9 activatable cell-penetrating imaging probes is caused by tumor-independent activation. *J Nucl Med.* 2011;52:279–286

23. Elmquist A, and Langel U. In vitro uptake and stability study of pVEC and its all-D analog. *Biol Chem.* 2003;384:387–393

24. Verdurmen WPR, Bovee-Geurts PH, Wadhwani P, et al. Preferential uptake of L- versus D-amino acid cell-penetrating peptides in a cell type-dependent manner. *Chem Biol.* 2011;18:1000-1010

25. El-Sayed A, Futaki S, and Harashima H. Delivery of macromolecules using arginine-rich cell penetrating peptides: Ways to overcome endosomal entrapment. *AAPS J.* 2009;11:13-22

26. Greenlee KJ, Werb Z, and Kheradmand F. Matrix metalloproteinases in lung: multiple, multifarious, and multifaceted. *Physiol Rev.* 2007;87:69-98

27. Deu E, Verdoes M, and Bogyo M. New approaches for dissecting protease functions to improve probe development and drug discovery. *Nat Struct Mol Biol.* 2012;19:9-16

28. Vanhoutte D, Schellings M, Pinto Y, et al. Relevance of matrix metalloproteinases and their inhibitors after myocardial infarction: a temporal and spatial window. *Cardiovasc Res.* 2006;69:604-613

29. Goun EA, Shinde R, Dehnert KW, et al. Intracellular cargo delivery by an octaarginine transporter adapted to target prostate cancer cells through cell surface protease activation. *Bioconjug Chem.* 2006;17:787-796

30. Yuan X, Lin X, Manorek G, et al. Challenges associated with the targeted delivery of gelonin to claudin expressing cancer cells with the use of activatable cell penetrating peptides to enhance potency. *BMC Cancer.* 2011;11:61-70

31. Whitney M, Crisp JL, Olson ES, et al. Parallel in vivo and in vitro selection using phage display identifies protease dependent tumor targeting peptides. *J Biol Chem.* 2010;285:22532-22541

32. Olson ES, Whitney MA, Friedman B, et al. In vivo fluorescence imaging of atherosclerotic plaques with activatable cell-penetrating peptides targeting thrombin activity. *Integr Biol.* 2012;4:595-605

33. Brilla CG, Zhou G, Matsubara L, et al.. Collagen metabolism in cultured adult rat cardiac fibroblasts: response to angiotensin II and aldosterone. *J Mol Cell Cardiol.* 1994;26:809-820

34. Takeda Y, Yoneda T, Demura M, et al. Calcineurin inhibition attenuates mineralocorticoid-induced cardiac hypertrophy. *Circulation.* 2002;105:677-679

35. Sun Y, Zhang J, Lu L, et al. Aldosterone-induced inflammation in the rat heart: role of oxidative stress. *Am J Pathol.* 2002;161:1773-1781

36. MacFayden RJ, Lee AFC, Morton JJ, et al. How often are angiotensin II and aldosterone concentrations raised during chronic ACE inhibitor treatment in cardiac failure? *Heart.* 1999;82:57-61

37. Schroen B, Heymans S, Sharma U, et al. Thrombospondin-2 is essential for myocardial matrix integrity. Increased expression identifies failure-prone cardiac hypertrophy. *Circ Res.* 2004;95:515-522

38. Fedak PWM, Moravec CS, McCarthy PM, et al. Altered expression of disintegrin metalloproteinase and their inhibitor in human dilated cardiomyopathy. *Circulation.* 2006;113:238-245

39. Rocchiccioli JP, McMurray JJV, and Dominiczak. Biomarkers in heart failure: a clinical review. *Heart Fail Rev.* 2010;15:251-273

40. Wang X, Oka T, Chow FL, et al. Tumor necrosis factor-a-converting enzyme is a key regulator of agonist-induced cardiac hypertrophy and fibrosis. *Hypertension.* 2009;54:575-582

41. Manso AM, Elsherif L, Kang S, et al. Integrins, membrane-type matrix metalloproteinases and ADAMs: Potential implications for cardiac remodeling. *Cardiovasc Res.* 2006;69:574-584

Summary

Molecular imaging is recognized as a powerful tool to visualize and characterize biological processes at the cellular and molecular level *in vivo*. In most imaging approaches, molecular probes are used to bind to disease-specific biomarkers highlighting disease target sites. In recent years, a new subset of molecular imaging probes, known as bioresponsive molecular probes, has been developed. **Chapter 1** reviews the several types of these activatable imaging probes and its potential *in vivo* applicability.

The goal of this thesis was the design, synthesis, and *in vitro* and *in vivo* characterization of novel bioresponsive imaging probes based on the elegant concept of activatable cell penetrating peptides (ACPPs).

The experimental part of this thesis starts with the development of radiolabeled matrix metalloproteinase-2, -9 (MMP-2/9) activatable cell penetrating peptides. The matrix metalloproteinases -2 and -9 play an important role in angiogenesis and metastasis in cancer, and in adverse cardiac remodeling after myocardial infarction. In **Chapter 2**, it is shown that the proposed MMP-2/9 sensitive peptide-based imaging probes were successfully synthesized on the solid phase, and could be efficiently labeled with radio-isotopes. A dual-isotope labeled ACPP is presented that could discriminate between uptake of the activated probe and the integral probe and this ACPP was used to follow the activation process *in vivo.* Despite the probe showed specific sensitivity towards MMP-2 and MMP-9 *in vitro*, *in vivo* studies in tumor-bearing mice demonstrated that the ACPP was not activated in MMP-expressing tumor tissue, but most likely already in the circulation.

Chapter 3 describes the *in vivo* characterization of the radiolabeled MMP-2/9 ACPPs in a mouse model of myocardial infarction. In this model, infarct-specific activation and retention of the MMP-2/9 ACPP was observed, as was assessed by biodistribution studies using the dual-isotope labeled ACPP. A significant correlation was found between MMP-2/9 expression and the degree of probe activation in infarcted and remote areas of the hearts. Furthermore, ACPP retention in infarcted regions was successfully visualized *ex vivo* using autoradiography. Nevertheless, also ACPP activation in the circulation resulted in retention of the activated probe in the surrounding tissues, especially in the liver. Consequently, a strong background signal was observed.

Chapter 4 focuses on the development of long circulating MMP-2/9 sensitive ACPPs to achieve an extended exposure time to the target proteases. Incorporation of two different albumin ligands i.e. palmitic acid (Palm) and deoxycholic acid (DOCA), in the ACPPs resulted in a strong increase in circulation time of these albumin-binding ACPPs compared to the ACPP without albumin ligand. *In vivo* biodistribution studies in a mouse model of myocardial infarction pointed towards local activation of a DOCA-conjugated ACPP in areas of cardiac remodelling. Despite the increased circulation time of this probe, the infarct-to-remote ratios and absolute probe uptake in infarcted areas of the heart was comparable to dACPP.

In view of the findings discussed in Chapters 2 and 3, we hypothesized that ACPPs sensitive for tissue-specific biomarkers should exhibit reduced activation in the vasculature and background probe uptake of the activated ACPP in all tissues. Consequently, this should improve the signal-to-background ratios of these probes. Therefore, **Chapter 5** and **Chapter 6** are dedicated to the development of radiolabeled ACPPs activatable by membrane-type matrix metalloproteinase-1 (MMP-14), and the transmembrane protein angiotensin converting enzyme (ACE), respectively.

In **Chapter 5**, the design and synthesis of MMP-14 sensitive ACPPs (ACPP-14) is addressed. MMP-14, like MMP-2 and -9, plays an important role in adverse cardiac remodeling. The most effective ACPP-14 probe was selected by employing MMP-14 sensitivity and enzyme specificity assays. This probe showed efficient cellular uptake upon activation. In a pilot *in vivo* biodistribution study, the level of *in vivo* background activation in the vasculature was decreased compared to MMP-2/9 ACPP (Chapters 2 and 3), while an increased uptake in infarcted heart tissue was observed compared to remote heart tissue, warranting further research into the *in vivo* biodistribution of this probe.

Chapter 6 presents the development of an ACPP sensitive for the carboxy exopeptidase angiotensin converting enzyme (ACE). Upregulated heart-associated ACE activity has been related to adverse cardiac remodeling in nearly all cardiovascular diseases. Using molecular modeling approaches, various ACE ACPPs were designed to fit into the catalytic pocket of ACE. These probes were subsequently synthesized, but unfortunately showed no *in vitro* sensitivity towards ACE.

Chapter 7 deals with the design of an ACPP that responds to hydrogen peroxide (H_2O_2). Production of reactive oxygen species like H_2O_2 typically occurs during elevated oxidative stress and contributes to the pathogenesis of several diseases, including cardiac ischemia-reperfusion injury. In this Chapter, we propose to extend the application of the ACPP imaging concept to the detection and imaging of H_2O_2 after cardiac ischemia-reperfusion injury. The suggested H_2O_2 ACPP uses a H_2O_2 self-immolative linker moiety to which the cell penetrating polycationic peptide and the polyanionic peptide are conjugated. H_2O_2-triggering initiates self-immolation of the linker, and thereby releases the polycationic cell penetrating peptide in H_2O_2-producing tissues. This H_2O_2 ACPP probe is currently in development.

Finally, **Chapter 8** concludes with a general discussion on the preceding chapters, followed by some future perspectives of activatable cell penetrating peptide imaging probes.

List of Publications

J.L. Vinkenborg, **S.M.J. van Duijnhoven**, and M. Merkx
Reengineering of a Chelating Fluorescent Zinc Sensor Yields the First Genetically Encoded Cadmium Probe.
Chemical Communications 2011; 47: 11879-11881.

S.M.J. van Duijnhoven, M.S. Robillard, K. Nicolay, and H. Grüll
Tumor Targeting of MMP-2/9 Activatable Cell Penetrating Imaging Probes Is Caused by Tumor-Independent Activation.
Journal of Nuclear Medicine 2011; 52: 279-286.

S.M.J. van Duijnhoven, M.S. Robillard, K. Nicolay, and H. Grüll
In Vivo Characterization of Dual Isotope Radiolabeled Cell Penetrating Imaging Probes Activatable by Tumoral Matrix Metalloproteinase-2 [abstract].
Nuclear Medicine and Biology 2010, 37: 693.

L.W.E. Starmans, **S.M.J. van Duijnhoven**, R. Rossin, S. Aime, M.J.A.P. Daemen, K. Nicolay, and H. Grüll
SPECT Imaging of Thrombi Using Fibrin-Binding Peptides.
Submitted.

S.M.J. van Duijnhoven, M.S. Robillard, S. Langereis, and H. Grüll
Bioresponsive Molecular Imaging Probes [review].
In preparation.

S.M.J. van Duijnhoven, M.S. Robillard, K. Nicolay, and H. Grüll
In Vivo Biodistribution of MMP-2/9 Activatable Cell-Penetrating Imaging Probes in Tumor-Bearing Mice With High MMP and Low Tumoral MMP Expression.
In preparation.

S.M.J. van Duijnhoven, M.S. Robillard, S. Hermann, M. Kuhlmann, M. Schäfers, K. Nicolay, and H. Grüll
In Vivo Detection of Cardiac Remodelling Using Radiolabeled MMP-2/9 Activatable Cell-Penetrating Imaging Probes.
In preparation.

S.M.J. van Duijnhoven, M.S. Robillard, K. Nicolay, and H. Grüll
Towards the Molecular Imaging of Transmembrane Matrix Metalloproteinases Using Activatable Cell-Penetrating Peptides.
In preparation.

Conference Proceedings (first author only)

S.M.J. van Duijnhoven, M.S. Robillard, K. Nicolay, and H. Grüll.
MMP-2/9 Detection in Cardiac Remodelling by Activatable Cell Penetrating Imaging Probes.
Imaging in 2020 Conference, September 2011, Jackson, WY.

S.M.J. van Duijnhoven, M.S. Robillard, K. Nicolay, and H. Grüll.
Characterization of Radiolabeled MMP-2/9 Activatable Cell Penetrating Imaging Probes in Tumor-Bearing Mice.
Imaging in 2020 Conference, September 2011, Jackson, WY.

S.M.J. van Duijnhoven, M.S. Robillard, K. Nicolay, and H. Grüll.
In Vivo Biodistribution of Radiolabeled MMP-2/9 Activatable Cell Penetrating Peptides in a Mouse Model of Myocardial Infarction.
World Molecular Imaging Congress, September 2011, San Diego, CA.

S.M.J. van Duijnhoven, M.S. Robillard, K. Nicolay, and H. Grüll.
Tumor Targeting Mechanism of Radiolabeled MMP-2/9 Activatable Cell Penetrating Imaging Probes.
World Molecular Imaging Congress, September 2011, San Diego, CA.

S.M.J. van Duijnhoven, M.S. Robillard, K. Nicolay, and H. Grüll.
Tumor Targeting Mechanism of MMP-2/9 Activatable Cell Penetrating Imaging Probes.
Biomedica Life Science Summit, April 2011, Eindhoven, The Netherlands.

S.M.J. van Duijnhoven, M.S. Robillard, K. Nicolay, and H. Grüll.
In Vivo Characterization of Dual Istotope Radiolabeled Cell Penetrating Imaging Probes Activatable by Tumoral Matrix Metalloproteinase-2.
Terachem Symposium, September 2010, Bressanone, Italy.

S.M.J. van Duijnhoven, M.S. Robillard, K. Nicolay, and H. Grüll.
In Vivo Biodistribution of Radiolabeled Matrix Metalloproteinase-2 Activatable Cell Penetrating Peptides.
5th European Molecular Imaging Meeting, May 2010, Warsaw, Poland.

Curriculum Vitae

Sander van Duijnhoven was born in Boekel, the Netherlands, on February 27, 1984. He completed the pre-university education (VWO) in 2002 at the Udens College in Uden, the Netherlands. In the same year, he started studying Biomedical Engineering at the Eindhoven University of Technology, the Netherlands. During his studies, he performed internships in the laboratory of Dr. D. Fygenson at the University of California, Santa Barbara (USA), and in the laboratory of Dr. P. Dawson at the Scripps Research Institute, La Jolla (USA), where he developed DNA nanotube-based and peptide-based molecular imaging probes, respectively. During his final research project he worked in the group of Prof. Dr. E.W. Meijer and Dr. M. Merkx on the development and characterization of genetically encoded zinc sensors. After receiving his Master of Science degree in 2008, he started as a Ph.D. student in the Biomedical NMR research group at the Eindhoven University of Technology under supervision of Prof. Dr. H. Grüll and Prof. Dr. K. Nicolay. The main goal of his project was to design and characterize bioresponsive molecular imaging probes to allow the non-invasive detection of biomarkers associated with cancer and adverse cardiac remodeling. The most important results of his Ph.D. research are described in this thesis.

172

Dankwoord

Met het tot stand komen van dit proefschrift is er een einde gekomen aan een plezierige en leerzame promotieperiode. Graag maak ik dan ook van de gelegenheid gebruik om iedereen te bedanken die heeft bijgedragen aan de realisatie van dit proefschrift. Er zijn een aantal mensen die ik in het bijzonder wil vermelden.

Als eerste wil ik mijn promotor Holger Grüll noemen. Holger, jouw enthousiasme tijdens ons eerste gesprek over de mogelijkheden om aan peptide-gebaseerde imaging probes te gaan werken, heeft zeker bijgedragen aan mijn keuze om het promotieonderzoek onder jouw begeleiding uit te gaan voeren. Ik vind het dan ook erg mooi om te zien dat jouw enthousiasme en eigen stijl van college geven door de BMT studenten wordt gewaardeerd en dat jij dit jaar weer de BMT-docenten award hebt gewonnen. De grote vrijheid die ik tijdens mijn promotie-onderzoek van jou kreeg, heeft ook zeker bijgedragen aan mijn persoonlijke ontwikkeling als zelfstandig onderzoeker en daar ben ik jou zeer dankbaar voor. Ik wil je ook bedanken voor de aanhoudende steun en de moeite die jij genomen hebt om mij in contact te brengen met verschillende laboratoria in de VS, wat hopelijk zal gaan leiden tot een succesvolle wetenschappelijke periode in Stanford. Ik hoop dan ook dat onze wegen elkaar in de toekomst nog eens zullen kruisen.

Daarnaast wil ik ook mijn copromotoren Marc Robillard en Klaas Nicolay bedanken. Marc, ik heb jouw begeleiding als zeer plezierig ervaren. Hierbij denk ik aan de waardevolle discussies en het kritisch lezen van de verschillende manuscripten. Ik wens je alle succes toe met je eigen bedrijf en ik hoop dat het een groot succes gaat worden. Klaas, graag zou ik jou samen met Holger willen bedanken dat jij mij de kans hebt gegeven om het promotietraject binnen de Biomedical NMR groep, in samenwerking met Philips Research, uit te voeren. Ik ben je zeer erkentelijk voor jouw snelle en waardevolle correcties, voor jouw ondersteuning om mijn wetenschappelijke carrière voort te zetten en voor jouw input tijdens de vakgroepmeetings.

Dank aan prof. dr. ir. Luc Brunsveld en prof. dr. Tilman Hackeng voor de deelname aan de kerncommissie en de beoordeling van mijn proefschrift. I would like to thank prof. dr. Michael Schäfers for the review of my thesis manuscript. Ik wil tevens prof. dr. Otto Boerman noemen voor het plaatsnemen in mijn promotiecommissie.

Ik zou ook graag Maarten Merkx en Wencke Adriaens willen noemen voor de mogelijkheden om gebruik te maken van de peptide synthesizer. Maarten, ik heb het altijd plezierig gevonden om met jou zo nu en dan over mijn onderzoek te praten en ik wil jou ook bedanken voor de periode dat ik bij jou in het laboratorium mijn afstudeerwerk kon doen. Jij hebt me de eerste stappen in de onderzoekswereld laten zetten. Dit is mij zeer goed bevallen en heeft ook zeker een rol gespeeld in de keuze om te gaan promoveren. Wencke, jij stond altijd klaar voor praktische zaken en ik vond het altijd gezellig om bij te kletsen als ik weer eens peptides kwam maken.

Ik wil Marloes en haar familie bedanken voor hun hulp met het ontwerp van de omslag. Ik ben Marloes ook dankbaar voor de taalkundige correcties van dit dankwoord. Marloes, ik hoop dat we het samen nog lang leuk gaan hebben.

Ik wil mijn broer Vincent en Marijn bedanken dat jullie mijn paranimfen willen zijn. Hierbij wil ik ook de vriendengroep bedanken voor alle leuke dingen die wij samen hebben gedaan in de afgelopen jaren en ik hoop dat wij dit in de toekomst zullen blijven doen. Als laatste wil ik naast mijn broer ook mijn zus Astrid en natuurlijk mijn ouders noemen. Zij hebben mij altijd gesteund tijdens mijn studie en promotie en hebben mij lekker mijn ding laten doen, ook al betekende dat ik pas regelmatig na het avondeten thuis kwam van het werk. Pap en mam, ik heb het thuis altijd goed gehad en ik heb op een fijne manier het schrijven van mijn proefschrift kunnen afronden.

Bedankt,

Sander